

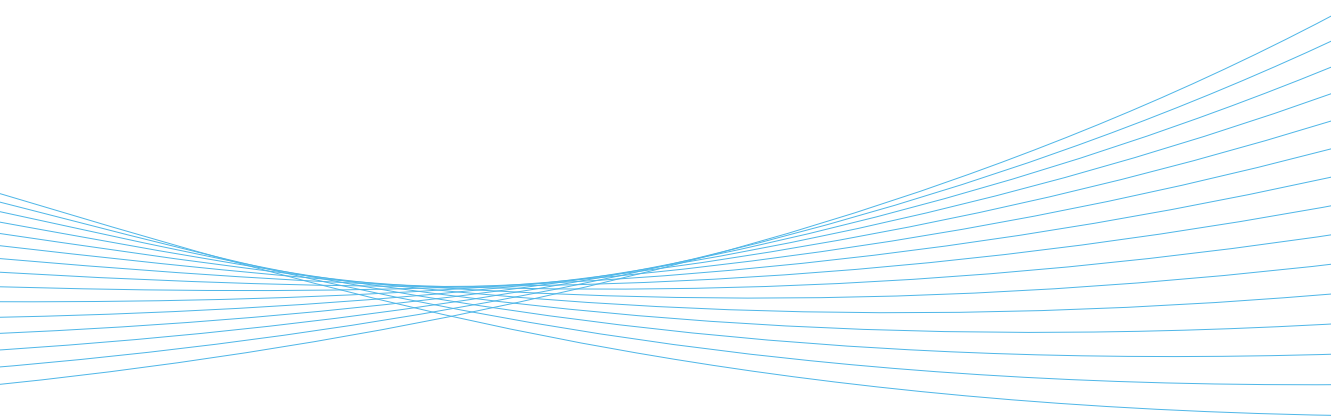


ILMATIETEEN LAITOS  
METEOROLOGISKA INSTITUTET  
FINNISH METEOROLOGICAL INSTITUTE

149  
CONTRIBUTIONS

# SEASONAL SNOW SURFACE ROUGHNESS AND ALBEDO

**KATI ANTTILA**





# Seasonal snow surface roughness and albedo

Kati Anttila

Faculty of Science  
Geophysics  
University of Helsinki  
Helsinki, Finland

Academic dissertation

To be presented, with the permission of the Faculty of Science of the University of Helsinki, for public criticism in E204 auditorium at Physicum (Gustaf Hällströmin katu 2 A, Helsinki) on April 26<sup>th</sup>, 2019, at 12 o'clock noon.

Helsinki, 2019

- Supervisors Dr. Terhikki Manninen  
Meteorological Research, Satellite and Radar Applications  
Finnish Meteorological Institute
- Research Professor Sanna Kaasalainen  
Navigation and Positioning, Sensors and Indoor Navigation  
Finnish Geospatial Research Institute of the National Land survey of Finland
- Professor (emeritus) Matti Leppäranta  
Institute for Atmospheric and Earth System Research/ Physics  
University of Helsinki
- Pre-examiners
- Dr. Lasse Makkonen  
VTT Technical Research Centre of Finland
- Dr. Ghislain Picard  
Institut des Géosciences de l'Environnement  
Université Grenoble Alpes, France
- Custos Professor Petteri Uotila  
Institute for Atmospheric and Earth System Research/ Physics  
University of Helsinki
- Opponent Professor Richard Essery  
School of Geosciences  
University of Edinburgh

ISBN: 978-952-336-063-1 (paperback)

ISBN: 978-952-336-064-8 (pdf)

ISSN: 0782-6117



Julkaisija  
Ilmatieteen laitos, ( Erik Palménin aukio 1)  
PL 503, 00101 Helsinki

Julkaisun sarja, numero ja raporttikoodi  
Finnish Meteorological Institute Contributions 149,  
FMI-CONT-149  
Julkaisuaika Huhthikuu 2019

---

Tekijä Kati Anttila

---

Nimeke

Kausittaisen lumipeitteen pinnan karkeus ja albedo

---

Tiivistelmä

Tämä väitöskirja käsittelee kausittaisen lumipeitteen pinnan karkeutta ja kirkkautta hyödyntäen optista satelliittiaineistoa ja laserkeilausta. Maan pinnan kaukokartoitus tarvitsee tietoa maan pinnan säteilyominaisuuksista. Lumipinnat heijastavat suurimman osan auringosta tulevasta säteilystä takaisin ilmakehään ja avaruuteen. Kausittainen lumipeite kattaa laajan alueen pohjoisen pallonpuoliskon maa- alasta. Alueellisen kattavuutensa ja kirkkautensa vuoksi sillä on merkittävä vaikutus maapallon energiataseeseen ja siten ilmastoon. Lumipinnan heijastusominaisuudet, kuten esimerkiksi pinnan karkeus, vaikuttavat suoraan lumipinnan kirkkauteen. Tässä väitöskirjassa on tarkasteltu kahta lumen pinnan karkeuden mittaamenetelmää. Ensimmäinen näistä tekniikoista perustuu lumeen asetetun mustan levyn valokuvaamiseen. Levystä ja lumipinnasta otetusta kuvasta etsitään automaattisesti lumipinnan profiili. Tämä tekniikka on helppokäyttöinen ja luotettava myös kenttäolosuhteissa. Sillä saadaan kerättyä tietoa lumen pinnan karkeudesta alle millimetrin tarkkuudella. Toisessa mittaamenetelmässä laserkeilainta liikutetaan moottorikelkalla. Näin saadaan katettua laaja alue, josta syntyy 3D havaintoja.

Pinnan karkeutta kuvaavien suureiden arvoihin vaikuttaa analysoidun profiilin pituus tai alueen laajuus. Kaukokartoituksen kannalta on oleellista mitata pinnankarkeutta kaikissa sovellukselle oleellisissa mittakaavoissa. Maan pinnan sirontamallit käyttävät pinnan karkeuden kuvaamiseen vain yhtä suuretta. Siten tämän suureen tulisi sisältää tietoa useista mittakaavoista. Tässä väitöskirjassa kerättiin Sodankylän alueelta 669 lumiprofiilia levymenetelmää käyttäen. Nämä profiilit analysoitiin käyttäen suureita, jotka kuvaavat profiilin korkeusvaihtelun riippuvuutta mitatusta matkasta ja sisältävät siten tietoa useista mittakaavoista. Käyttämällä näitä suureita kyettiin erottelemaan eri lumipintoja niiden iän ja lumityypin mukaan.

Satelliittien instrumentit mittaavat kerralla laajoja alueita. Maan pinnalla tehtävillä pistemäisiä alueita kuvaavilla havainnoilla selvitetään, kuinka laadukkaita satelliittituotteet, kuten lumi- ja albedotuotteet, ovat. Koska pintahavaintojen ja satelliittihavaintojen kattamat alueet eivät ole samat, itse havainnotkaan eivät täysin vastaa toisiaan. Laserkeilausaineistot kattavat laajempia alueita kuin perinteisin menetelmin tuotetut havainnot ja ovat siten lupaavia satelliittiaineistojen arviointiin. Tämän väitöskirjan sisältämä tutkimus lasersäteiden käyttäytymisestä lumipinnoilla edistää laserkeilausaineistojen käytettävyyttä lumeen liittyvässä tutkimuksessa ja satelliittiaineistojen laadun määrittämisessä. Tulosten mukaan kuivasta lumesta lasersäde heijastuu takaisin aivan lumen pinnasta, kun taas märässä lumessa se heijastuu noin 1 cm syvyydestä. Takaisin heijastuneen lasersäteiden kirkkaus riippuu tulokulmasta samalla tavalla erityyppisillä lumipinnoilla. Siten tulokulman vaikutus laserhavainnon kirkkauteen voidaan korjata samalla tavalla kaikilla mitatuilla lumipinnoilla.

Tämän väitöskirjan viimeisessä osassa tutkittiin kausittaisen lumipeitteen peittämien alueiden pinnan kirkkauden (albedon) ja sulamiskauden ajankohdan muutoksia vuosina 1982-2015 pohjoisen pallon puoliskon maa-alueilla leveyspiirien 40°N ja 80°N välillä. Tutkimus keskittyi sulamiskautta edeltävään pinnan kirkkauteen, joka oli muuttunut huomattavasti boreaalisen metsävyöhykkeen alueella. Muutos oli erisuuntaista eri alueilla. Tundralla sulamista edeltävä pinnan kirkkaus ei ollut muuttunut. Sulamiskausi oli aikaistunut Keski-Siperian ylängöllä ja pidentynyt Kiinan, Mongolian ja Venäjän rajaa ympäröivällä alueella sekä Kanadan Kalliovuorten pohjois-osissa. Pinnan kirkkauden muutokset olivat sidoksissa kasvillisuuden muutoksiin, kun taas sulamiskauden ajankohdan muutoksiin vaikuttivat enemmän ilmastolliset tekijät.

Tämä väitöskirja parantaa kausittaisen lumipeitteen pinnan sirontaominaisuuksien ymmärtämistä ja sen tuloksia voidaan käyttää kaukokartoitusaineistojen ja ilmastomallien kehittämisessä.

---

Julkaisijayksikkö

Ilmatieteen laitos

---

Luokitus (UDK) 551.32, 528.8, 550.3

Asiasanat lumi, albedo, kaukokartoitus, laserkeilaus

---

ISSN ja avainnime

0782-6117 Finnish Meteorological Institute Contributions

---

ISBN

978-952-336-063-1 (nid.) 978-952-336-064-8 (pdf)

Kieli

englanti

Sivumäärä

162

---



Published by Finnish Meteorological Institute  
(Erik Palménin aukio 1),  
P.O. Box 503  
FIN-00101 Helsinki, Finland

Series title, number and report code of publication  
Finnish Meteorological Institute Contributions 149,  
FMI-CONT-149  
Date April 2019

---

Author Kati Anttila

---

Title Seasonal snow surface roughness and albedo

---

Abstract

The topic of this dissertation is the seasonal snow surface roughness and albedo. These are studied using optical satellite data and terrestrial laser scanning.

The use of remote sensing data requires knowledge on the optical properties of the measured surface. For snow, these properties are affected by surface roughness. In this dissertation, two different methods for measuring snow surface roughness were validated and used in the field. One of them is based on plate photography. It is easy to use in the field and able to study surface features in sub-millimeter scale. The other method is based on mobile laser scanning and is able to produce 3D surface descriptions of large areas. The plate-photography-based method was used in the field to gather 669 profiles of the snow surface. The profiles were analyzed using multiscale parameters.

The validation of satellite data requires observations at the surface. This validation data typically consists of pointwise measurements, whereas the satellite data observations cover larger areas. Laser scanning provides data that cover larger areas, thus more in line with the satellite data. This could in the future be used for satellite data validation. The usability of laser scanning data on snow surfaces was improved by studying the incidence angle dependency of the laser scanning intensity data on different snow types. A function for correcting the incidence angle effect on all measured snow types was developed. The backscattering of laser beam on snow surface was found to take place at the very surface for dry snow, and within 1cm depth for wet snow.

The final part of this dissertation studies the changes in surface albedo prior to melting and the timing of the melt season in Northern Hemisphere land areas between 40°N and 80°N. The albedo prior to melt had changed significantly in the boreal forest area, but not in the tundra. The direction of change is different in different areas. The melt season takes place at the same time of year for most of the study area, but for Central Siberian Plane the melt season takes place earlier. In Northern Canadian Rocky Mountains and in the area around the borders of Russia, China and Mongolia the melt starts earlier and ends later, thus resulting in longer melt seasons. The changes observed in the pre-melt albedo are related to vegetation, whereas the melt season timing is more related to the climatic parameters.

The results of this dissertation can be used in developing remote sensing data and climate models through improved understanding of seasonal snow surface roughness and albedo.

---

Publishing unit Finnish Meteorological Institute

---

Classification (UDC) 551.32, 528.8, 550.3    Keywords: snow, albedo, laser scanning, remote sensing

---

ISSN and series title

0782-6117 Finnish Meteorological Institute Contributions

---

ISBN	Language	Pages
978-952-336-063-1 (nid.) 978-952-336-064-8 (pdf)	English	162

---





# PREFACE

The work presented in this dissertation was carried out both at the former Finnish Geodetic Institute and The Finnish Meteorological Institute in 2009-2018. During these years I have come to learn that being a scientist is not about what you know, it's what the people around you know. It is never possible to know everything you need, so having people around you whose skills complement yours is essentially important. I have been surrounded by skillful and kind people whose support and expertise has been invaluable.

First and foremost I would like to express my deepest gratitude to my advisors, Dr. Terhikki Manninen and Professor Sanna Kaasalainen. Besides all the skill you need while being a scientist, you have taught me integrity and persistence. You have shown me how to survive in the world of science as it is today and supported me on the rocky parts of the path. Your passion and commitment is truly inspiring.

I also wish to thank my supervisor from the university, Professor (emeritus) Matti Leppäranta and the custos for this defense, Professor Petteri Uotila. You have served as a link to the university and have guided me through the jungle of the changing university protocol.

I thank Professor Essery for agreeing to be the opponent for this dissertation, and Dr. Ghislain Picard and Dr. Lasse Makkonen for their constructive comments as pre-examiners. These comments have improved the readability and content of is introduction.

Most of the daily work is done with the group members and co-authors of the papers included in this dissertation: Terhikki, Sanna, Panu, Aku, Niilo, Emmihenna, Antero, Harri, Teemu, Olli, Anssi, Anttoni, Elena, Viivi, Kerttu, Ljuba, Vesa, Aulikki, Tuure. Your effort and support on the stormy seas of publishing and project work is truly appreciated. Your work made this dissertation possible.

I also wish to thank my colleagues at FMI and FGI, with whom I have had so many inspiring and supportive conversations over the years on all aspects of life. You have offered me support when times have been rough and helped me organize my thoughts when I have lost the direction and big picture. You have helped me laugh at the obscurities and unfairness. The work of a scientist today is project work in international teams. I wish to thank my colleagues in the CM SAF and H SAF projects teams, DWD, SMHI, KNMI, MeteoSwiss, RMI, UKMO, SYKE, MeteoFrance and CNRS.

Besides being a job, the doctoral studies are a process of personal growth. I wish to thank my friends and relatives for the invaluable support you have given me. You have helped me forget work from time to time and reminded me of the real life. You have helped me put things in perspective and reminded me of the importance of laughter.

Finally, I would like to thank my parents and sister for their never-ending faith in me, also in times when my own faith has been missing. I thank you for your patience and support and your efforts to create circumstances that enable me to concentrate on the work at hand. Without you I would never have gotten to where I am now. You remind me by existing, that with or without PhD, life will continue. Now at the final parts of this project I feel that this whole path is a proof on what you have taught me: things do tend to work out.

Helsinki, 13<sup>th</sup> November 2018

Kati Anttila



# CONTENTS

<b>PREFACE .....</b>	<b>5</b>
<b>CONTENTS.....</b>	<b>5</b>
<b>LIST OF PUBLICATIONS AND AUTHOR'S CONTRIBUTION .....</b>	<b>6</b>
<b>ABBREVIATIONS .....</b>	<b>8</b>
<b>SYMBOLS .....</b>	<b>9</b>
<b>1. INTRODUCTION.....</b>	<b>10</b>
<b>2. LIGHT TRANSFER, OPTICAL PROPERTIES AND ALBEDO OF SNOW .....</b>	<b>13</b>
<b>3. SURFACE ROUGHNESS OF SEASONAL SNOW .....</b>	<b>17</b>
3.1. Surface roughness parameters.....	18
3.2. Methods for measuring surface roughness of snow.....	20
3.3. Plate photography method .....	21
3.4. Plate method results .....	23
<b>4. LASER SCANNING OF SNOW COVERED SURFACES .....</b>	<b>27</b>
4.1. Depth of backscatter .....	29
4.2. The incidence angle dependency of the intensity of laser backscatter from different snow surfaces .....	34
4.3. Mobile laser scanning measurements of snow surface roughness .....	37
<b>5. THE ALBEDO OF THE AREAS COVERED BY SEASONAL SNOW.....</b>	<b>47</b>
5.1. Changes in surface albedo prior to melt in areas covered by seasonal snow	48
5.1.1. Methods for retrieving melt season timing and albedo .....	49
5.1.2. Trends in surface albedo prior to melt .....	50
5.1.3. Trends in melt season timing .....	53
<b>6. CONCLUSIONS .....</b>	<b>56</b>
<b>REFERENCES .....</b>	<b>59</b>



# LIST OF PUBLICATIONS AND AUTHOR'S CONTRIBUTION

This dissertation contains an introductory review, followed by five research papers. In the introductory part, the articles are referred to by their roman numerals.

- I** Manninen, T., Anttila, K., Karjalainen, T., & Lahtinen, P. (2012). Automatic snow surface roughness estimation using digital photos. *Journal of Glaciology*, 58(211), 993-1007.

In paper I Anttila took part in planning the calibration measurements, made the measurements, and participated in the analysis of the calibration measurements and writing the paper.

- II** Anttila, K., Manninen, T., Karjalainen, T., Lahtinen, P., Riihelä, A., & Siljamo, N. (2014). The temporal and spatial variability in submeter scale surface roughness of seasonal snow in Sodankylä Finnish Lapland in 2009–2010. *Journal of Geophysical Research: Atmospheres*, 119(15), 9236-9252.

In paper II Anttila took part in the field measurements, having conducted most of the 2010 plate measurements and some of the snow pit measurements. She analyzed the extracted profiles and snow pit data and wrote most of the paper.

- III** Kukko, A., Anttila, K., Manninen, T., Kaasalainen, S., & Kaartinen, H. (2013). Snow surface roughness from mobile laser scanning data. *Cold Regions Science and Technology*, 96, 23-35.

In paper III Anttila made the plate measurements and the data analysis on the plate and laser scanning profiles. She also wrote the paper together with the first author A. Kukko.

- IV** Anttila, K., Hakala, T., Kaasalainen, S., Kaartinen, H., Nevalainen, O., Krooks, A., ... & Jaakkola, A. (2016). Calibrating laser scanner data from snow surfaces: Correction of intensity effects. *Cold Regions Science and Technology*, 121, 52-59.

In paper IV Anttila planned and conducted the measurements with help from the other authors. She also analyzed the results and wrote most of the paper.

- V** Anttila, K., Manninen, T., Jaaskelainen, E., Riihela, A., & Lahtinen, P. (2018). The Role of Climate and Land Use in the Changes in Surface Albedo Prior to Snow Melt and the Timing of Melt Season of Seasonal Snow in Northern Land Areas of 40°N–80°N during 1982–2015. *Remote Sensing*, 10(10), 1619, <https://doi.org/10.3390/rs10101619>

In paper V Anttila analyzed the extracted melt season parameters and wrote most of the paper.



# ABBREVIATIONS

ALS	Airborne Laser Scanning
BRDF	Bidirectional Reflectance Distribution Function
CLARA-A2 SAL	Satellite Application Facility for Climate Monitoring (CM SAF, funded by EUMETSAT) Clouds, Albedo and RAdiation second release Surface ALbedo (CLARA-A2 SAL) data record
CM SAF	Satellite Application Facility for Climate Monitoring
ECMWF	The European Centre for Medium-Range Weather Forecasts
ECV	Essential climate variable
ERA-Interim	Reanalysis data record by ECMWF
EUMETSAT	the European Organisation for the Exploitation of Meteorological Satellites
FGI	Finnish Geodetic Institute
FGI ROAMER	Road Environment Mapping System of the Finnish Geodetic Institute
FMI	Finnish Meteorological Institute
FMI-ARC	The Arctic Research Center of the Finnish Meteorological Institute
GCOS	Global Climate Observing System
HSL	Hyperspectral Laser Scanning
IMU	Inertial Measurement Unit
IPCC	Intergovernmental Panel on Climate Change
MLS	Mobile Laser Scanning
NDVI	Normalized Difference Vegetation Index
TLS	Terrestrial Laser Scanning
rms	root mean square
SAL	Surface albedo
SCE	Snow Cover Extent
SNORTEX	Snow Reflectance Transition Experiment
SSA	Specific Surface Area
SWE	Snow Water Equivalent
UNFCCC	United Nations Framework Convention on Climate Change





# SYMBOLS

$\alpha_{ia}$	Incidence angle
$\alpha_{bsa}$	Black sky surface albedo
$\beta_t$	Transmitter beam width
$\theta_v$	Zenith angle of reflected solar radiation
$\theta_s$	Zenith angle of the incident solar radiation
$P$	reflectance
$\sigma_h$	root mean square height variation
$\sigma_b$	Backscatter cross section
$\phi_v$	Azimuth angle of the reflected solar radiation
$\phi_s$	Azimuth angle of the incident solar radiation
$D_r$	Receiver aperture
$P_r$	Power received by radar
$P_t$	Transmitter power
$R^2$	Coefficient of determination
$R_l$	Range of radar measurement



---

# 1. INTRODUCTION

---

Seasonal snow cover can occupy 50% of the land area of the Northern Hemisphere (Mialon et al. 2005). This affects both the lives of people living in the area by putting strains on the infrastructure (Makkonen 1989) and the environment. The large spatial coverage together with the high reflectivity of snow makes it an important factor for the global energy budget (Flanner et al. 2011). The reflective properties of the snow surface are directly dependent on the geophysical properties of the snow. Given the high variability of snow geophysical properties around the globe, also the behavior of light on the snow surface varies between different areas. Understanding climate requires understanding the reflective properties, such as surface albedo, of snow, and thus the geophysical processes and characteristics, such as surface roughness, of the snow. This is the motivation behind the work presented in this dissertation.

One of the geophysical properties affecting the reflectance of the snow surface is snow surface roughness. The measurements of snow surface roughness are relatively few and they are made in different scales and resolutions. Most of the existing studies on snow surface roughness describe the large scale roughness (Leroux & Fily 1998, Warren et al. 1998, van der Veen et al. 2009, Kuchiki et al. 2011, Zhuravleva & Kokhanovsky 2011, Picard et al. 2016). The work on small scale roughness is still very limited, possibly due to the lack of methods available. Also the present day surface albedo models include information on the large scale surface roughness, but small scale surface roughness is still missing. The work on small scale roughness is starting fast, with new methods being developed and parameters being tested. This dissertation contributes to developing methods to study small and medium scale surface roughness by presenting two new methods to measure the snow surface structures.

Small-scale roughness can be measured using a background plate that is partially inserted into the snow. The interface between the plate and the snow surface forms a profile of the snow surface, which is then used to describe the surface features. Different methods have different ways of extracting the profile, which are in different scales, resolutions and level of accuracy. Large-scale roughness is often measured using laser scanning, typically airborne laser scanning having relatively low resolution.

The parameters used to describe snow surface roughness are many. The applications related to the optical properties of the snow surface use root mean square height variation, correlation length, and autocorrelation functions, which are also the parameters used in scattering models. Since the snow surface roughness (being the height variation) depends on the measured scale and resolution, the parameters used should be

able to describe the surface at all relevant scales. This dissertation studies the use of multiscale parameters in describing the snow surface height variation.

In climate studies, the brightness of the surface is described as surface albedo. It is an essential climate variable (ECV) defined in the Implementation Plan for Global Observing System for Climate in support of the United Nations Framework Convention on Climate Change (GCOS Secretariat 2006). The relationship between large scale surface roughness and albedo has been studied previously (Leroux & Fily 1998, Warren et al. 1998, Kuchiki et al. 2011, Zhuravleva & Kokhanovsky 2011), but the effect of small scale surface roughness on surface albedo is still largely unknown. The existing studies show both a darkening of surface albedo (Leroux & Fily 1998, Warren et al. 1998, Kuchiki et al. 2011, Zhuravleva & Kokhanovsky 2011) and a change in small scale surface roughness as the snow ages (paper II), suggesting a link between surface albedo and surface roughness. However, further studies are needed to know the relationship in more detail.

The importance of surface albedo on the global and local climate requires the understanding of the behavior of albedo at a global scale. In practice, this means using satellite data and products. Recently the advancements in satellite data processing and availability have enabled the processing of surface albedo data records that are long enough for climate studies. Paper IV utilizes one of these data records (CLARA-A2 SAL) to study the changes in surface albedo prior to melt and melt season timing of areas covered with seasonal snow.

The satellite-based albedo and snow products need to be validated against in situ measurements. Most of these are pointwise measurements or cover only a small area. Since the satellite data comes in resolutions of tens of meters to kilometers, there is a clear gap between the scales of the satellite and validation data. In addition to this, the in situ measurements typically cover only one type of surface, whereas the reflectance observed by the satellite instrument comes from a mixture of different land cover types and the atmosphere. Therefore the in situ measurements do not fully represent the areas covered by the footprints of the satellite observations. This is especially the case in areas with fractured land use features, such as in the boreal forest zone, where the land surface features vary in small scales.

In order to be able to validate satellite-derived albedo and snow products, the validation data would need to cover larger areas. Laser scanning offers a means to cover larger areas, thus providing a better representativeness for the satellite data validation (Kenner et al. 2011, Egli et al. 2012, paper III, Picard et al. 2016). So far the use of laser scanning data for satellite data validation is not common and methods are still being developed. More information is still needed on the behavior of laser scanning range and intensity data on snow surfaces. Once the open issues about the data have been solved, laser scanning can be used in several glaciological applications. This dissertation provides information on the backscattering of laser beam from different types of snow surfaces, thus enhancing the usability of laser scanning on measuring snow surfaces.

The improved satellite-based albedo and snow products give means to study the changes in these on a global scale. Recently, global satellite-derived time series on snow and albedo of several decades have provided information on the long-term changes in the snow cover. The studies on the time series data reveal changes in the snow cover extent, melt season timing and albedo during the spring months of northern hemisphere (Derý & Brown 2007, Markus 2009, Brown & Robinson 2011, Derksen & Brown 2012, Wang et al. 2013, Atlaskina et al. 2015, Chen et al. 2015, Malnes et al. 2016).

The main objective of this dissertation is to study the seasonal snow surface roughness and albedo using optical satellite data and laser scanning. This includes developing methods to measure snow surface roughness and studying the usability of laser scanning on snow surface, which could potentially be used for satellite data validation and snow surface scattering modelling. The work presented here provides the basis for future work on studying the role of small scale surface roughness on seasonal snow surface albedo.

The specific objectives of this dissertation are:

- To develop methods for measuring small scale seasonal snow surface roughness (papers I, II, III)
- To study the usability of multiscale parameters to describe the snow surface roughness (paper II)
- To study the behavior of small scale surface roughness of seasonal snow in boreal forest zone (paper II)
- To develop methods and improve the usability of laser scanning on snow-covered surfaces (papers III and IV)
- To study the changes in large scale surface albedo of snow-covered surfaces (paper V)



---

## 2. LIGHT TRANSFER, OPTICAL PROPERTIES AND ALBEDO OF SNOW

---

The optical properties of snow depend on the type of snow crystals, surface roughness and amount of liquid water at and near the surface of the snowpack. The scattering properties are most heavily determined by particle size and shape (Shi & Dozier 2000). Also surface roughness depends on the type of snow crystals and their arrangement on the surface.

The characteristics of the snow surface are first affected by the falling snowflakes, which can take several different forms (Nakaya 1954, Magono & Lee 1966, Libbrecht 2005, Lamb & Verlinde 2011). As the snowflakes reach the ground, the cohesion between snow crystals makes the crystals attach to the surface at first contact instead of being arranged to a position of minimum energy (Löwe et al. 2007). The arrangement of the crystals also depends on the prevailing wind conditions. After the snowflakes have fallen on the ground they start to reshape. These metamorphic processes can be divided into mechanic, dry and wet metamorphism (Sommerfeld & LaChapelle 1970). Mechanic metamorphism is typical in cold temperatures, where the absence of liquid water gives the wind possibility to redistribute and mechanically round the crystals. During transportation by air, the surface snow particles change shape by breaking into smaller particles and gaining mass from moisture in the surrounding air both through accretion and aggregation (Armstrong & Brun 2008). New snow falling on top of the crystals also causes mechanical breaking of the crystals.

If the snowpack is dry, that is, there is no liquid water, the ice sublimates from the snow crystals and possibly gathers on other crystals. This causes angular crystals to become rounded crystals as the water vapor is sublimated from the convex surfaces and gathered in the concave parts (Colbeck 1982a). In addition to rounding of the crystals by sublimation, sintering forms ice bonds between different grains resulting in larger grains (Colbeck 1997) and kinetic growth metamorphism causes the rounded crystals to grow into faceted crystals (Colbeck 1982b). In wet snow, there is liquid water within the snowpack. The melting and refreezing of water reshape the grains and forms layers of different density and grain structure in the snowpack (Figure 1).

At the snow surface, solar radiation can either be reflected back to the atmosphere or absorbed into the snowpack. At the visible wavelengths, absorption is much weaker than reflectance through scattering (Warren 1982). The scattering of solar radiation at the snow surface can be divided into 3 different types of processes: single, multiple and

volume scattering. In single scattering, the incoming radiation is reflected directly back to the atmosphere. Multiple scattering refers to the scattering of radiation from one flat particle surface to another and in the end back to the atmosphere (Woodhouse 2006). Volume scattering results from the bulk properties of the snowpack (Shi & Dozier 2000). The amount of these depends on the hardness and roughness of the surface (Warren et al. 1998, Nagler & Rott 2000). The rougher the surface is, the more multiple and volume scattering takes place.



*Figure 1 Seasonal snowpack layering at Sodankylä airport 5th April 2013. The photo shows a thin slice of natural seasonal snow (with a small branch of pine (Picea Abies)). The photo was taken by Teemu Hakala, FGI.*

In climate studies, the brightness of the earth's surface is typically parameterized by surface albedo. It describes the fraction of the incoming solar radiation that is reflected back to the atmosphere and potentially to the space from the earth's surface. There are different ways to define surface albedo depending on the range of wavelength and the angular distributions included. The albedo used in the study presented in chapter 5.1 is the directional –hemispherical reflectance (so-called black-sky albedo,  $\alpha_{bsa}$ ) of a given area on the surface describing the incoming solar radiation from one direction, versus the



reflected radiation in all directions, mathematically written as (Schaepman-Strub et al., 2006)

$$\alpha_{bsa}(\theta_s, \phi_s) = \int_0^{2\pi} \int_0^{\pi/2} \rho(\theta_s, \phi_s; \theta_v, \phi_v) \cos(\theta_v) \sin(\theta_v) d\theta_v d\phi_v \quad (1)$$

where  $(\theta_s, \phi_s)$  are the vertical and horizontal direction of the incoming radiation (a single incident direction),  $(\theta_v, \phi_v)$  are the viewing directions of the reflected radiation in the zenithal and azimuthal planes and  $\rho$  is the reflectance.

The albedo values of different surfaces vary considerably. Liquid water, such as oceans and lakes have very low albedo values typically around 10 percentage units (Jin et al 2002). Fresh clean snow surface, on the other hand, can have albedo values of up to 90 % (Warren 1982). The albedo of snow depends on the snow surface crystal type, size and distribution on the surface, the scale and directionality of the surface features (surface roughness), impurities, amount of liquid water, Sun and observation angles, and wavelengths in question (Warren 1982, 1984, Warren & Brandt 1998). The most important factor determining the albedo of the snow surface is the grain size (Warren & Wiscombe 1980, Wiscombe & Warren 1980). The albedo values decrease as the grain size increases (Wiscombe & Warren 1980), which explains the darkening of snow surface as the snow ages. There are several methods developed to automatically derive snow crystal size (Ingvander et al. 2012, 2013, Pirazzini et al. 2015). Many of them are based on photogrammetry, where crystal size is derived automatically from crystal images. Also other ways have been developed to describe the effect of snow surface grains on snow optical properties. One of these is specific surface area (SSA), which describes the surface area of the grain per unit mass (Gallet et al. 2009, Gallet et al. 2014).

As the snow starts to melt the grains size and amount of liquid water in the snow increases. This leads to lower values of surface albedo. With the darkening surface the amount of solar energy being absorbed by the snow surface increases, further enhancing the melt and decrease of the albedo. This phenomenon is called the ice-albedo feedback (also known as snow-albedo feedback) (Arrhenius 1896, Budyko 1969, Warren & Wiscombe 1980). The albedo of snow is also affected by surface roughness. So far most of the studies concentrate on large scale roughness, such as sastrugis and smaller scale wind induced formations (Leroux & Fily 1998, Warren et al. 1998, Kuchiki et al. 2011, Zhuravleva & Kokhanovsky 2011). For none-smooth snow surfaces where surface roughness is randomly oriented the albedo is smaller for rougher surfaces due to trapping of radiation in the troughs (Warren 1982). For regular surface features the effect of surface roughness depends on the direction of the Sun relative to the surface features.

Besides the snow geophysical factors, the albedo of snow also depends on the Sun elevation angle, impurities, and cloudiness (Warren 1982, 1984). When clouds are absent, the albedo of a smooth horizontal snow surface increases with decreasing solar elevation. This is due to the likelihood of near horizontal radiation to escape the snow surface instead of being absorbed by the surface. The grain shape becomes more important as the solar elevation decreases, and at low solar elevations the albedo of faceted grains is higher than for other types of grains (Choudhury & Chang, 1981). On cloudy weather, the albedo can be higher than with clear skies due to the multiple scattering of light from the clouds. (Wiscombe & Warren 1980). At the wavelengths where snow exhibits significant absorption, the albedo of a snow surface is higher at lower solar elevations (Wiscombe & Warren 1980, Pirazzini 2004).

The optical properties of seasonal snow depend on several different factors. These include the physical structure of the snow pack, such as crystal size and shape, amount of liquid water and air and the impurities of the snow pack. They contribute to the basis for the surface roughness of the snow, which is discussed in more detail in the following chapter.

---

### 3. SURFACE ROUGHNESS OF SEASONAL SNOW

---

Surface roughness affects the optical properties of seasonal snow. The roughness depends on several different processes and environmental conditions. Some of these are global, (e.g. sun elevation, maritime/continental climate, vegetation zone...) and some are local (e.g. prevailing wind direction and speed, amount and type of precipitation, distance to the canopy...). The dominant factors affecting the surface roughness depend on the scale and environment. At the microscale, the crystal shape and distribution determine the roughness. These depend on the type of crystals that fall on the surface and the metamorphosis of the snow crystals, as described in the previous chapter. In climates where air (surface) temperature stays much colder than the freezing point, the surface features and metamorphosis of snow crystals are mostly affected by reshaping and rearranging of the crystals by aeolian processes. In climates where air temperature rises near or above melting point also sublimation, melting, and refreezing of the snow crystals affect the surface features (Sturm et al. 1995).

At larger scales, the surface features are caused by wind, melting and the topography of the ground. The redistribution of particles by wind modify the crystals and determine the accumulation patterns on the snow surface (Mellor 1965, Jaedicke et al. 2000), such as wind induced ripples and dunes. The macro scale roughness includes also features caused by other factors such as topography, land use and canopy type (Winkler et al. 2005, Deems et al. 2006, Schirmer & Lehning 2011, Eveland et al. 2013, Gruenewald et al. 2013, Scipi3n et al. 2013, Veitinger et al. 2013). The vicinity of tree trunks affects the surface in a complex way. Forested sites have milder diurnal temperature variation and lower wind speeds than open areas. In open areas wind is often the dominant process affecting the distribution of snow (Lehning et al. 2008) whereas forests tend to attenuate the weather extremes, keeping the air warmer during cold condition and shadowing the surface from direct warming of solar radiation in the spring. This results in slower melting in the spring in forested sites. Trees also affect the distribution of snow. Next to tree trunks under the large branches snowpack is typically shallower. On the other hand, smaller trees with fewer branches can enhance snow accumulation at the root of the tree trunk as the tree trunk acts as a snow fence. At forested sites snow gathers also on the trees. Eventually this snow will fall down to the snow surface causing surface features of different scales. The small particles from vegetation, such as branches and old dried leaves and needles, fall on the snow surface, forming scars and enhancing the melt in the springtime.

Surface roughness and the amount of liquid water are the main parameters affecting the microwave backscatter from wet snow (Williams & Gallagher 1987, Nagler & Rott 2000). The microwave remote sensing data is particularly important in the Polar Regions, where winters do not have enough sunlight and the weather is often cloudy. Also, the bidirectional reflectance distribution function (BRDF) of snow is heavily affected by surface roughness (Warren et al. 1998, Peltoniemi et al. 2010). Therefore, understanding the effect of surface roughness on remote sensing signals on snow-covered surfaces could enhance the quality of both optical and microwave remote sensing based snow and albedo information and enhance the quality of remote sensing based products and climate models.

Seasonal snow surface roughness is a result of several different environmental processes, with different processes being the dominant influence on different scales. The importance of surface roughness on the optical properties of snow surfaces are recognized but the detailed description of the relationship between small scale surface roughness and albedo is still fairly poorly known, with most of the work focusing on the large scale roughness. The understanding of surface roughness would require methods to measure it and large data sets. Examples of these are presented in the following chapters.

### ***3.1. SURFACE ROUGHNESS PARAMETERS***

Several different parameters have been developed for describing surface roughness (Church 1988, Manninen 2003, Manes et al. 2008, Fassnacht et al. 2009a, a good overview in Dong et al. 1992, 1993, 1994a, 1994b). The choice of parameters depends on the surface features relevant to the application and the material that is described.

For snow, there are two main fields interested in surface roughness: The studies on the atmosphere-surface interactions describe the surface roughness by using atmospheric roughness length. This is the parameter used in most surface-atmosphere models. It describes the height above the surface at which the mean wind speed reduces to zero when extrapolating the logarithmic wind speed profile down through the surface layer (Manes et al. 2008, Gromke et al. 2011). The roughness of the snow surface affects the wind speed near the surface. This, in turn, affects the exchange of chemicals between the snow and the atmosphere, and the latent and sensible heat flux between these two. The studies on snow surface scattering properties describe the surface by geometric roughness. These include studies on the brightness of the snow surface, scattering modeling of snow, and optical and microwave remote sensing.

The geometrical roughness of snow surfaces is typically described using correlation length and root mean square height variation ( $\sigma_h$ ). The values of these parameters depend on the measured scale and the orientation (Manninen et al. 1998). For example, in remote sensing, the surface radiative properties are affected by the roughness from the used wavelength up in fractions of the used scale (Ulaby et al. 1982, Fung 1994, Rees & Arnold

2006). Therefore also the measurements and parameters should describe all the scales that are relevant (Keller et al. 1987, Church 1988, Manninen 1997a, Manninen et al. 1998, Fassnacht & Deems 2006). So far, most of the existing surface roughness studies are made in different scales, directions, and resolutions, which makes it difficult to compare them. Furthermore, most of the existing studies have measured only a single scale, and are thus not fully able to describe the surface. Some multiscale parameters have been developed (Manninen 1997a, 1997b, 2003, Davidson et al. 2000, Löwe et al. 2007, Manes et al. 2008, Fassnacht et al. 2009a), but the directionality has not been taken into account in the parameters as often (Herzfeld 2002, Trujillo et al. 2007).

The parameters used in the papers I-III are based on the root mean square height variation ( $\sigma_h$ ), which is a typical descriptor of surface roughness in microwave surface backscattering models (Ulaby et al. 1982, Fung 1994). Since these depend on the measured length (scale), the  $\sigma_h$  is calculated as a function of measured length. The  $\sigma_h$  of a single scale was replaced by the mean  $\sigma_h$  of all the subprofiles of equal length along the whole profile (similarly to the sliding window technique). The  $\sigma_h$  of each profile is calculated using the following equations:

$$\langle \sigma_{h_i} \rangle = \frac{1}{(n-in_0)} \sum_{j=1}^{n-in_0} \sigma_{h_{ij}}, \quad i = 1, \dots, n_i \quad (2)$$

where  $\sigma_{h_{ij}}$  is the rms height of a subprofile of  $in_0$  points. The size of the smallest subprofile is  $n_0$  and it is enlarged with an increment of  $i$  so that the size of a subprofile is  $in_0$ , where  $i = 1, \dots, n_i$  and  $n_i$  is the number of different subprofile lengths. The subprofile is moved from the beginning of the whole profile by an increment of  $j$ . The total number of points in the 1 meter profile is  $n$ .

According to Keller et al. (1987), for natural surfaces the logarithm of the rms height variation  $\sigma_h$  is linearly dependent on the logarithm of the length  $x$  for which it is determined, giving:

$$\sigma_h(x) = e^a x^b \quad (3)$$

where  $a$  and  $b$  are constant parameters. These parameters will be used in the analysis presented in chapter 3.4.

The parameter values are affected by the inner and outer scale effect. In the inner scale effect, the low number of points in each subprofile or causes statistical uncertainty. In the outer scale effect, the low number of subprofiles has the same effect. The outer scale effect starts to influence the data at subprofile lengths longer than 60% of the maximum length (Manninen et al. 1998). Therefore the analysis in paper II is made using the values for  $a$  and  $b$  at 60% of the maximum profile length.

The parameters presented here give means to describe seasonal snow surface roughness in a way that takes into account all measured scales. This is important for scattering modelling, which typically include single input for describing surface roughness when in fact the roughness affects the scattering on many scales.

## **3.2. METHODS FOR MEASURING SURFACE ROUGHNESS OF SNOW**

The studies on snow surface roughness are relatively few. One of the reasons for this is the difficulty of measuring it. Lacroix et al. (2008) have put together an overview of the history of snow surface roughness measurements. Many of these are based on inserting a plate partially into the snow and measuring a profile of the snow surface. These plate-based measurements started in the 1980's by Rott (1984) and Williams et al. (1988). After this, the methods have improved regarding accuracy and resolution (Rees 1998, Rees & Arnold 2006, Löwe et al. 2007, Manes et al. 2008, Elder et al. 2009, Fassnacht et al. 2009a, 2009b, Gromke et al. 2011, paper I). Some of these methods are manual in the sense that the height variation is measured using, for instance, a ruler (Rees 1998) and some incorporate photography (Löwe et al. 2007, Manes et al. 2008, Fassnacht et al. 2009a, paper I). The different methods have been used to measure different types of snow, such as melting snow or freshly fallen snow.

In addition to the plate-based measurements, there are some methods that are based on laser scanning. Most of the methods have measured individual profiles but laser scanning data could be used to cover larger 3-d areas of the surfaces. In addition to improving the accessibility and spatial and statistical coverage, laser scanning gives the potential for studying the directionality of the height variation. It also leaves the surface intact, which gives the possibility to repeat the measurements at the same areas at different times. Then again, this data does not have as high resolution or accuracy as some of the plate methods. More details on laser scanning are given in chapter 4.

In this dissertation, two methods for measuring snow surface roughness are presented. One is based on plate photography, and it is described in detail in the following chapter. It was used in the field in Sodankylä, Finnish Lapland, and the snow profiles were extracted using a fully automatic algorithm developed by Manninen et al. (2012). The results of the

analysis of these profiles are presented in chapter 3.4. The other method is based on mobile laser scanning (MLS), and it is presented in chapter 4.3.

### **3.3. PLATE PHOTOGRAPHY METHOD**

The method used in papers I-III is based on photographing a 1.06 m x 0.4 m wide black board with scales on the sides (Figure 2). The black area in the middle is 1 m x 0.4 m. The scales consist of three rows of black-and-white squares of 1, 5 and 10 mm in size.

While measuring, the plate is carefully inserted into snow so that the top of the plate remains above the snow (Figure 3). The plate is photographed perpendicularly using a Canon PowerShot G10 digital pocket camera. The camera has a 4416 x 3312 pixels and a zoom lens with an optical image stabilizer. One image is enough for retrieving the profile, but to ensure good image quality, three images were taken from each profile. The resolution of the images and the profiles depend on how close to the plate the photograph is taken, but was on average 0.27 mm.

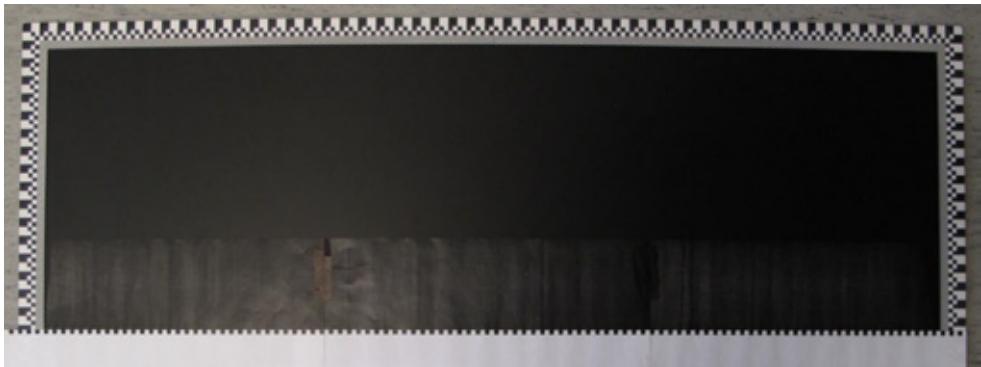


*Figure 2 The background used in the plate photography method for measuring snow surface roughness. The calibration of the plate method was made using an artificial tooth rack profile shown in the figure.*

The plate and camera are easy to carry during field measurements. Therefore it can be used in a wide area. It can also be taken to the areas surrounded by trees, which can be a limiting factor for the laser scanning based methods, where the tree trunks limit the visibility of the snow surface. The limits to the use of this method come from the resolution of the camera. Also, in some cases, if the snow is loose or has an icy cover, inserting the plate into the snow and holding it in place without disturbing the snow surface profile can be difficult. However, for most cases in the boreal forest zone this is

not the case. Snowfall can also be a problem to the method because falling snowflakes appear as white spots on top of the black plate. These can still be analyzed with little manual assistance, but if the falling flakes appear on top of the snow profile or at the corners of the black area the profile extraction will not be successful.

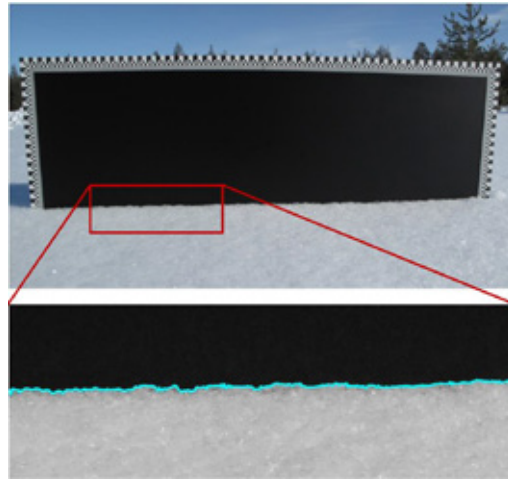


*Figure 3 Plate photograph with enlargement of the extracted profile. The profile is from Tähtelä, site index 10, 16<sup>th</sup> March 2010 with fresh snow.*

The vertical accuracy of the coordinates of the profiles was tested by taking a photograph of a straight horizontal paper edge and analyzing it with the method described above. The average absolute deviation of the measured height variation from zero was 0.93 mm with a parabola shape ( $y = 0.0000144x^2 - 0.01479x + 2.609$ ;  $R^2 = 0.99$ ). This is most likely due to the scales of the board being 1 mm above the black background. It may also be due to residual error from the barrel distortion correction. When the coordinates were corrected according to the parabola the absolute deviation of the coordinates from zero was 0.07 mm.

The vertical and horizontal accuracy was studied in more detail by taking photographs of an artificial profile with rack-tooth pattern (Figure 2). The rack-tooth pattern dimensions were 5 mm x 5 mm. The test data consisted of 50 images taken from different angles and distances. From this, a subset of 30 profiles was chosen to represent the realistic measurement settings. The profile was placed on top of the image in different angles for different cases. This dataset was used to construct a residual barrel distortion correction. Based on the rack-tooth –profile analysis the overall horizontal analysis is on average 0.1 mm, with 80% of the cases having an error smaller than  $\pm 0.6$  mm. The overall vertical accuracy is on average 0.04mm with 80% of errors in a range smaller than  $\pm 0.2$  mm.



The repeatability of the method was tested by analyzing three different images taken from the same set of the rack-tooth profiles. Twenty-one of the cases had three successful images and were included in the analysis. The profiles were analyzed using root mean square height variation of subprofiles of different length at different parts of the profile (similar to sliding window technique). The mean values of rms height variation for each length of subprofiles were calculated. The subprofiles longer than 60% of the maximum length were obtained from the analysis because the mean value of the longer subprofiles is calculated from only a few individual subprofiles, thus causing statistical uncertainty (Figure 5 in Manninen et al. 1998). The standard deviation of the rms values per measurement is <0.02 mm. The variation of the rms height measurement is typically <1% of the mean value.

The effect of the temperature variation on the dimensions of the scale was estimated to be <0.1 % for a typical measurement temperature range. The detected reasons for the failure of automatic analysis are blurred or out-of-focus images, a very large dark object at the front of the image, snowflakes at the corners of the black area and on scales, and extremely poor contrast of the image intensity.

The plate photography –based method presented here is able to describe the snow surface roughness in scales smaller than 1 m with resolution less than 1 mm. The method is easy to use also in field conditions: it is light to carry, does not require complicated or expensive technical device, and it tolerates moisture and cold weather. Therefore it offers means to gather large data sets on roughness in many different conditions.

### **3.4. PLATE METHOD RESULTS**

The snow surface roughness measurements presented in this dissertation were made as part of the SNORTEX (Snow Reflectance Transition Experiment) campaign (Roujean et al. 2010, Manninen & Roujean 2014). The campaign took place in Sodankylä, Finnish Lapland (67.4°N, 26.6°E) during winters 2008-2010. The base of the campaign during field measurements was in the premises of Finnish Meteorological Institutes Arctic Research Centre (FMI-ARC). The campaign was led by FMI and Météo-France. Also the Finnish Geodetic Institute (FGI, now Finnish Geospatial Research Institute of National Land Survey of Finland), University of Helsinki, University of Eastern Finland, the Laboratoire de Glaciologie et Géophysique de l'Environnement, and the Finnish Environment Institute. The campaign aimed at studying the different factors affecting the boreal forest albedo during the melt seasons. It included both airborne and ground-based measurements.

The surface roughness plate measurements made during the SNORTEX-campaign were analyzed using the multiscale parameters developed by Manninen (1997b, 2003, see chapter 3.1). The aim of the study was to gather information on the snow surface roughness of the study area and to investigate the use of the plate-based method and the parameters in question in describing the seasonal snow surface roughness. The

measurements covered different types of natural snow, including fresh, old, wet and dry snow. The measurements cover different types of land use, including forests, open bogs and lake ice (Figure 4). The plate profiles were analyzed using the parameters  $a$  and  $b$  (Eq. 3)

The parameter  $a$  and  $b$  (Eq. 3) react differently to the features along the profile they describe. Parameter  $a$  reacts to the height variation of the shorter wavelengths. Therefore fresh fluffy snow gets high values of  $a$ , and aged snow gets lower values correspondingly. The parameter  $b$  reacts to the longer wavelength characteristics and irregularity of the occurrence of height variations. The surface features of older snow have less variation in the crystal level, but larger variation in the longer wavelengths. This variation is caused by melting, impurities, and scars made by animals on top of the snow. These are more irregular in nature than the wind induced ripples or crystal level features and therefore old melting snow gets high values of  $b$ .

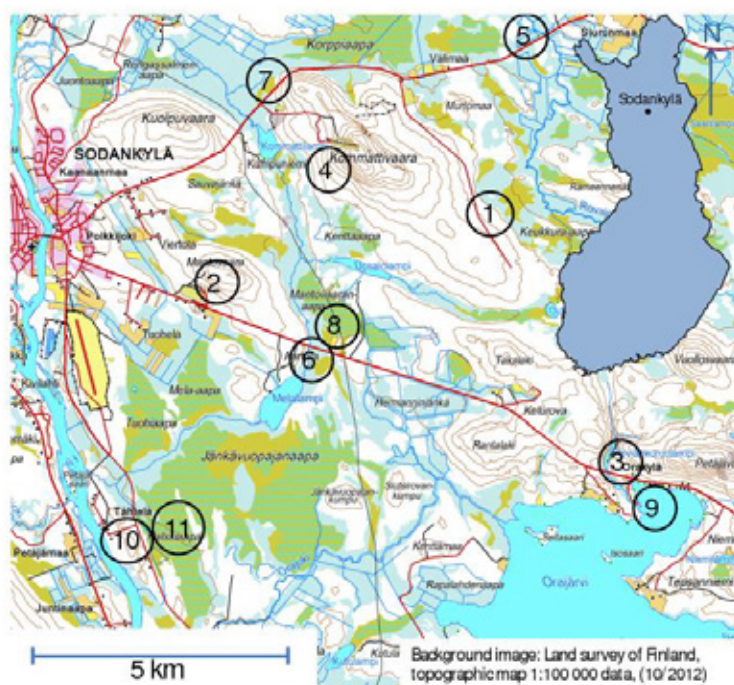


Figure 4 The measurement sites for plate photography measurements during SNORTEX campaign.

The different character and sensitivity of the parameters can be seen in Figure 5. The figure presents the values for  $a$  and  $b$  for all measured profiles. The parameters from the

March 2009, February 2010 and March 2010 profiles show similar combinations for the values for the two parameters but the profiles measured in April 2009 form a separate group of values. This is because April 2009 was melt season whereas the other months did not yet experience as much melting. For April 2009 the values for  $b$  are generally higher for the corresponding values for  $a$  than for the other months. This is because in the melt season the new fresh snow is not able to level out the irregular pits and peaks of the already melting snow surface.

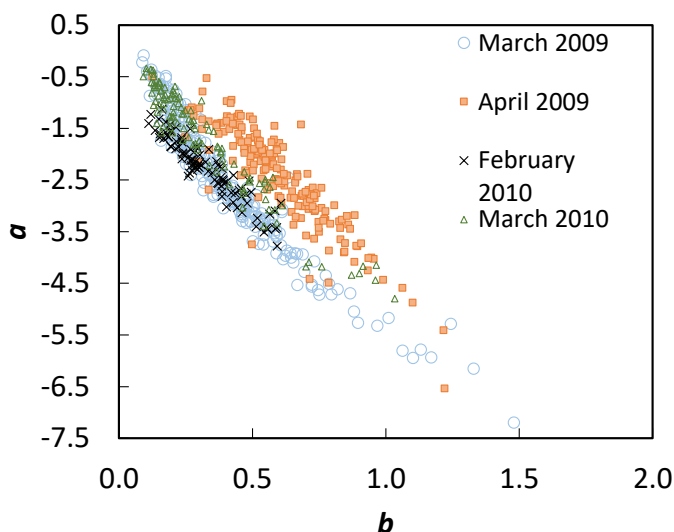


Figure 5 The parameters  $a$  and  $b$  of Eq. 3 for 60% of the maximum length for all plate profiles from 2009 and 2010.

The effect of a single snowfall event on the values for parameter  $a$  can be seen in Figure 6, which shows the values for the two parameters for Tähtelä (site 10 in Figure 4) for March and April 2009. At the beginning of the field campaign in March 2009 the snow surface was aging. At the evening of 15<sup>th</sup> March, it began to snow, continuing in short periods until the morning of 18<sup>th</sup> March. This can be seen in the values for parameter  $a$ , which gets relatively low values at the beginning of March 2009. Then, as the snowfall starts, the values increase, and after the snowfall they gradually decrease. The values for  $a$  are in the range of -4 to -0.5. This is also the range of values for  $a$  in all the measurement sites in March 2009. This shows that the weather conditions can largely explain the distribution of  $a$ . In April 2009 there was no snowfall during the measurement period.

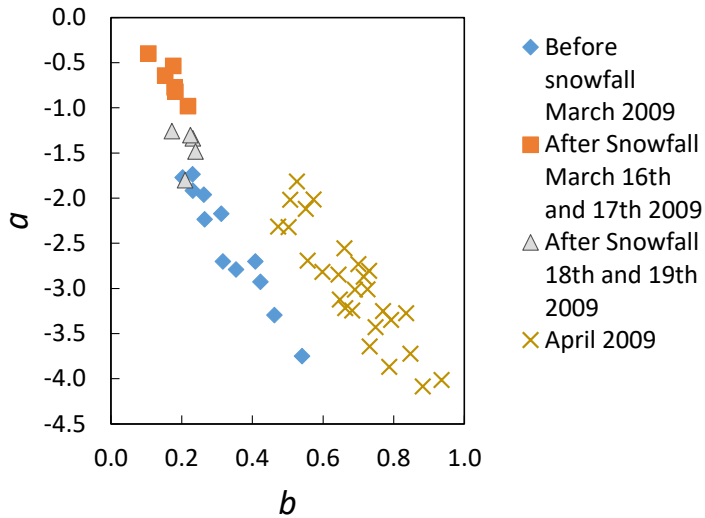


Figure 6 The temporal variation of parameters  $a$  and  $b$  of Eq. 3 in Tähtelä from 11<sup>th</sup> March 2009 to 28<sup>th</sup> April 2009.

The results here present a large data set of small scale surface roughness measurements. The measurements cover many different types of environments and thus snow types of the Boreal Forest. The parameters used here were able to distinguish between old and fresh snow surfaces, as well as the difference between mid-winter and melt season snow. Previous studies have shown that the albedo of snow decreases as the snow gets older. The study presented here shows that the small scale surface roughness changes as the snow gets older. This suggests that the small scale surface roughness has an effect on surface albedo.

---

## 4. LASER SCANNING OF SNOW COVERED SURFACES

---

Laser scanning is a technique ideal to use in 3D mapping of different targets, such as topography, forest, vegetation, buildings and indoors areas. It has proven to be particularly good at measuring inaccessible and dangerous environments. It also leaves the measured surface intact, which means it can also be used for change detection.

The applications for laser scanning are rapidly increasing as the scanning systems are becoming cheaper and easier to use. The laser scanning methods can be divided into airborne and terrestrial methods. In airborne laser scanning (ALS) the scanning system is installed onboard an aircraft. These systems can cover large areas, but the resolution and accuracy of the data is not as good as with terrestrial laser scanning (TLS), where the scanner is on ground, typically mounted on a tripod (Rees & Arnold 2006, Van Der Veen et al. 2009, Hollaus et al. 2011). The measurements presented here are made using TLS.

In the recent years, several different methods have been developed, where the scanning system is mounted on a moving vehicle. These mobile laser scanning systems (MLS) cover larger areas than stationary laser scanning and the data has higher resolution and accuracy than the airborne data. The MLS systems typically have a 2-d profiling laser scanner mounted on a moving vehicle, where the movement of the vehicle provides the third dimension for the point cloud. The systems consist of a scanner, a moving vehicle, a GPS-device and an inertial measurement unit (IMU). The MLS system used in the study presented in chapter 4.3 is the FGI ROAMER (Kukko et al. 2007).

Laser scanning is based on the scanner sending a laser beam towards an object or area and then measuring the backscatter of the beam. The direction to which the beam was sent, and the time it took until the photodiode of the scanner detected the backscattered beam gives the location of the reflecting surface. The range measurement can be based either on the time-of-flight or on the phase-based measurement principle. Changing the direction of the outgoing beam the observations can be combined into a 3D point cloud, where the data of each measured point contains x, y and z coordinates and the intensity of the backscattered beam. The 3D point cloud can then be analyzed using either photogrammetric methods to extract different objects or by modeling the surfaces.

The intensity data of a point cloud tells the relative intensity of the backscatter of the laser beam for each measured point within the scan. The data has not yet been used for many applications, but the methods utilizing also this information are increasing. Since the intensity data is gathered automatically while scanning, making it usable for data analysis would bring added value to the work and create new possibilities for applications. For

snow surfaces, this could mean for example automatic classification of snow surface types.

The intensity value of a laser point is affected by the backscattering properties of the reflecting object. With snow, this means the grain size and shape (Kaasalainen et al. 2006) and the surface structure (Zhuravleva & Kokhanovsky 2011). The backscattering properties of the target then affect the angular dependency of the intensity, that is, the incidence angle effect (Kaasalainen et al. 2011, Krooks et al. 2013). The effect of measurement geometry and its correction has been studied by Sicart et al. (2001) and Weiser et al. (2015). Knowing the effect of incidence angle is particularly important for MLS data which typically covers a larger area and thus wider range of incidence angles.

In order to be able to use the intensity value, it needs to be calibrated since the absolute intensity value changes between different datasets. This is typically done using objects whose reflectance is pre-known (Kaasalainen et al. 2009). In field conditions, these can be placed in the view of the scanner and later extracted from the data and used as reference values to calibrate the data. This also enables the comparison of different datasets. Different radiometric calibrating systems have been developed by, for instance, Ahokas et al. (2006), Coren & Sterzai (2006), Höfle et al. (2007), Kaasalainen et al. (2009) and Wagner et al. (2006). Calibrated intensity data has previously been used for range data segmentation and classification (Höfle et al. 2007, Yan et al. 2012).

Using laser scanning on snow surfaces requires knowledge on the behavior of laser beam on the snow surface. The usability of MLS in snow applications was studied by Kaasalainen et al. (2010). Since some types of the snow surface crystals are transparent in the direction of the optical axes of the crystal, and the surface may contain liquid water, there is a chance that the laser beam backscatter does not come from the surface, but from lower levels of the snowpack. Prokop (2008) has studied the depth the backscattering represents by placing reflective foils and blankets on the snow and comparing the range data from the blanket and the snow. According to his study, there was less than 1 cm difference in the surface height of the different surfaces. Here the depth from which the backscattering takes place is studied by placing black metal plates horizontally into the snowpack and observing the effect they have on the intensity value of the backscatter (chapter 4.1).

To be able to use the laser scanning intensity data for snow surfaces several factors need to be taken into account. First, the snow BRDF is highly varying. In stationary terrestrial laser scanning data, the direction of the laser beam changes as the scanner rotates. This means that each laser point observation represents the backscattering for a different angular composition of the BRDF. The incidence angle between the scanner and snow surface changes also along the scan line. The effect of these need to be taken into account while using the intensity data. This dissertation presents a study on the incidence angle dependence of the intensity data from different snow types (chapter 4.2).

In glaciology laser scanning has mostly been used for snow depth measurements and the applications have focused on using the range data (Arnold et al. 2006, Várnai & Cahalan

2007, Kaasalainen et al. 2008, Prokop 2008, Prokop et al. 2008, Hood & Hayashi 2010, Helfricht et al. 2014, Picard et al. 2016). Some first attempts have been made to use airborne laser scanning data for glacier surfaces (Lutz et al. 2003, Höfle et al. 2007). The surface roughness studies using laser scanning have focused on different snow-free surfaces (Lacroix et al. 2008, Eitel et al. 2011). ALS has been used to study the roughness of larger areas, such as ice sheets (Van Der Veen et al. 2009) and forest canopy (Weligepolage et al. 2012). This dissertation presents a study on the feasibility of MLS data on snow surface roughness mapping (chapter 4.3).

## 4.1. DEPTH OF BACKSCATTER

The depth from which the backscattering takes place was studied by placing black metal plates horizontally into the snowpack and observing the effect they have on the intensity value of the backscatter. As soon as the intensity value starts to change the laser beam has reflected from the depth of the plate. The measurements were made using Leica HDS6100 scanner. It measures at 650-690 nm wavelength. The beam diameter at exit was 3 mm, having a beam divergence of 0.22mrad. The range measurements were based on phase detection. Additional measurements were made with a Sick LMS151 laser scanner to compare the results of the phase-based scanner with the pulse-based one. The Sick scanner measures at 905 nm wavelength and has an 8 mm beam exit with 15 mrad beam divergence.

The intensity detector of the Leica scanner is linear and follows the  $R^2$  dependence ( $R_i$  being the range) of the radar equation (Wagner et al. 2006) at distances greater than 10 m (Kaasalainen et al. 2011):

$$P_r = \frac{P_t D_r^2}{4\pi R_i^4 \beta_t^2} \sigma_b \quad (4)$$

where  $P_r$  is the received power,  $P_t$  is the transmitted power,  $D_r$  is the receiver aperture,  $R_i$  is the range, and  $\beta_t$  is the transmitter beam width.  $\sigma_b$  is the backscatter cross section, which is related to target reflectivity and the measurement geometry. In this study, all parameters, including the range  $R_i$ , remained constant, except for  $\sigma_b$ , which depends on the incidence angle (cf. Shaker et al. 2011, Kaasalainen et al. 2011).

According to Höfle & Pfeifer (2007), the  $\sigma_b$  depends on the incidence angle as follows:

$$\sigma_b = \pi \rho R^2 \beta_t^2 \cos \alpha_{ia} \quad (5)$$

where  $\rho$  is the target reflectance,  $R_l$  is the range,  $\theta_t$  is the laser beam width and  $\alpha_{ia}$  is the incidence angle. With plates in the snowpack closer than where the backscattering would take place, it would affect the surface reflectivity, which is also contained in the cross-section parameter  $\sigma_b$  (Wagner et al. 2006).

The measurements were made at the premises of FGI in Kirkkonummi (60.1°N, 24.5°E), Finland. The snow cover in this region is typical taiga snow with ice lenses and several layers with different density and crystal shape (Sturm et al. 1995). The relevant geophysical properties of the snow were documented and the overall weather conditions, such as air temperature, were monitored during the measurements.

The snow cover was studied using standard snow pit measurements. After this, a clear cut in the snowpack was made, and black aluminum plates were inserted into the snow at different depths in a horizontal position similar to the snow surface (Figure 7). The plates were 50 cm x 25 cm and 15 cm x 10 cm in size. The bigger plates were used deeper in the snowpack to ensure that they cover the sample area. The smaller plates were used near the surface where the snow was less packed and therefore inserting the plates into the snow without destroying the surface was more difficult. They were also easier to place at an exact depth.

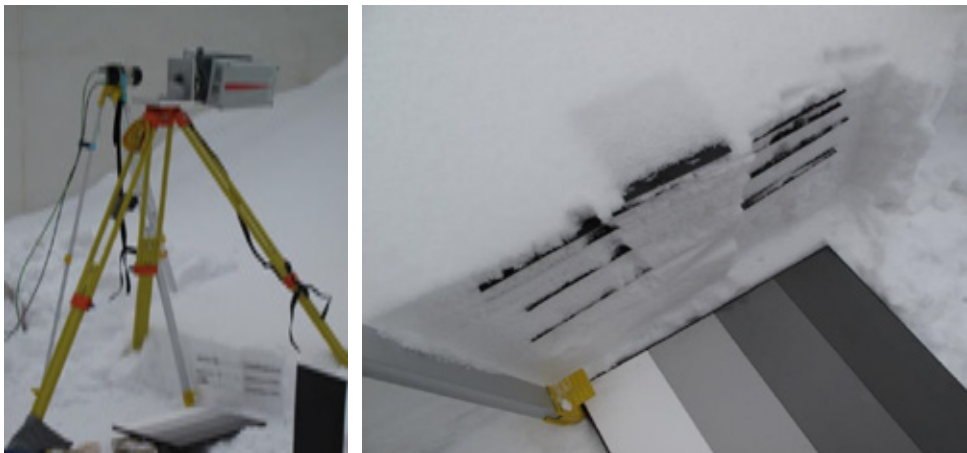


*Figure 7 The set up for measuring the depth of backscatter. Left: The scanners were placed above the snow surface (here both Leica on the right and Sick on the left). Right: The Spectralon<sup>®</sup> reflectance panel was placed in the view of the scanner and black metal plates were inserted into the snow.*





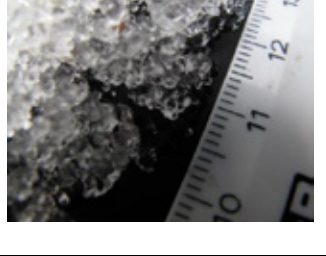
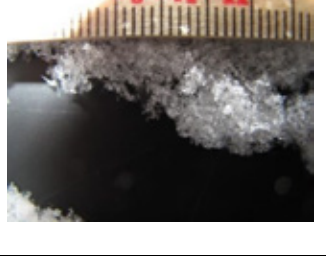

The scanner was placed so that the incidence angle was as close to perpendicular to the surface as possible. A Spectralon® reflectance panel was placed in the view of the scanner next to the snowpack (Figure 7). The first scanning was done without plates, followed by the case where the plate was at the deepest (typically 20 cm depth). In order to not break the snowpack, the plate was left in the snow and a new plate was placed above it. The closer to the surface the plates were, the less difference there was between the depths of different plates. Near the surface, the scanning was made at 0.5 cm depth interval. After collecting the data, a sample of the laser scanning data from the snow surface above the plates was extracted from the point cloud and the differences in the intensity values from samples of different plate depths were compared. The typical sample size was 10 x 10 cm.

The measurements were repeated on different days with different types of snow. The snow types covered fresh fluffy dendritic snow to old wet slushy snow. Images of the different snow surface crystals together with the weather data are seen in Table 1. If the snow was scanned from a too short distance there would be a risk of oversaturating the intensity values. Therefore the scanning was carried out from different locations as straight above the snow sample as possible but still far enough.

The mean normalized intensity values for measurements of different snow types with plates at different depths are shown in Figure 8. The values are normalized using the mean intensity value of the 99 % backscattering plate of Spectralon® reflectance panel. According to the measurements for dry snow, the backscattering takes place from the very surface of the snow. The results were similar to the results obtained by the Sick scanner. For wet snow, the black plate starts to affect the intensity values already at 0.5 to 1 cm depth. This indicates that the majority of the backscatter comes from this depth. Since natural snow is not a featureless plane the depths of the black plates should be considered as approximate.

The use of laser scanning on describing snow surface feature requires the understanding the behavior of laser beam on snow surfaces. The work presented above shows that the backscattering of the laser beam takes place at the very surface of the snow.

Table 1 Weather and snow conditions of each day of the backscatter depth measurements: The scales in the crystal images are in cm.

<p><b>26<sup>th</sup> January 2012</b></p> <p><b>Scanner position:</b> next to the snow, see Figure 3</p> <p><b>Snow depth (cm):</b> 34</p> <p><b>Air temperature:</b> -5°C</p> <p><b>Surface crystals:</b> DFbk/PPsd, dendrites, and broken dendrites</p>	
<p><b>16<sup>th</sup> February 2012</b></p> <p><b>Scanner position:</b> from a window on a higher floor</p> <p><b>Snow depth (cm):</b> 32</p> <p><b>Air temperature:</b> -2.5°C</p> <p><b>Surface crystals:</b> DFbk, dendrites and broken dendrites</p>	
<p><b>13<sup>th</sup> March 2012</b></p> <p><b>Scanner position:</b> from a roof</p> <p><b>Snow depth (cm):</b> 30</p> <p><b>Air temperature:</b> +5°C, half cloudy</p> <p><b>Surface crystals:</b> RGl, MFcl, large rounded clustered crystals, very wet</p>	
<p><b>7<sup>th</sup> February 2013</b></p> <p><b>Scanner position:</b> from a roof</p> <p><b>Snow depth (cm):</b> 25</p> <p><b>Air temperature:</b> 0°C</p> <p><b>Surface crystals:</b> DFbk, wet but fresh, sticky dendrites and broken dendrites</p>	
<p><b>14<sup>th</sup> February 2013</b></p> <p><b>Scanner position:</b> from a window on a higher floor</p> <p><b>Snow depth (cm):</b> 75</p> <p><b>Air temperature:</b> 0°C, cloudy</p> <p><b>Surface crystals:</b> MFcl, wet rounded clusters, some evidence of earlier freezing with sharp edges</p>	

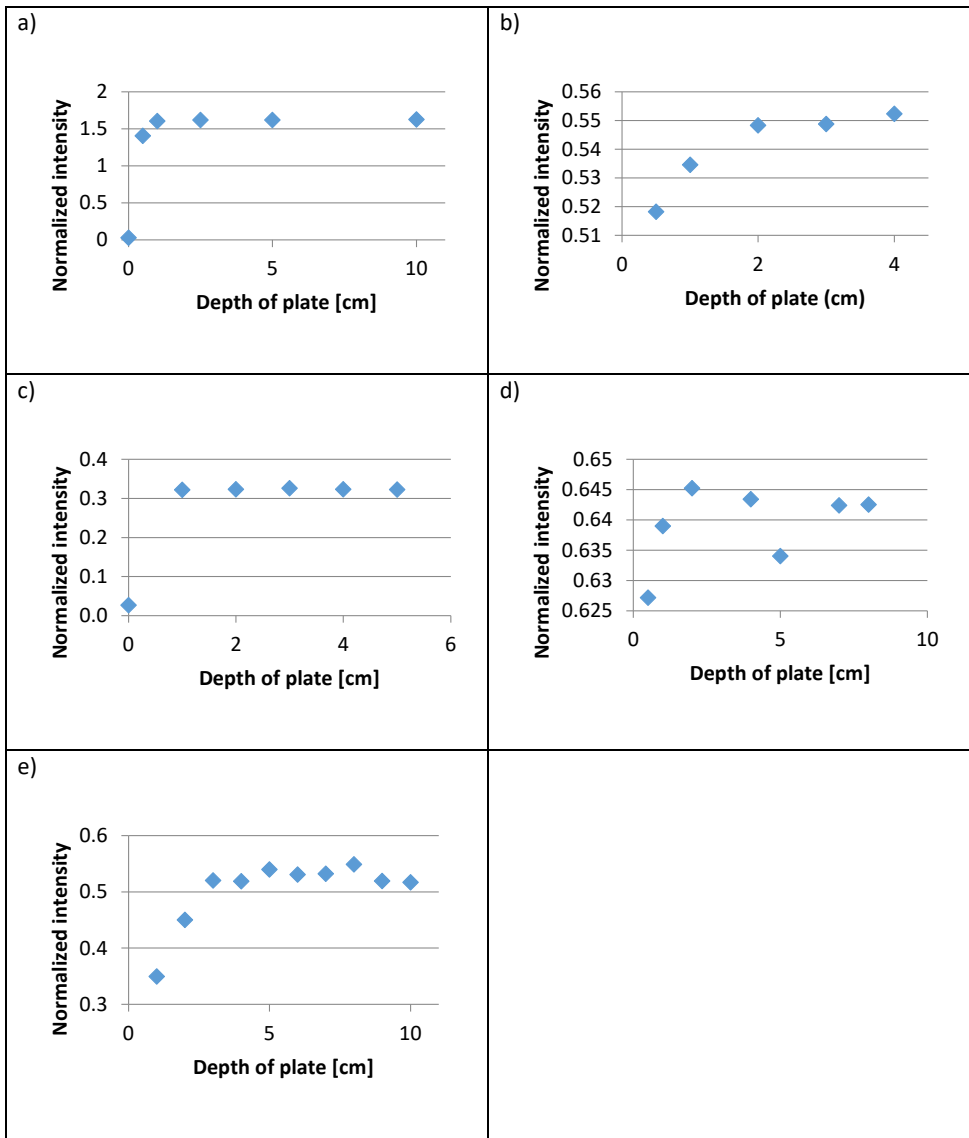
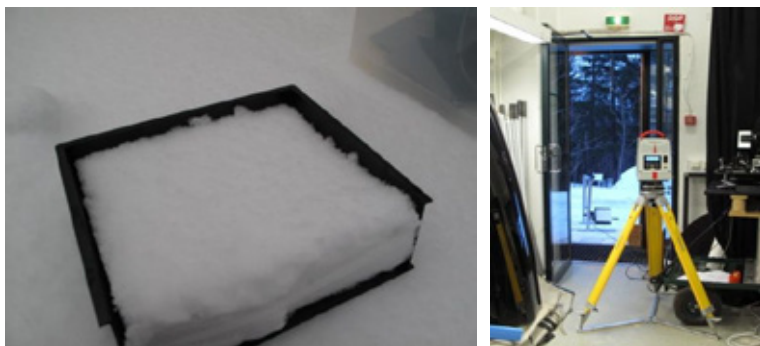


Figure 8 The normalized intensities of the snow surfaces for the different measurements. The measurements were made a) 26<sup>th</sup> January 2012: dry dendrites b) 16<sup>th</sup> February 2012: dry dendrites c) 13<sup>th</sup> March 2012: wet rounded and clustered d) 7<sup>th</sup> February 2013: wet fresh dendrites e) 14<sup>th</sup> February 2013: wet rounded clusters. The horizontal axes shows the depths of the plates.

## **4.2. THE INCIDENCE ANGLE DEPENDENCY OF THE INTENSITY OF LASER BACKSCATTER FROM DIFFERENT SNOW SURFACES**

The dependence of the incidence angle effect on snow type was measured using the Leica HDS6100 scanner presented in the previous chapter. The wavelength dependency of the incidence angle effect was studied using Hyperspectral Lidar (HSL) developed at FGI (Hakala et al. 2012). During measurements, the scanners were placed indoors in a laboratory and the snow samples were kept outdoors (Figure 9).



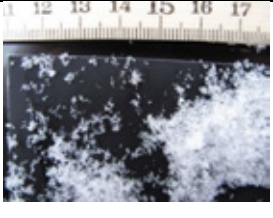
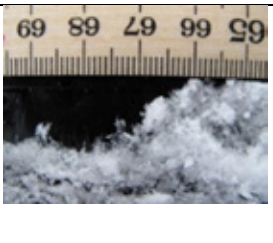
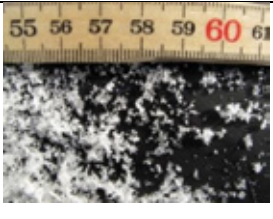
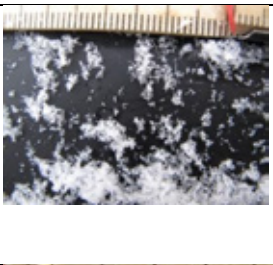

*Figure 9 Left: The snow sample of natural snow in a plastic container. Right: The setup for the scanning. The scanner is at the front of the image and the snow sample with the rotator is on the back.*

The different snow surfaces were studied by cutting 20 cm x 20 cm samples of different snow surface using a thin plastic box with one side wall open (Figure 9). The samples were 6-8 cm thick. The sample was kept in the same box during the measurements. The box was installed on a URB100CC rotation stage (Newport, Irvine, CA). The rotation device was mounted on an aluminum frame along with a mirror. The snow sample was then scanned several times, each having the sample in a different angle. The distance between the snow sample and the scanner (via mirror) was about 5 m. The mirror was used to enable measurements of greater angles without destroying the snow sample.

The data were analyzed by fitting a plane to the point cloud from the snow sample to measure the incidence angle more precisely. The analysis is based on the mean and median values of the intensity values for the snow sample. A similar set of measurements were made during several days having different snow surface. Snow crystal images together with weather information for the different measurements can be seen in Table 2. The crystals have been classified according to Fierz et al. (2009). Additional

measurements with different wavelengths were made using HSL (Hakala et al. 2012) 21th February 2012. The backscatter was measured at 8 wavelengths (554.8 nm, 623.5 nm, 691.1 nm, 725.5 nm, 760.3 nm, 795.0 nm, 899.0 nm, 1000.4 nm).

*Table 2 The weather and snow conditions of the measurements of the incidence angle effect. The number of the scale in the images of the snow surface crystals is in centimeters.*

<p><b>4<sup>th</sup> February 2013</b></p> <p><b>Snow depth (cm):</b> 18  <b>Air temperature:</b> 0°C  <b>Surface crystals:</b> DFdc, broken dendrites and needles, fresh fallen snow</p>	
<p><b>14<sup>th</sup> February 2013</b></p> <p><b>Snow depth (cm):</b> 41  <b>Air temperature:</b> 0°C  <b>Surface crystals:</b> DFdc, needles and decomposed dendrites, that have partially melted and then refrozen</p>	
<p><b>21<sup>st</sup> February 2013</b></p> <p><b>Snow depth (cm):</b> 37  <b>Air temperature:</b> 0°C  <b>Surface crystals:</b> DFdc, old broken crystals that have been clustered but are not yet very rounded</p>	
<p><b>4<sup>th</sup> March 2013</b></p> <p><b>Snow depth (cm):</b> 30.5  <b>Air temperature:</b> -5.5°C  <b>Surface crystals:</b> DFdc, needles and broken dendrites</p>	
<p><b>19<sup>th</sup> March 2013</b></p> <p><b>Snow depth (cm):</b> 33.5  <b>Air temperature:</b> -6°C  <b>Surface crystals:</b> DFbk/PPsd, a fresh fluffy layer of dendrites</p>	

To ensure the stability of the setting during the different scans, a four-step Spectralon® (Labsphere Inc.) reflectance target with 12 %, 25 %, 50 % and 99 % reflectance panels was placed near the snow sample in the view of the scanner. During the data analysis, the 99 % panel was used to monitor the comparability of the different scans. The stability of the measurements was monitored also by measuring air temperature next to the snow sample during measurements, visually monitoring the snow sample between the scans and during the rotation, and sampling the snow point cloud both through the mirror and directly.

The mean intensities for different snow types as a function of incidence angle are shown in Figure 10. The incidence angle dependency seems to be similar to all measured snow types. The differences between the measurements are smaller than the standard deviations of intensity values of the samples. The intensity values were typically normally distributed. Therefore the mean value represents the sample well. The similar dependency of the intensity of the different snow types on the incidence angle gives the possibility to use similar correction function for the intensity values for all snow types. A first-order cosine function for the incidence angle was fitted to the intensity data. Due to the measurement setting the other variables are static. The fitting of the first-order cosine function gives an empirical correction:

$$0.1009 + 0.8812(\cos\alpha_{ia}) \quad (6)$$

The  $R^2$  for the fitting was 0.9884. A more precise fitting needs to be done when a larger data set including wet snow is available. The intensity values for different wavelengths seem to have a similar dependency on incidence angle.

The incidence angle measurements originally included a sample set of wet snow, but the data turned out to be corrupted. Therefore it was excluded from the analysis. It is noteworthy though that the excluded data followed the same pattern as the other snow types. This is in line with the previous experiments including also different incidence angles from wet snow (Anttila et al. 2011).

The results presented above show that the incidence angle dependency of the laser scanning intensity value is similar to all snow types. More similar measurements need to be made in the future to form a more precise correction function for the incidence angle effect. These results will enhance the usability of the intensity data in laser scanning based methods for snow cover mapping.

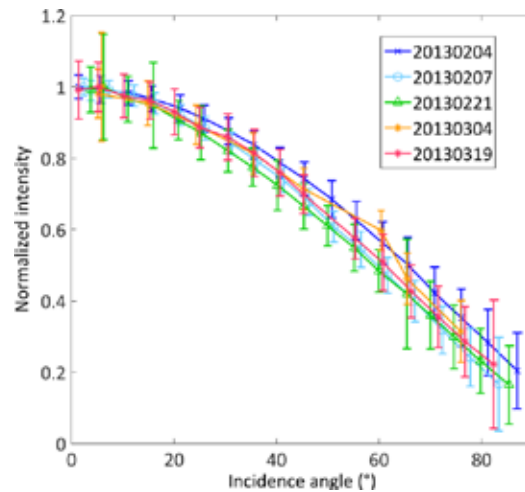


Figure 10 The mean backscattering intensity of the snow samples. The intensity values have been normalized using the maximum values of each measurement set. The error bars show the standard deviation of the snow samples.

### **4.3. MOBILE LASER SCANNING MEASUREMENTS OF SNOW SURFACE ROUGHNESS**

The MLS and validation measurements of seasonal snow surface roughness were made during the SNORTEX campaign 18<sup>th</sup> March 2010. The scanning was made using the FGI ROAMER system, which includes a FARO Photon 120 laser scanner and a NovAtel SPAN GPS-IMU system, together with data synchronizing and recording devices. A summary of the equipment can be seen in Table 3. FGI Roamer was mounted on a sleigh and driven by snowmobile along a 2.5 km long track (Figure 11 and Figure 12). The track followed a marked snowmobile track and covered sparse pine forest and open bogs. The GPS-IMU system measures the platform movements and observes the GPS satellites to reproduce the system trajectory for the scanner data. The data is recorded as a function of time at 100 Hz data rate. At post-processing, the scanner point data is time synchronized with the trajectory data from the GPS-IMU, producing a 3D point cloud.

The data from 18<sup>th</sup> March 2010 was surveyed using 49 Hz scanning frequency and point measurement rate of 244 000 pts/s. The scanner head was mounted upwards on the sleigh for vertical profiling to produce across-track swaths. The point density of the data in hand varies between 100 pts/m<sup>2</sup> and 3000 pts/m<sup>2</sup>. The spacing between the scan

swaths in the data was approximately 2-6 cm depending on the speed of the vehicle. A sample of the gathered laser data can be seen in Figure 13.

*Table 3 Technical details for FGI ROAMER.*

<b>Scanner</b>	FARO Photon 120
	120-976 000 pts/s, user selectable
The maximum field of view	320°
Scan frequency	3-61 Hz, user selectable
Wavelength	785 nm
	Phase shift ranging
Spot size	3.3 mm + 0.16 mrad divergence
Georeferencing system	NovAtel SPAN GPS-IMU
	NovAtel DL-4plus receiver and GPS-702 antenna
	L1 and L2 frequencies
	Honeywell HG1700 AG11 tactical-grade RLG IMU
	Gyro bias 1.0 deg/h
	Random walk 0.125 deg/rt-h
	Data rate 100 Hz
Bi-trigger synchronization	
	Delivers scanner triggers to receiver log
	Camera triggering × 4
Rugged laptops for data recording	



*Figure 11 The FGI ROAMER mounted on a sleigh, moved by snowmobile.*



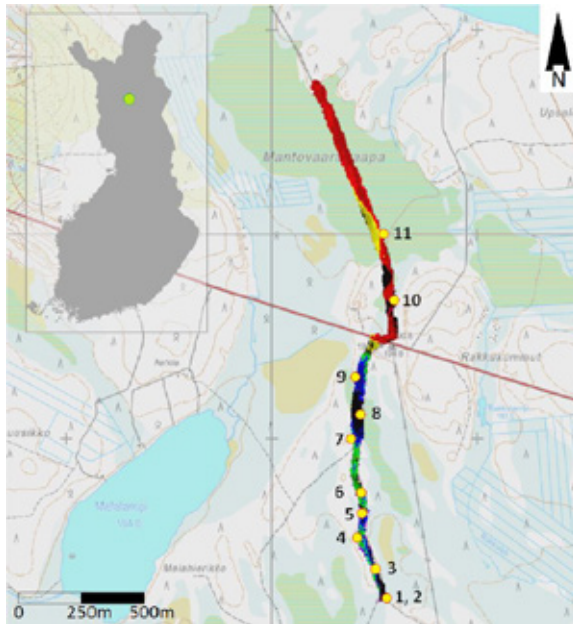


Figure 12 The MLS data coverage for 18th March and plate profile validation sites (yellow dots). Map data courtesy: NLS of Finland.

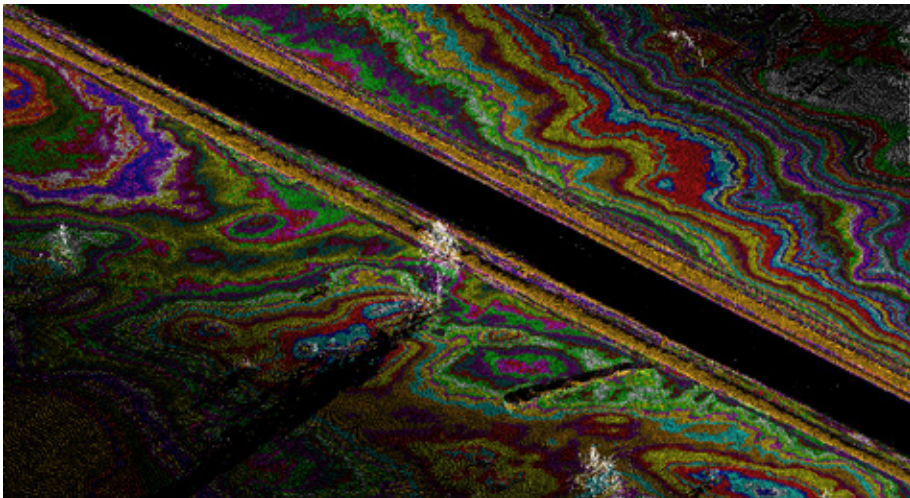


Figure 13 A sample of MLS data from 18th March 2010. The colors come from surface elevation variation. The white objects are trees and the 2.5 m wide black area is the area near the scanner for which data could not be collected due to shadowing of the scanner.

According to the scanner manufacturer, the point measurement accuracy of the scanner is 2 mm with 1 mm repeatability for 90 % reflective target. In practice, however, the accuracy depends on the object surface type, reflectivity and object angle relative to the scanning beam. The relative point accuracy of this system is estimated to be a few millimeters. The absolute positioning accuracy is at centimeter level. The largest source of error in the data is the direct georeferencing of the mapping sensor data with global satellite navigation and inertial positioning.

To study the usability of this data for snow surface roughness mapping, plate measurements of snow surface roughness similar to the ones presented in chapters 3.3 and 3.4 were made along the track. The plate profiles were measured in the same direction as the swath (perpendicular to the scan lines) at 11 locations (shown in Figure 12) shortly after the scanning. Corresponding surface profiles were extracted from the laser scanning data. The profiles were cut using 3 cm and 5 cm wide boxes. The profiles were cut both along the scan swath and perpendicular to it (similar to the plate profile). At some locations, an additional set of profiles were cut from the scanning data closer to the scanner in order to get better resolution for the laser scanning profile. This was done only if the original plate measurement was far from the trajectory and the snow surface between the plate profile and the scanner was intact.

The corresponding plate and laser scanning profiles were compared using rms height variation calculated as a function of measured length (Eq. 2). The linearly rectified profiles can be seen in Figure 14. The profiles can be divided into two groups according to the comparison results: The profiles that match rather well considering the shape and magnitude, and the profiles that do not match quite as well.

The plate profile locations were located from the laser data using distinct visible objects such as placing of tree trunks relative to the profile. In some cases, the laser data turned out to be too sparse for meaningful profile extractions, and the profiles were cut purposely from a different location. This mismatch of locations is also causing some differences in the comparison between the plate and the laser scanning profiles. Some differences are expected to be caused by the fact that the laser scanning profiles show centimeter level roughness, whereas the plates measure roughness with sub-millimeter resolution. At validation site 9 the surface shows a slight bump while at validation sites 3 and 6 there is some wind induced ripples, and the profiles from different sources seem to have been taken at a different phase of the ripple formation. However, for relatively flat and smooth snow surface, such as the one measured here, the variation in scales larger than millimeters is so little, that the miss-locations may not have as large effect on the rms height variation as it could have at different surfaces. This is also demonstrated by the fact that in some cases the laser scanning profiles measured parallel to the plate profiles match the plate profiles even better than the laser profiles measured in the same direction as the plate profile. The surface height variation along the profiles is typically in centimeter scale, as can be seen in the plots in Figure 15, and the scale of variation is the same for both the methods.

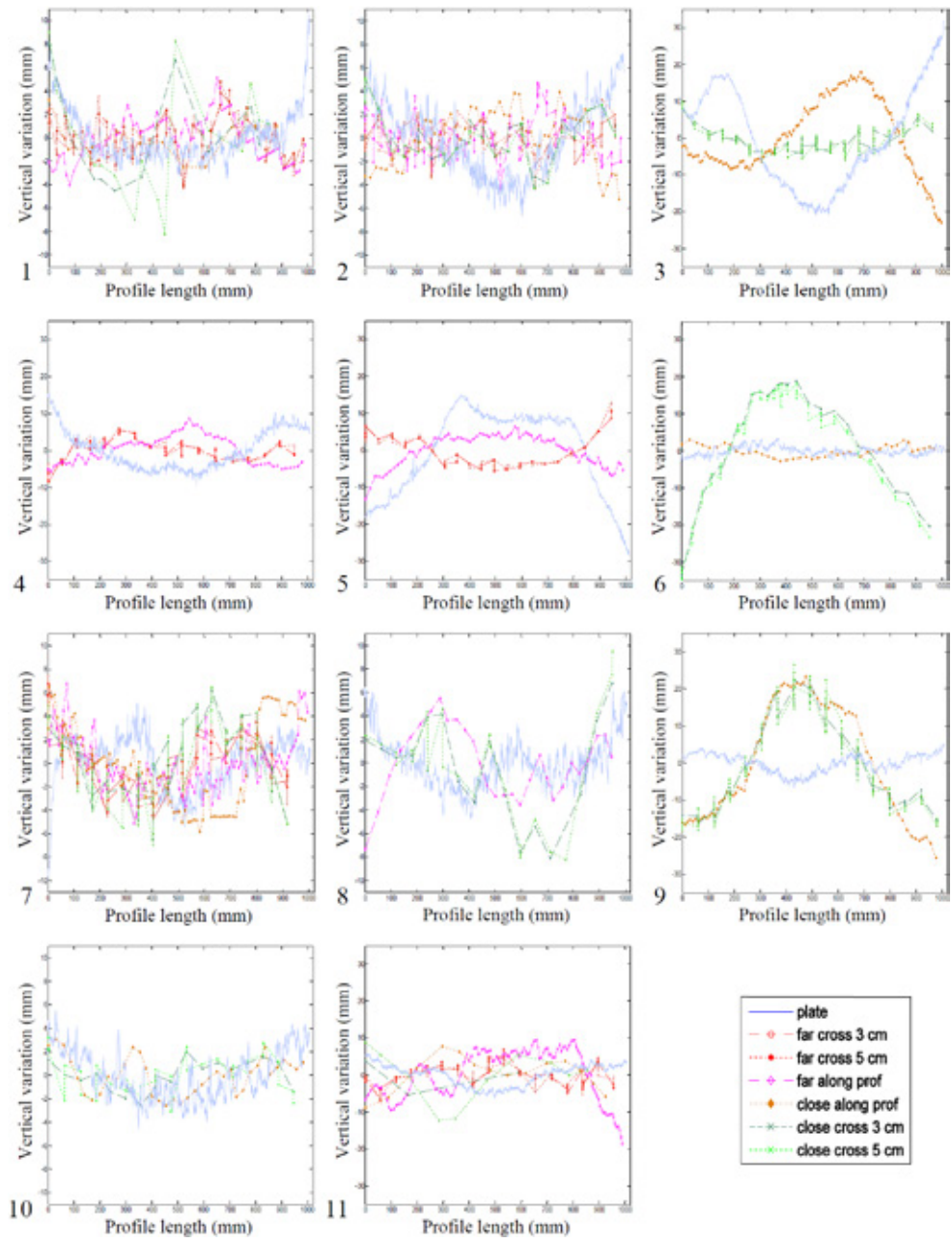


Figure 14 Snow surface profiles derived by using plate photography and MLS. The profiles taken at the same location as the plate profile are indicated as "close" and the profiles extracted further away from the plate profile are indicated as "far".

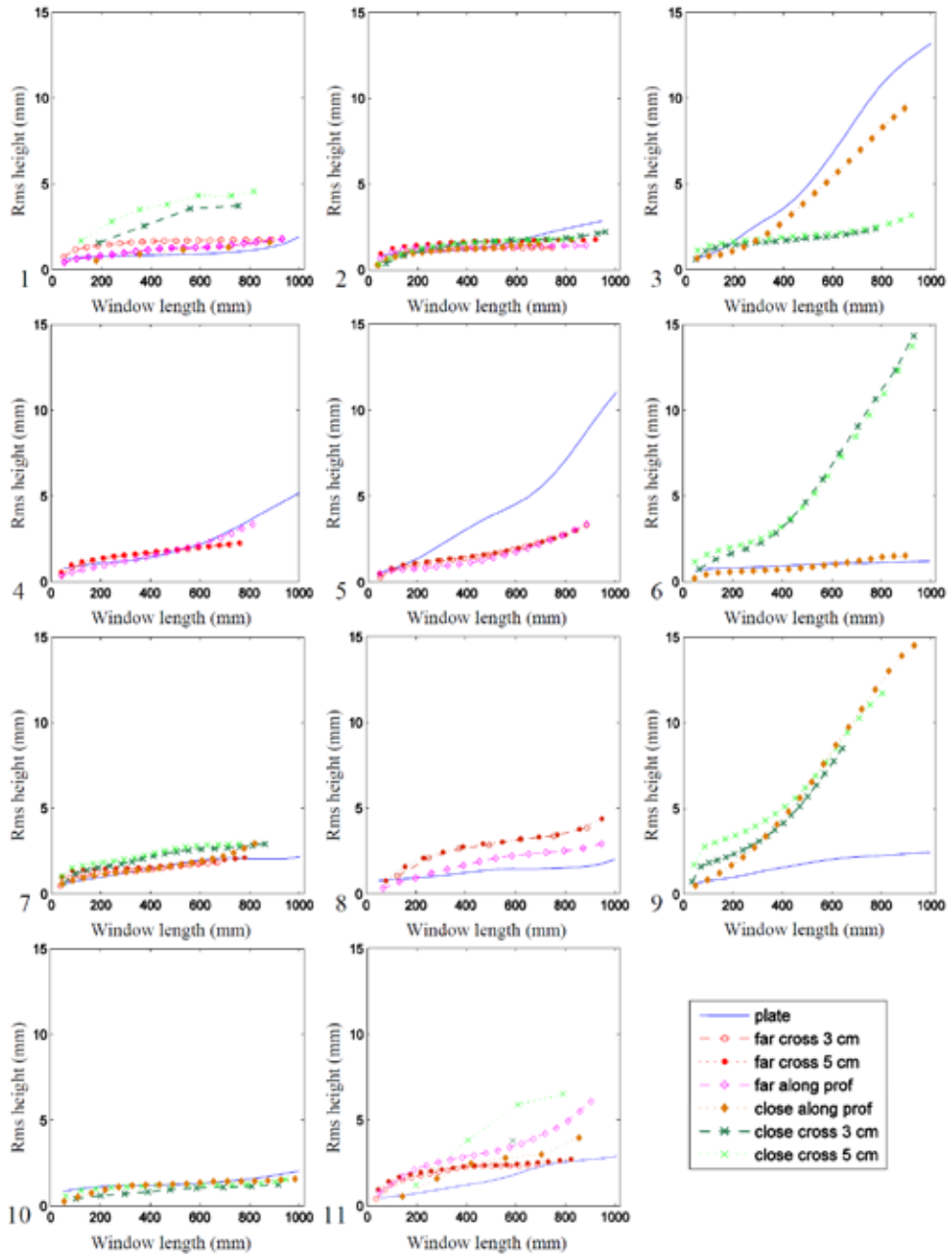


Figure 15 The rms height variation of the MLS and plate profiles.

The resolution of the laser profiles parallel to the laser swath (along scanline) is typically much higher than the profiles that were cut across the swath. The role of resolution, uneven point density, laser spot size, wavelength and function of range and incidence angle on the surface roughness parameters should be studied in more detail. In this study

the laser spot size at the far edge of the snow surface data is about 30 mm, taking into account also the effect of incidence angle. The used wavelength, 785 nm, is so close to optical wavelengths, that the penetration and absorption to the surface are expected to have little effect (Warren et al. 2006). The depth from which the backscattering takes place on snow surfaces is studied in more detail in paper IV. The differences between the rms functions from the two methods are within 2 mm, especially for scales 50-60 cm. In the cases where the differences are larger, they are still on the scale of 10 mm.

After the MLS data was shown to be potential for snow surface, a method to obtain snow surface roughness (MLS grid) by using surface classification and 3D samples was developed. The method starts with cleaning the data from noise points and separating the snow surface from observations of other targets. Points with less than five points within the radius of 20 cm from the point in question were removed. This step caused the removal of some points from snow cover at far distances (greater than 25 m). Therefore, the stray points were not removed directly but classified as "sky points", giving the possibility to restore them in case they are needed at later application.

After filtering the noise points from the data, the snow surface was extracted from the point cloud. The snow surface classification followed the method introduced by Axelsson (1999). The method starts by building a surface model from points given by the user, in this case, the points still left in the point cloud after cleaning. The model consists of triangles and it is then gradually extended by iteratively adding points to the point cloud. A set of parameters determine how far a point can be to still be included in the model. The method performs generally very well, but in the close vicinity of the scanner, some points are lost. These are typically peak points of small ripples 3-10 mm in size. Some of these were returned to the snow surface by searching for points less than 2 cm above the snow surface with 10 cm maximum triangle edge lengths.

After extracting the snow surface, the surface roughness was calculated. It was done by first selecting a resolution and radius for the areas for which the method is applied. Then a plane is fitted to each resolution unit center, and minimum distance from the plane is calculated for each point less than the predefined radius from the center point. The minimum distance from the plane is determined similarly to the plate profile method so that the roughness is defined as the mean minimum distance of the points to the plane. A sample of the MLS grid roughness data is shown in Figure 16.

The results from the MLS grid method were compared to the plate profiles. The MLS grid test data had 1-meter grid sampling. The sample diameters were from 10 cm to 100 cm in 10 cm intervals. The sample points closest to the plate profiles were used for the comparison. The rms height data of both the methods can be seen in Figure 17. The figure shows that the increase in sample size increases the rms height value of the MLS grid data, as was expected. The largest increase was found for the sites with the largest variation in surface topography. The 10 cm scale turned out to be the most challenging one for MLS grid, which can be explained by the number of points within this area being quite low,

thus causing statistical uncertainty. The low number of points can also affect the accuracy of the plane fitting. This can be helped by measuring denser point clouds in the future.

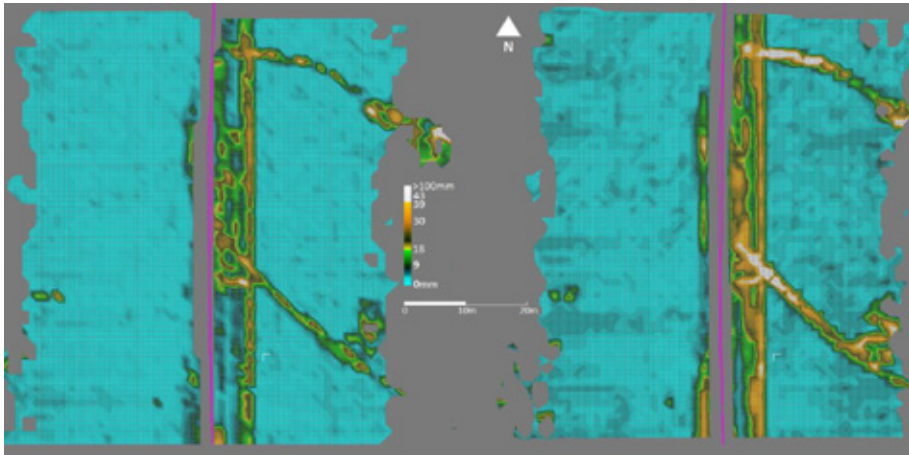


Figure 16 Snow surface roughness from MLS data with 10 cm (left) and 100 cm (right) sample diameters at 1 m grid.

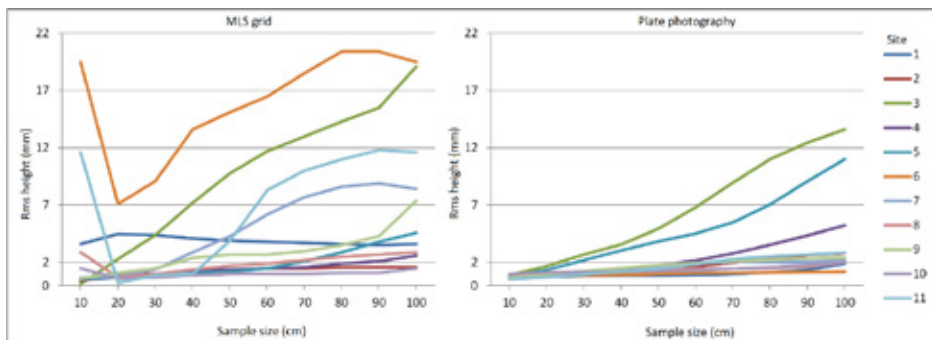


Figure 17 The rms height variation of the snow surface derived by validation plate profiles and MLS grid 3D.

Based on the results the MLS grid method and MLS data show great potential for surface roughness mapping, especially at above centimeter scales. The MLS data can be used to cover large areas, which is particularly useful for satellite data validation and for studying the variability of the snow surface in different environments, such as forested vs open areas.

---

## 5. THE ALBEDO OF THE AREAS COVERED BY SEASONAL SNOW

---

Due to the importance of seasonal snow and surface albedo to the climate, it is important to study them at a global scale. This means vast and remote areas. The in-situ ground measurements do not have sufficient spatial coverage to provide the means to do this, but satellite remote sensing data covers large areas and is available for several decades.

The changes in the albedo of snow covered areas can be studied using satellite-based snow and albedo products. The products use the microwave and/or optical instruments, which are sensitive to the brightness of the surface at measured wavelengths. The optical instruments have typically a higher spatial resolution than the microwave instruments, and can detect even thin snow covers or surface hoar. Therefore they provide data suitable for mapping the snow cover extent, fraction of snow cover and surface albedo. The microwave instruments in turn are more sensitive to the liquid water at and near the surface. This makes microwave instruments good at measuring properties like snow water equivalent, which is a key parameter for hydrological applications such as flood predictions. Furthermore, microwave measurements are typically not sensitive to cloud cover, which prohibits observations of the earth's surface from the optical sensors.

Currently, there are several snow cover and albedo products available, some of which are more observations-based and some incorporate modeling in the retrieval algorithms (Schaaf et al. 2002, Siljamo & Hyvärinen 2011, Barlage et al. 2015, Riggs & Hall 2015, Anttila et al. 2016). The products can be further divided into operational products designed for snow cover and albedo monitoring, and time series, which are meant for climate studies. The operational products are meant for climate and hydrological monitoring, and weather and flood prediction. They are produced at regular intervals, for example, weekly, biweekly or monthly. The long data records of intercalibrated satellite data form the basis of longer time series, giving means to study long-term climatological changes in snow cover and surface albedo. The surface albedo products can also be used to observe changes in the snow cover, as is done in paper V.

Deriving broadband surface albedo from satellite radiance observations requires several steps. First, the satellite instruments make observations above the atmosphere. If this data is used to derive the albedo of the earth surface, then the observations from clouds also need to be removed and the effect of the atmosphere, both downwards and upwards, needs to be taken into account. Second, the earth surface itself has many different types of land surfaces, which all have different scattering properties (BRDF). Since the satellites measure the reflectance at only one direction, the BRDF is needed to describe the scattering in all other directions to derive the hemispherical reflectance



needed for the surface albedo derivation. Third, satellites observe radiance at a limited number of wavelengths. If the data is used for deriving broadband albedo, then the spectral albedos of the observed wavelengths need to be converted into broadband albedo.

The surface albedo of the snow covered areas consists of reflectance from both the snow cover and the vegetation. Furthermore, the snow conditions vary both spatially and temporally. For instance, the reflective properties are different for different snow surfaces, the trees can be covered by snow or be totally snow free, the fraction of the ground covered by snow can be anything from 0% to 100%, and the snow surface can be either clean or dirty. Thus, it is easy to understand why describing the surface albedo of snow-covered surfaces in the climate models is particularly difficult for the vegetated areas, such as the boreal forest zone. (Essery 2013, Thackeray et al. 2015, Abe et al. 2017). Given the large area covered by the boreal forest, and the large variation in albedo values for this area, more information is needed on the phenomena affecting the albedo and snow cover of this area.

The previous studies have already observed changes in the snow cover and vegetation, which have affected the surface albedo over snow covered areas of the Northern Hemisphere (Hall 2004, Smith et al. 2004, Derý & Brown 2007, Trenberth et al. 2007, Brown & Robinson 2011, Flanner et al. 2011, Derksen & Brown 2012, Foster et al. 2013, Stocker 2014, Atlaskina et al. 2015, Fassnacht et al 2016). The studies on snow cover have focused on the changes in snow cover extent, which has been observed to be decreasing, especially in the spring (Derý & Brown 2007, Brown & Robinson 2011, Derksen & Brown 2012). This has an effect on the springtime albedo during the melt season (Atlaskina et al. 2015). Also, the timing of the melt season has changed, with different trends for different areas (Markus 2009, Wang et al. 2013; Chen et al. 2015, Malnes et al. 2016).

## ***5.1. CHANGES IN SURFACE ALBEDO PRIOR TO MELT IN AREAS COVERED BY SEASONAL SNOW***

The changes in albedo and SCE during the melt season have been well reported, but there is very little information on the possible changes in surface albedo prior to the melt season. The study presented here utilizes global albedo data to define the start and end of the melt season, and to look at the albedo level at the start of the melt season to see if there have been changes in surface albedo already before the melt. The albedo levels are derived from the exact time of the start and end of melt.



### 5.1.1. Methods for retrieving melt season timing and albedo

The melt season parameters are derived from sigmoid fittings of yearly surface albedo data of the 34 years long CLARA-A2 SAL (the Satellite Application Facility for Climate Monitoring (CM SAF, funded by EUMETSAT) Clouds, Albedo and RAdiation second release Surface ALbedo data record (Anttila et al. 2016, Karlsson et al. 2017)) data record. The albedo values of CLARA-A2 SAL are derived from optical satellite data (AVHRR instruments onboard the NOAA and MetOp satellites). The final albedo data used here consists of pentad mean values of black-sky surface albedo corresponding to the wavelengths 0.25 - 2.5  $\mu\text{m}$ . The data is given in 0.25° resolution and covers the years from 1982 to 2015.

The sigmoids fittings are done to each pixel and each year using nonlinear regression (Böttcher et al. 2014) (Figure 18). Only pentads from the end of January until end of August were used. The date of snowmelt onset was defined to be the date at which the sigmoid reached 99 % of its variation range. The corresponding threshold for the end date of the snow melt season was defined to be 1%. The length of the melt season was the time difference between the start and end date of the melt season. The albedo values at the time of the onset and end of melt were used as to represent the albedo values preceding and following the melt season.

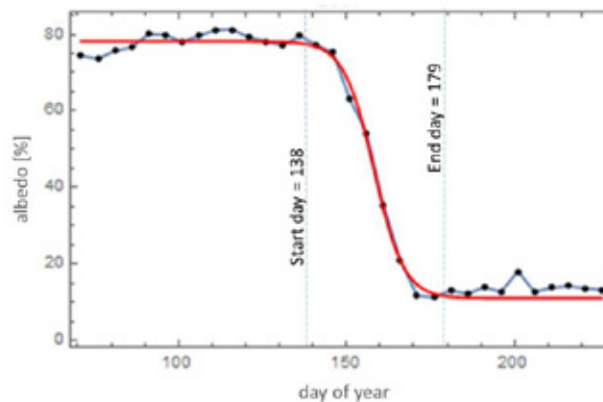


Figure 18 An example of the sigmoid fitting for location 68.125°N, 120.125°E for the year 2007.

The final analysis included only the pixels for which at least 10 years of data were available, the difference between the albedo values at the end and start of melt was larger than 5 % absolute albedo units, and both start and end day of melt were derived successfully. The mean values of  $R^2$  and root mean square error (RMSE) of the final

sigmoid regressions were 0.989 and 5.55 (albedo percentage), respectively. The analysis was made by using only the pixels for which  $R^2 > 0.95$  and  $RMSE < 20$ . This resulted in discarding about 2 % of the data. The final dataset consisted of 2.46 million pixel level melt seasons.

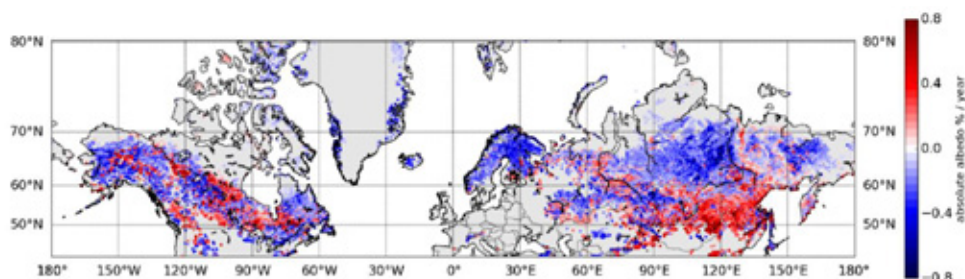
The trends for the melt season parameters were determined per pixel over the 34 years using linear regression of rolling five year means. 5-year mean values with fewer than 3 observations were excluded from the analysis. The linear fitting was carried out only for the pixels that had at least 20 mean values. In the end, trends for 72092 pixels were retrieved successfully.

### *5.1.2. Trends in surface albedo prior to melt*

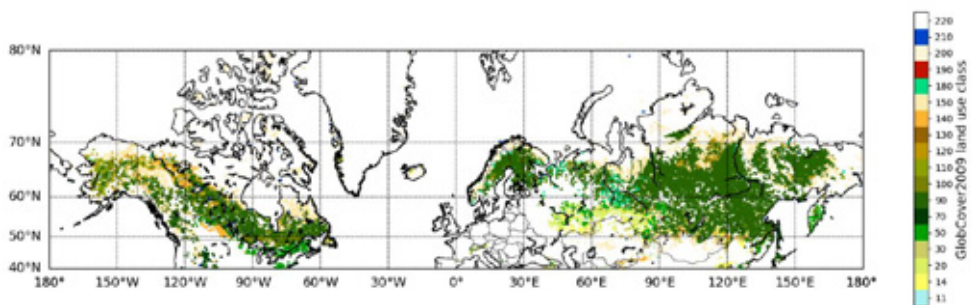
The trends in the albedo at the start of melt season show large spatial variation (Figure 19). The areas of increasing and decreasing albedo values appear in large homogeneous areas typically in the boreal forest zone. Most of the tundra areas do not have statistically reliable ( $R^2 > 0.5$  for the trend fitting) trends. This can be seen in Figure 19b, which shows the land use classes from GlobCover2009 (Arino et al. 2010) for the areas with observed reliable trends in albedo prior to melting. The GlobCover2009 classes are listed in Table 4. In North America, the trends are more scattered when it comes to the direction of change than they are in Eurasia. This fractured nature of the direction of change may be caused by man-made changes in land use types and surface properties, such as cultivation and forestry.

The surface albedo observations prior to melt onset are based on satellite observations. Therefore the albedo values include signal from all land use types at the measured area. The potential effect of vegetation on the observed changes can be estimated by looking at the changes in surface albedo after melt season (Figure 20). These are changes in surface reflectance after the snow has disappeared and before the vegetation has started greening. The albedo after melt shows large areas of homogenous change. The changes are weaker than for albedo prior to melt, as can be expected. The spatial patterns of the post-melt albedo again have similarities with the pre-melt albedo trends suggesting that the causes for the change in winter albedo are related to what is causing the changes in the albedo after melt, but only in some areas. The southern edge of tundra shows weak decreasing trends for the albedo both before and after melt, which could be explained by the shrubification of tundra (Sturm et al. 2001, 2005, Tape et al. 2006, Myers et al. 2011, Pearson et al. 2013, Domine et al. 2016). In northern tundra there are no observed changes, except for some areas near the northern coast of Eurasia, which show increasing trends. These areas correspond roughly with the areas of increased accumulated precipitation prior to melt, which can be seen in Figure 7 of paper V. In the eastern parts of the Eurasian boreal forest zone the albedo after melt season has decreased. This is also the case in North America in Southern Alaska, Canadian Rocky Mountains, most of

Labrador Peninsula and the northern islands of the Canadian Archipelago. These changes could be explained by larger trees.



(a)



(b)

Figure 19 a) The rate of change in albedo at the start of melt (absolute albedo percentage) over 1982 to 2015. The figure shows cases for which the  $R^2$  for the trend fitting was larger than 0.5. b) The GlobCover2009 land use classes of the pixels with reliable albedo trends.

The role of climate change in the changes observed in pre-melt albedo were studied by using the ERA-Interim re-analysis data (Dee et al. 2011) on wind speed (10 m height), total precipitation, amount of snowfall, air temperature (2 m height) and number of days when the maximum air temperature was above 0°C, 4°C and 10°C degrees. The parameters were studied using the 14 day mean values prior to the onset of melt. The correlation between the climatic parameters and the albedo before melt is shown in Figure 21. Explaining the change in albedo before the onset of melt required six climatic parameters (all except snowfall) derived from ERA-Interim, giving a mean  $R^2$  value for the whole area to be 0.64. The climatic parameters were best at explaining the observed change in pre-melt albedo in Northern China, Scandinavia, and parts of Canadian Archipelago.

Also other factors may have affected the surface albedo. The optical properties of the snow cover (mostly grain size and shape and surface roughness) may have changed due to the large-scale changes in climate (Wiscombe & Warren 1980, Domine et al. 2006). The existing studies show changes in vegetation, permafrost and impurities on snow, all of which can have an effect on surface albedo (Rigina 2002, Smith et al. 2004, Dumont et al. 2009, Piao et al. 2011, Ménédroz et al. 2013, Xu et al. 2013, Buitenwerf et al. 2015, Bullard et al. 2016, Helbig et al. 2016). The changes in these show similar patterns as the changes in pre-melt surface albedo, but these similarities are not consistent throughout the study area. This could mean that the changes in them are related to the changes observed on albedo, but the dominating cause for the changes in albedo is different for different areas. It is also noteworthy that the effect of these changes on surface albedo is not the same in all areas.

*Table 4 GlobCover2009 classes and the number of occurrences they were found to be the most common land use class in the area of one SAL pixel.*

LUC class	Label	number of occurrences
11	Post-flooding or irrigated croplands (or aquatic)	420
14	Rainfed croplands	5137
20	Mosaic cropland (50-70%) / vegetation (grassland/shrubland/forest) (20-50%)	5771
30	Mosaic vegetation (grassland/shrubland/forest) (50-70%) / cropland (20-50%)	2996
50	Closed (>40%) broadleaved deciduous forest (>5m)	7775
70	Closed (>40%) needleleaved evergreen forest (>5m)	2472
90	Open (15-40%) needleleaved deciduous or evergreen forest (>5m)	31415
100	Closed to open (>15%) mixed broadleaved and needleleaved forest (>5m)	3605
110	Mosaic forest or shrubland (50-70%) / grassland (20-50%)	2299
120	Mosaic grassland (50-70%) / forest or shrubland (20-50%)	1883
130	Closed to open (>15%) (broadleaved or needleleaved, evergreen or deciduous) shrubland (<5m)	1371
140	Closed to open (>15%) herbaceous vegetation (grassland, savannas or lichens/mosses)	3869
150	Sparse (<15%) vegetation	28741
180	Closed to open (>15%) grassland or woody vegetation on regularly flooded or waterlogged soil - Fresh, brackish or saline water	1639
190	Artificial surfaces and associated areas (Urban areas >50%)	103
200	Bare areas	7523
210	Water bodies	115239
220	Permanent snow and ice	11022

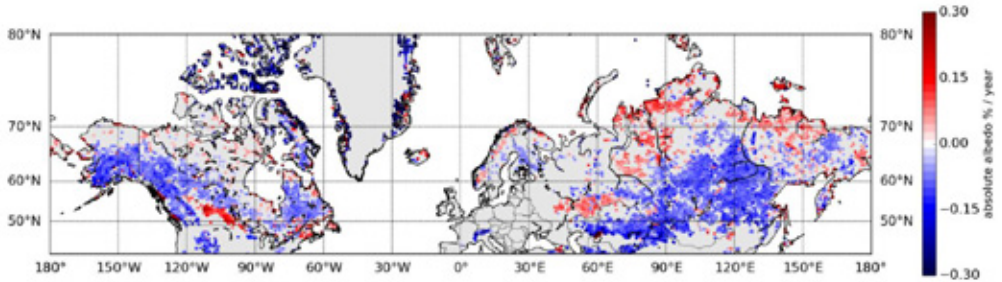


Figure 20 The rate of change in albedo at the end of melt (absolute albedo percentage) from 1982 to 2015. The figure shows cases for which the  $R^2$  for the trend fitting was larger than 0.5. The negative values mean decreasing albedo and the positive values mean increasing albedo.

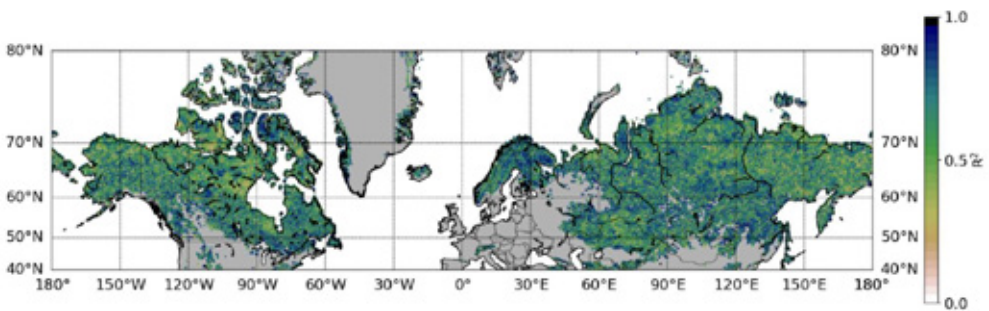
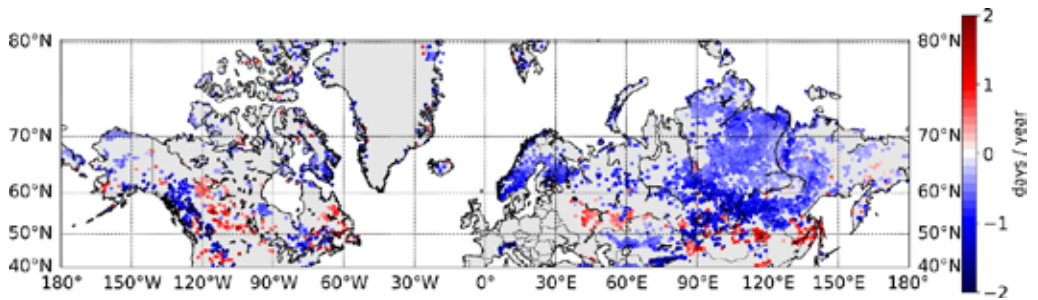


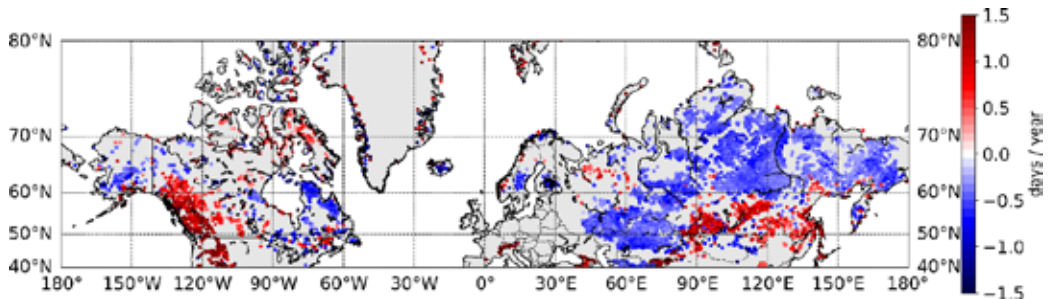
Figure 21 The correlation ( $R^2$ ) between the albedo before the onset of melt and 6 climatic parameters derived from ERA-Interim climate data for 14 days prior to melting. The climatic parameters were the mean air temperature, mean wind speed, total precipitation and the number of days when the air temperature was above 0°C, 4°C and 10°C degrees.

### 5.1.3. Trends in melt season timing

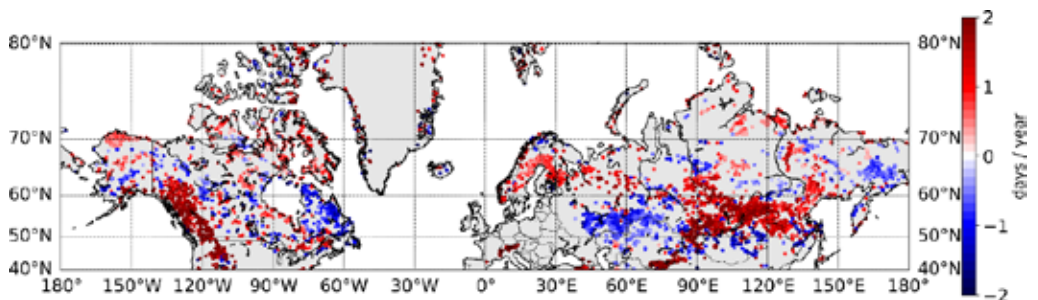
The statistically reliable ( $R^2 > 0.5$ ) changes in melt season timing also concentrate on larger homogeneous areas (Figure 22). The changes are significant, but the direction of change varies within the study area. The majority of the observations show no clear trends. The trends do not seem to be as strongly linked to the vegetation type as the pre-melt albedo. For example, the whole of Central Siberian Plain shows trends towards earlier onset and end of melt, with the length of melt season remaining the same, even though the area includes both boreal forest and tundra. Most of the observed clear trends were towards longer melt seasons and earlier onset of melt, as was the case with Northern Canadian Rocky Mountains and Northern China and Mongolia. As with albedo, in North America the trends are typically more scattered than in Eurasia showing small-scale spatial variation.



(a)



(b)



(c)

Figure 22 a) The rates of change for the start day of melt between 1982 and 2015 showing cases for which  $R^2$  of the fit was larger than 0.5. The negative values mean earlier onset of melt and the positive values mean later dates of onset of melt. b) The rates of change for the end day of melt between 1982 and 2015 using 5-year rolling mean albedo (showing cases for which  $R^2$  of the fit was larger than 0.5). The negative values mean the earlier end of melt and the positive values mean later dates of end of melt. c) The rates of change for the length of the melt season between 1982 and 2015 (showing cases for which  $R^2$  of the fit was larger than 0.5). The negative values mean shorter melt seasons and the positive values mean longer melt seasons.

Looking at the correlation between the start day of melt and climate, three parameters were enough to explain the observed change, with the  $R^2$  value being 0.65 (Figure 23). The climatic parameters used were mean air temperature, mean wind speed, and

accumulated precipitation. The observed changes in start day of melt season were best explained by the climatic parameters in Northern China and Mongolia, where the climatic parameters were able to explain the change almost completely. The parameter best explaining the change was the mean air temperature (mean  $R^2=0.51$  for the whole area), but the climatic parameter best explaining the change was different in different areas.

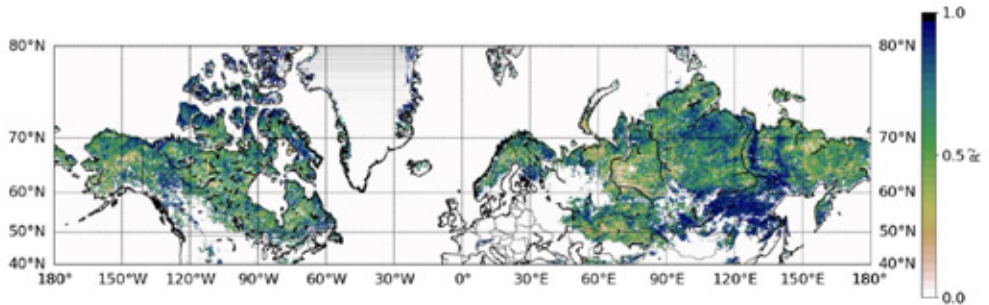


*Figure 23 The correlation ( $R^2$ ) between the start day of melt and 3 climatic parameters derived from ERA-Interim climate data for 14 days prior to melting. The climatic parameters used here were mean air temperature, mean wind speed, and accumulated precipitation.*

The albedo prior to melt season of Northern Hemisphere land areas with seasonal snow cover has changed over the period 1982 to 2015. The direction of change depends on the area. Also the timing of melt season has changed over the same time period. These changes vary between different areas. The changes in albedo prior to melt are linked to changes in vegetation, whereas the changes in melt season timing are linked to changes in climatic conditions. More research is needed to study the local drivers for the observed changes.





---

## 6. CONCLUSIONS

---

The brightness of seasonal snow affects the climate and global energy budget. The reflective properties of seasonal snow are also important parameters for remote sensing and climate models. This dissertation has contributed to the understanding of snow optical properties and improved the usability of remote sensing data (both optical satellite data and laser scanning data) on snow-covered surfaces.

The main contributions of this dissertation have been:

- Currently, there are no standardized methods to measure snow surface roughness as it is difficult to measure. Here, new methods have been created, validated and tested.
  - The plate photography based method for measuring snow surface roughness has been validated and the method has been used in the field. It has proven to be easy and reliable also in field conditions.
  - The mobile laser scanning based method for measuring snow surface roughness has been validated against plate profiles and the mobile laser scanning data has been shown to be suitable for mapping the height variation of the snow surface.
- The surface roughness of natural snow depends on the measured scale. Therefore the surface features should be described using parameters that cover all necessary scales.
  - The multiscale parameters describing snow surface roughness have been used on an extensive field data set of plate photography –profiles. They have been shown to describe the regularity of the surface features as well as the magnitude of the height variation. They are also able to distinguish between old and fresh snow.
- Validating satellite remote sensing data on snow cover needs validation data that includes information from larger areas instead of pointwise measurements. In this dissertation, the usability of terrestrial laser scanning data has been improved by studying the behavior of laser backscatter on different snow surfaces.
  - The depth of the backscatter of the laser beam has been shown to take place at the very surface.
  - The incidence angle dependency of the intensity of the backscattering of laser scanning data does not depend on the surface crystal type. Therefore in the future, the backscattering intensity data can be used for snow cover classifications and snow brightness studies.

- Long-term changes in the surface brightness of snow-covered areas need to be studied on a global scale. Here the remote sensing data on surface albedo has been used to study the changes in surface albedo on snow-covered areas.
  - The changes in surface albedo of snow-covered surfaces prior to melt season in Northern Hemisphere land areas between 40°N and 80°N have been investigated. The reliable trends seem to concentrate on the boreal forest zone. The pre-melt albedo of the tundra area has not yet experienced noticeable change.
  - The timing of the melt season in Northern Hemisphere land areas between 40°N and 80°N has changed in particular in the Central Siberian Plane, where the melt season takes place earlier, and in Northern China and Mongolia, and Canadian Archipelago, where the melt season starts earlier, ends later, and lasts for longer. The changes are related to climatic factors.

During the writing of this dissertation, the work on studying small scale roughness is taking first steps with methods and parameters being developed by several groups of researchers around the world. The importance of small scale surface roughness on the optical properties of snow has been recognized by the international community, but very little has been done on studying it in detail. Typically the studies cover only a few profiles and snow types, and the parameters that are used vary from study to study. The multiscale nature of the phenomenon is recognized by some, but the directionality is still largely left without notice.

Today, 10 years after the SNORTEX -campaign, the plate-photography data set of surface roughness profiles and supporting geophysical measurements is still the largest data set on the surface roughness of natural snow cover that is available, covering several different snow cover types. After the development of the methods to measure surface roughness presented in this dissertation, new methods have been created, but they are mostly used for medium and large scale roughness.

Laser scanning has become a standard measurement technique for snow depth and is used in an increased number of operational measuring sites. The applications on snow surfaces that use the backscattering intensity are few, but show great potential. The intensity information of the backscattering of the laser beam provides means to study the reflectance of snow surface in one direction. As new methods are being developed, this data could in the future be used to study the hemispherical reflectance of the snow surface.

The global climate change, greening and browning of Boreal Forests and tundra and the changes in surface albedo, vegetation and permafrost is an area of study that is progressing with huge steps. Papers on this are published on a weekly basis. The research on the changes in albedo of areas with seasonal snow have focused on monthly means and melt season. The data and results presented in this dissertation define the exact timing of the melt season and thus enable more detailed studies on the changes in surface

albedo of areas with seasonal snow. The results have risen large interest in particular amongst the modelling community, and there is currently co-operation with several different modelling and reanalysis groups.

In the future, the surface roughness data set should be accompanied with other similar data sets from different areas of the world to globally cover the different snow types. The plate methods could be adapted to use a smaller plate that could be used for measuring surface roughness in even smaller scales. Together, the plate-photography -based methods and the MLS method could be used to incorporate information on surface roughness in a larger range of scales, from crystal scale to kilometer scale. The methods could be used to gather data on a larger variety of snow types around the globe. This information could be used to combine the two surface roughness parameters into one and to develop more accurate scattering descriptions of seasonal snow.

The role of surface roughness on reflectance not only on single directions, but hemispherical reflectance (surface albedo) should be studied further. The large variation of snow types and surface features, combined with all the factors influencing surface albedo makes the relationship between surface roughness and albedo a very complex entity. The increasing amount of data on surface roughness and albedo will help to progress this work in the future.

The changes in pre-melt surface albedo of snow-covered areas should be studied further to investigate the role of vegetation and land use type in more detail, perhaps using also stem height and forest density information. The change in albedo and melt season timing could be studied in more detail to describe the variability of change during the 34 years. The results could be used to look in more detail on the local drivers of the observed changes.

These results improve the possibility to gather and analyze snow surface roughness information also from vast, remote and potentially dangerous areas. The improved understanding of seasonal snow surface roughness and albedo will contribute to the accuracy of climate models and remote sensing data. The improved parameterization of seasonal snow surface roughness gives means to incorporate the knowledge on surface roughness to scattering models of snow. This will contribute to the accuracy of remote sensing based surface albedo products, which can serve as validation data for climate models and input parameters for reanalysis data. The understanding of the changes in surface albedo for the last decades improves our understanding of the changing climate and the effect it has on the snow-covered areas.



# REFERENCES

- Abe, M., Takata, K., Kawamiya, M., & Watanabe, S. (2017). Vegetation masking effect on future warming and snow albedo feedback in a boreal forest region of northern Eurasia according to MIROC-ESM. *Journal of Geophysical Research: Atmospheres*, *122*, doi:10.1002/2017JD026957.
- Ahokas, E., Kaasalainen, S., Hyyppä, J., & Suomalainen, J. (2006). Calibration of the Optech ALTM 3100 laser scanner intensity data using brightness targets. *Int. Arch. Photogramm. Remote. Sens. Spat. Inf. Sci.*, *34*, 3-6.
- Anttila, K., Kaasalainen, S., Krooks, A., Kaartinen, H., Kukko, A., Manninen, T., Lahtinen, P., & Siljamo, N. (2011). Radiometric calibration of TLS intensity: Application to snow cover change detection. *Int. Arch. Photogramm. Remote. Sens. Spat. Inf. Sci.*, *38* (5 / W12).
- Anttila, K., Jääskeläinen, E., Riihelä, A., Manninen, T., Andersson, K., & Hollman, R. (2016). Algorithm Theoretical Basis Document: CM SAF Cloud, Albedo, Radiation data record ed. 2 – Surface Albedo. Doi: 10.5676/EUM\_SAF\_CM/CLARA\_AVHRR/V002 (2016).
- Atlaskina, K., Berninger, F. & Leeuw, G. (2015). Satellite observations of changes in snow-covered land surface albedo during spring in the Northern Hemisphere. *The Cryosphere*, *9*, 1879-1893.
- Arino, O., J. Ramos, V. Kalogirou, P. Defourny, & F. Achard, 2010: GlobCover 2009. *Proceedings of the living planet Symposium*, SP-686, June 2010.
- Armstrong, R.L. & Brun E., ed. (2008). Snow and climate, Cambridge University Press, New York.
- Arnold, N. S., Rees, W. G., Devereux, B. J., & Amable, G. S. (2006). Evaluating the potential of high-resolution airborne LIDAR data in glaciology. *International Journal of Remote Sensing*, *27*(6), 1233-1251.
- Axelsson, P. (1999). Processing of laser scanner data — algorithms and applications. *ISPRS Journal of Photogrammetry and Remote Sensing*, *54*(2-3), 138-147.
- Barlage, M., Zeng, X., Wei, H., & Mitchell, K. E. (2005). A global 0.05° maximum albedo dataset of snow-covered land based on MODIS observations. *Geophysical Research Letters*, *32*, L17405, doi: 10.1029/2005GL022881.
- Böttcher, K., Aurela, M., Kervinen, M., Markkanen, T., Mattila, O.-P., Kolari, P.,... & Pulliainen, J. (2014). MODIS tile-series-derived indicators for the beginning of the growing season in boreal coniferous forest – A comparison with the CO<sub>2</sub> flux measurements and phenological observations in Finland. *Remote Sensing of Environment*, *140*, 625-638.
- Brown, R.D., & Mote, P.W. (2009). The response of Northern Hemisphere snow cover to a changing climate. *Journal of Climate*, *22*, 2124-2144.
- Brown, R.D., & Robinson, D.A. (2011). Northern Hemisphere spring snow cover variability and change over 1922– 2010 including an assessment of uncertainty. *The Cryosphere*, *5*, 219-229, doi:10.5194/tc-5-219-2011.
- Budyko, M. I. (1969). The effect of solar radiation variations on the climate of the earth. *tellus*, *21*(5), 611-619.
- Buitenwerf, R., Rose, L., & Higgins, S. (2015). Three decades of multi-dimensional change in global leaf phenology. *Nature Climate Change*, *5*, 364-368.

- Bullard, J., Baddock, M., Bradwell, T., Crusius, J., Darlington, E., Gaiero, D., ... & Thorsteinsson, T. (2016). High-latitude dust in Earth system. *Reviews on Geophysics*, *54*, 447–485, doi:10.1002/2016RG000518.
- Chen, X., Liang, S., Cao, Y., Cao, T., & Wang, D. (2015). Observed contrast changes in snow cover phenology in northern middle and high latitudes from 2001-2014. *Science Reports*, *5*, doi: 10.1038/srep16820.
- Choi, G., Robinson, D.A., & Kang, S. (2010). Changing Northern Hemisphere snow seasons. *Journal of Climate*, *23*, 5305-5310.
- Choudhury, B. J., & Chang, A. T. C. (1981). The albedo of snow for partially cloudy skies. *Boundary-Layer Meteorology*, *20*(3), 371-389.
- Church, E. L. (1988). Fractal surface finish. *Appl. Opt.*, *27*(89), 1518–1526.
- Colbeck, S.C. (1982a). An overview of seasonal snow metamorphism. *Reviews of Geophysics and Space Physics*, *20*(1), 45-61.
- Colbeck, S.C. (1982b). Growth of faceted crystals in a snow cover. CRREL Report 82-29. 27 pp.
- Colbeck, S. C. (1997). *A Review of Sintering in Seasonal Snow* (No. CRREL-97-10). COLD REGIONS RESEARCH AND ENGINEERING LAB HANOVER NH.
- Coren, F., & Sterzai, P. (2006). Radiometric correction in laser scanning. *International Journal of Remote Sensing*, *27*, 3097-3104.
- Davidson, M., Le Toan, T., Mattia, F., Manninen, T., & Borgeaud, M. (2000). On the characterisation of agricultural random roughness for radar remote sensing studies. *IEEE Transactions on Geoscience and Remote Sensing*, *38*(2), 630–640.
- Dee, D. P., Uppala, S. M., Simmons, A. J., Berrisford, P., Poli, P., Kobayashi, S., ... & Bechtold, P. (2011). The ERA-Interim reanalysis: Configuration and performance of the data assimilation system. *Quarterly Journal of the royal meteorological society*, *137*(656), 553-597.
- Deems, J. S., Fassnacht, S. R., & Elder, K. J. (2006). Fractal distribution of snow depth from LiDAR data. *Journal of Hydrometeorology*, *7*(2), 285-297.
- Derksen, C., & Brown, R. (2012). Spring snow cover extent reductions in the 2008–2012 period exceeding climate model predictions. *Geophysical Research Letters*, *39*, L19504.
- Déry, S., & Brown, R. (2007). Recent Northern Hemisphere snow cover extent trends and implications for the snow-albedo feedback. *Geophysical Research Letters*, *34*, L22504.
- Domine, F., Salvatori, R., Legagneux, L., Salzano, R., Fily, M., & Casacchia, R. (2006). Correlation between the specific surface area and the short wave infrared (SWIR) reflectance of snow. *Cold Regions Science and Technology*, *46*(1), 60–68.
- Domine, F., Barrere, M., & Morin, S. (2016). The growth of shrubs on high Arctic tundra at Bylot Island: impact on snow physical properties and permafrost thermal regime. *Biogeosciences*, *13*(23), 6471.
- Dong, W. P., Sullivan, P. J., & Stout, K. J. (1992). Comprehensive study of parameters for characterizing three-dimensional surface topography I: Some inherent properties of parameter variation. *Wear*, *159*, 161–171.

- Dong, W. P., Sullivan, P. J., & Stout, K. J. (1993). Comprehensive study of parameters for characterizing three-dimensional surface topography II: Statistical properties of parameter variation. *Wear*, *167*, 9–21.
- Dong, W. P., Sullivan, P. J., & Stout, K. J. (1994a). Comprehensive study of parameters for characterizing three-dimensional surface topography III: Parameters for characterising amplitude and some functional properties. *Wear*, *178*, 29–43.
- Dong, W. P., Sullivan, P. J., & Stout, K. J. (1994b). Comprehensive study of parameters for characterizing three-dimensional surface topography IV: Parameters for characterising spatial and hybrid properties. *Wear*, *178*, 45–60.
- Dumont, M., Brun, E., Picard, G., Michou, M., Libois, Q., Petit, J. R., ... & Josse, B. (2014). Contribution of light-absorbing impurities in snow to Greenland's darkening since 2009. *Nature Geoscience*, *7*(7), 509.
- Egli, L., Jonas, T., Grünewald, T., Schirmer, M., & Burlando, P. (2012). Dynamics of snow ablation in a small Alpine catchment observed by repeated terrestrial laser scans. *Hydrological Processes*, *26*(10), 1574–1585.
- Eitel, J. U. H., Williams, C. J., Vierling, L. A., Al-Hamdan, O. Z., & Pierson, F. B. (2011). Suitability of terrestrial laser scanning for studying surface roughness effects on concentrated flow erosion processes in rangelands. *CATENA* *87*(3), 398–407.
- Elder, K., Cline, D., Liston, G., & Armstrong, R. (2009). NASA Cold Land Processes Experiment (CLPX 2002/03): Field measurements of snowpack properties and soil moisture. *Journal of Hydrometeorology*, *10*, 320–329.
- Essery, R. (2013). Large-scale simulations of snow albedo masking by forests. *Geophysical Research Letters*, *40*, doi: 10.1002/grl.51008
- Eveland, J. W., Gooseff, M. N., Lampkin, D. J., Barrett J. E., & Takacs-Vesbach, C. D. (2013). Seasonal controls on snow distribution and aerial ablation at the snow patch and landscape scales, McMurdo Dry Valleys, Antarctica. *The Cryosphere*, *7*, 917-913.
- Fassnacht, S., Cherry, M., Venable, N., & Saavedra, F. (2016). Snow and albedo climate change impacts across the United States Northern Great Plains. *The Cryosphere*, *10*, 329-339.
- Fassnacht, S. R., & Deems, J. D. (2006). Measurement sampling and scaling for deep montane snow depth data. *Hydrological Processes*, *20*, 829–838.
- Fassnacht, S. R., Stednick, J. D., Deems, J. S., & Corrao, M. V. (2009a). Metrics for assessing snow surface roughness from digital imagery. *Water Resources Research*, *45*, W00D31, doi:10.1029/2008WR006986.
- Fassnacht, S. R., Williams, M. W., & Corrao, M. V. (2009). Changes in the surface roughness of snow from millimetre to metre scales. *Ecological Complexity*, *6*(3), 221-229.
- Fierz, C., Armstrong, R.L., Durand, Y., Etchevers, P., Greene, E., McClung, D.M., Nishimura, K., Satyawali, P.K., & Sokratov, S.A. (2009). The International Classification for Seasonal Snow on the Ground. IHP-VII Technical Documents in Hydrology N°83, IACS Contribution N°1, UNESCO-IHP, Paris.
- Flanner, M.G., Shell, K.M., Barlage, M., Perovich, D.K., & Tschudi, M.A. (2011). Radiative forcing and albedo feedback from the northern hemisphere cryosphere between 1979 and 2008. *Nature Geosciences*, *4*, 151–155. <http://dx.doi.org/10.1038/ngeo1062>

- Foster, J. L., Cohen, J., Robinson, D. A., & Estilow, T. W. (2013). A look at the date of snowmelt and correlation with the Arctic Oscillation. *Annals of Glaciology*, *54*, 196-204.
- Fung, A. K. (1994). *Microwave Scattering and Emission Models and Their Applications*, pp. 573, Artech House, Boston.
- Gallet, J. C., Domine, F., Zender, C. S., & Picard, G. (2009). Measurement of the specific surface area of snow using infrared reflectance in an integrating sphere at 1310 and 1550 nm. *The Cryosphere*, *3*, 167-182, doi:10.5194/tc-3-167-2009.
- Gallet, J. C., Domine, F., & Dumont, M. (2014). Measuring the specific surface area of wet snow using 1310 nm reflectance. *The Cryosphere*, *8*(4), 1139.
- GCOS Secretariat (2006). Systematic observation requirements for satellite-based products for climate. Technical Report 107, Global Climate Observing System, World Meteorological Organization, 7 bis, Avenue de la Paix P.O. Box No. 2300 CH-1211 Geneva 2, Switzerland.
- Gromke, C., Manes, C., Walter, B., Lehning, M., & Guala, M. (2011). Aerodynamic roughness length of fresh snow. *Boundary Layer Meteorology*, *141*, 21–34.
- Hakala, T., Suomalainen, J., Kaasalainen, S., & Chen, Y. (2012). Full Waveform Hyperspectral LiDAR for Terrestrial Laser Scanning. *Optics Express*, *20*(7), 7119-7127. <http://dx.doi.org/10.1364/OE.20.007119>
- Hall, A. (2004). The role of surface albedo feedback in climate. *Journal of Climate*, *17*, 1550-1568.
- Helbig, M., Wischnewski, K., Kljun, N., Chasmer, L. E., Quinton, W. L., Detto, M., & Sonnentag, O. (2016). Regional atmospheric cooling and wetting effect of permafrost thaw-induced boreal forest loss. *Global Change Biology*, *22*(12), 0448-4066.
- Helfricht, K., Kuhn, M., Keuschnig, M., & Heilig, A. (2014). Lidar snow cover studies on glaciers in the Ötztal Alps (Austria): comparison with snow depths calculated from GPR measurements. *The Cryosphere*, *8*, 41-57.
- Herzfeld, U. C. (2002). Vario functions of higher order—Definition and application to characterization of snow surface roughness. *Computers & geosciences*, *28*(5), 641-660.
- Höfle, B., Geist, T., Rutzinger M., & Pfeifer, N. (2007). Glacier surface segmentation using airborne laser scanning point cloud and intensity data, *Proceedings of ISPRS Workshop Laser Scanning SilviLaser*, *36*, pp. 195–200, International Archives of Photogrammetry and Remote Sensing, Espoo, Finland part 3/W52.
- Höfle, B., & Pfeifer, N. (2007). Correction of laser scanning intensity data: Data and model-driven approaches. *ISPRS journal of photogrammetry and remote sensing*, *62*(6), 415-433.
- Holland, M. M., Serreze, M. C., & Stroeve, J. (2010). The sea ice mass budget of the Arctic and its future change as simulated by coupled climate models. *Climate Dynamics*, *34*(2-3), 185-200.
- Hollaus, M., Aubrecht, C., Höfle, B., Steinnocher, K., & Wagner, W. (2011). Roughness mapping on various vertical scales based on full-waveform airborne laser scanning data. *Remote Sensing*, *3*, 503–523.
- Hood, J. L., & Hayashi, M. (2010). Assessing the application of a laser rangefinder for determining snow depth in inaccessible alpine terrain. *Hydrology and Earth System Sciences*, *14*(6), 901.
- Hori, M., Sugiura, K., Kobayashi, K., Aoki, T., Tanikawa, T., Kuchiki, K., Niwano, M., & Enomoto, H. (2017). A 38-year (1978–2015) Northern Hemisphere daily snow cover extent product derived



using consistent objective criteria from satellite-borne optical sensors. *Remote Sensing of Environment*, 191, 402–418.

Ingvander, S., Brown, I. A., Jansson, P., Holmlund, P., Johansson, C., & Rosqvist, G. (2013). Particle size sampling and object-oriented image analysis for field investigations of snow particle size, shape, and distribution. *Arctic, antarctic, and alpine research*, 45(3), 330-341.

Ingvander, S., Johansson, C., Jansson, P., & Pettersson, R. (2012). Comparison of digital and manual methods of snow particle size estimation. *Hydrology Research*, 43(3), 192-202.

Jaedicke, C., Thiis, T.K., & Bang B. (2000). The snowdrift pattern around a small hill in the Arctic. Snow engineering – recent advances and developments. Proceedings of the Fourth International Conference on Snow Engineering, In File, Trondheim, Norway, Rotterdam, A.A. Balkema 75-80.

Jin, Z., Charlock, T. P., & Rutledge, K. (2002). Analysis of broadband solar radiation and albedo over the ocean surface at COVE. *Journal of Atmospheric and Oceanic Technology*, 19(10), 1585-1601.

Kaasalainen, S., Kaasalainen, M., Mielonen, T., Suomalainen, J., Peltoniemi, J. I., & Näränen, J. (2006). Optical properties of snow in backscatter. *Journal of Glaciology*, 52, 574–584.

Kaasalainen, S., Kaartinen, H., & Kukko, A. (2008). Snow cover change detection with laser scanning range and brightness measurements. *EARSel eProceedings*, 7, 133–141.

Kaasalainen, S., Hyyppä, H., Kukko, A., Litkey, P., Ahokas, E., Hyyppä, J., Lehner, H., Jaakkola, A., Suomalainen, J., & Akujärvi, A. (2009). Radiometric calibration of LIDAR intensity with commercially available reference targets. *IEEE Transactions on Geoscience and Remote Sensing*, 47, -598.

Kaasalainen, S., Kaartinen, H., Kukko, A., Anttila, K., & Krooks, A. (2010). Brief communication: application of mobile laser scanning in snow cover profiling. *The Cryosphere*, 5, 135–138.

Kaasalainen, S., Jaakkola, A., Kaasalainen, M., Krooks, A., & Kukko, A. (2011). Analysis of incidence angle and distance effects on terrestrial laser scanner intensity: Search for correction methods. *Remote Sensing*, 3(10), 2207-2221.

Karlsson, K.-G., Anttila, K., Trentmann, J., Stengel, M., Meirink, J. F., Devasthale, A., ... & Benas, N. (2017). CLARA-A2: the second edition of the CM SAF cloud and radiation data record from 34 years of global AVHRR data. *Atmospheric Chemistry and Physics*, 17(9), 5809-5828.

Keller, J. M., Crownover, R. M., & Chen, R. Y. (1987). Characteristics of natural scenes related to the fractal dimension. *IEEE Transactions on Pattern Analysis and Machine Intelligence*, (5), 621-627.

Kenner, R., Phillips, M., Danioth, C., Denier, C., Thee, P., & Zraggen, A. (2011). Investigation of rock and ice loss in a recently deglaciated mountain rock wall using terrestrial laser scanning: Gemsstock, Swiss Alps. *Cold Regions Science and Technology*, 67(3), 157–164.

Krooks, A., Kaasalainen, S., Hakala, T., & Nevalainen, O. (2013). Correction of Intensity Incidence Angle Effect in Terrestrial Laser Scanning. *ISPRS Ann. Photogramm. Remote Sens. Spatial Inf. Sci.* II-5/W2, 145-150. [www.isprs-ann-photogramm-remote-sens-spatial-inf-sci.net/II-5-W2/145/2013/](http://www.isprs-ann-photogramm-remote-sens-spatial-inf-sci.net/II-5-W2/145/2013/)

Kuchiki, K., Aoki, T., Niwano, M., Motoyoshi, H. & Iwabuchi, H. (2011). Effect of sastrugi on snow bidirectional reflectance and its application to MODIS data. *Journal of Geophysical Research*, 116(D181101).

- Kukko, A., Andrei, C. O., Salminen, V. M., Kaartinen, H., Chen, Y., Rönholm, P., ... & Kosonen, I. (2007). Road environment mapping system of the Finnish Geodetic Institute—FGI Roamer. *Int. Arch. Photogramm. Remote Sens. Spat. Inf. Sci.*, *36*, 241-247.
- Kukko, A., Anttila, K., Manninen, T., Kaartinen, H., & Kaasalainen, S. (2013). Snow surface roughness from mobile laser scanning data. *Cold Regions Science and Technology*, *96*, 23–35.
- Lacroix, P., Legrésy, B., Langley, K., Hamran, S. E., Kohler, J., Roques, S., Rémy, F., & Dechambre, M. (2008). Instruments and methods: In situ measurements of snow surface roughness using a laser profiler. *Journal of Glaciology*, *54*(187), 753–762.
- Lamb, D., & Verlinde, J. (2011). *Physics and chemistry of clouds*. Cambridge University Press.
- Lehning, M., Löwe, H., Ryser, M., & Raderschall, N. (2008). Inhomogeneous precipitation distribution and snow transport in steep terrain. *Water Resources Research*, *44*, W07404, doi:10.1029/2007WR006545.
- Lehning, M., Grünwald, T., & Schirmer, M. (2011). Mountain snow distribution governed by an altitudinal gradient and terrain roughness. *Geophysical Research Letters*, *38*, L19504, doi:10.1029/2011GL048927.
- Leroux, C. & Fily, M. (1998). Modeling the effect of sastrugi on snow reflectance. *Journal of Geophysical Research*, *103*(E11). Libbrecht, K. G. (2005). The physics of snow crystals. *Reports on progress in physics*, *68*(4), 855.
- Löwe, H., Egli, S., Bartlett, S., Guala, J.M.M., & Manes, C. (2007). On the evolution of the snow surface during snowfall. *Geophysical Research Letters*, *34*, L21507.
- Lutz, E. R., Geist, T., & Stötter, J. (2003). Investigations of Airborne Laser Scanning Signal Intensity on glacial surfaces: utilizing comprehensive Laser Geometry Modeling and Surface Type Modeling; (a case study: Svartisheibreen, Norway). *Int. Arch. Photogramm. Remote. Sens. Spat. Inf. Sci.*, *34* (3/W13).
- Magono, C., & Chung, W. (1966). Meteorological classification of natural snow crystals. *Journal of the Faculty of Science, Hokkaido University. Series 7, Geophysics*, *2*(4), 321-335.
- Makkonen, L. (1989). Estimation of wet snow accretion on structures. *Cold Regions Science and Technology*, *17*(1), 83-88.
- Malnes, E., Karlsen, R. S., Johansen, B., Bjerke, J. W., & Tømmervik, H. (2016). Snow season variability in a boreal-Arctic transition area monitored by MODIS data. *Environmental Research Letters*, *11*(12), 125005.
- Manes, C., Guala, M., Löwe, H., Bartlett, S., Egli, L., & Lehning, M. (2008). Statistical properties of fresh snow roughness. *Water Resources Research*, *44*, W11407, doi:10.1029/2007WR006689.
- Manninen, A. T. (1997a). Multiscale surface roughness and backscattering. *Prog. Electromagnet. Res. PIER*, *16*, 175–203.
- Manninen, A. T. (1997b). Surface roughness of Baltic sea ice. *Journal of Geophysical Research*, *102*(C1), 1119–1139, doi:10.1029/96JC02991.
- Manninen, A. T. (2003). Multiscale surface roughness description for scattering modeling of bare soil. *Physica A*, *319*, 535–551.
- Manninen, T., & Roujean, J. L. (2014). SNORTEX field campaigns 2008–2010. Finnish Meteorological Institute Reports 2014, 7.

- Manninen, T., Rantasuo, M., Le Toan, T., Davidson, M., Mattia, F., & Borgeaud, M. (1998). Multiscale surface roughness of bare soil, in Proceedings of the IGARSS'98, pp. 1203–1206, IEEE International, Seattle, 6–10 July.
- Markus, T., Stroeve, J. C., & Miller, J. (2009). Recent changes in Arctic sea ice melt onset, freezeup, and melt season length. *Journal of Geophysical Research*, *114*, C12024, doi: 10.1029/2009JC005436.
- Martini, A., Desieu, J.-P., Ferro-Famil, L., Bernier, M., & Pottier, E. (2006). Snow extent mapping in alpine areas using polarimetric SAR data. *EARSeL proceedings*, *5*, 129-136.
- Mellor, M. (1965). Cold Regions Science and Engineering part III, Section A3c: Blowing Snow. Cold Regions Research and Engineering Laboratory, Hanover, USA.
- Ménégoz, M., Krinner, G., Balkanski, Y., Cozic, A., Boucher, O., & Ciais, P. (2013). Boreal and temperate snow cover variations induced by black carbon emissions in the middle of the 21st century. *The Cryosphere*, *7*(2), 537-554.
- Mialon, A., Fily, M., & Royer, A. (2005). Seasonal snow cover extent from microwave remote sensing data: comparison with existing ground and satellite based measurements. *EARSeL eProceeding*, *4*, 215–225 ([http://www.e proceedings.org/static/vol04\\_2/04\\_2\\_mialon1.pdf](http://www.e proceedings.org/static/vol04_2/04_2_mialon1.pdf)).
- Myers-Smith, I. H., Forbes, B. C., Wilmsking, M., Hallinger, M., Lantz, T., Blok, D., ... & Boudreau, S. (2011). Shrub expansion in tundra ecosystems: dynamics, impacts and research priorities. *Environmental Research Letters*, *6*(4), 045509.
- Nagler, T., & Rott, H. (2000). Retrieval of wet snow by means of multitemporal SAR data. *Transactions on Geoscience and Remote Sensing*, *38*(2), 754-765.
- Nakaya, U. (1954). *Snow crystal, natural and artificial*. Harvard University Press.
- Pan, Y. D., Birdsey, R.A., Fang, J., Houghton, R., Kauppi, P.E., Kurz, W.A., Phillips, O.L., Shvidenko, A., Lewis, S.L., Canadell, J.G., Ciais, P., Jackson, R.B., Pacala, S.W., McGuire, A.D., Piao, S., Rautiainen, A., Sitch, S., & Hayes, D. (2011). A large and persistent carbon sink in the world's forests. *Science*, *333*, 988-993.
- Pearson, R. G., Phillips, S. J., Lorant, M. M., Beck, P. S., Damoulas, T., Knight, S. J., & Goetz, S. J. (2013). Shifts in Arctic vegetation and associated feedbacks under climate change. *Nature Climate Change*, *3*(7), 673.
- Peltoniemi, J. I., Suomalainen, J., Hakala, T., Puttonen, E., Näränen, J., Kaasalainen, S., Torppa, J., & Hirschmugl, M. (2010). Reflectance of various snow types: measurements, modelling and potential for snow melt monitoring. In *Light Scattering Reviews 5: Single Light Scattering and Radiative Transfer*, chapter 9, 393-450. Springer Berlin Heidelberg. Doi: 10.1007/978-3-642-10336-0.
- Petrovic, J. J. (2003). Review Mechanical properties of ice and snow. *Journal of Materials Science*, *38*, Issue 1, 1–6.
- Piao, S., Wang, X., Ciais, P., Zhu, B., & Wang, T. (2011). Changes in satellite-derived vegetation growth trend in temperate and boreal Eurasia from 1982 to 2006. *Global Change Biology*, *17*, 3228-3239.
- Picard, G., Arnaud, L., Panel, J. M., & Morin, S. (2016). Design of a scanning laser meter for monitoring the spatio-temporal evolution of snow depth and its application in the Alps and in Antarctica. *The Cryosphere*, *10*, 1495-1511.

- Pirazzini, R. (2004). Surface albedo measurements over Antarctic sites in summer. *Journal of Geophysical Research*, 109(D20118).
- Pirazzini, R., Räisänen, P., Vihma, T., Johansson, M., & Tastula, E. M. (2015). Measurements and modelling of snow particle size and shortwave infrared albedo over a melting Antarctic ice sheet. *The Cryosphere*, 9(6), 2357-2381.
- Prokop, A. (2008). Assessing the applicability of terrestrial laser scanning for spatial snow depth measurements. *Cold Regions Science and Technology*, 54, 155–163.
- Prokop, A., Schirmer, M., Rub, M., Lehning, M., & Stocker, M. (2008). A comparison of measurement methods: terrestrial laser scanning, tachymetry and snow probing for the determination of the spatial snow-depth distribution on slopes. *Annals of Glaciology*, 49, 210–216.
- Rees, W. G. (1998). A rapid method for measuring snow surface profiles. *Journal of Glaciology*, 44(148), 674–675.
- Rees, W. G., & Arnold, N. S. (2006). Scale-dependent roughness of a glacier surface: Implications for radar backscatter and aerodynamic roughness modelling. *Journal of Glaciology*, 52, 214– 222.
- Riggs, G. A., & Hall, D. K. (2015). MODIS Snow Products Collection 6 User Guide. <https://nsidc.org/sites/nsidc.org/files/files/MODIS-snow-user-guide-C6.pdf>
- Rigina, O. (2002). Environmental impact assessment of the mining and concentration activities in the Kola Peninsula, Russia by multivariate remote sensing. *Environmental monitoring and assessment*, 75, 11-31.
- Rott, H. (1984). The analysis of backscattering properties from SAR data of mountain regions. *Journal of Oceanic Engineering*, OE-9(5), 347–355.
- Roujean, J. L., Manninen, T., Kontu, A., Peltoniemi, J., Hautecoeur, O., Riihelä, A., ... & Sukuvaara, T. (2009, July). SNORTEX (Snow Reflectance Transition Experiment): Remote sensing measurement of the dynamic properties of the boreal snow-forest in support to climate and weather forecast: report of IOP-2008. In *Geoscience and Remote Sensing Symposium, 2009 IEEE International, IGARSS 2009* (Vol. 2, pp. II-859). IEEE.
- Schaaf, C. B., Gao, F., Strahler, A. H., Lucht, W., Li, X., Tsang, T., ... & Lewis, P. (2002). First operational BRDF, albedo nadir reflectance products from MODIS. *Remote sensing of Environment*, 83(1-2), 135-148.
- Schaepman-Strub, G., Schaepman, M. E., Painter, T. H., Dangel, S., & Martonchik, J.V. (2006). Reflectance quantities in optical remote sensing – definitions and case studies. *Remote Sensing of Environment*, 103, 27-42.
- Schirmer, M., & Lehning, M. (2011). Persistence in intra-annual snow depth distribution: 2. Fractal analysis of snow depth development. *Water Resources Research*, 47, W09517, 14 pp.
- Scipión, D. E., Mott, R., Lehning, M., Schneebeli, M., & Berne, A. (2013). Seasonal small-scale spatial variability in alpine snowfall and snow accumulation. *Water Resources Research*, 49, 1446-1457.
- Shaker, A., Yan, W. Y., & El-Ashrawy, N. (2011). The effects of laser reflection angle on radiometric correction of the airborne lidar intensity data. *Int. Arch. Photogramm. Remote Sens. Spat. Inf. Sci.*, 38 (5/W12), 213-217.

- Shi, J., & Dozier, J. (2000). Estimation of Snow Water Equivalence Using SIR-C/X-SAR, Part II: Inferring Snow Depth and Particle Size. *IEEE Transactions on Geosciences and Remote Sensing*, 38(6), 2475-2488.
- Sicart, J. E., Ribstein, P., Wagnon, P., & Brunstein D. (2001). Clear-sky albedo measurements on a sloping glacier surface: A case study in the Bolivian Andes. *Journal of Geophysical Research*, 106 (D23), 31729–31737, doi:10.1029/2000JD000153.
- Siljamo, N., & Hyvärinen, O. (2011). New Geostationary Satellite–Based Snow-Cover Algorithm. *Journal of Applied Meteorology and Climatology*, 50(6), 1275-1290.
- Smith, N., Saatchi, S., & Randerson, J. (2004). Trends in high northern latitude soil freeze and thaw cycles from 1988 to 2002. *Journal of Geophysical Research*, 109, D12101, 14 p.
- Sommerfeld, R. A., & LaChapelle, E. (1970). The classification of snow metamorphism. *Journal of Glaciology*, 9(55), 3-17.
- Stocker, T. (Ed.). (2014). *Climate change 2013: the physical science basis: Working Group I contribution to the Fifth assessment report of the Intergovernmental Panel on Climate Change*. Cambridge University Press.
- Sturm, M., Holmgren, J., & Liston, G. (1995). A Seasonal Snow Cover Classification System for Local to Global Applications. *Journal of Climate*, 8, 1261-1283.
- Sturm, M., Racine, C., & Tape, K. (2001). Climate change: increasing shrub abundance in the Arctic. *Nature*, 411(6837), 546.
- Sturm, M., Douglas, T., Racine, C., & Liston, G. (2005). Changing snow and shrub conditions affect albedo with global implications. *Journal of Geophysical Research: Biogeosciences*, 110, G01004, doi:10.1029/2005JG000013.
- Tape, K. E. N., Sturm, M., & Racine, C. (2006). The evidence for shrub expansion in northern Alaska and the Pan-Arctic. *Global Change Biology*, 12(4), 686-702.
- Thackeray, C. W., Fletcher, C. G., & Derksen, C. (2015). Quantifying the skill of CMIP5 models in simulating seasonal albedo and snow cover evolution. *Journal of Geophysical Research: Atmospheres*, 120(12), 5831-5849.
- Trenberth, K.E. et al. In Solomon, S. (Ed.). (2007). *Climate change 2007-the physical science basis: Working group I contribution to the fourth assessment report of the IPCC (Vol. 4)*. Cambridge University Press.
- Trujillo, E., Ramírez, J. A., & Elder, K. (2007). Topographic, meteorological, and canopy controls on the scaling characteristics of the spatial distribution of snow depth fields, *Water Resources Research*, 43, W07409, doi: 10.1029/2006WR005317.
- Ulaby, F. T., Moore, R. K., & Fung, A. K. (1982). *Microwave Remote Sensing*, vol. II, Addison-Wesley, Reading.
- Van der Veen, C. J., Ahn, Y., Csatho, M., Mosley-Thompson, E., & Krabill, W. B. (2009). Surface roughness over the northern half of the Greenland Ice Sheet from airborne laser altimetry. *Journal of Geophysical Research*, 114, F01001, doi:10.1029/2008 JF001067.
- Várnai, T., & Cahalan, R. F. (2007). Potential for airborne offbeam lidar measurements of snow and sea ice thickness. *Journal of Geophysical Research: Oceans*, 112(C12).

- Veitinger, J., Sovilla, B., & Purves, R. S. (2014). Influence of snow depth distribution on surface roughness in alpine terrain: a multi-scale approach. *The Cryosphere*, 8(2), 547.
- Wagner, W., Ullrich, A., Ducic, V., Melzer, T., & Studnicka, N. (2006). Gaussian decomposition and calibration of a novel small footprint full-waveform digitizing airborne laser scanner. *ISPRS Journal of Photogrammetry and Remote Sensing*, 60, 100-112.
- Wang, L., Derksen, C., Brown, R., & Markus, T. (2013). Recent changes in pan-Arctic melt onset from satellite passive microwave measurements. *Geophysical Research Letters*, 40, 1-7.
- Warren, S. (1982). Optical properties of snow. *Reviews of Geophysics and space physics*, 20(1), 67-89.
- Warren, S. (1984). Impurities in snow: effects on albedo and snowmelt (review). *Annals of Glaciology*, 5, 177-179.
- Warren, S. G., Brandt, R. E., & Grenfell, T. C. (2006). Visible and near-ultraviolet absorption spectrum of ice from transmission of solar radiation into snow. *Applied optics*, 45(21), 5320-5334.
- Warren, S., Brandt, R., & Hinton, P. (1998). Effect of surface roughness on bidirectional reflectance of Antarctic snow. *Journal of Geophysical Research*, 103(E11), 25789-25807.
- Warren, S. G., & Wiscombe, W. J. (1980). A model for the spectral albedo of snow. II: Snow containing atmospheric aerosols. *Journal of the Atmospheric Sciences*, 37(12), 2734-2745.
- Weiser, U., Olefs, M., Schöner, W., Weyss, G., & Hynek, B. (2016). Correction of broadband snow albedo measurements affected by unknown slope and sensor tilts. *The Cryosphere*, 10, 775-790.
- Weligepolage, K., Gieske, A. S. M., & Su, Z. (2012). Surface roughness analysis of a conifer forest canopy with airborne and terrestrial laser scanning techniques. *International journal of applied earth observation and geoinformation: JAG*, 14, 192–203 (1).
- Williams, L. D., & Gallagher, J. G. (1987). The Relation of Millimetre-Wavelength Backscatter to Surface Snow Properties. *IEEE Transactions on Geoscience and Remote Sensing*, GE-25(2), 188-193.
- Williams, L. D., Gallagher, J. G., Sugden, D. E., & Birnie, R. V. (1988). Surface snow properties effects on millimeter-wave backscatter. *Transactions on Geoscience and Remote Sensing*, 26(3), 300–306.
- Winkler, R. D., Apittlehouse, D. L., & Golding, D. L. (2005). Measured differences in snow accumulation and melt among clearcut, juvenile and mature forests in southern British Columbia. *Hydrological Processes*, 19, 51-62.
- Wiscombe, W. J., & Warren, S. G. (1980). A Model for the Spectral Albedo of Snow, I: Pure Snow. *Journal of the Atmospheric Sciences*, 37, 2712– 2733.
- Woodhouse, I.H. (2006). Introduction to Microwave remote sensing, Taylor and Francis Group, Boca Ranton.
- Xu, L., Myneni, R. B., Iii, F. C., Callaghan, T. V., Pinzon, J. E., Tucker, C. J., ... & Euskirchen, E. S. (2013). Temperature and vegetation seasonality diminishment over northern lands. *Nature Climate Change*, 3(6), 581-586.
- Yan, W.Y., Shaker, A., Habib, A., & Kersting, A.P. (2012). Improving classification accuracy of airborne LiDAR intensity data by geometric calibration and radiometric correction. *ISPRS J. Photogramm. Remote Sens.*, 67, 35-44.

Zhuravleva, T. B., & Kokhanovsky, A. A. (2011). Influence of surface roughness on the reflective properties of snow. *Journal of Quantitative Spectroscopy and Radiative Transfer*, 112, 1353–1368.







# PAPER I

Reprinted from the Journal of Glaciology  
with permission of the International Glaciological Society  
© Glaciological Society



## Instruments and Methods

# Automatic snow surface roughness estimation using digital photos

Terhikki MANNINEN, Kati ANTTILA, Tuure KARJALAINEN,\* Panu LAHTINEN

*Finnish Meteorological Institute, Helsinki, Finland  
E-mail: terhikki.manninen@fmi.fi*

**ABSTRACT.** A surface roughness measurement system for snow is presented. It is based on a background board with scales on the edges and a digital camera. Analysis software is developed for automatic processing of images to produce calibrated profiles. The image analysis and calibration was fully automatic in >99% of the studied cases. In the others, the intensity adjustment or board detection needed manual intervention. Profile detection, control point picking and calibration always worked autonomously. The accuracy of the system depends on the photographing configuration, and is typically of the order of 0.1 mm vertically and 0.04 mm horizontally. The method tolerates relatively well cases of snowfall, traces of wiping the black background dry, uneven shading, reflected sunlight, reflected flash light, litter on the snow surface and a tilted plate. The repeatability of the system is at least 1%.

### 1. INTRODUCTION

The surface roughness of the snowpack controls the transfer of wind energy to the surface (Fassnacht and others, 2009a,b). It is also an important factor for the scattering of light and thereby related to the surface albedo (Warren, 1982; Leroux and Fily, 1998; Warren and others, 1998; Mishchenko and others, 1999; Zhuravleva and Kokhanovsky, 2011), which is one of the essential climate variables (ECV) defined in the Implementation Plan for the Global Observing System for Climate in support of the United Nations Framework Convention on Climate Change (UNFCCC; <http://unfccc.int/2860.php>). In addition, the backscattering in microwaves is sensitive to surface roughness. The roughness information needed is related to the microwave wavelength (Manninen, 2003). The length of the profile should cover at least ten times the wavelength, and the pixel size should be smaller than  $\sim 0.1$  times the wavelength. For example, to describe roughness relevant for C-band the profile should be at least 50 cm long and the pixel size should be  $< 5$  mm. Our system fulfils both requirements.

Snow surface roughness depends on the complete history of the snowpack and the prevailing status starting from the precipitation event. The changing weather conditions (temperature, wind and humidity) cause metamorphism until the snow melts completely. In addition, every snowfall after the formation of the first snow layer causes step-function-like changes in the surface structure.

There are dozens of commonly used surface-roughness-describing parameters, and the proper choice depends on the application (Dong and others, 1992, 1993, 1994a,b). In remote-sensing applications the root-mean-square (rms) height and correlation length are typically used, but if they are treated as scale-invariant parameters they do not characterize natural surfaces well (Keller and others, 1987; Church, 1988; Manninen, 1997, 2003). Therefore, multiscale surface roughness characterization methods more or less related to fractals and fractional Brownian motion (fBm) have been developed (Davidson and others, 2000; Manninen,

2003). The multiscale nature of snow surface roughness was recently demonstrated by Fassnacht and others (2009a,b).

In order to properly characterize the temporal and spatial variation of the snow surface, one has to be able to gather a large number of profiles in variable land-cover types. Therefore the measurement system should be robust and lightweight and preferably one should be able to work the whole day without needing to recharge batteries. Taking photographs of the snow surface against a dark background plate fulfils these requirements. In addition, it is easy to use this technique in dense forests and difficult terrain, where many other measurements are difficult to carry out. Fassnacht and others (2009a,b) demonstrated the use of digital images of the snow surface against a board partially buried in the snowpack. Their image analysis was interactive and the calibration was made by comparison with manual measurements. Elder and others (2009) used a similar technique for snow surface profiling. The only drawback so far has been the time-consuming image analysis and calibration afterwards. Here we present an advanced version of this kind of profiling technique, which is based on automatic image analysis and calibration including removal of barrel distortion of the images. This study presents a fully automatic procedure for analysing the photographs and calibrating the profiles in millimetres. Even if manual interaction is needed in exceptionally difficult cases, the snow profile and control points are always automatically determined, so the result is operator-independent.

### 2. MEASUREMENT SYSTEM

The measurement system consists of a background board and a digital camera. The middle part of the board (100 cm  $\times$  40 cm) is black (Fig. 1). The surrounding edges are covered by three rows of black-and-white squares with dimensions of 1, 5 and 10 mm. The width of the scale bands is 10 mm for all three scales. The board is made of a 3 mm thick white I-bond aluminium layer plate, whose surface layers are made of thin aluminium while the inner parts are made of polythene. The plate is covered with black matte tape. The scales at the edges are engraved on a 0.8 mm thick

\*Present address: Mericon Oy, Sinimäentie 10 B, Espoo, Finland.



**Fig. 1.** The plate used as background and scale for the snow surface roughness measurements, here shown in calibration measurements using a print of scaled tooth pattern.

laser engraving plate, which is attached to the board using thin two-sided tape. The weight of the board is 1.9 kg.

The photographs were taken with a Canon PowerShot G10 digital pocket camera. This was chosen because a pocket camera is practical in field measurements due to its light weight and ease of handling. The camera has a sensor of  $4416 \times 3312$  pixels and a zoom lens from 6.1 to 30.5 mm having an optical image stabilizer. The range of focal lengths used varied between 6.1 and 25 mm, which yield angular fields of view from  $63.8^\circ \times 47.1^\circ$  (vertical) to  $17.3^\circ \times 12.1^\circ$ , respectively. The longer focal lengths were used when it was not possible to get closer to the board (e.g. when the snow surface needed to be kept intact for later use). The use of a wider field of view produces more barrel distortion, but is generally easier to handle in the field. The camera can produce both JPG and raw image formats. JPG format was used, as the file size is much smaller, it is a well-supported format, and the extra bit-depth (12 bits vs 8 bits per pixel) or linearity of the image data were not needed in this application.

Snow measurements are carried out by carefully inserting the plate partially into the snowpack and taking a photograph roughly perpendicularly to the background board surface, so that a picture containing the snow/board interface is obtained. One photograph is sufficient to retrieve the surface profile, but, in field measurements, taking redundant

images is recommended to increase the possibility of fully automatic analysis for each profile; varying illumination conditions and (possible) snowflakes in the plate area cause a challenge for completely automatic image analysis.

The measurement system was constructed for the Snow Reflectance Transition Experiment (SNORTEX) campaign in Sodankylä, northern Finland (Roujean and others, 2010), and the majority of the demonstration images presented were taken during that campaign. The analysis method was first adapted to that dataset, but slight modifications were needed later to guarantee automatic analysis for the Radiation, Snow Characteristics and Albedo at Summit (RASCALS) campaign at the Greenland summit (Riihelä and others, 2011) and for method consistency measurements carried out in Kirkkonummi, Finland, by the Finnish Geodetic Institute.

### 3. ANALYSIS METHOD

The snow surface is retrieved from the blue channel of the red, green, blue (RGB) image as a threshold between light and dark pixels. In practice, automatic snow surface recognition is much more difficult due to problems related to real-world conditions. The following main problems are identified:

varying contrast between images due to varying illumination conditions

varying contrast within an image (e.g. due to specular reflection of sunlight; shadows on the snow surface; flash light; partial wetness of the board surface)

litter (such as needles) on the snow surface

snowflakes in the area of the plate due to a snowfall during measurements

varying orientation and size of the visible part of the background board

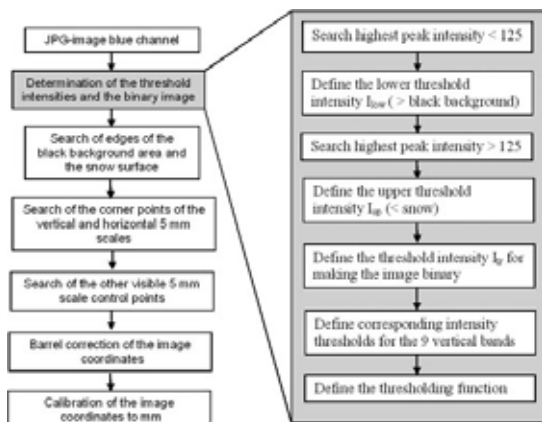


**Fig. 2.** Logistic of the search of the snow surface pixels and calibration to millimetres.

The main logic for finding the snow surface is shown in Figure 2. Full details of the method are not given here, as the code is 25 pages long in the notebook form of Wolfram Mathematica 8.0.1.0. The orientation and fraction of the plate visible in the image can vary over a wide range, because the board will sink deep down in a fluffy snowpack, whereas in the hardest snowpacks one has to saw a slot, before the board can be inserted into the snow. The starting point for the analysis is to find the location of the background

board in the image. The board is located on the basis of the image intensity distribution characteristics of the lower half of the image. The upper half is not used, because its intensity values may vary in a wide range depending on whether the background is dominated by the sky or trees.

The highest peak of the intensity distribution smaller than or equal to 125 is sought first. Starting from intensity matching the peak frequency, the intensity values for which the frequency has dropped to 10% of the peak value are determined on either side of the peak. The smaller intensity value is  $I_1$  and the higher  $I_2$ . The lower threshold intensity is then defined as  $I_{low} = I_2 + (I_2 - I_1)/2$ . The black area of the plate should mostly have intensity values smaller than  $I_{low}$ . Likewise the highest peak larger than 125 is sought. The lower and higher intensity values matching the 10% height of this peak are  $I_3$  and  $I_4$ . The upper threshold intensity is chosen to be  $I_{up} = I_3 + (I_4 - I_3)/2$ . The snow intensities should mostly be higher than  $I_{up}$ . The threshold intensity  $I_{tr}$  used to make a binary version of the image is then the average of  $I_{low}$  and  $I_{up}$ , so that, in the binary image, intensities lower than  $I_{tr}$  are -1 and intensities higher than  $I_{tr}$  are 1 (and intensities equal to  $I_{tr}$  are 0). Before starting the analysis the image is cropped in order to speed up processing and to decrease the effect of the image background. This step is, however, not absolutely necessary and its details are not described here.

Due to varying illumination and specular reflection of sunlight, the intensity of the black part of the plate is not constant. Therefore the intensity distribution of the quarter of the image just below the middle is analysed in nine vertical bands situated from 14% up to 82% of the image width (Fig. 3). The larger width of one band is only due to historical reasons. The original number of bands was fewer than nine, but it was increased when more problematic images appeared. Distribution analysis is a relatively slow operation, hence only the number of bands really needed is used, regardless of the fact that one band has double width. The threshold intensity is determined for each band  $i$  as  $I_{tri} = (4I_{lowi} + I_{upi})/5$ . Here  $I_{lowi}$  and  $I_{upi}$  are determined for each band in the same way as for the whole image. A second-order polynomial is then fitted to the values  $I_{tri}$  as a function of the band centre horizontal coordinate. Additional fine tuning not described here is applied to the threshold function, which is then used in the following process instead of a constant intensity threshold for the whole image. The edges of the visible part of the black area of the background board are then sought. Starting from the black background area, the right, left, top and bottom edges are derived using intensity thresholds based on the threshold polynomial (Fig. 3). For the vertical edges the starting point is pixel columns one-third and two-thirds of the image width. For the horizontal edges, the starting point is the middle height row of the image. The intersections of the top, bottom, left and right edges found this way are used to discard the tail parts of these edges, so that an essentially rectangular point set is left. The detected edge coordinates are then iterated using distribution analysis so that in the end second-order polynomial fits to the point sets of each edge produce high values for the coefficients of determination for the regression (Fig. 4).

The snow surface is normally searched starting from the middle part of the black background plate in order to avoid problems of litter or shadows on the snow surface. In the event of snowfall, it is assumed that the snow surface is pure and without shadows. The snow profile is then searched starting from the lower edge of the image, detecting the

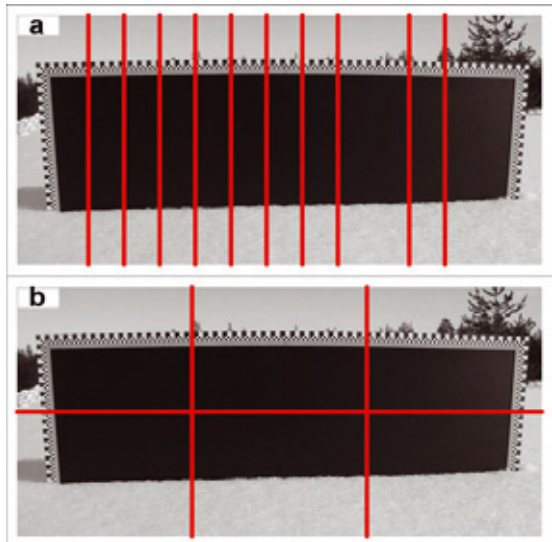


**Fig. 3.** (a) Location of the nine vertical bands used to determine the intensity distribution. (b) Location of the vertical and horizontal lines used as starting points for searching the left, right and top edges of the black background and the snow surface.

threshold of pixel values when moving from the snow pixels to the black area of the background board.

The intersections of the polynomials fitted to the left and right edges and the upper edge of the black background area are used as starting points in searching for the corner points of the vertical and horizontal 5 mm scales surrounding the plate. Knowledge of the chequer pattern of the plate in the corner area is used as the basis in this process, which is carried out using the binary version of the image. Examples of detected corner points are shown in Figure 5. The rest of the control points to be detected are cross sections, which are corner points of four 5 mm squares. The shapes of the polynomials fitted to the left, right and upper edges of the black area are used as directional guidance in the search of the control points. Detection of the upper edge points is facilitated by the knowledge that there are exactly 205 points to be detected on top of the corner points. When the corners are found, the curve between them contains 203 control points almost evenly spaced, because the viewing direction is in measurement configuration almost perpendicular to the plate surface. The positions of those control points are found iteratively starting from the rough evenly spaced positions. Changing of the black and white areas from right to left and from above to below the guidance curves is checked. The number of the visible left and right control points varies, but it is clear that no control points can be detected from below the snow surface, so that the left and right ends of the snow surface profile are used as limiting factors. The exact location of all control points is determined iteratively to achieve the best match to the black-and-white structure. Examples of detected control points are shown in Figure 4.

The wide-angle optics used here caused barrel distortion to the image coordinates. This effect had to be removed from the detected snow-surface and control-point image coordinates before calibrating them to mm values. The coordinates of an ideal undistorted image  $f_u(x, y)$  and the distorted image

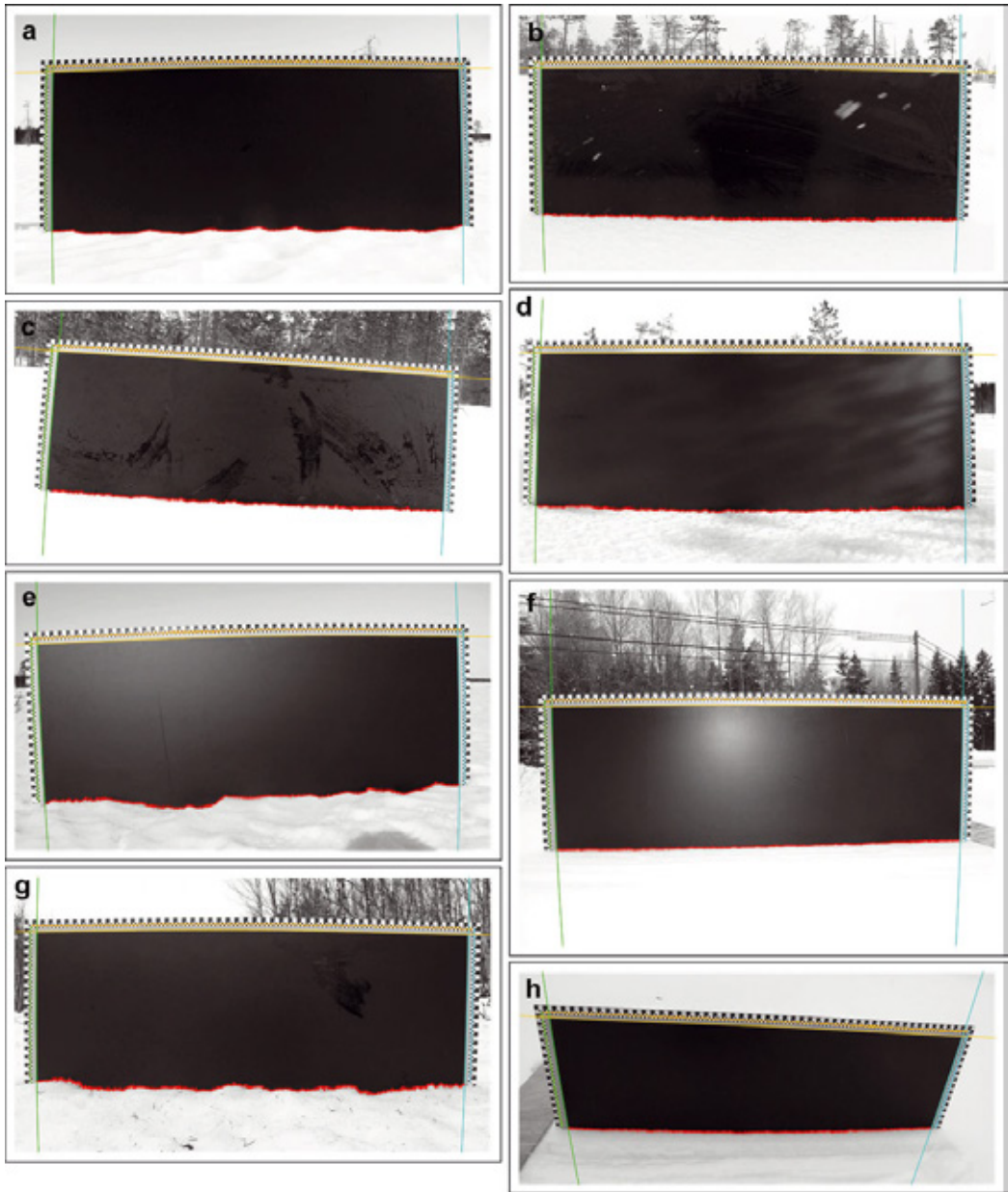


**Fig. 4.** Examples of automatic detection of the edges of the black background area. (a) is an example of easy analysis. The other panels demonstrate fully automatically analysed, but more challenging, cases of (b) snowfall (c) traces of wiping the black background dry, (d) uneven shading, (e) reflected sunlight, (f) reflected flash light, (g) needles on the snow surface and (h) a tilted plate. The detected edges of the black background are indicated with continuous curves. All the automatically detected control points of the 5 mm scale used for calibration of the images are also shown.

$f_d(\tilde{x}, \tilde{y})$  are related by (Farid and Popescu, 2001)

$$\begin{aligned}
 \tilde{x} &= x(1 + \kappa r^2) \\
 \tilde{y} &= y(1 + \kappa r^2) \\
 r^2 &= x^2 + y^2 \\
 \tan \theta &= y/x = \tilde{y}/\tilde{x}
 \end{aligned} \tag{1}$$

where  $r$  is the radius of the point in the undistorted image,  $\theta$  is

the azimuth angle of the point and  $\kappa$  is either negative (convex distortion) or positive (concave distortion). Here it is assumed that the lens is spherically symmetrical. In the configuration used in this study,  $\kappa$  is always negative. The value for  $\kappa$  is determined so that it minimizes the difference of the true control point coordinates and their estimates derived using Eqn (1). The undistorted coordinate values of the snow surface profile are then calculated applying this



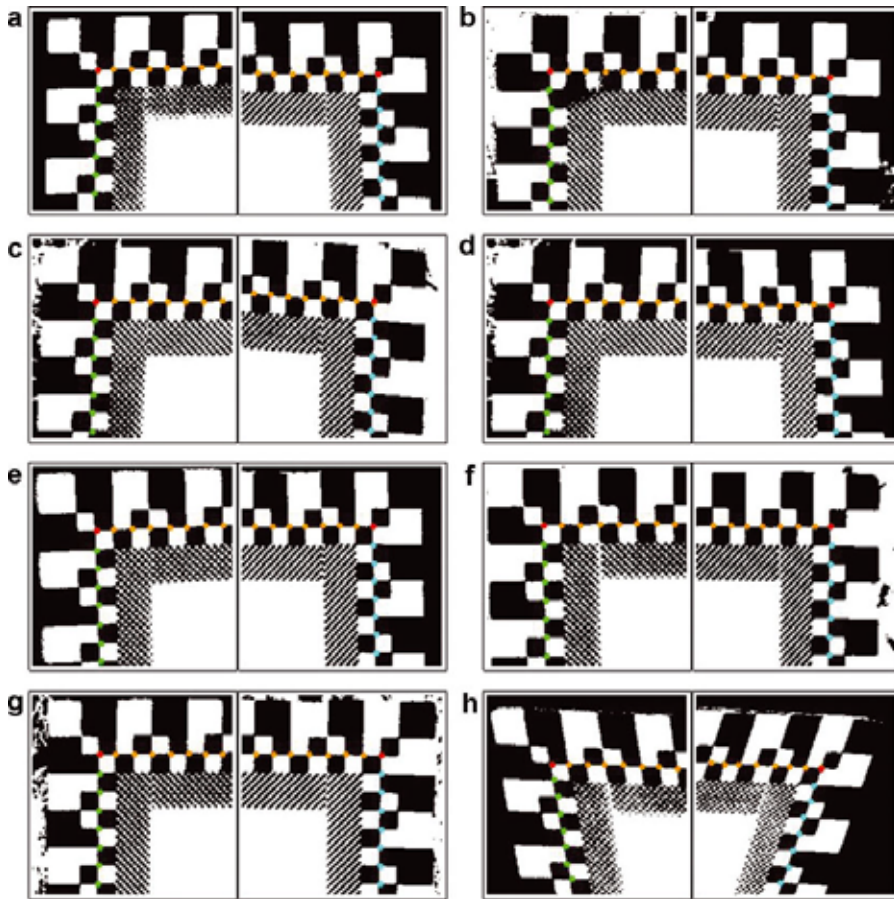


**Fig. 5.** An example of automatic detection of the corner points (red) of the 5 mm scale used to calibrate the images. The other control points fitting in the image are shown in other colours. The background image is the thresholded negative of the original image, Figure 4a–h.

optimal value of  $\kappa$  and the image coordinates of the detected snow surface points to Eqn (1). The lens distortion parameter is derived for every image separately in order to achieve maximal accuracy. The mean value for  $\kappa$  was  $-0.018$ , and the standard deviation was 22% of the mean value.

If fixed optics were used instead of a zoom lens system, the camera could be calibrated in laboratory conditions and the same barrel distortion would apply to all images. However, taking photographs in forest often restricts the possible viewing angle so that without zoom it would not always be possible to take a photo so that the whole plate is visible in the image.

Coordinates can easily be converted from one plane to another using the transformation introduced by Haggren and others (1995). Thus the coordinates in the image plane ( $x, y$ ) are related to the coordinates with respect to the background board scales ( $x_{mm}, y_{mm}$ ) via

$$\begin{aligned} x_{mm} &= \frac{m_1 x + m_2 y + m_3}{1 + m_7 + m_8} \\ y_{mm} &= \frac{m_4 x + m_5 y + m_6}{1 + m_7 + m_8} \end{aligned} \quad (2)$$

where parameters  $m_i$  ( $i=1-8$ ), can be determined using four

control points, for which both the image and board coordinates are known. However, the imaging configuration is not ideal for coordinate transformations since there are no control points below the detected snow profile. Therefore we use all detected control points as the basis of the coordinate transformation into mm values and determine the  $m_i$ -parameter values by regression. After calibration into millimetres, the profiles may be inclined with respect to the horizontal axes depending on the orientation of the background plate in the snowpack (Fig. 6). The profiles are then rectified with linear regression so that the average slope is zero. In addition, the profiles are corrected with the residual calibration parabola fitted to the horizontal axes (Section 4) to obtain the final profiles (Fig. 7).

The software developed also produces a copy of the original image, where the profile and control points are merged. The copy can also be used for quality-check purposes. The main point of the visual inspection is to check that all control points are found and located correctly. Detection of the vertical control points is especially demanding, as it is not possible to know in advance how many of them will be visible in the image. Correct snow profile detection does not normally cause difficulties.

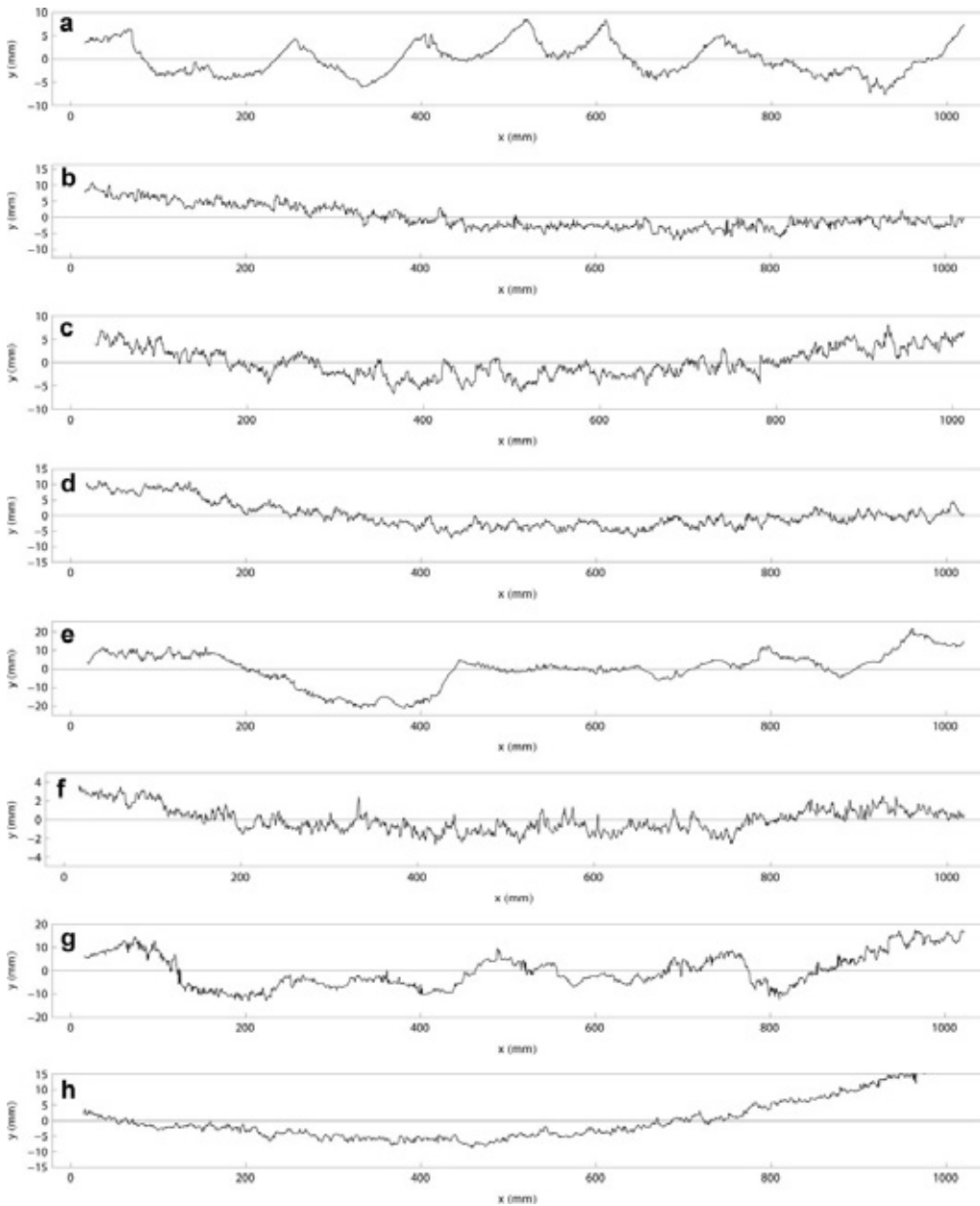


Fig. 6. Examples of automatically detected profiles corresponding to the images, Figure 4a–h.

#### 4. CALIBRATION

The vertical accuracy of the coordinates was first tested by taking a photo of a straight horizontal paper edge and analysing it with the same automatic method as used for the snow profiles. The average absolute deviation of the measured height from zero was 0.93 mm with a distinct parabola shape ( $y = 0.0000144 x^2 - 0.01479x + 2.609$ ;  $R^2 = 0.99$ ). When the coordinates were corrected with respect to the fitted parabola, the remaining average absolute deviation from zero height was 0.07 mm. The parabola is believed to be due to the scale being projected slightly (1 mm) above the

plane of the black background. Partly it may also be residual error from the barrel distortion correction.

The horizontal and vertical accuracy was studied more thoroughly by taking photos of a rack-tooth pattern with dimensions of 5 mm × 5 mm from different heights and angles (Fig. 1; Appendix 1). About three images were taken for each setting, and one image per setting was included in the dataset of 50 images used in the analysis. In addition, a smaller dataset of 30 images, which included only the cases with realistic measurement settings, was chosen (Appendixes 1 and 2). For instance, images with (1) >1.5 m distance



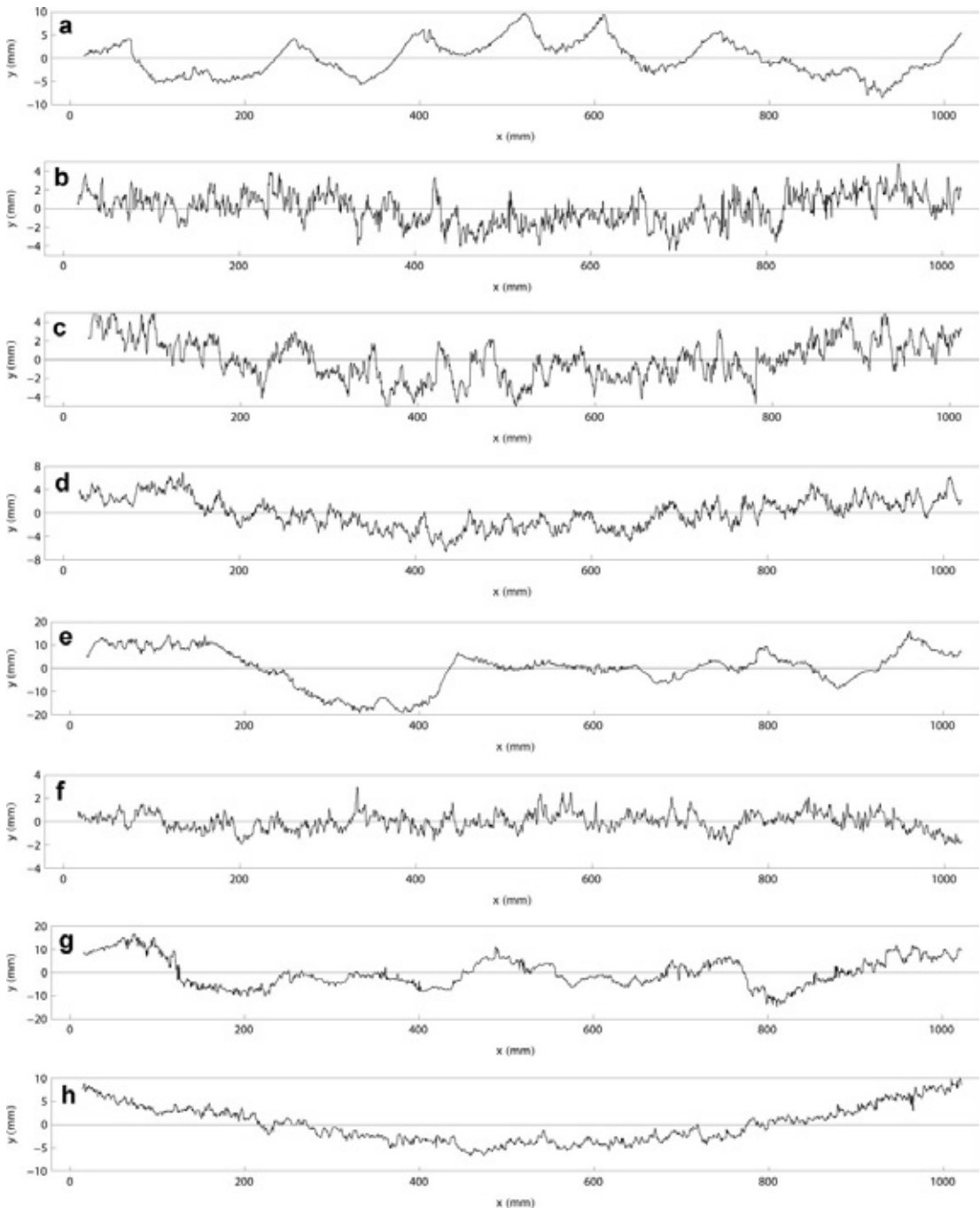


**Fig. 7.** Examples of automatically detected and rectified profiles corresponding to the images in Figure 4. The calibration paraboloid has been subtracted from the profiles.

from the plate, (2) extreme measuring angles or (3) extreme positioning of the rack-tooth patterned profile on the plate were excluded.

In general, the measured profiles are not located at the same part of the image; hence the residual barrel distortion is individual. The varying positioning of the rack-tooth

pattern (Appendix 1) was used to test this. It turned out that the second-order coefficient of the residual paraboloid was correlated with the parameter  $\kappa$  of Eqn (1) and the coordinates of the starting and end points of the profile ( $R^2 = 0.61$  images representing viewing variation in typical range). A simple second-order rational polynomial of these

**Table 1.** Statistics for the profiled rack-tooth dimensions. The three different statistical parameter values correspond to Appendix 2. The values are shown for the whole dataset (All) and a subset corresponding to cases with realistic measurement settings (Selection). For the rack-tooth heights, median and 0.9 quantile were calculated. For the rack-tooth widths, median 0.9 and 0.1 quantile values were calculated (see Appendix 2 for values of individual profiles). For each of these, average, median, 0.1 quantile and 0.9 quantile were calculated. (See Appendix 1 for the original images used for the figures)

		uc		gc		oc	
		All	Selection	All	Selection	All	Selection
<i>Rack-tooth height</i>							
Median	Average	4.93	5.06	4.93	5.04	4.95	5.04
	Median	5.02	5.05	5.02	5.04	5.02	5.03
	0.1 quantile	4.85	4.97	4.89	4.99	4.87	4.96
	0.9 quantile	5.14	5.15	5.13	5.13	5.14	5.14
0.9 quantile	Average	5.23	5.26	5.25	5.23	5.18	5.22
	Median	5.20	5.23	5.21	5.22	5.19	5.22
	0.1 quantile	5.08	5.10	5.09	5.14	5.05	5.13
	0.9 quantile	5.41	5.41	5.36	5.36	5.34	5.35
<i>Rack-tooth width</i>							
Median	Average	5.07	5.11	5.07	5.11	5.07	5.11
	Median	5.06	5.06	5.06	5.06	5.06	5.06
	0.1 quantile	4.96	5.02	4.95	5.02	4.96	5.02
	0.9 quantile	5.14	5.11	5.11	5.11	5.12	5.11
0.1 quantile	Average	4.07	4.41	4.08	4.40	4.06	4.41
	Median	4.44	4.54	4.43	4.52	4.44	4.54
	0.1 quantile	2.89	4.19	3.02	4.19	2.89	4.19
	0.9 quantile	4.71	4.74	4.72	4.74	4.71	4.74
0.9 quantile	Average	6.19	5.64	6.50	5.64	6.19	5.64
	Median	5.57	5.44	5.56	5.46	5.57	5.44
	0.1 quantile	5.34	5.33	5.34	5.33	5.34	5.33
	0.9 quantile	6.28	5.79	6.23	5.82	6.28	5.79

three variables was then constructed and used for residual barrel correction. The parameter values of the polynomial were derived using both (1) all images and (2) the subset of typical viewing configurations. For each measurement, statistical parameters were derived for three alternatives: (1) no residual barrel distortion correction, uc, (2) general residual barrel distortion correction, gc, (function parameters identical for all profiles) and (3) optimized residual barrel distortion correction, oc (function parameters optimized separately for each image).

The median and 0.9 quantile of the heights of the rack teeth were calculated for each profile using the distance between the upper and lower rack-tooth envelope surfaces (Appendix 2). The 0.1 quantile was not relevant since it was mostly dominated by points midway between the envelope surfaces. The distances between successive ascending-edge horizontal coordinates of the rack teeth and the distances between successive descending-edge horizontal coordinates of the rack teeth were also calculated. From these values median, 0.1 quantile and 0.9 quantile for each profile were derived. Finally the average, median, 0.1 quantile and 0.9 quantile values of the individual profile statistical parameters were calculated (Table 1). The summary values of the three alternatives are similar and, curiously, the optimized version is not always the best. In addition, corresponding summary statistics were calculated for the smaller dataset that included only the cases with realistic measurement settings (Appendixes 1 and 2). The median and average values of the subset were about the same as for the total, but the 80% variation range was markedly better for the subset than for the whole dataset.

On the basis of the rack-tooth pattern analysis, the estimated overall horizontal accuracy of the measurement system is on average 0.1 mm, and in 80% of cases the error varies in a range smaller than  $\pm 0.6$  mm. Likewise the estimated overall vertical accuracy is on average 0.04 mm, and in 80% of cases the error varies in a range smaller than  $\pm 0.2$  mm.

With rack-tooth surface height difference measurements, the method had clear problems with images 6252, 6329, 6332, 6378, 6381 and 6392 (Appendixes 1 and 2). These are all cases that do not describe realistic field measurement settings and were not included in the realistic subset. For image 6392 the problems are probably caused by the fact that the left-side scale is only visible for such a short distance. This complicates the fitting of the polynomial on the side of the plate, thus causing error in the results. For images 6378 and 6381 the vertical scales on both sides are short.

For image 6252 the failure has to do with the focus of the image or some other factor related to this particular image. For another image of this particular setting (6251), the corresponding values for the median of the height difference between rack-tooth surfaces are 5.0544(uc), 5.028(gc) and 5.0291(oc). Values for the horizontal length of the rack-tooth surfaces in the 0.1 quantile are 2.43 (uc), 2.42(gc) and 2.43(oc), and in the 0.9 quantile are 7.61(uc), 7.62(gc) and 7.61(oc). These values are more in line with the rest of the measurements.

As there was no suitable tripod/camera support available, the images were taken hand-held, causing some random blurring to the images. Images 6329 and 6332 were taken from 2 m height and the resolution was modest. The result

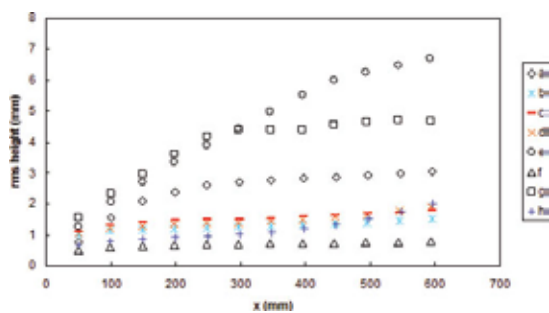


Fig. 8. The rms height variation of the measured profiles as a function of distance.

was that some of the slightly blurred vertical edges of the rack teeth were not detected or were 'detected twice' (Appendix 2). For the horizontal accuracy measures of the rack-tooth pattern, the images that stand out in addition to those already analysed in the vertical accuracy values are 6271 and 6283. In the 0.9 quantile, values of the horizontal length of the rack-tooth surfaces for image 6283 were close to 10 mm. This error is likely to be caused by the angle of photography and camera, and the position of the plate close to the edge of the image, as the barrel distortion is largest at the edge parts of the images.

The repeatability of the method was tested by comparing the three different images taken from one measurement setting (Appendix 3). Twenty-one settings had three successful images of them and thus were included in the analysis. The root-mean-square (rms) height variation was calculated for each image using a moving window of varying size. The average rms values corresponding to each window size were then calculated. The wider the window is, the fewer separate rms values are available for the average. Therefore the average rms values representing the longest distances have a high random variation, so it is better not to use the values obtained for longer distances than ~60% of the whole profile (Manninen and others, 1998). The calculated statistics include the mean value, standard deviation, the difference between the highest and lowest rms value and the percentage of this variation of the mean value for every triplet of rms values. In addition, the mean value and the standard deviation of the triplets' statistics are shown for each parameter. The results show that the standard deviation of the rms values per measurement is <0.02 mm. The variation of the rms height measurement is typically <1% of the mean value. The measurements that have poor figures are 7, 11, 13 and 14. These measurements typically have one image in the set that has values noticeably different from the other two images. Many of these also had problems defining the rack-

tooth pattern dimensions correctly, indicating that these settings include an image that is out of focus.

The effect of the temperature variation on the dimensions of the scale was estimated to be <0.1% for a typical measurement temperature range.

## 5. RESULTS

So far, 1190 profiles have been analysed using the presented method. More than 99% of them passed the automatic processing. Examples are shown in Figure 7. The snow surface is mostly off from the background plane. Therefore all profiles are corrected for the residual parabola (see Section 4), although the effect was normally negligible (of the order of 0.01 mm) at the mean height of the rack teeth. The rms height variation with distance is shown in Figure 8 for the studied profiles. Clearly the visual impression of roughness is confirmed by the rms height values. The variation of the rms height with distance is in line with the results of Fassnacht and others (2009a,b). Detected reasons for failure of automatic analysis are (1) blurred or out-of-focus image, (2) a very dark object at the front of the image, (3) snowflakes at the corners of the black background, (4) snowflakes on the scale part of the image or (5) extremely poor contrast of the image intensity, i.e. the 1 mm scale squares cannot be thresholded to produce a black-and-white chequer pattern. But even in a case when manual intervention was needed to detect the board or adjust the intensity thresholds, the actual snow surface profile and control point determination was always carried out fully automatically.

The repeatability of the measurement system was tested by taking three different photos of the same plate positioning. Because the surface was the same, the end result should also be equal, although the viewing configuration of the manually held camera certainly varied between the triplets so that neither the inclination nor the azimuth direction of the camera was constant. Illumination and weather conditions did not usually change so rapidly that the same snow surface could be analysed in different conditions. Results of such triplet profiles are shown in Figure 9. The standard deviation of the profiles varied in the range 4.7–4.8 mm, and the corresponding relative value was within 0.98–1.01% of the mean value. This example corresponds to a normal viewing configuration variation.

To test the effect of varying viewing configuration in a wider range in field conditions, a set of nine images was taken (Fig. 10). The viewing angle was varied in a wider range than in normal measurements, and the contrast of the image was varied as much as was possible in the prevailing illumination conditions. Finally, some shoots of spruce were added at the front area of the image to test their effect on the analysis. For these nine images, the mean rms height value

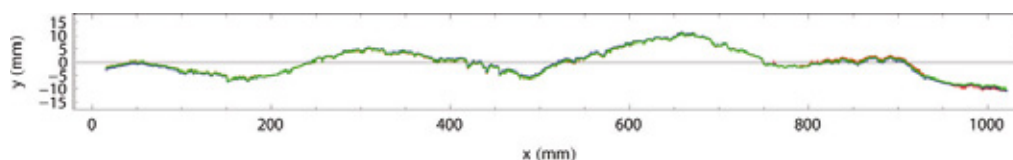


Fig. 9. Three different profiles (red, blue and green) of the same surface analysed automatically.

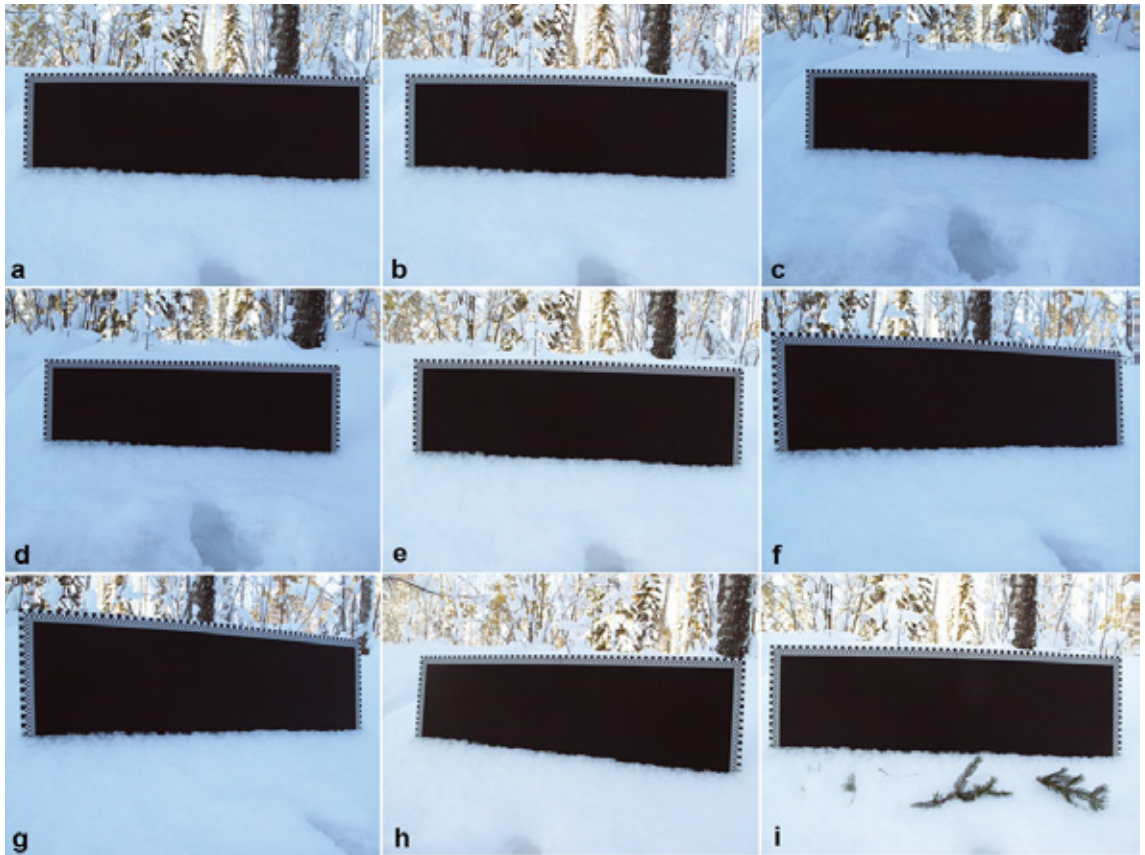


Fig. 10. Nine different viewing configurations for the same surface profile.

corresponding to 600 mm distance was 2.42 mm, with a standard deviation of 2.7% of the mean value. The largest deviation from the mean value came from images c, d and h. The first two images represented cases in which the resolution was clearly poorer due to the choice of the zoom position. The last case corresponded to an exceptionally large azimuth viewing angle, which caused marked resolution deterioration at the left edge of the image. When these three images were excluded, the mean rms height value was 2.45 mm, with a standard deviation of 1.2%. It is natural that reducing resolution decreased the rms height, because more details were smeared out.

## 6. DISCUSSION

The zoom lens was chosen to enable photos to be taken even in relatively dense forests, where it is not possible to use long distance between the camera and the plate. Therefore the lens parameter needed for the barrel distortion correction has to be determined for every image separately. Here it was assumed that the distortion is spherically symmetric, but this is not necessarily the case. Thus it is possible that some of the residual distortion is due to this assumption. One could have allowed different distortion parameter values in the vertical and horizontal directions,

but sometimes the visible parts of the vertical edges were so short that it was not considered wise to use them to determine separate vertical distortion parameters.

Because the plate is planned to be portable in various kinds of terrain and land cover, the width is limited to 1 m. Hence, the current plate is suited to surface roughness measurements corresponding to the wavelengths of radars in C- and X-band. The height variation that can be measured using the plate is ~40 cm, which was sufficient in all studied cases. However, if the snow cover has large-scale roughness features so sparsely distributed that they do not necessarily appear within the width of the plate, the large-scale roughness will not be properly characterized with this measurement technique. This kind of roughness can typically be found on lake ice, where the wind may accumulate the snow in sparse scale-shaped bumps.

For surface albedo, all roughness scales from the grain size upwards to larger topographical features are meaningful. This measurement technique is suitable for characterizing the smaller edge of the roughness scale, but the larger features need other instruments unless the surface is so clearly fractal that the 1 m long profiles can be used for upscaling the roughness values (Manninen, 2003).

Although the analysis method worked well enough to provide automatic results in most cases, an even more robust

algorithm could be generated if the plate were slightly improved. In difficult illumination and weather conditions, finding the edges of the black background caused difficulties. Detection of the black area would be easier if it were surrounded by a few continuous 5 mm wide white and black bands instead of the innermost 1 mm chequerboard band. When the illumination is low, the contrast between the black and white squares is relatively poor and causes difficulties in picking up the control points. Using highly reflecting paint for the white squares might improve this. One side of the plate could be black and white, as now, for bright daylight work, and on the other side the white could be replaced by a highly reflective paint for moonlight and twilight work.

Although the software in its current form cannot be readily distributed (as it is tailored to the plate used), we invite readers interested in the code to contact us. We will be happy to cooperate in making the code generally available. If an improved version of the plate is made as suggested above, the code could also be markedly simplified.

## 7. CONCLUSIONS

The developed analysis method for snow surface roughness measurements works autonomously in 99% of cases, so the accuracy is operator-independent. The system requires only a photo and information as to whether it was taken during a snowfall or not. The vertical average accuracy is 0.04 mm and the horizontal average accuracy 0.1 mm.

Typical causes for failure of the fully automatic analysis are: (1) insufficient contrast of the image, (2) snowflakes covering the control point scale or upper corners of the black background and (3) fuzzy photo. In order to maximize quality, one should pay attention to the resolution and available light in field conditions. It is a good option to take photos with and without flash, when the illumination is low. The viewing angle is normally perpendicular enough to not reduce the quality of the results.

## ACKNOWLEDGEMENTS

This work was financially supported by EUMETSAT through the project Satellite Application Facility in Climate Monitoring and the project Satellite Applications on Support to Operational Hydrology and Water Management, and by the Finnish Academy of Sciences through the project 'New techniques in active remote sensing: hyper spectral laser in environmental change detection' (255534).

## REFERENCES

- Church EL (1988) Fractal surface finish. *Appl. Opt.*, **27**(8), 1518–1526
- Davidson MWJ, Le Toan T, Mattia F, Satalino C, Manninen T and Borgeaud M (2000) On the characterization of agricultural soil roughness for radar remote sensing studies. *IEEE Trans. Geosci. Remote Sens.*, **38**(2), 630–640 (doi: 10.1109/36.841993)
- Dong WP, Sullivan PJ and Stout KJ (1992) Comprehensive study of parameters for characterizing three-dimensional surface topography I: some inherent properties of parameter variation. *Wear*, **159**(2), 161–171 (doi: 10.1016/0043-1648(92)90299-N)
- Dong WP, Sullivan PJ and Stout KJ (1993) Comprehensive study of parameters for characterizing three-dimensional surface topography II: statistical properties of parameter variation. *Wear*, **167**(1), 9–21 (doi: 10.1016/0043-1648(93)90050-V)
- Dong WP, Sullivan PJ and Stout KJ (1994a) Comprehensive study of parameters for characterising three-dimensional surface topography III: parameters for characterising amplitude and some functional properties. *Wear*, **178**(1–2), 29–43 (doi: 10.1016/0043-1648(94)90127-9)
- Dong WP, Sullivan PJ and Stout KJ (1994b) Comprehensive study of parameters for characterising three-dimensional surface topography IV: parameters for characterising spatial and hybrid properties. *Wear*, **178**(1–2), 45–60 (doi: 10.1016/0043-1648(94)90128-7)
- Elder K, Cline D, Liston GE and Armstrong R (2009) NASA Cold Land Processes Experiment (CLPX 2002/03): field measurements of snowpack properties and soil moisture. *J. Hydromet.*, **10**(1), 320–329 (doi: 10.1175/2008JHM877.1)
- Farid H and Popescu AC (2001) Blind removal of lens distortion. *J. Opt. Soc. Am.*, **18**(9), 2072–2078 (doi: 10.1364/JOSAA.18.002072)
- Fassnacht SR, Williams MW and Corrao MV (2009a) Changes in the surface roughness of snow from millimetre to metre scales. *Ecol. Complex.*, **6**(3), 221–229 (doi: 10.1016/j.ecocom.2009.05.003)
- Fassnacht SR, Stednick JD, Deems JS and Corrao MV (2009b) Metrics for assessing snow surface roughness from digital imagery. *Water Resour. Res.*, **45**(W0), W00D31 (doi: 10.1029/2008WR006986)
- Hagggrén H, Manninen T, Peräläinen I, Pesonen J, Pöntinen P and Rantasuo M (1995) *Airborne 3D-profilometer*. Technical Research Centre of Finland, Espoo (VTT Research Notes 1667)
- Keller JM, Crownover RM and Chen RY (1987) Characteristics of natural scenes related to the fractal dimension. *IEEE Trans. Patt. Anal. Mach. Intell.*, **PAMI-9**(5), 621–627
- Leroux C and Fily M (1998) Modeling the effect of sastrugi on snow reflectance. *J. Geophys. Res.*, **103**(E11), 25 779–25 788 (doi: 10.1029/98JE00558)
- Manninen AT (1997) Surface roughness of Baltic Sea ice. *J. Geophys. Res.*, **102**(C1), 1119–1140 (doi: 10.1029/96JC02991)
- Manninen AT (2003) Multiscale surface roughness description for scattering modelling of bare soil. *Physica A*, **319** 535–551 (doi: 10.1016/S0378-4371(02)01505-4)
- Manninen T, Rantasuo M, Le Toan T, Davidson M, Mattia F and Borgeaud M (1998) Multiscale surface roughness of bare soil. In *18th International Geoscience and Remote Sensing Symposium (IGARSS 1998), 6–10 July 1998, Seattle, WA, USA. Proceedings, Vol. 3*. Institute of Electrical and Electronic Engineers, Piscataway, NJ, 1203–1206
- Mishchenko MI, Dlugach JM, Yanovitskij EG and Zakharova NT (1999) Bidirectional reflectance of flat, optically thick particulate layers: an efficient radiative transfer solution and applications to snow and soil surfaces. *J. Quant. Spectrosc. Radiat. Transfer*, **63**(2–6), 409–432 (doi: 10.1016/S0022-4073(99)00028-X)
- Riihelä A, Lahtinen P and Hakala T (2011) The radiation, snow characteristics and albedo at summit (RASCALS) expedition report. *Finn. Meteorol. Inst. Rep.* 2011:8 <https://helda.helsinki.fi/handle/10138/28678>
- Roujean J-L and 20 others (2010) SNORTEX: remote sensing measurement of snowmelt in European boreal forest. *iLEAPS Newsl.* 9, 56–58
- Warren SG (1982) Optical properties of snow. *Rev. Geophys.*, **20**(1), 67–89 (doi: 10.1029/RG020i001p00067)
- Warren SG, Brandt RE and Hinton OP (1998) Effect of surface roughness on bidirectional reflectance of Antarctic snow. *J. Geophys. Res.*, **103**(E11), 25 789–25 805 (doi: 10.1029/98JE01898)
- Zhuravleva TB and Kokhanovsky AA (2011) Influence of surface roughness on the reflective properties of snow. *J. Quant. Spectrosc. Radiat. Transfer*, **112**(8), 1353–1368 (doi: 10.1016/j.jqsrt.2011.01.004)

**APPENDIX 1**

Images used in the rack-tooth pattern profile measurements.  
The images marked with \* are also used in the subselection of realistic measurement cases (see Table 1).





**APPENDIX 2**

Statistics for the height and width of individual rack-tooth pattern profiles. Images marked with \* in the Image No. column were also used in the subselection of realistic measuring cases (Table 1). Three different sets of statistical parameters were used: (1) without extra correction for the residual curvature (uc), (2) with general correction for the residual curvature (gc) and (3) with correction of the residual

curvature optimized separately for each image (oc). The median and 0.9 quantile of the rack-tooth height were calculated for each profile for the distances between the two adjoining rack-tooth surfaces. For the rack-tooth width the median, 0.1 quantile and 0.9 quantile are shown here. Both the ascending and descending edge differences were included in the statistics. Each image represents a separate measurement. For the images see Appendix 1.

Image No.	Camera height m	Rack-tooth height									Rack-tooth width					
		Median			Quantile 0.9			Median			Quantile 0.1			Quantile 0.9		
		uc	gc	oc	uc	gc	oc	uc	gc	oc	uc	gc	oc	uc	gc	oc
		mm	mm	mm	mm	mm	mm	mm	mm	mm	mm	mm	mm	mm	mm	mm
6213*	0.9	5.10	5.09	5.09	5.18	5.19	5.19	5.06	5.06	5.06	4.54	4.54	4.54	5.40	5.40	5.40
6216*	0.9	5.10	5.10	5.11	5.20	5.19	5.19	5.08	5.08	5.08	4.74	4.74	4.74	5.36	5.36	5.36
6219*	0.9	5.02	5.07	5.08	5.21	5.18	5.18	5.14	5.14	5.14	4.52	4.52	4.52	5.33	5.33	5.33
6222*	0.9	5.06	5.04	5.04	5.32	5.25	5.25	5.16	5.16	5.16	4.19	4.19	4.19	5.50	5.50	5.50
6227*	0.9	5.18	5.11	5.14	5.24	5.26	5.26	5.06	5.07	5.06	4.64	4.66	4.64	5.32	5.32	5.32
6230*	0.9	5.00	5.01	5.00	5.26	5.28	5.28	5.11	5.11	5.11	4.46	4.45	4.46	5.53	5.53	5.53
6234*	1	5.07	5.01	5.01	5.15	5.15	5.15	5.02	5.02	5.02	4.75	4.75	4.75	5.25	5.25	5.25
6237	1	5.05	5.05	5.06	5.35	5.28	5.28	5.07	5.07	5.07	4.44	4.44	4.44	5.55	5.55	5.55
6240*	1	5.18	5.16	5.16	5.22	5.22	5.23	5.02	5.03	5.03	4.71	4.71	4.71	5.34	5.34	5.34
6243	1	5.03	5.04	5.03	5.29	5.26	5.26	5.08	5.08	5.08	4.41	4.42	4.41	5.57	5.57	5.57
6246*	1	5.11	5.13	5.13	5.23	5.21	5.22	5.03	5.03	5.03	4.75	4.75	4.75	5.32	5.32	5.32
6250*	1	4.99	5.01	4.99	5.27	5.25	5.26	5.06	5.06	5.06	4.75	4.75	4.75	5.35	5.35	5.35
6252	1	3.43	3.11	3.43	4.54	4.51	4.54	4.59	4.48	4.59	0.96	0.42	0.96	7.42	7.37	7.42
6255	1	5.01	5.01	5.01	5.19	5.20	5.19	4.85	4.77	4.85	2.23	2.07	2.23	7.76	7.73	7.76
6263*	1	4.97	4.98	4.96	5.19	5.18	5.18	5.04	5.05	5.05	4.58	4.58	4.58	5.48	5.48	5.48
6266*	1	4.96	4.99	4.96	5.08	5.12	5.05	5.04	5.06	5.04	4.22	4.23	4.21	5.79	5.80	5.79
6269*	1	5.00	5.02	4.99	5.10	5.15	5.06	4.98	5.04	4.98	4.11	4.08	4.11	5.73	5.82	5.73
6271*	1	4.87	4.90	4.87	4.98	5.02	4.94	4.95	4.94	4.95	3.14	2.74	3.14	6.15	6.11	6.15
6283*	1	5.12	5.13	5.14	5.43	5.40	5.35	6.55	6.49	6.52	2.96	3.05	2.96	9.66	9.38	9.66
6287*	1	5.05	5.05	5.06	5.43	5.42	5.42	5.11	5.11	5.11	4.35	4.35	4.35	5.64	5.63	5.64
6289*	1	5.08	5.08	5.08	5.23	5.26	5.24	5.04	5.04	5.04	4.35	4.35	4.35	5.67	5.67	5.67
6292	1	5.05	5.04	5.04	5.27	5.28	5.30	5.05	5.05	5.05	4.59	4.59	4.59	5.50	5.50	5.50
6298*	1.5	5.05	4.99	5.00	5.09	5.14	5.13	5.09	5.09	5.09	4.21	4.22	4.21	5.81	5.82	5.82
6301*	1.5	5.03	5.02	5.03	5.27	5.28	5.25	5.10	5.09	5.10	4.42	4.33	4.42	5.65	5.68	5.65
6303*	1.5	4.96	4.90	4.92	5.16	5.15	5.16	5.08	5.08	5.08	4.59	4.60	4.59	5.44	5.44	5.44
6306*	1.5	5.02	5.04	5.03	5.19	5.23	5.20	5.03	5.03	5.03	4.27	4.26	4.27	5.64	5.67	5.64
6310	1.5	4.93	4.92	4.92	5.17	5.16	5.16	5.01	5.01	5.01	4.44	4.44	4.44	5.59	5.59	5.59
6313	1.5	5.01	5.02	5.00	5.17	5.16	5.17	5.03	5.04	5.03	4.61	4.61	4.61	5.49	5.50	5.49
6316	1.5	4.87	4.90	4.90	5.08	5.07	5.05	5.09	5.09	5.09	4.55	4.56	4.53	5.58	5.57	5.58
6319	1.5	4.95	4.95	4.95	5.13	5.13	5.11	5.08	5.08	5.08	4.51	4.52	4.51	5.56	5.53	5.56
6323	1.5	5.04	5.04	5.03	5.29	5.30	5.30	5.05	5.06	5.05	4.61	4.61	4.61	5.47	5.47	5.47
6326	2	5.14	5.13	5.16	5.21	5.25	5.20	5.19	5.18	5.19	4.59	4.30	4.59	5.78	5.81	5.78
6329	2	4.49	3.70	4.48	4.63	4.63	4.62	5.14	4.97	5.11	0.77	0.63	0.77	19.72	29.77	19.72
6332	2	3.18	3.20	3.19	4.49	7.49	4.44	5.17	5.50	5.16	0.47	0.46	0.47	14.76	20.20	14.76
6335	2	4.85	4.86	4.85	5.20	5.18	5.17	5.09	5.07	5.09	4.27	4.27	4.27	5.75	5.77	5.75
6338	2	4.97	4.94	4.97	5.09	5.13	5.08	4.96	4.96	4.96	4.32	4.16	4.32	5.59	5.76	5.59
6357	0.6	5.00	5.03	5.00	5.19	5.22	5.17	5.10	5.10	5.10	4.23	4.22	4.23	5.88	5.91	5.89
6360*	1	5.07	5.05	5.04	5.16	5.16	5.16	5.07	5.07	5.07	4.21	4.20	4.21	5.64	5.64	5.64
6363*	1	5.05	5.02	5.02	5.17	5.17	5.18	5.05	5.06	5.05	4.29	4.32	4.29	5.65	5.66	5.65
6367*	1	5.00	5.00	5.00	5.29	5.29	5.29	5.02	5.02	5.02	4.71	4.66	4.71	5.35	5.36	5.35
6369*	1	4.99	5.01	5.00	5.28	5.30	5.29	5.10	5.10	5.10	4.64	4.63	4.64	5.43	5.46	5.43
6372*	1	4.99	4.99	4.98	5.12	5.09	5.13	5.06	5.05	5.06	4.70	4.72	4.70	5.37	5.35	5.37
6375*	1	5.15	5.15	5.18	5.37	5.36	5.37	5.05	5.05	5.05	4.72	4.72	4.72	5.42	5.42	5.42
6378	1	4.80	4.80	4.80	5.08	5.07	5.05	5.04	5.02	5.04	4.32	4.36	4.32	5.67	5.66	5.67
6381	1	5.46	5.42	5.46	5.70	5.68	5.71	4.99	5.00	5.00	3.64	3.64	3.64	6.05	6.05	6.05
6385*	1	5.13	5.10	5.10	5.41	5.38	5.38	5.09	5.09	5.09	4.69	4.69	4.69	5.34	5.34	5.34
6388*	1	5.36	5.11	5.11	6.14	5.20	5.20	4.95	4.93	4.95	4.55	4.50	4.55	5.35	5.36	5.35
6392	1	3.41	5.25	5.20	6.79	5.34	5.31	4.67	4.72	4.67	0.83	3.17	0.83	5.60	5.52	5.60
6395*	1	5.06	5.07	5.09	5.32	5.33	5.34	5.08	5.08	5.08	4.66	4.66	4.66	5.36	5.36	5.36
6401	1	4.90	4.90	4.90	5.14	5.16	5.14	5.02	5.02	5.02	4.06	4.09	4.06	6.04	5.98	6.04





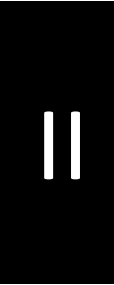
Image	Measurement	rms height variation for 60% of max length			Mean per measurement			Std dev. per measurement			Variation of rms value within measurement			Variation of rms value within measurement		
		uc mm	gc mm	oc mm	uc mm	gc mm	oc mm	uc mm	gc mm	oc mm	uc mm	gc mm	oc mm	uc %	gc %	oc %
6387	20	2.61	2.57	2.57	2.61	2.58	2.57	0.00	0.00	0.00	0.01	0.01	0.00	0.36	0.27	0.15
6395	21	2.58	2.55	2.55												
6396	21	2.58	2.57	2.55												
6397	21	2.58	2.54	2.54	2.58	2.55	2.55	0.00	0.02	0.00	0.01	0.03	0.01	0.22	1.18	0.33
<b>Mean:</b>					2.58	2.54	2.52	0.01	0.01	0.01	0.02	0.02	0.02	0.69	0.82	0.62
<b>Std dev.:</b>					0.08	0.03	0.04	0.01	0.01	0.01	0.01	0.02	0.01	0.56	0.74	0.56

*MS received 8 July 2011 and accepted in revised form 13 March 2012*



## PAPER II

Reprinted from the Journal of Geophysical Research Atmosphere  
with permission of Wiley and Sons, licence number:4358611140471  
© Wiley and Sons





## RESEARCH ARTICLE

10.1002/2014JD021597

## Key Points:

- Seasonal snow surface roughness depends on measured length and direction
- Multiscale parameters derived from rms height and correlation length are used
- The parameters can distinguish between different snow types

## Correspondence to:

K. Anttila,  
kati.anttila@fmi.fi

## Citation:

Anttila, K., T. Manninen, T. Karjalainen, P. Lahtinen, A. Riihelä, and N. Siljamo (2014), The temporal and spatial variability in submeter scale surface roughness of seasonal snow in Sodankylä Finnish Lapland in 2009–2010, *J. Geophys. Res. Atmos.*, 119, 9236–9252, doi:10.1002/2014JD021597.

Received 3 FEB 2014

Accepted 26 JUN 2014

Accepted article online 30 JUN 2014

Published online 4 AUG 2014

## The temporal and spatial variability in submeter scale surface roughness of seasonal snow in Sodankylä Finnish Lapland in 2009–2010

Kati Anttila<sup>1,2</sup>, Terhikki Manninen<sup>1</sup>, Tuure Karjalainen<sup>3</sup>, Panu Lahtinen<sup>1</sup>, Aku Riihelä<sup>1</sup>, and Niilo Siljamo<sup>1</sup>

<sup>1</sup>Finnish Meteorological Institute, Helsinki, Finland, <sup>2</sup>Finnish Geodetic Institute, Kirkkonummi, Finland, <sup>3</sup>Mericon Oy, Espoo, Finland

**Abstract** Seasonal snow surface roughness is an important parameter for remote sensing data analysis since it affects the scattering properties of the snow surface. To understand the phenomenon, snow surface roughness was measured near the town of Sodankylä, in Finnish Lapland, during winters 2009 and 2010 using a photogrammetry-based plate method. The images were automatically processed so that an approximately 1 m long horizontal profile was extracted from each image. The data set consists of 669 plate profiles from different times and canopy types. This large data set was used to study the temporal and spatial variability of seasonal snow surface roughness. The profiles were analyzed using parameters derived from the root mean square height ( $\sigma$ ) and correlation length ( $L$ ) as functions of measured length. Also, the autocorrelation functions were calculated and analyzed. The ( $\sigma$ ) and ( $L$ ) were found to be so strongly correlated ( $R^2 \sim 0.97$ ) that a more detailed analysis was made using only the scaling parameters derived from  $\sigma$ . These parameters are related to the distance dependence of the rms height. The results show that they react to different characteristics of the profiles and are therefore well able to distinguish between different types of snow. They also show a clear difference between midwinter snow and melting snow, and the effects of snowfall events and slower melting in forested areas are evident in the data.

### 1. Introduction

The albedo and extent of the seasonal snow cover react rapidly to the changes in the climate and weather. These in turn affect the surface albedo and the radiation budget of the Earth. Currently, at the beginning of the 21<sup>st</sup> century, half of the Earth's continental surface is seasonally occupied by snow. Remote sensing enables studying the change in snow cover properties over large areas [e.g., Takala et al., 2011; Nolin, 2010; Hall et al., 1995].

Surface roughness is one of the key variables affecting the remote sensing data of snow-covered areas. According to Williams and Gallagher [1987] the microwave backscatter and emission from wet snow cover depend mostly on surface roughness. Microwave satellite data are particularly important in the polar regions because of the cloudiness and the lack of sunlight during the winter. Nagler and Rott [2000] stated that the strong seasonal variations in the synthetic aperture radar (SAR) backscattering from wet snow are mainly due to changes in the liquid water content and surface roughness. The bidirectional reflectance distribution function (BRDF) of snow is also significantly affected by the roughness of the snow surface [Peltoniemi et al., 2010b; Warren et al., 1998]. In radiative models the albedo of a snow layer is reduced when surface roughness is taken into account [Zhuravleva and Kokhanovsky, 2011]. Understanding how roughness affects the signal received by satellite instruments and knowing the connections between surface roughness and the geophysical properties of the snow pack (for example crystal size and shape, density, specific surface area, and state of crystal metamorphosis) could support the use of surface roughness information in interpreting the state of snow cover from remote sensing data, e.g., the level of melting. The surface roughness of snow is affected by several factors. The type of snow deposited on the surface and the metamorphism of these crystals by temperature and wind determines the microscale roughness. Löwe et al. [2007] pointed out that because of cohesion between the snow crystals the falling snow attaches to the surface immediately at first contact, instead of being rearranged to a position of minimum potential energy. The local climate and weather conditions near the surface determine the dominating processes affecting the snow surface features. In areas where the winter air temperatures rise close to freezing point, the snowpack is

restructured by melting and freezing. In colder climates, where the winter air temperatures stay constantly below the freezing point, melting only takes place at the end of the snowy season and most of the surface evolution is caused by wind which redistributes and breaks individual snow crystals [Sturm *et al.*, 1995].

The landscape, including topography and canopy type, has a clear impact on the snow as well [Eveland *et al.*, 2013; Deems *et al.*, 2006; Grünewald *et al.*, 2013; Scipión *et al.*, 2013; Schirmer and Lehning, 2011; Veitinger *et al.*, 2013]. The structure and vicinity of canopy further complicate the surface forming processes. Tree trunks affect the snow in several ways. For example, snow accumulates less next to the tree trunks than further away from them because the branches above keep the snow from falling all the way to the ground and the trunk inhibits transportation by the wind. In addition, at melting temperatures the snow falling from the branches generates local depressions in the snow surface. The canopy affects the snow water equivalent (SWE) and depth, and also the density, though less clearly [Adams, 1976; Winkler *et al.*, 2005]. It decreases the amount of direct solar radiation that reaches the snow surface and the amount of upwelling radiation from under the trees. It affects the wind speed and keeps the air temperatures near the surface more stable. All these in turn affect the temporal evolution of the snowpack [Gelfan *et al.*, 2004]. In open areas wind is often the dominant process affecting the distribution of snow cover [Lehning *et al.*, 2008]. The changes inside the snow pack affect the surface in several scales by reforming the bed on which the surface forms. In all, snow surface roughness is affected by several processes, which makes it a complex feature to model.

There are a large number of established parameters used to describe surface roughness [Church, 1988; Manes *et al.*, 2008; Manninen, 2003; Fassnacht *et al.*, 2009a; Hollaus *et al.*, 2011; Lacroix *et al.*, 2008; Rees and Arnold, 2006, a good overview in Dong *et al.*, 1992, 1993, 1994a, 1994b]. The material of the surface and the feature that is crucial for the application of interest defines which parameters are used. For snow surface roughness studies there are two main motivators with two different sets of parameters typically used. First, surface roughness affects the interface between atmosphere and snow surface, which has an impact on wind speed and exchange of chemicals and latent and sensible heat between these two. These studies typically use atmospheric roughness length as the main parameter since it is used in most models on surface-atmosphere interaction [Manes *et al.*, 2008; Gromke *et al.*, 2011].

The second motivator is the effect of snow surface roughness on the radiative properties of snow, which in turn affects the energy budget of the Earth and optical and microwave remote sensing data. These studies typically use geometrical roughness with correlation length ( $L$ ) and root mean square height ( $\sigma$ ) as parameters. The problem with using these parameters is that their values depend on the scale and direction and are thus not fully capable of describing surface roughness if a single scale is selected [Keller *et al.*, 1987; Church, 1988; Manninen, 1997a; Manninen *et al.*, 1998; Fassnacht and Deems, 2006]. The surface radiative characteristics (incl. BRDF) are affected by surface roughness from scales of fractions of the used wavelength upward [Rees and Arnold, 2006; Ulaby *et al.*, 1982; Fung, 1994].

Therefore, it is important to take all the necessary scales into account. Some multiscale parameters have been developed [Manninen, 1997a, 1997b, 2003; Davidson *et al.*, 2000; Löwe *et al.*, 2007; Manes *et al.*, 2008; Fassnacht *et al.*, 2009a], but the number of attempts to capture the directionality of the surface roughness is considerably smaller. Herzfeld [2002] investigated the use of higher order vario functions in snow surface roughness descriptions, and Trujillo *et al.* [2007] made a directional spectral analysis on the spatial distribution of snow.

Lacroix *et al.* [2008] provide an overview of the history of measuring snow surface roughness. The measurements based on a plate inserted into the snow have first been made in the 1980's by Rott [1984] and Williams *et al.* [1988]. Since then some versions with improvements on the accuracy and resolution have been made [Rees, 1998; Rees and Arnold, 2006; Löwe *et al.*, 2007; Manes *et al.*, 2008; Elder *et al.*, 2009; Fassnacht *et al.*, 2009a, 2009b; Gromke *et al.*, 2011; Manninen *et al.*, 2012]. Fassnacht *et al.* [2009a] measured the snow surface roughness with a plate method using a fixed optics lens. The advantage of this approach is that the setup can be calibrated in laboratory conditions. Löwe *et al.* [2007] used a plate method to measure the growth and evolution of snow surface during a single snowfall event. They wanted to study the role of settling snow crystals in surface formations and therefore made the measurements in conditions where the wind could not affect the snow surface.

The measurements were made during and after snowfalls that consisted of homogeneous snow crystals. *Gromke et al.* [2011] investigated the connection between aerodynamic roughness length and geometrical roughness using wind tunnel experiments. *Manninen et al.* [2012] have developed a fully automatic algorithm for deriving the profile from plate imagery. The optics used in this method had a zoom lens to enable measuring in various conditions, such as dense forests. The measured surface was natural snow, including the effects of all the surface forming processes present. This method has been used in the study presented here.

In addition to the plate measurements some methods based on laser scanning have been developed for measuring the snow surface roughness. These have larger spatial coverage than the plate methods and form truly three-dimensional data sets which show great potential for the analyses of the directionality of snow surfaces. Because these laser scanning methods are non-destructive, measurements can be repeated in the same area allowing better temporal analysis. However, the resolution and accuracy are typically not yet as high as with the photogrammetry-based plate methods. Aerial laser scanning and radar-based measurements have good spatial coverage, but the resolution and accuracy are not very high [*Höfle et al.*, 2007; *Hollaus et al.*, 2011; *Van der Veen et al.*, 2009; *Rees and Arnold*, 2006; *Lehning et al.*, 2011]. The resolution of a typical airborne laser scanning data acquired in a scanning mode is 1 m. Terrestrial laser scanning data have better resolution but can cover only relatively small areas. In addition to these, first attempts have been made to use mobile laser scanning in obtaining snow surface roughness data [*Kukko et al.*, 2013; *Lacroix et al.*, 2008]. The preliminary results on snow surface roughness obtained using the method developed in the Finnish Geodetic Institute [*Kukko et al.*, 2013] were validated using a subset of the plate measurements presented here.

In this paper, we study the use of multiscale parameters derived from root mean square (rms) height ( $\sigma$ ) and correlation length ( $L$ ) [*Manninen*, 1997b, 2003] in describing the effect of metamorphism, weather, and canopy on seasonal snow surface roughness. The autocorrelation functions (ACF) were also calculated and analyzed. The reason for choosing these surface roughness parameters is that they are the surface roughness descriptors used in microwave surface backscattering models [*Ulaby et al.*, 1982; *Fung*, 1994]. The plate photography method of *Manninen et al.* [2012] mentioned earlier was used in the measurements. The method is based on photographing a black plate with scales on the sides. The scales are used for calibration and automatic extraction of the profile of the plate-snow interface profile. The extracted profile is approximately 1 m long. This scale is particularly useful for data from the C-band microwave satellite instruments, such as ERS-1, ERS-2, Radarsat and Radarsat-2, Sentinel-1, and ENVISAT/ASAR. Because the method is easy to use in the field and the extraction of the profile from the photograph is automatic, this method enables large data sets to be gathered and analyzed. The good areal coverage of the ground data is particularly important for interpreting coarse resolution remote sensing data. The data set consists of 669 plate measurements made in varying conditions and locations. The data were collected along other daily measurements of snow geophysical and radiative properties. Standard snow pit measurements were made in all locations to characterize the snow pack. This data set gives good coverage on temporal, spatial, and scale variability of the snow of the study area.

The second section of this paper provides details of the algorithms and theoretical background of the analysis. In the third section we introduce the measurement settings including the locations, measuring conditions, and methods used. The fourth section presents the results, and in the fifth section we discuss the results and conclusions in more detail.

## 2. The Theoretical Basis for Multiscale Surface Roughness Parameters

The parameters used here are based on the root mean square height ( $\sigma$ ) and correlation length ( $L$ ) [*Manninen*, 1997a, 1997b, 2003, *Manninen et al.*, 1998]. Because the roughness of snow surface is scale dependent, the parameters were calculated as function of measured length. A single  $\sigma$  was replaced with the mean value  $\langle\sigma\rangle$  of the measured subprofile of equal length derived along the whole profile at all the measured parts of the profile. This is performed with a method similar to a sliding window technique where a window/subprofile of fixed length is moved along a profile,  $\sigma$  is calculated for each location, and in the end the mean value of all the  $\sigma$  values of the same window size/subprofile length is used.

The rms height  $\langle\sigma_i\rangle$ , autocorrelation function  $\langle\rho_i(\xi)\rangle$ , and correlation length  $\langle L_i\rangle$  of a profile as functions of measured length are calculated as described above using the following equations [Manninen, 1997b, 2003]:

$$\langle\sigma_i\rangle = \frac{1}{(n - in_0)} \sum_{j=1}^{n-in_0} \sigma_{ij}, \quad i = 1, \dots, n_i \quad (1)$$

$$\langle\rho_i(\xi)\rangle = \frac{1}{(n - in_0)} \sum_{j=1}^{n-in_0} \rho_{ij}(\xi), \quad i = 1, \dots, n_i \quad (2)$$

$$\langle L_i\rangle = \langle\rho_i^{-1}(e^{-1})\rangle, \quad (3)$$

where  $\sigma_{ij}$  is the rms height and  $\rho_{ij}(\xi)$  the autocorrelation function corresponding to a subprofile of  $in_0$  points. Here  $\xi$  is a variable of distance. The size of the smallest subprofile is  $n_0$ , and it is enlarged with an increment of  $i$  so that the size of a subprofile is  $in_0$ , where  $i = 1, \dots, n_i$  and  $n_i$  is the number of different subprofile lengths. The subprofile is moved from  $e$  beginning of the whole profile by an increment of  $j$ . The total number of points in the 1 m profile is  $n$ .  $L_i$  is the point where  $\rho_i(\xi)$  gets the value of  $e^{-1}$ , with  $e$  being the Napier's constant. Here  $\rho_i^{-1}$  denotes the inverse function of  $\rho_i$ . More detailed definitions are available in the Appendix A.

For natural surfaces the logarithm of the rms height  $\sigma$  is usually linearly dependent on the logarithm of the length  $x$  for which it is determined [Keller et al., 1987], which gives

$$\sigma(x) = e^a x^b \quad (4)$$

where  $a$  and  $b$  are constant parameters. They will be used as the basis of surface roughness analysis [Manninen, 1997b].

Correlation length of natural surfaces is typically linearly dependent on the length  $x$  for which it is determined [Church, 1988]:

$$L = \alpha + \beta x \quad (5)$$

where  $\alpha$  and  $\beta$  are regression parameters. For an ideal Brownian fractal surface  $\alpha = 0$  and the correlation length  $L = L_B$ , which is related to the surface roughness parameter  $b$  (equation (4)) according to [Manninen, 2003]

$$L_B = \frac{2b^2}{1 + 4b} x. \quad (6)$$

With short subprofiles the number of points in each subprofile is so low that it causes statistical uncertainty. On the other hand, for very long subprofiles the number of different subprofiles derived from the profile is small. Consequently, when the length of the subprofile exceeds 60% of the maximum length of the profile the individual values for correlation length are not statistically reliable. This can be seen in the behavior of correlation length values for different subprofile lengths. Due to these inner and outer scale effects the values of  $a$  and  $b$  calculated using  $\sigma$  values for the first 60% of the maximum profile length were found to be the most representative [Manninen et al., 1998] for the whole profile.

### 3. Data

#### 3.1. Campaign

The snow surface roughness measurements were made as part of the SNORTEX (Snow Reflectance Transition Experiment) campaign [Roujean et al., 2010; Manninen and Roujean, 2014] in the Sodankylä region in the Finnish Lapland (67.4°N, 26.6°E). During the field measurement periods the base of the campaign was in the premises of the Arctic Research Centre of Finnish Meteorological Institute (FMI-ARC). The campaign was led by the Finnish Meteorological Institute (FMI) and Météo-France. Other institutes involved were the Finnish Geodetic Institute (FGI), University of Helsinki, University of Eastern Finland, the Laboratoire de Glaciologie et Géophysique de l'Environnement (LGGE), and the Finnish Environment Institute (SYKE). The aim of the campaign was to study how various snow-related parameters affect boreal forest albedo during the melting season. Extensive airborne and ground-based measurements were carried out [Karjalainen, 2010; Peltoniemi et al., 2009, 2010a, 2010b; Domine et al., 2010; Hakala et al., 2010; Anttila et al., 2011; Kaasalainen et al., 2011; Manninen et al., 2012; Kukko et al., 2013].



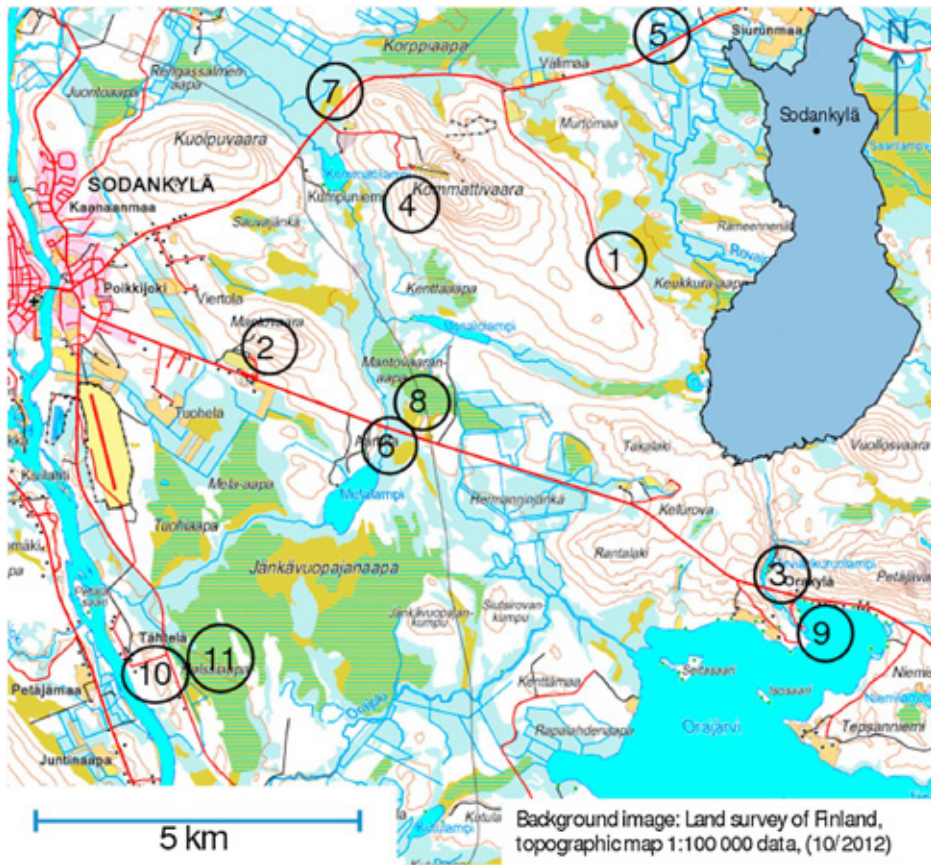


**Figure 1.** Map of snow surface roughness measurement sites. The indices correspond to the indices in Table 1. The location of the Sodankylä area is shown in the blue subimage of Finland. The meteorological station is located at index 10.

In 2009 the snow measurements were carried out in more than 50 locations in the campaign area of 10 km in diameter [Manninen and Roujean, 2014]. Each day the measurement team moved to a predefined test site and conducted the daily ground-based measurements including the plate and tachymeter (total station) profiles of surface roughness and snow pits for snow properties. Values for snow depth, density, and SWE were obtained. Profiles of snow temperature, volumetric moisture content, density, and grain size were also obtained at each location. Most of the places were measured twice, first in March 2009, then in April 2009. In April, albedo and spectrometer measurements were also carried out in the test sites. In 2010 more than 20 of these places were remeasured. The plate measurement test sites (Figure 1) were of varying land cover classes including open and semi-open bogs, several types of forests with varying densities and undergrowth, and snow-covered lake ice.

The weather conditions varied from sunny to snow fall and from +9.6°C to −29.6°C. Table 1 shows the locations of the measurements, and Table 2 shows the measurement days and overall weather conditions for the days. In 2009 the study area was first covered by snow in 8 October 2009. The temperatures before the campaign in March were colder than freezing, and some 2 cm of new snow had fallen 2 March 2009. In 2010 first snow of the season fell 24 October 2010. The air temperatures in February varied from −5°C to −38°C. There were several snowfall events at the beginning of the month and one at 14 and 15 of February

**Table 1.** The Plate Measurement Sites of SNORTEX and NoSREX With Coordinates and Canopy Types<sup>a</sup>

Index	Name	Coordinate N	Coordinate E	Canopy	Other
1	Kommattivaara	6725.3	2647.7	Pine forest	Sandy soil
2	Ravirata	6724.4	2640.4	Cultivated pine forest	Sandy soil
3	Hirviäkuru	6722.6	2651.3	Mixed forest	Steep topography
4	Kommattilampi	6725.8	2643.4	Pine forest	On a hillside
5	Siurunmaa	6726.9	2649.2	Birch forest	
6	Melalampi	6723.6	2643.8	Semi-open bog	Peat soil
7	Korppiaapa	6726.4	2641.9	Open bog	Peat soil
8	Mantovaaranaapa	6724.0	2643.8	Open bog	Peat soil
9	Orajärvi	6722.4	2651.9	Lake ice	
10	Tähtelä	6721.8	2637.9	Open with small pines	Sandy soil, flat
11	Halssiaapa	6722.0	2638.9	Open bog	Peat soil

<sup>a</sup>The indices correspond to the ones in Figure 1. The coordinates are in EUREF-FIN (~WGS84). The trees in sites 1, 2, 4, 6, and 10 are pines (*Pinus sylvestris*), in site 5 birch (*Betula pubescens*), and for site 3 a mixture of these two with pine as the dominant species. For the open bogs the vegetation is typical aapa mire vegetation.

that each added snow depth with a few centimeters. In March the air temperatures varied between  $-35^{\circ}\text{C}$  and melting point having a strong diurnal cycle caused by the warming effect of the sun during the day and radiative cooling during the nights. The average temperature was well colder than freezing. At the beginning of April 2009 the air temperatures remained similar to March, but from 10 April onward the air temperatures varied around melting point. There were no significant snowfall events during the month, and the snow

**Table 2.** The Measuring Days and Corresponding Test Sites Indicated With Same Indices As in Table 1 and Figure 1<sup>a</sup>

Date	Index in Figure 1	Daily Max Air T(°C)	Daily Min Air T(°C)	Daily Mean Air T(°C)	Snowfall Observed	Snow Depth (mm, 8 pm Local Time)	Number of Profiles
<b>2009</b>							
March 11	1	-6.8	-24.4	-14.2	No	60	41
March 12	2	-2.8	-11.9	-6.1	No	60	39
March 13	3	0	-4.3	-2	No	60	34
March 14	4	0.6	-2.6	-1.1	No	60	25
March 15	5	1.2	-1.3	-0.1	No	59	15
March 16	6	0.6	-2.3	-0.9	Yes	59	40
March 17	7	3.7	-10.9	-3.5	Yes	60	20
March 18	8	2.1	-15.5	-5.4	No	58	29
March 19	10	-1.7	-15.4	-7.1	No	60	2
April 20	1	0.5	-7.2	-3.4	No	48	11
April 21	6	5.1	-7	0.4	No	47	24
April 22	8	9	-4.8	3.5	No	46	27
April 23	7	9.5	-3.1	3.8	No	43	33
April 24	4	8.4	-3.3	3.2	No	41	25
April 25	3	9.7	-2.3	5	No	38	18
April 26	5	9.6	1.7	5.7	No	36	15
April 27	2	6.6	-2.7	2.3	No	33	15
April 28	10	4.3	-0.6	2.1	No	34	3
<b>2010</b>							
February 23	10	-16.6	-29.6	-23.8	No	70	54
February 24	11	-14.2	-27.6	-18.1	Yes	71	42
March 16	10	-6	-35	-19.3	No	78	23
March 17	8	-3.7	-27.4	-15.3	No	78	22
March 18	6	-3.7	-29.6	-17.4	No	77	13
March 19	4	-3.3	-28.8	-13.8	No	77	12
March 20	2	-3.2	-6.3	-5.8	Yes	81	6
March 21	9	-2.3	-17.5	-9.9	No	83	10
March 22	7	-2	-20.7	-8.5	No	82	10
March 23	No measurements	-0.7	-6.5	-4.1	No	82	0
March 24	9, 3	-0.6	-14.8	-7.8	No	81	3

<sup>a</sup>In addition to these measurements were made at the end of each day in Tähtelä. The weather data are from the Finnish Meteorological Institutes weather station located at Tähtelä. The snowfall information is based on in situ observations made by the field team.

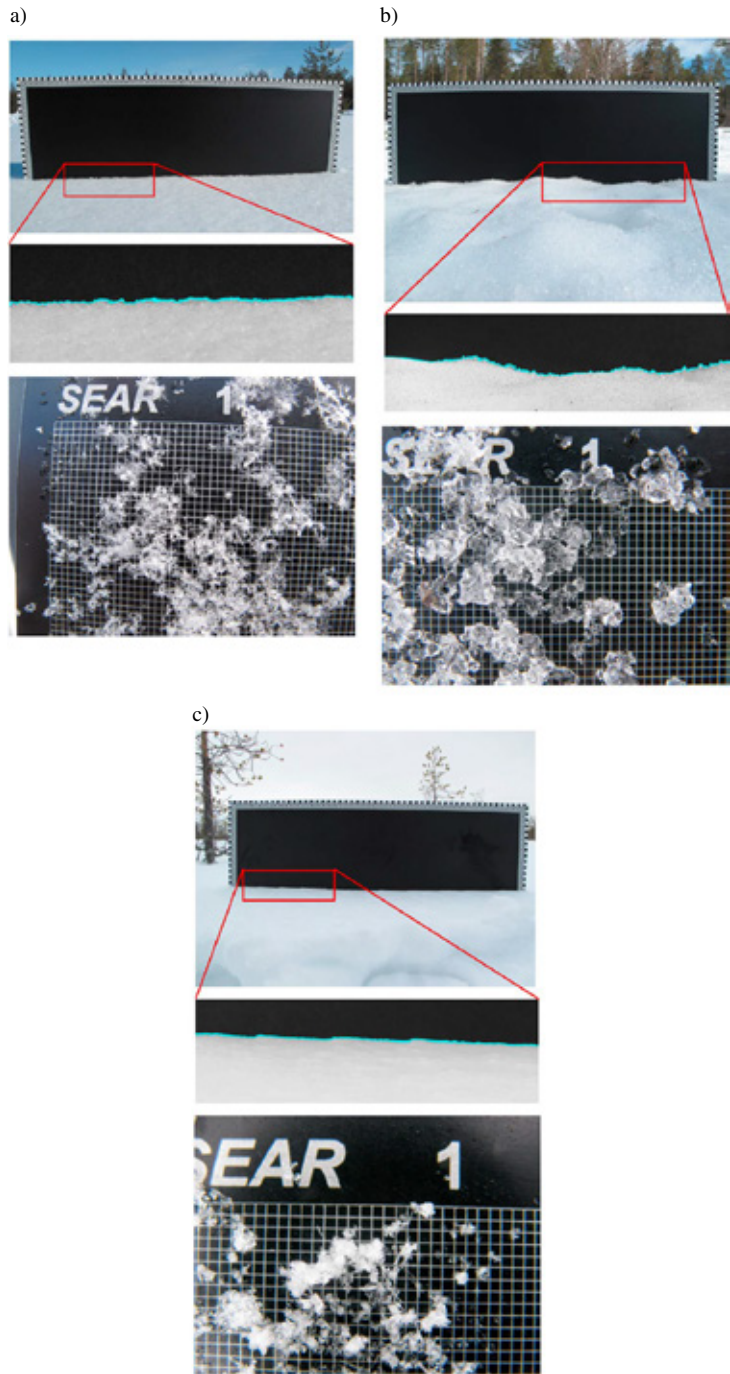


Figure 2

depth started to drop at 10 April continuing to drop for the rest of the month. The snow in the Sodankylä region is typical taiga snow with thick layers of depth hoar at the bottom of the snow pack and metamorphosed crystals on the top with wind having only a limited role in the metamorphosis of the crystals [Sturm *et al.*, 1995].

### 3.2. Small-Scale Surface Roughness Measurements

The snow surface roughness measurements were made alongside other daily field measurements in different test sites every day (Figure 1). Several profiles were measured at all test sites to have better spatial and statistical coverage, since one single profile is not fully capable of capturing the 3D surface characteristics of the measurement area even below the 1 meter scale. A single profile may also be dominated by some random features of the surface, such as snow that has fallen from a tree, footsteps of animals, or uneven melting caused by an individual piece of vegetation that has fallen to the snow surface. Since the location of the measurements changed daily, a set of surface roughness measurements was repeated every day at Tähtelä (site number 10 in Figure 1) near the FMI-ARC premises. These measurements were made as the last measurements of the day. The Tähtelä time series gives information on the temporal evolution of the surface structure.

In 2009 the plate profiles were measured along tachymeter profiles. The tachymeter data will be introduced here only to give an idea of the plate profile measurement settings. The data itself will not be analyzed in this article in more detail. In each location two to five tachymeter lines were measured resulting in 75 lines for the whole campaign. The lines at each site were perpendicular to each other and were typically about 100 m long. Due to the field conditions in some cases the lines were reduced to 50 or 25 m. This has been the case if the vegetation did not permit a clear line of 100 m or the snow had already melted in some parts of a profile. Due to the roads and trees present, the length of the Tähtelä tachymeter line was reduced to 80 meters. The orientation of the tachymeter lines determined also the orientation of the plate profiles, which were measured every 10 or 20 m along the 100 m lines, every 10 m along the 50 m lines and every 5 m along the 25 m lines. Since no tachymeter data were measured in March 2010, the plate measurements were made in the vicinity of the other daily measurements (next to snow pits, spectrometer, albedometer, unmanned aerial vehicle (UAV), and bidirectional reflectance function (BRF) measurements) and along mobile laser scanning routes [Kukko *et al.*, 2013]. Some additional plate measurements were made as transections in two locations (sites 10 and 11) near FMI-ARC during the Nordic Snow Radar Experiment (NoSREx) [Lemmetyinen *et al.*, 2010] in February 2010. In total, the snow surface roughness data set consist of 459 plate profiles and 75 tachymeter lines measured in March and April 2009, 96 plate profiles measured in February 2010, and 114 plate profiles measured in March 2010. In March 2009, February 2010, and March 2010 the air temperatures stayed colder than freezing and little or no melting taking place in the snowpack. In April 2009 the temperatures varied from  $-6.8^{\circ}\text{C}$  to  $+9.5^{\circ}\text{C}$ , the melting was already rapid and the snow cover was patchy.

The plate measurements were made using a black board of  $1.06\text{ m} \times 0.4\text{ m}$  with scales on the sides. The black area from which the profile is extracted is 1 m wide [Manninen *et al.*, 2012]. The plate is a layered 3 mm thick aluminum plate, and the surface of the plate is covered with a matt black tape. The plate was carefully inserted into the snow so that the snow surface was altered as little as possible. The plate with the snow-plate interface was photographed with a Canon PowerShot G10 digital pocket camera. The camera has a sensor of 4416 by 3312 pixels and a zoom lens from 6.1 to 30.5 mm having an optical image stabilizer. Three images were taken of every profile to ensure good image quality and correct focus. Figure 2 shows the plate with three examples of plate images having different kinds of snow characteristics. Figure 2a shows a fresh snow surface with dry snow, Figure 2b shows a typical melting season surface with irregular shapes and smoother

**Figure 2.** Plate photographs with enlargements of each image including the captured surface profile for closer detail. Each image represents a different type of snow surface. The images are from (a) Tähtelä, site index 10, 16 March 2010 with fresh snow, (b) Ravirata, site index 2, 27 April 2009 with melting season snow, and (c) Melalampi, site index 6, 16 March 2009, with wind formed ripples at an open marsh. Photos of the snow crystals were taken from the surface layers at snow pits near the profiles. The scale of the grids at the images is 1 mm.

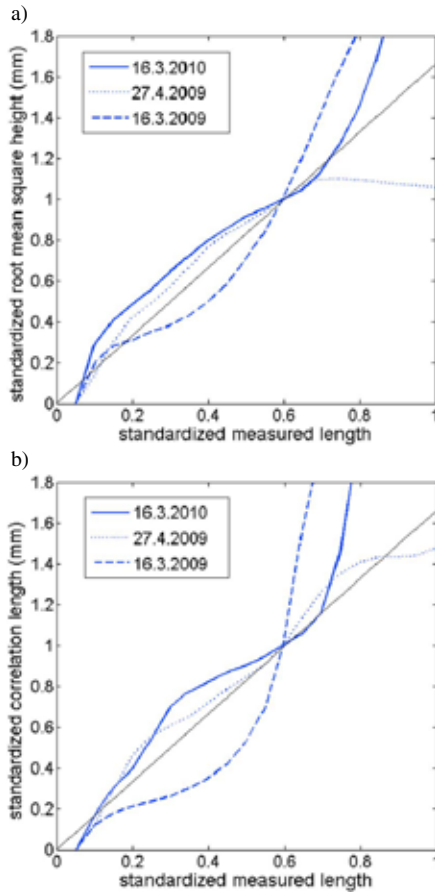


**Figure 3.** Examples of (a) rms height ( $\sigma$ ) and (b) correlation length ( $L$ ) variation with distance of profiles extracted from plate photographs from 16 March 2010, 27 April 2009, and 16 March 2009 presented in Figure 2. The rms height and correlation length have been standardized using the values for 0 and 60% of maximum measured length and distance using the minimum and maximum measured length.

surface at crystal level, and Figure 2c shows an image taken at a marshland with wind induced ripples. Crystal images of snow surfaces taken at snow pits near the profiles have also been included in the figures.

The images were later automatically analyzed in the office, and the profile from the snow-plate interface was extracted using an automatic algorithm. The algorithm first finds the black area of the plate, then the corner points. The images go through several corrections including the barrel distortion of the lens used and the errors caused by the orientation and location of the plate in the image. This was made by fitting polynomials to the grids on the sides of the plate by first finding the corner points of the plate and then using the corner points of the vertical and horizontal 5 mm scales surrounding the plate in fitting the polynomials. The resolution of the profiles depends on how close to the plate the image was taken but was on average 0.27 mm. A thorough description of how the profile is extracted from the photograph as well as validation analysis of the photogrammetric method can be found in *Manninen et al.* [2012].

**4. Results**

We studied the use of multiscale parameters derived from  $L$  and  $\sigma$  in describing the temporal and spatial change and canopy effect on seasonal snow surface roughness. Examples of  $\sigma$  and  $L$  as function of measured length for three different profiles are shown in Figure 3. They show that the measured values depend heavily on the measured length and that the shape of the curves depends on the type of the surface. The reason to restrict the use of the profile to 60% of the total measured length can be seen in the behavior of the  $\sigma$  and  $L$  values. The restrictions related to the shortest lengths are also evident (see section 2).

**4.1. Correlation Length and Autocorrelation Functions**

We compared the calculated values of  $L$  (the distance  $L$  at which  $ACF(L) = e^{-1}$ ) from the plate profiles to the theoretical values of  $L_B$ . The results are shown in Figure 4a. It seems that short correlation lengths of snow surfaces before the start of the spring melting have a Brownian character (the values of  $L$  and  $L_B$  are close), but for longer correlation length values, as well as melting snow, the surface is not purely Brownian. This may imply that the surface structures caused by crystals and their metamorphosis form Brownian structure, but for longer scales, with structures caused mainly by melting and wind, the surface is not Brownian. A closer look at the data reveals that the fresh snow surfaces have very small values for  $L$ . As the snow starts to age the range of the values for  $L$  grows, but the range of the values for  $L_B$  grow even faster and eventually surface profiles lose the Brownian character completely. This can be seen in Figure 4b, which shows the  $L$  values for profiles of three different days in March 2009. These days represent surfaces before and after a snow fall. The snowfall event



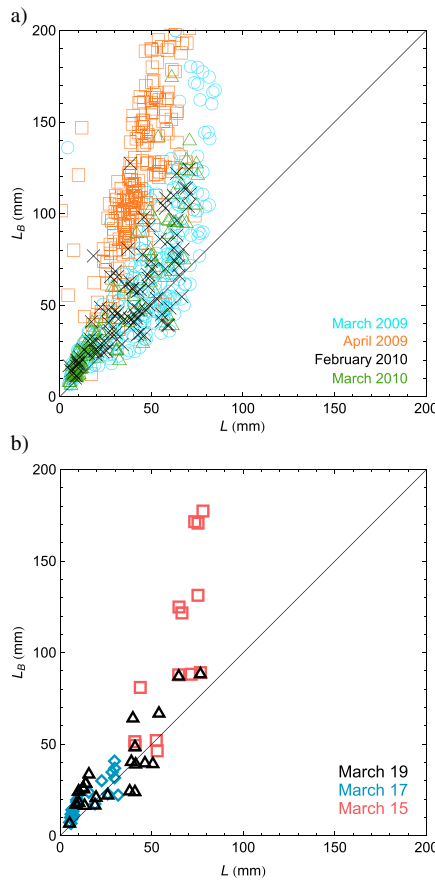


**Figure 4.** The measured values of  $L$  for the profiles compared to a Brownian surface correlation length  $L_B$ . Figure 4a shows all the profiles. The blue circles are the values for March 2009, red squares for April 2009, grey crosses for February 2010, and green triangles for March 2010. Figure 4b shows the  $L$  values for the profiles measured in 15 March 2009 (before snow fall, red squares), 17 March 2009 (after snowfall, blue diamonds), and 19 March 2009 (after snowfall, black triangles).

significant role in modeling the scattering behavior of snow surface. The change of snow characteristics with time is also manifested in Figure 5 as the distance needed for decreasing the ACF value to  $1/e$  ( $\sim 0.37$ ) is about five times longer in April than in March.

started gradually at the evening of 15 March, continued until 17 of March and added 5 cm of fresh snow to the snow pack.

The autocorrelation functions for the profiles were also calculated. They were compared with three commonly used ACF types both in single scale and multiscale form. Table 3 shows the number of experimental autocorrelation functions that fit best to each type tested. The fitting was made by minimizing the rms error by using linear regression, and the case having the highest value of the coefficient of determination  $R^2$  was considered the best alternative. The part of the ACF included in the regression covered the distance from zero to the correlation length. In midwinter (February and March) the autocorrelation functions of most of the profiles were of the multiscale exponential type [Manninen, 2003]. In March 2009 the multiscale Gaussian ACF was equally common as the single scale exponential, whereas in 2010 the single scale exponential was more typical. At the melting time (April) the single scale Gaussian type ACF was the most common and the multiscale Gaussian the second most common ACF type. Only a few profiles of the melting period showed exponential (single or multiscale) type autocorrelation. The multiscale power law ACF was the best fitting in only a few cases, and no profile showed single scale power law autocorrelation characteristics. The differences in  $R^2$  between the best fit and the second best fit were typically small ( $<0.01$ ). Examples of the most common ACF types are shown in Figure 5.

Even though the differences in the  $R^2$  values are small the difference between two ACF types can be significant due to the locations of large root mean square errors. For instance, if the experimental ACF curve deviates markedly from the ideal ACF curve at the shortest distances when the ACF is close to unity, it can have a

**Table 3.** Number of ACFs of Measured Profiles That Best Fit Each ACF Type Tested<sup>a</sup>

	Exponential	Multiscale Exponential	Gaussian	Multiscale Gaussian	POWER LAW	Multiscale Power Law
March 2009	58	134	7	62	0	3
April 2009	22	9	88	73	0	3
March 2010	25	67	9	12	0	1
February 2010	16	67	0	13	0	0

<sup>a</sup>The total number of profiles is 669 (2009 March: 264, 2009 April: 195, 2010 March: 114, 2010 February: 96).

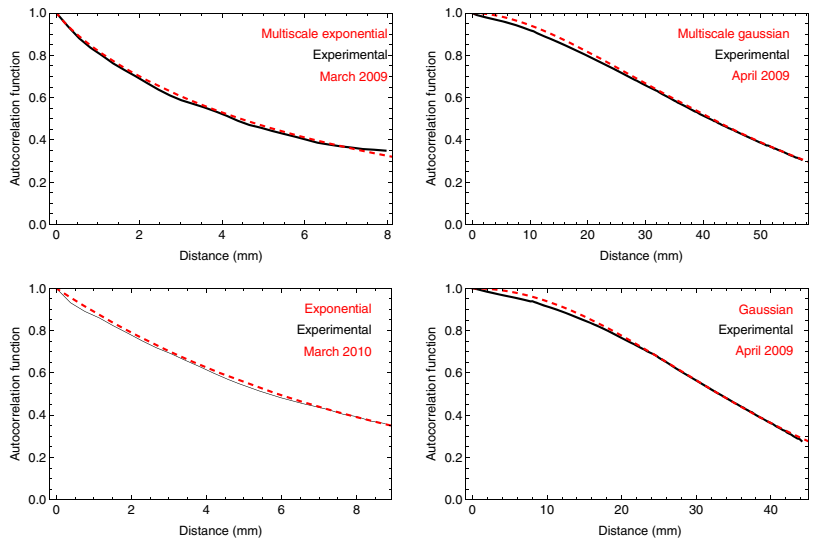


**Figure 5.** Examples of common autocorrelation function shapes measured in March 2009, April 2009, and March 2010. The best fit curves of single and multiscale exponential and Gaussian types are shown for comparison. The example for multiscale exponential type is from 16 March 2009 (Tähtelä, site 10), for Multiscale Gaussian from 23 April 2009 (Tähtelä, site 10) for exponential from 18 March 2010 (Melalampi site 6), and for Gaussian from 21 April 2009 (Melalampi, site 6).

**4.2. Rms Height**

**4.2.1. Sensitivity to Changes in the Snow Surface**

The measured values of  $L$  proved to be strongly correlated with the measured values of  $\sigma$  ( $R^2 \sim 0.97$ ). Therefore, the remaining analysis will concentrate on the parameters derived from  $\sigma$ . The chosen parameters  $a$  and  $b$  (equation (4)) react differently to the changes in the surface characteristics. The higher the values are, the rougher the surface is. The parameter  $a$  is more sensitive to the shorter wavelength/scale variation and  $b$  to the regularity of the surface structure. Therefore,  $a$  reacts rapidly to crystal size changes. Fresh snow crystals form a surface with more crystal level height variation than older snow surfaces which consist of old rounded crystals or wind broken and packed crystals. This causes fresh snow surfaces to get higher values for  $a$ . Parameter  $b$  reacts to longer wavelength characteristics and the irregularity of their position along the profile. Its value is restricted to be in the range  $0 \dots 1$ , because the fractal dimension of the profile equals  $2 - b$  [Manninen, 2003]. Older snow surfaces have more irregular shapes caused by, e.g., melting of the snow, impurities, and scars made by animals. These features are typically unevenly distributed on the surface, and therefore the values for  $b$  tend to be higher for older snow, such as snow during the melting season, at least in the boreal forest zone. During snowfalls and directly after them new fallen snow tends to be redistributed by wind so that it gathers in pits of the surface and thus smoothens the irregular features. This as well causes the values of  $b$  to be lower for fresh snow surfaces than for the same surface just before the

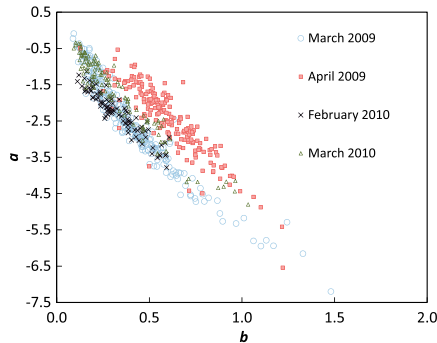


**Figure 6.** Temporal variation of snow surface roughness parameters of equation (4) for 60% of the maximum length.

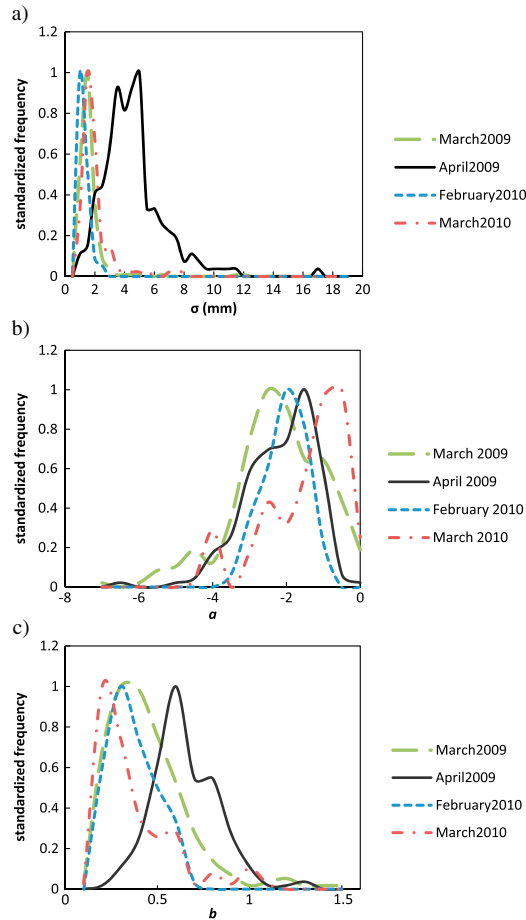


**Figure 7.** Standardized frequencies of (a)  $\sigma$  (equation (4)), (b) parameter  $a$ , and (c) parameter  $b$  values for 60% of the maximum length.

snow fall. All metamorphic processes that affect the height variation affect also the values of these parameters. Sintering between crystals and the rounding of crystal gaps cannot be seen using data with this resolution before it starts to affect the crystals in millimeter scale.

**4.2.2. Fresh Snow Versus Melting Snow**

The temporal change of snow surface roughness can be seen in Figure 6. The profiles for April 2009 get higher values for  $b$  corresponding to 60% of the maximum length than the March 2009 profiles. This is because in March 2009 the weather and snow conditions were typical for midwinter with temperatures colder than freezing, whereas in April 2009 the melting had already started. During the melting season irregular shapes begin to form on the snow as a consequence of faster melting and larger amount of liquid water in the snow pack. In February 2010 the air temperature was permanently colder than freezing and the Sun caused hardly any melting in the snowpack. In March 2010 there was some melting but not as much as in April 2009. Figure 7 shows the distributions of  $\sigma$  and parameters  $a$  and  $b$  for different months. The values were determined for 60% of the profile length. Here it can be seen again that the values of  $\sigma$  and  $b$  differ between the melting season and midwinter, but the values of  $a$  show no clear difference for the different months. The data sets for the different months differ considerably

in size, the data sets of 2010 being smaller than the data sets of 2009. This can affect the standardized distributions. Since parameter  $a$  reacts faster to the changes in roughness, it may seem that using parameter  $b$  is not necessary. However, using only parameter  $a$ , or  $b$ , it would not be possible to distinguish between the midwinter and melting season surfaces as the values of both  $a$  and  $b$  overlap for the two snow surface types.

**4.2.3. Effect of Snowfall**

The large distribution of  $a$  and  $b$  can be explained by a single snow fall event. Figure 8 shows the values for parameters  $a$  and  $b$  for Tähtelä (site 10) for March and April 2009. At the beginning of the field measurements in March 2009 the snow was aging. In the evening of 15 March it began to snow in short periods continuing until the morning of 18 March. This causes the values of parameter  $a$  to increase and parameter  $b$  to decrease, as fresh snow adds microscale edginess and evens out the larger scale irregularities of the surface. After the snowfall, as the surface snow begins to age, the values of parameter  $a$  gradually decrease and  $b$  increase. The values for  $a$  for March 2009 get values between  $-4$  and  $-0.5$ . This is also the distribution of  $a$  for all the profiles measured in all locations in March 2009. Since the values of  $a$  in one location in a few days cover the whole variation range of  $a$ , it can be said that the weather conditions alone can, to a large extent, explain the distribution of  $a$ . The role of weather on the values for  $b$  is



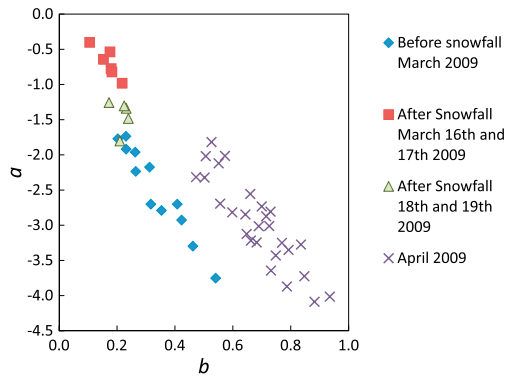


**Figure 8.** Temporal variation of parameters of equation (4) in Tähtelä from 11 March 2009 to 28 April 2009.

similar. The absolute values and magnitude of the change depend on the type of crystals that fall, the duration and amount of snow fall, and the conditions of the underlying snow pack (for example temperature, amount of liquid water and original roughness).

**4.2.4. Canopy**

The test sites were selected to feature different canopy types to better study how canopy affects the snow surface roughness. The measurements, other than Tähtelä, were made in one location (having one canopy type) per day. For the analysis, the different canopy types have been classified to two main categories: open and forest. The Tähtelä (open area) measurements have been excluded from

these and form a separate class. All the test sites are in the vicinity of Tähtelä. Therefore, it can be assumed that the weather conditions at the test sites are similar to the conditions in Tähtelä and the time series of all the locations should show a similar trend to the time series of Tähtelä. Figure 9 shows a growing trend for the  $\sigma$  values for all three classes (Tähtelä, forest, open) supporting the view that all the test sites have similar weather conditions.

The slower melting of forested sites can be seen while comparing the parameters  $a$  and  $b$  of the measurements at forested test sites to the time series measured at Tähtelä (Figure 10). The median values of parameter  $a$  for forested and open areas is below the trend of daily averages of Tähtelä in March 2009, whereas in April it shifts above it (Figure 10a). A similar shift can be seen with parameter  $b$ , only in the opposite direction (Figure 10b). The measurements at open areas are so few that they are not used in further analysis. The difference between the parameter value evolution at the forested sites and the Tähtelä time series can be explained by the slower melting of the forested sites. The canopy keeps the temperatures more stable at the surface level by preventing the incoming solar radiation from reaching the surface and hindering the thermal outflow and radiative cooling. This also keeps the temperature gradients in forested sites less steep and slows down the melting in spring, which causes slower changes in the parameter values toward the melting season values in forested sites than in open areas. That is, the values of  $a$  decrease, and

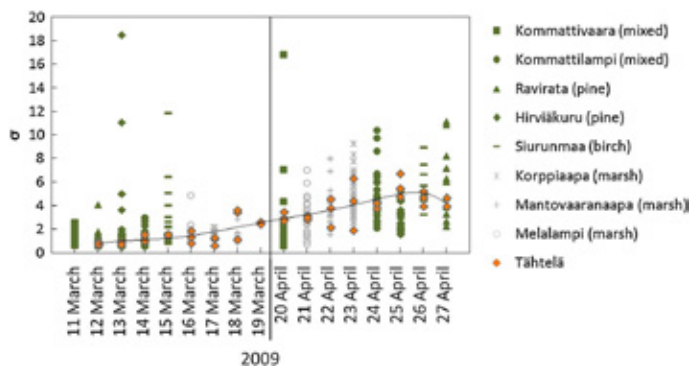


**Figure 9.** The values of  $\sigma$  for 60% of the maximum length for daily measurements per day in 2009. The values for forested sites are marked with green markers with fill, and the lighter grey markers are sites with open canopy. The measurements carried out in Tähtelä are shown in orange rhombuses.

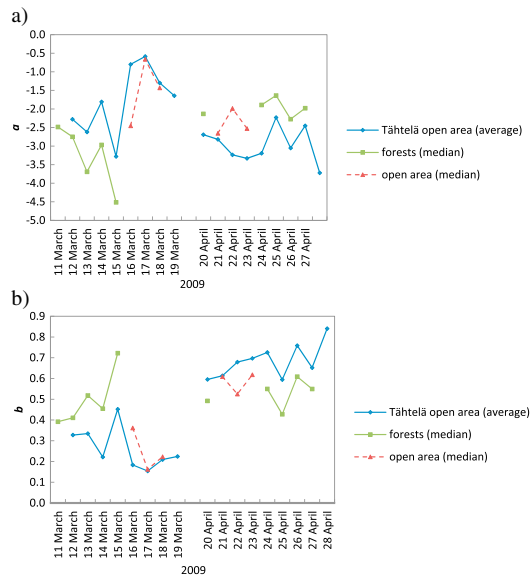


**Figure 10.** The median values for parameters (a)  $a$  and (b)  $b$  of equation (4) for daily measurements in 2009 using the length 60% of the maximum. The sites are classified as open or forested, and Tähtelä values are excluded from the other two classes. For Tähtelä, average values are used instead of median.

the values of  $b$  increase later in the forested sites than in the open areas. A similar trend cannot be detected in the evolution of  $\sigma$ . The behavior of the parameters showed no other connections to the weather data (air temperature and humidity) than the one with snow fall and the difference between the forested and open areas.

**5. Discussion**

Natural surfaces have different roughness characteristics in different scales. Therefore, using  $\sigma$  of one single scale is not appropriate for describing the surface. The multiscale roughness parameters  $a$  and  $b$  used in this study include information on all the scales measured. They are independent of the plate method and can be modified to be used in 3D analysis of snow surface roughness, such as made in Kukko *et al.* [2013]. They can be directly used for profiles of different lengths. Using a smaller plate with better resolution shows great potential for studying microscale metamorphosis processes. However, since the profile can be

measured only once from each exact spot a statistical approach to the analysis seems more applicable. For remote sensing this is often the more desired way, since data sets with large areal coverage are needed instead of small details of one spot. The parameters  $a$  and  $b$  can also be used to further study the snow surface roughness in different parts of the world. The applicability of their absolute values for the snow geophysics presented in this paper for other types of snow in different areas of the world should be studied further. The snow cover in the Alps for instance is somewhat different of the taiga snow.

So far the plate measurement method has been used only at daylight, but possibly replacing the white paint used in the scales with a highly reflecting paint would enable measurements also in darkness. Preliminary studies have shown that a smaller plate and higher resolution photos can be used to capture the fine scale micro structural evolution of the crystals, which may be one significant difference between forested and open areas. It can also be used to study the relationship between falling snow flake types and the surface they form. The whole evolution of snow surface from snow fall to melting could be measured using a combination of different methods, such as the plate photography and mobile laser scanning, to obtain information on different scales. This would make it possible to study the whole range of scales and their scaling behavior, as well as the directionality of the surface features.

The effect of canopy on snow surface roughness provides a number of questions to study in the future. It is difficult to determine when an area should be defined as open or forested. Is one tree or shrub enough to make a forest from the snow surface roughness point of view? What is the role of the tree/shrub height and shape? What distance to a forest still has an effect on the snow accumulation and metamorphosis? Does a power line pole have a similar effect as a tree? The Tähtelä test site, for instance, is a relatively small opening with small pines surrounded by pine forest. It can be argued whether this site should have been classified as open or forested site. Similar problems exist also with the other open test sites, since there was some vegetation even at the most open sites. However, the sites classified as forested sites in Figures 9 and 10 have clearly more trees than present at Tähtelä. Therefore, the effect of canopy should be stronger at sites

classified as forests. Other remaining questions related to canopy are the role of the type of canopy, including the different species, the shape and leaf type of the trees, the forest density, etc. Also, the distance to tree trunks affects snow accumulation and melting. Understanding the canopy effect better would provide valuable information for interpreting remote sensing data used to monitor the snow cover in boreal forest zone that includes different types of vegetation from thick forests to open marshlands.

Satellite data often cover large areas with different snow types. Therefore, it is important to gain knowledge on the spatial variation of snow surface features and their effect on the radiative properties. The differences in surface roughness characteristics also affect the Earth's energy budget via albedo and therefore climate. The parameters used here can be incorporated in radiation models and thus help improve the interpretation of remote sensing data. This in turn can give knowledge on the snow-climate interactions and improve the climate and weather models.

### 6. Conclusions

Microscale seasonal snow surface roughness was measured with a method based on plate photography to study spatial and temporal variation of the surface roughness. The method is easy to apply and use wherever measurements need to be made. The results show that the rms height variation values of seasonal snow surface roughness vary significantly depending on the scale used. The parameters of equation (4),  $a$  and  $b$ , determined from the rms height values, bring additional information on the surface evolution as compared to using only rms values. Using both the parameters together gives additional information on the surface.

1. The results show a clear difference in snow surface roughness between the melting season and midwinter.
2. The aging of the snow shows decreasing values for parameter  $a$  and increasing values for  $b$ .
3. A snowfall event causes the values for parameter  $a$  to increase and parameter  $b$  to decrease.
4. The canopy effect is less clear, but the slower evolution toward melting season in forested sites is visible when using the multiscale parameters derived from the rms height variation.

More information is needed on the relationship between falling snow crystal types and the roughness of the surface formed. The usability of the parameters tested here should be studied in other regions of the world. Having parameters that are able to distinguish between different types of snow gives means to further study the geophysical features of snow and better interpret the properties of snow-covered areas observed by remote sensing means.

### Appendix A: Definitions for Multiscale Root Mean Square Height Variation and Autocorrelation Function Types

The rms height  $\sigma_{ij}$  of the subprofile  $ij$  consisting of  $in_0$  points and starting from point  $j$  of the whole profile is defined as

$$\sigma_{ij} = \sqrt{\frac{1}{in_0} \sum_{k=0}^{in_0-1} (y_{j+k} - \bar{y})^2}$$

where  $y_{j+k}$  is the height of point  $x_{j+k}$ ,  $\bar{y}$  is the average height of the subprofile  $ij$ , and  $n_0$  is the increment of points in successive subprofile lengths. The autocorrelation function  $\rho_{ij}(\zeta)$  of the subprofile  $ij$  depends on distance  $\zeta$  according to

$$\rho_{ij}(\zeta) = \frac{\frac{1}{in_0-1-n_\zeta} \sum_{k=0}^{in_0-1-n_\zeta} (y(x_{j+k} + \zeta) - \bar{y})(y(x_{j+k}) - \bar{y})}{\frac{1}{in_0} \sum_{k=0}^{in_0-1} (y(x_{j+k}) - \bar{y})^2}$$

where  $y(x_{j+k}) = y_{j+k}$  is the height of point  $x_{j+k}$  and  $y(x_{j+k} + \zeta)$  is the height of point  $x_{j+k} + \zeta$ . Here  $n_\zeta$  is the number of points corresponding to length  $\zeta$ .

Common one-dimensional single scale autocorrelation function types and the corresponding semi-infinite multiscale autocorrelation functions are [Manninen, 2003]

Gaussian, single scale

$$\rho(\zeta) = \exp[-\zeta^2/L^2]$$

Gaussian, multiscale

$$\rho(\zeta) = \frac{1}{2} (1 + 2b) \left( \frac{\zeta^2}{k_0^2 \lambda_0^2} \right)^{\frac{1}{2}+b} \Gamma \left( -\frac{1}{2} - b, \frac{\zeta^2}{k_0^2 \lambda_0^2} \right)$$

Exponential, single scale

$$\rho(\zeta) = \exp \left[ -\sqrt{\frac{\zeta^2}{L^2}} \right]$$

Exponential, multiscale

$$\rho(\zeta) = (1 + 2b) \left( \frac{\sqrt{\zeta^2}}{k_0 \lambda_0} \right)^{1+2b} \Gamma \left( -1 - 2b, \frac{\sqrt{\zeta^2}}{k_0 \lambda_0} \right)$$

Transformed exponential, single scale

$$\rho(\zeta) = 1/[1 + \zeta^2/L^2]^{3/2}$$

Transformed exponential, multiscale

$$\rho(\zeta) = \frac{(1+2b)}{2(2+b)} \left( \frac{\zeta^2}{k_0^2 \lambda_0^2} \right)^{-\frac{3}{2}} {}_2F_1 \left( \frac{3}{2}, 2 + b; 3 + b; -\frac{k_0^2 \lambda_0^2}{\zeta^2} \right)$$

### Acknowledgments

The authors would like to thank Sanna Kaasalainen for all support with the paper, the staff of FMI-ARC for providing infrastructure and equipment for the SNORTEX-campaign, and Ali Nadir Arslan for help with the measurements during the NoSREx campaign. The study was financially supported by the EUMETSAT H-SAF project and the Academy of Finland (project "New techniques in active remote sensing: hyperspectral laser in environmental change detection" (255534)). The measured surface roughness profiles are available upon request from the corresponding author.

### References

- Adams, W. P. (1976), Areal differentiation of snow cover in East Central Ontario, *Water Resour. Res.*, 12(6), 1226–1234, doi:10.1029/WR012i006p01226.
- Anttila, K., S. Kaasalainen, A. Krooks, H. Kaartinen, A. Kukko, T. Manninen, P. Lahtinen, and N. Siljamo (2011), Radiometric calibration of TLS intensity: Application to snow cover change detection, *International Society for Photogrammetry and Remote Sensing, The International Archives of the Photogrammetry, Remote Sensing and Spatial Information Sciences*, ISPRS Workshop, Part 5 / W12, volume XXXVIII, Commission VI, WG VI/4.
- Church, E. L. (1988), Fractal surface finish, *Appl. Opt.*, 27(89), 1518–1526.
- Davidson, M., T. Le Toan, F. Mattia, T. Manninen, and M. Borgeaud (2000), On the characterisation of agricultural random roughness for radar remote sensing studies, *IEEE Trans. Geosci. Remote Sens.*, 38(2), 630–640.
- Deems, J. S., S. R. Fassnacht, and K. J. Elder (2006), Fractal distribution of snow depth from LiDAR data, *J. Hydrometeorol.*, 7(2), 285–297.
- Domine, F., G. Krinner, M. Menegoz, J. Bock, J.-C. Gallet, and K. Anttila (2010), Snow-climate feedbacks driven by changes in snow thermal conductivity, *IPY Oslo Science Conference*.
- Dong, W. P., P. J. Sullivan, and K. J. Stout (1992), Comprehensive study of parameters for characterizing three-dimensional surface topography I: Some inherent properties of parameter variation, *Wear*, 159, 161–171.
- Dong, W. P., P. J. Sullivan, and K. J. Stout (1993), Comprehensive study of parameters for characterizing three-dimensional surface topography II: Statistical properties of parameter variation, *Wear*, 167, 9–21.
- Dong, W. P., P. J. Sullivan, and K. J. Stout (1994a), Comprehensive study of parameters for characterizing three-dimensional surface topography III: Parameters for characterising amplitude and some functional properties, *Wear*, 178, 29–43.
- Dong, W. P., P. J. Sullivan, and K. J. Stout (1994b), Comprehensive study of parameters for characterizing three-dimensional surface topography IV: Parameters for characterising spatial and hybrid properties, *Wear*, 178, 45–60.
- Elder, K., D. Cline, G. Liston, and R. Armstrong (2009), NASA Cold Land Processes Experiment (CLPX 2002/03): Field measurements of snowpack properties and soil moisture, *J. Hydrometeorol.*, 10, 320–329.
- Eveland, J. W., M. N. Gooseff, D. J. Lampkin, J. E. Barrett, and C. D. Takacs-Vesbach (2013), Seasonal controls on snow distribution and aerial ablation at the snow patch and landscape scales McMurdo Dry Valleys, Antarctica, *Cryosphere*, 7, 917–913.
- Fassnacht, S. R., and J. S. Deems (2006), Measurement sampling and scaling for deep montane snow depth data, *Hydrol. Processes*, 20, 829–838.
- Fassnacht, S. R., J. D. Stednick, J. S. Deems, and M. V. Corrao (2009a), Metrics for assessing snow surface roughness from digital imagery, *Water Resour. Res.*, 45, W00D31, doi:10.1029/2008WR006986.
- Fassnacht, S. R., M. W. Williams, and M. V. Corrao (2009b), Changes in the surface roughness of snow from millimetre to metre scales, *Ecol. Complexity*, 6, 221–229.
- Fung, A. K. (1994), *Microwave Scattering and Emission Models and Their Applications*, pp. 573, Artech House, Boston.
- Gelfan, A. N., J. W. Pomeroy, and L. S. Kuchment (2004), Modeling forest cover influences in snow accumulation, sublimation and melt, *J. Hydrometeorol.*, 5, 785–803.
- Gromke, C., C. Manes, B. Walter, M. Lehning, and M. Guala (2011), Aerodynamic roughness length of fresh snow, *Boundary Layer Meteorol.*, 141, 21–34.
- Grünwald, T., J. Stötter, J. W. Pomeroy, R. Dadic, I. Moreno Baños, J. Marturià, M. Spross, C. Hopkinson, P. Burlando, and M. Lehning (2013), Statistical modelling of the snow depth distribution in open alpine terrain, *Hydrol. Earth Syst. Sci.*, 17, 3005–3021.
- Hakala, T., J. Suomalainen, and J. Peltoniemi (2010), Acquisition of Bidirectional Reflectance Factor Dataset Using a Micro Unmanned Aerial Vehicle and a Consumer Camera, *Remote Sens.*, 2(3), 819–832.
- Hall, D., G. A. Riggs, and V. Salomonson (1995), Development of methods for mapping global snow cover using moderate resolution imaging spectroradiometer data, *Remote Sens. Environ.*, 54(2), 127–140.
- Herzfeld, U. C. (2002), Vario functions of higher order – Definition and application to characterization of snow surface roughness, *Comput. Geosci.*, 28, 641–660.
- Höfle, B., T. Geist, M. Rutzinger and N. Pfeifer (2007), Glacier surface segmentation using airborne laser scanning point cloud and intensity data, *Proceedings of ISPRS Workshop Laser Scanning SilviLaser*, vol. 36, pp. 195–200, International Archives of Photogrammetry and Remote Sensing, Espoo, Finland part 3/W52.
- Hollaus, M., C. Aubrecht, B. Höfle, K. Steinnocher, and W. Wagner (2011), Roughness mapping on various vertical scales based on full-waveform airborne laser scanning data, *Remote Sens.*, 3, 503–523.
- Kaasalainen, S., H. Kaartinen, A. Kukko, K. Anttila, and A. Krooks (2011), Brief communication: Application of mobile laser scanning in snow cover profiling, *Cryosphere*, 5, 135–138, doi:10.5194/tc-5-135-2011.
- Karjalainen, T. (2010), Lumen pinnankärkeudenmittaaminen (measuring the surface roughness of snow), Insinööriyö. Metropolia Ammattikorkeakoulu, 48 pp.

- Keller, J. M., R. M. Crownover, and R. Y. Chen (1987), Characteristics of natural scenes related to the fractal dimension, *IEEE Trans. Pattern Anal. Mach. Intell. PAMI*, *9*, 621–627.
- Kukko, A., K. Anttila, T. Manninen, H. Kaartinen, and S. Kaasalainen (2013), Snow surface roughness from mobile laser scanning data, *Cold Reg. Sci. Technol.*, *96*, 23–35.
- Lacroix, P., B. Legrésy, K. Langley, S. E. Hamran, J. Kohler, S. Roques, F. Rémy, and M. Dechambre (2008), Instruments and methods: In situ measurements of snow surface roughness using a laser profiler, *J. Glaciol.*, *54*(187), 753–762.
- Lehning, M., H. Löwe, M. Rysler, and N. Raderschall (2008), Inhomogeneous precipitation distribution and snow transport in steep terrain, *Water Resour. Res.*, *44*, W07404, doi:10.1029/2007WR006545.
- Lehning, M., T. Grünwald, and M. Schirmer (2011), Mountain snow distribution governed by an altitudinal gradient and terrain roughness, *Geophys. Res. Lett.*, *38*, L19504, doi:10.1029/2011GL048927.
- Lemmetyinen, J., A. Kontu, J. Pulliainen, A. Wiesmann, C. Werner, T. Nagler, H. Rott and M. Heiding (2010), Technical assistance for the deployment of an X to Ku band scatterometer during the Nosrex [2010] experiment, final report, ESA ESTEC contract 22671/09/NL/JA.
- Löwe, H., S. Egli, S. Bartlett, J. M. M. Guala, and C. Manes (2007), On the evolution of the snow surface during snowfall, *Geophys. Res. Lett.*, *34*, L21507, doi:10.1029/2007GL031637.
- Manes, C., M. Guala, H. Löwe, S. Bartlett, L. Egli, and M. Lehning (2008), Statistical properties of fresh snow roughness, *Water Resour. Res.*, *44*, W11407, doi:10.1029/2007WR006689.
- Manninen, A. T. (1997a), Multiscale surface roughness and backscattering, *Prog. Electromagnet. Res. PIER*, *16*, 175–203.
- Manninen, A. T. (1997b), Surface roughness of Baltic sea ice, *J. Geophys. Res.*, *102*(C1), 1119–1139, doi:10.1029/96JC02991.
- Manninen, A. T. (2003), Multiscale surface roughness description for scattering modeling of bare soil, *Phys. A*, *319*, 535–551.
- Manninen, T., and J.-L. Roujean (Eds.) (2014), SNORTEX field campaigns 2008–2010, *Finnish Meteorological Institute Reports 2014*(7), in press.
- Manninen, T., M. Rantasuo, T. Le Toan, M. Davidson, F. Mattia, and M. Borgeaud (1998), Multiscale surface roughness of bare soil, in *Proceedings of the IGARSS'98*, pp. 1203–1206, IEEE International, Seattle, 6–10 July.
- Manninen, T., K. Anttila, T. Karjalainen, and P. Lahtinen (2012), Automatic snow surface roughness estimation using digital photos, *J. Glaciol.*, *58*(211), 993–1007.
- Nagler, T., and H. Rott (2000), Retrieval of wet snow by means of multitemporal SAR data, *Trans. Geosci. Remote Sens.*, *38*(2), 754–765.
- Nolin, A. W. (2010), Recent advances in remote sensing of seasonal snow, *J. Glaciol.*, *56*(200), 1141–1150.
- Peltoniemi, J., T. Hakala, J. Suomalainen, and E. Puttonen (2009), Polarised bidirectional reflectance factor measurements from soil, stones, and Snow, *J. Quant. Spectrosc. Radiat. Transfer*, *110*, 1940–1953, doi:10.1016/j.jqsrt.2009.04.008.
- Peltoniemi, J. I., T. Manninen, J. Suomalainen, T. Hakala, E. Puttonen, and A. Riihela (2010a), Land surface albedos computed from BRF measurements with a study of conversion formulae, *Remote Sens.*, *2*(8), 1918–1940.
- Peltoniemi, J. I., J. Suomalainen, T. Hakala, E. Puttonen, J. Näränen, S. Kaasalainen, J. Torppa, and M. Hirschmugl (2010b), Reflectance of various snow types: Measurements, modelling and potential for snow melt monitoring, in *Light Scattering Reviews 5: Single Light Scattering and Radiative Transfer*, Springer Praxis Books, chap. 9, pp. 393–450, Springer, Berlin, Heidelberg, doi:10.1007/978-3-642-10336-0.
- Rees, W. G. (1998), A rapid method for measuring snow surface profiles, *J. Glaciol. Correspondence*, *44*(148), 674–675.
- Rees, W. G., and N. S. Arnold (2006), Scale-dependent roughness of a glacier surface: Implications for radar backscatter and aerodynamic roughness modelling, *J. Glaciol.*, *52*, 214–222.
- Rott, H. (1984), The analysis of backscattering properties from SAR data of mountain regions, *J. Oceanic Eng.*, *OE-9*(5), 347–355.
- Roujean, J.-L., et al. (2010), SNORTEX (Snow Reflectance Transition Experiment): Remote sensing measurement of the dynamic properties of the boreal snow-forest in support to climate and weather forecast, Report of IOP-2008, in *Proceedings of IGARSS 2009*.
- Schirmer, M., and M. Lehning (2011), Persistence in intra-annual snow depth distribution: 2. Fractal analysis of snow depth development, *Water Resour. Res.*, *47*, W09517, doi:10.1029/2010WR009429.
- Scipión, D. E., R. Mott, M. Lehning, M. Schneebeli, and A. Berne (2013), Seasonal small-scale spatial variability in alpine snowfall and snow accumulation, *Water Resour. Res.*, *49*, 1446–1457, doi:10.1002/wrcr.20135.
- Sturm, M., J. Holmgren, and G. Liston (1995), A seasonal snow cover classification system for local to global applications, *J. Clim.*, *8*, 1261–1283.
- Takala, M., K. Luojus, J. Pulliainen, C. Derksen, J. Lemmetyinen, J.-P. Kärnä, J. Koskinen, and B. Bojkov (2011), Estimating northern hemisphere snow water equivalent for climate research through assimilation of space-borne radiometer data and ground-based measurements, *Remote Sens. Environ.*, *115*(12), 3517–3529.
- Trujillo, E., J. A. Ramirez, and K. Elder (2007), Topographic, meteorological, and canopy controls on the scaling characteristics of the spatial distribution of snow depth fields, *Water Resour. Res.*, *43*, W07409, doi:10.1029/2006WR005317.
- Ulaby, F. T., R. K. Moore, and A. K. Fung (1982), *Microwave Remote Sensing*, vol. II, Addison-Wesley, Reading.
- Van der Veen, C. J., Y. Ahn, M. Csatho, E. Mosley-Thompson, and W. B. Krabill (2009), Surface roughness over the northern half of the Greenland Ice Sheet from airborne laser altimetry, *J. Geophys. Res.*, *114*, F01001, doi:10.1029/2008JF001067.
- Veitinger, J., B. Sovilla, and R. S. Purves (2013), Influence of snow depth distribution on surface roughness in alpine terrain: A multi-scale approach, *Cryosphere Discuss.*, *7*, 4633–4680.
- Warren, S., R. Brandt, and P. Hinton (1998), Effect of surface roughness on bidirectional reflectance of Antarctic snow, *J. Geophys. Res.*, *103*(E11), 25,789–25,807, doi:10.1029/98JE01898.
- Williams, L. D., and J. G. Gallagher (1987), The relation of millimetre-wavelength backscatter to surface snow properties, *IEEE Trans. Geosci. Remote Sens.*, *GE-25*(2), 188–193.
- Williams, L. D., J. G. Gallagher, D. E. Sugden, and R. V. Birnie (1988), Surface snow properties effects on millimeter-wave backscatter, *Trans. Geosci. Remote Sens.*, *26*(3), 300–306.
- Winkler, R. D., D. L. Apittlehouse, and D. L. Golding (2005), Measured differences in snow accumulation and melt among clearcut, juvenile and mature forests in southern British Columbia, *Hydrol. Processes*, *19*, 51–62.
- Zhuravleva, T. B., and A. A. Kokhanovsky (2011), Influence of surface roughness on the reflective properties of snow, *J. Quant. Spectrosc. Radiat. Transfer*, *112*, 1353–1368.



## PAPER III

Reprinted from the Cold Regions Science and Technology  
with permission of Elsevier  
© Elsevier









## Snow surface roughness from mobile laser scanning data



A. Kukko <sup>a,\*</sup>, K. Anttila <sup>a,b</sup>, T. Manninen <sup>b</sup>, S. Kaasalainen <sup>a</sup>, H. Kaartinen <sup>a</sup>

<sup>a</sup> Finnish Geodetic Institute, Department of Remote Sensing and Photogrammetry, Masala, Finland

<sup>b</sup> Finnish Meteorological Institute, Earth Observation, Helsinki, Finland

### ARTICLE INFO

#### Article history:

Received 4 September 2012

Accepted 3 September 2013

#### Keywords:

Seasonal snow  
Snow properties  
Surface roughness  
Mobile mapping  
Laser scanning

### ABSTRACT

Mobile laser scanning is a rapid and flexible method for acquisition of high resolution three-dimensional topographic data. Lidar based mobile mapping system produces three-dimensional point cloud from the surrounding objects. Typically, a two-dimensional profiling scanner is mounted on the system and the third dimension is achieved by the movement of the vehicle. The characteristics of the obtained point cloud depend largely on the sensor arrangement and the sensor properties.

In this paper we discuss an application of mobile laser scanning for producing snow surface roughness information for climate data validation. The ROAMER, a single-scanner mobile laser scanning system, was deployed for the survey of three dimensional snow surface data.

Relatively large areas could be reached with mobile laser scanning, which improves the output of surface roughness measurements and increases the statistical validity.

The accuracy and precision of the mobile scanning system used in the study are almost at the same level as those of terrestrial laser scanners. The relative point precision for the system is estimated to be a few millimetres with centimetre level absolute positioning. The results show that the roughness produced from the data is in agreement with the validation data obtained from the plate photography process. This means that mobile laser scanning can be successfully used in snow surface roughness determination from large areas. The major challenge is related to direct georeferencing of mapping sensor data with global satellite navigation and inertial positioning. However, computation of surface roughness is a local operation, where the absolute accuracy is of little significance, but good relative precision is essential. The dense sampling of the surface enabled us to study multi-scale approach for surface roughness modelling, which is discussed more in this paper.

We believe that even in the near future, mobile laser scanning will be considerably exploited in many applications in the environmental modelling and monitoring e.g. in forestry, hydrology, glaciology and climate sciences.

© 2013 Elsevier B.V. All rights reserved.

## 1. Introduction

Laser scanning is a technology that has revolutionized the surveying industry in producing topographic information in the past two decades (Bufton, 1989; Flood and Gutelius, 1997; Lohr and Eibert, 1995). Its use has contributed in microscale and fine topographic mapping of the Earth from satellite and airborne platforms (Garvin et al., 1996; Haala et al., 1998; Hyyppä et al., 2001; Kraus and Pfeifer, 1998; Maas and Vosselman, 1999; Naesset, 1997). Since the advent of this technology, laser scanning has been used to produce in ever more detailed mapping and modelling of terrestrial systems (Alho et al., 2011; Connor et al., 2009; Heritage and Milan, 2009; Hyyppä et al., 2012; Jaakkola et al., 2008; Kaartinen and Hyyppä, 2006; Lehtomäki et al., 2011; Rutzinger et al., 2011; Zhu et al., 2011). This means a vast diversity in sensor systems applied on to static or mobile platforms. Static laser scanning provides details and accuracy, but is limited with coverage. Kinematic

applications of laser scanning are becoming more into use as they provide effective data collection over larger spaces.

Mobile laser scanning (MLS) is a method for acquiring three-dimensional topographic data. The survey is conducted as the ground vehicle moves around while the navigation system, typically based on a global navigation satellite system (GNSS) and inertial measurement unit (IMU), tracks the vehicle's trajectory and attitude for producing a 3D point cloud from the range data collected by the onboard scanners.

The characteristics of the obtained point cloud depend largely on the sensor arrangement and the sensor properties. The use of MLS for snow surface measurement and monitoring was studied in our previous paper (Kaasalainen et al., 2010). The first results demonstrated the potential of MLS for fast and accurate snow profiling of large areas, which is further investigated in this study.

Surface albedo is one of the essential climate variables (ECV) defined in the Implementation Plan for the Global Observing System for Climate in Support of the United Nations Framework Convention on Climate Change (UNFCCC) (<http://unfccc.int/2860.php>). The reflectance of new pure snow can be 98% (Warren and Wiscombe, 1980). The

\* Corresponding author at: PO Box 15, FI-02431 Masala, Finland. Tel.: +358 9 29 555 301.  
E-mail address: [Antero.Kukko@fgi.fi](mailto:Antero.Kukko@fgi.fi) (A. Kukko).

seasonal snow cover can occupy 50% of the land area of the Northern Hemisphere (Mialon et al., 2005) thus having a considerable effect on the earth's energy budget. Therefore it is essential to understand the behaviour of seasonal snow cover and in particular its optical properties.

The importance of the snow and ice albedo for climate and the earth's energy budget has been widely recognized (e.g., Hudson, 2011). Surface roughness is one of the main features affecting the optical properties of snow cover (Warren, 1982) including the bidirectional reflectance distribution function (BRDF) (Warren et al., 1998) and surface albedo (Shuravleva and Kokhanovsky, 2011). Therefore it is an important variable in remote sensing. According to Williams and Gallagher (1987) the microwave backscatter and emission from snow cover depends mostly on wet snow surface roughness. Despite the importance very little research has been done on the subject.

Surface roughness in general has been widely studied and described with a number of parameters (Church, 1988; Fassnacht et al., 2009a, 2010; Hollaus et al., 2011; Lacroix et al., 2008; Manes et al., 2008; Manninen, 2003; Rees and Arnold, 2006), and a good overview can be found in Dong et al. (1992, 1993, 1994a, 1994b). The choice of parameters depends on the application. In remote sensing the most commonly used parameters are the root-mean-square (rms) height and the correlation length. However, snow surface roughness is a multi-scale and multi-directional phenomenon affected by several factors, some of which are global (sun elevation, maritime/continental, tundra/taiga) and some local (prevailing wind direction, distance to the canopy, undergrowth, moisture and temperature of the soil, rain and other climate conditions). All these factors affect the snow metamorphism and through that the surface roughness (Fassnacht, 2010, 2004). Therefore the rms height and the correlation length are not fully able to describe the nature of surface roughness (Church, 1988; Keller et al., 1987; Manninen, 1997a). Some multi-scale parameters have been developed (Davidson et al., 2000; Manninen, 1997b, 2003) but attempts to capture the directionality of the surface roughness are considerably fewer. Herzfeld (2002) used higher order vario functions in snow surface roughness descriptions and Trujillo et al. (2007) presented a directional spectral analysis on the spatial distribution of snow. Lacroix et al. (2008) present a recent review of snow surface roughness measurements.

One reason for the lack of research on surface roughness can be the difficulty of measuring it. In remote sensing all surface roughness scales above the wavelength used are important (Rees and Arnold, 2006). Many studies have been made to measure roughness by airborne laser scanning systems and satellite based radars (Höfle et al., 2007; Hollaus et al., 2011; Van der Veen et al., 2009). These methods are able to measure the meso- and topography scale roughness. Manes et al. (2008) presented the roughness effects in terms of two categories: type I for grain size scale and type II for structures up to 16 times the average crystal size. The small scale roughness is typically measured with photography-based methods. Elder et al. (2009), Fassnacht et al. (2009a, 2009b), Manes et al. (2008), Manninen et al. (2012) and Rees (1998) have measured the small scale surface roughness by partially inserting a plate in the snow, photographing the plate with the snow-plate interface and later analysing the profile. This method gives a detailed profile for the width of the plate (typically approx. 1 m). The downside of these methods is that the length of the profile is limited. Also, if you want to cover larger areas it is labour intensive and time consuming. In addition to this, the profile measurements produce 2D-data, while snow surface roughness is a 3D phenomenon with considerable directionality.

The use of airborne and terrestrial laser scanning on snow covered areas has previously been focused on forming surface models and monitoring changes in snow depth (Arnold et al., 2006; Hood and Hayashi, 2010; Kaasalainen et al., 2008; Prokop, 2008; Prokop et al., 2008). Snow properties that have been studied with lidar are, for example, snow thickness, water contents (Schaffhauser et al., 2008; Schirmer et al., 2011; Várnai and Cahalan, 2007) and depth distribution of snow (Schirmer and Lehning, 2011). Lehning et al. (2011) used terrestrial laser scanning

data to model snow distribution. Also the use of laser intensity data has been studied for snow characterization (Anttila et al., 2011).

Compared to airborne laser scanning (ALS), MLS suits better for areas that are limited in size, and where precision and level of details are of any concern. It also provides considerable advantage over traditional manual data acquisition processes in terms of data coverage and effort. In addition, MLS can be used for acquiring precise multi-temporal data for change detection, and for studying processes causing them, like wind erosion.

Different laser scanning-based surface roughness measurement systems have been developed (Lacroix et al., 2008). TLS data have been used and found useful for surface modelling for, e.g., river-bed roughness in fluvial geomorphology (Heritage and Milan, 2009) and for soil erosion models (Eitel et al., 2011). ALS has proven efficient for the characterization of roughness over large areas, such as ice sheets (van der Veen et al., 2009) or forest canopy (Weligepolage et al., 2012), or to be used as input in the modelling of natural hazards (Hollaus et al., 2011).

In this paper we study the applicability and accuracy of mobile laser scanning data in characterizing snow surface roughness. The mobile laser scanning data were acquired with the FGI ROAMER (see Kukko et al., 2007, 2012 for system details and performance) in Sodankylä, Finnish Lapland during the melting period in spring 2010. We compare the results with surface roughness plate measurements made at the same location shortly after the scanning. The measurements were made as a part of Snow Reflectance Transition Experiment (SNORTEX)-campaign (Roujean et al., 2010).

## 2. Surface data capture and mobile laser scanning system

### 2.1. Study site

The measurements were carried out in Sodankylä, Finnish Lapland (67.4°N, 26.6°E) during the series of SNORTEX-campaigns taking place during the melting seasons of 2008, 2009 and 2010. The MLS and validation measurements were made 18<sup>th</sup> of March 2010. The 2.5 km long mobile laser scanning route and corresponding scan data are shown in Fig. 1, and followed the marked snow mobile trail that passes through open marshland and sparse pine forests. The reference surface roughness plate measurements (described in Section 3) were made along the trajectory shortly after the scanning at 11 locations shown in Fig. 1 as well.

### 2.2. Mobile laser scanning system

The FGI ROAMER mobile laser scanning system was deployed for capturing the three-dimensional snow surface topography. It is a system primarily developed for urban mapping, but its use for environmental applications is increasing. The ROAMER system is equipped with a FARO Photon 120 laser scanner and NovAtel SPAN GPS-IMU system, altogether with data synchronizing and recording devices. Table 1 summarizes the equipment and main characteristics. The laser unit provides a scanning (cross-track swath) frequency range of 3–61 Hz and point measurement rate of 120–976 kHz with ranging ability up to 150 m. The point measurement accuracy of the scanner is 2 mm with 1 mm repeatability for 90% reflective target according to the scanner manufacturer, but depends in practice on the object surface type and reflectivity, as well as the object orientation relative to the scanning beam.

The integrated tactical grade GPS-IMU system observes the GPS satellites and platform movements in order to reproduce the system trajectory for laser scanner data georeferencing. When fused in post-processing, the GPS-IMU data provide the laser scanner position and attitude recordings as function of time at 100 Hz data rate. The laser point data are time synchronized to the trajectory data in order to produce a three-dimensional point cloud of the scanned area similar to airborne laser scanning.

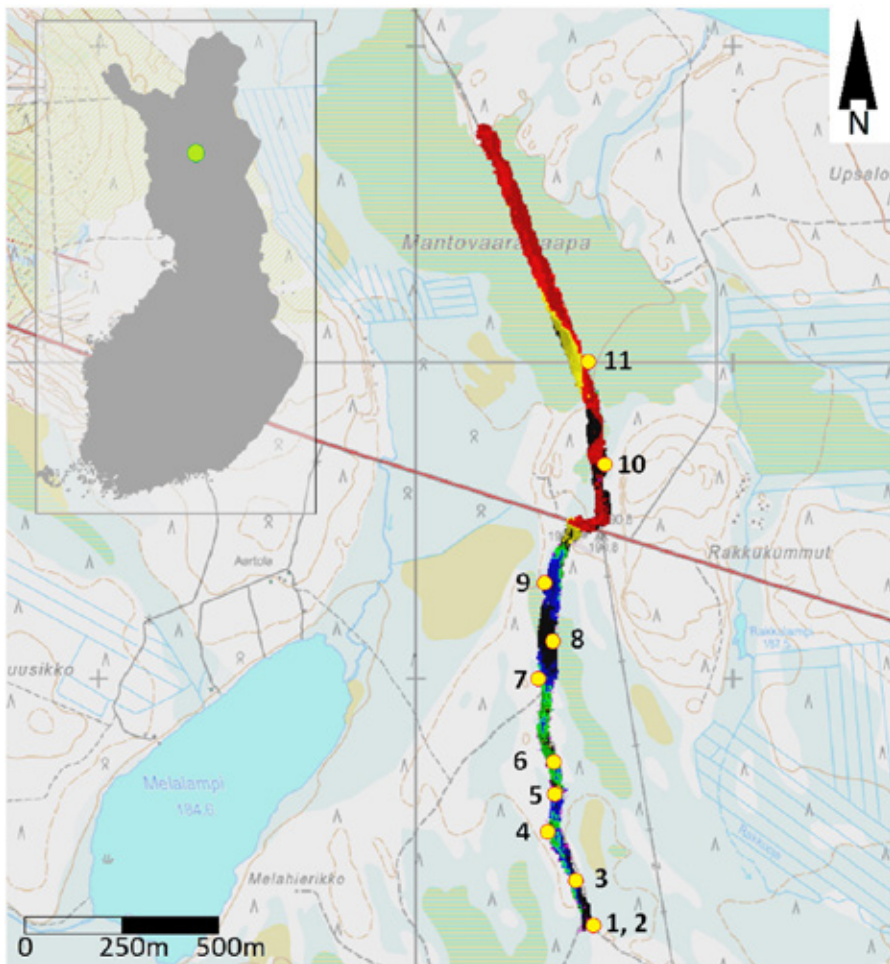


Fig. 1. MLS data coverage on the study site and validation site locations (numbers 1–11). Study site locates in northern Finland above the Arctic Circle. Map data courtesy: NLS of Finland.

For mobility in the snow the MLS system was mounted on a snow mobile-towed sleigh. The set-up is seen in Fig. 2. However, deep and soft snow makes it difficult to manoeuvre and thus the snow plate

validation sites were selected to be close to the official snowmobile trail. The length of the mapped route on 18 March 2010 was around 2.5 km, and it was surveyed with 49 Hz scanning frequency and point measurement rate of 244 000 pts/s. The scanner head was mounted upwards for vertical profiling to produce across-track swaths.

Due to the scanner characteristics, the ROAMER is capable of producing high density three dimensional point clouds for mapping of surface topography and object dimensions around its trajectory. In the data set at hand the point density on snow surface varies between 100 pts/m<sup>2</sup> and 3000 pts/m<sup>2</sup> according to the horizontal distance from the scanner. Spacing between the sequential scan swaths in the data was approximately 2–6 cm depending on the platform velocity. Fig. 3 shows an example of one data block as 3D point cloud visualization. Colour coding reveals the surface elevation changes and level of detail observed by the system. The relative point precision of the system is estimated to be at the sub-centimetre level, but the point position is eventually defined absolutely (i.e. in Earth system) by the accuracy of the navigation solution that could be provided through post-processing. According to the latest performance studies on MLS systems, the ROAMER system could measure objects with 20 mm absolute accuracy in good GPS visibility conditions (Kaartinen et al., 2012, 2013; Kukko et al., 2012).

**Table 1**  
ROAMER MLS system characteristics.

FARO Photon 120 scanner
120–976 000 pts/s, user selectable
320° maximum field of view
3–61 Hz scan frequency, user selectable
785 nm wavelength, phase shift ranging
Spot size 3.3 mm + 0.16 mrad divergence
NovAtel SPAN GPS-IMU
NovAtel DL-4plus receiver and GPS-702 antenna,
L1 and L2 frequencies
Honeywell HG1700 AG11 tactical-grade RLG IMU
Gyro bias 1.0 deg/h
Random walk 0.125 deg/rt-h
Data rate 100 Hz
Bi-trigger synchronization
Delivers scanner triggers to receiver log
Camera triggering ×4
Rugged laptops for data recording



**Fig. 2.** The ROAMER MLS system and the snowmobile employed for the data acquisition. The GPS antenna and IMU boxes are seen in front of the platform, the laser scanner unit is topped with green insulation.

### 3. Field reference data

#### 3.1. Snow roughness reference with plate photography

The surface roughness plate measurement system was constructed for the SNORTEX campaign (Karjalainen, 2010; Manninen et al., 2012; Roujean et al., 2010). The measurement system consists of a background plate and a digital camera (Fig. 4). The size of the plate is

100 cm × 40 cm. The edges are covered by three rows of scales (1 mm, 5 mm and 10 mm) that consist of black and white squares. The middle part of the board is black. The board is made of a 3 mm thick white l-bond aluminium layer plate that is covered with black matt tape. The photographs were taken with the Canon PowerShot G10 digital pocket camera that has a sensor of 4416 by 3312 pixels and a zoom lens from 6.1 mm to 30.5 mm with an optical image stabilizer.

The snow profile measurements were carried out by inserting the plate partially into the snow and taking a photo containing the plate and the snow–plate interface. The snow–plate interface is later automatically detected from the photograph, resulting in an appr. 1 metre long 2D profile representing the snow surface. The profile can be retrieved by using one image but for the SNORTEX campaign typically three images were taken from each of the locations in order to make sure the success of fully automatic analysis for each profile.

The snow surface is retrieved from the image based on a threshold between light and dark pixels. The method is described in more detail in Manninen et al. (2012). In practice, defining the right threshold value between the light and dark pixels and extracting the snow–plate interface have proven to be challenging due to problems related to varying illumination conditions, varying contrast within image, and snowflakes in the area of the plate in case of photo capturing during snowfall. However, the only a priori information the method needs is whether the image was taken during snowfall or not. The accuracy of the system depends on the photographing configuration, and is typically of the order of 0.1 mm vertically and 0.04 mm horizontally.

For the evaluation of the roughness data measured with the MLS, surface roughness plate measurements were made at 11 locations shown in Fig. 1. The plate measurements were made parallel to the mobile route, one profile from each site.

#### 3.2. Measurement settings

Correspondingly to the plate measurement sites (Fig. 1), the following 1 m long profiles were cut from the MLS laser data, as close as possible to the plate profile:

1. A 3 cm wide box parallel to the plate measurement.
2. A 5 cm box similar to 1.
3. A cross-track sample perpendicular to the plate measurement, consisting of points from a single laser swath.

In some cases an additional set of profiles was extracted closer to the trajectory of the mobile laser scanner in order to achieve a better

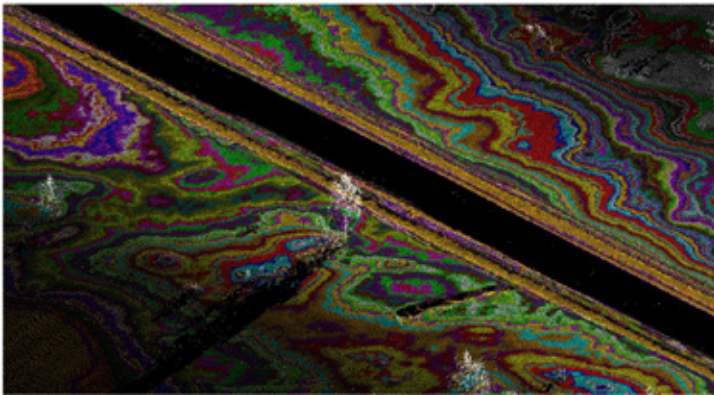


**Fig. 3.** High resolution MLS point cloud from snow surface collected with ROAMER system. Colouring is used to illustrate the macroscopic surface elevation changes. White objects are trees and the 2.5 m wide black streak splitting the data is caused by the instrument shadow.





Fig. 4. Validation snow profiles were measured with plate photography by inserting a 1 m wide black plate in the snow. The profiles were automatically extracted from the photographs for deriving snow roughness.

resolution for the profile analysis. This was done only if the original plate measurement at the site was far away from the trajectory (e.g., in validation site 8, see Fig. 1), and if it was possible to cut the profiles from the natural snow cover with no disturbance due to the snow mobile trail.

At validation site 4 it was not possible to cut 1 m laser profiles at the same location as the plate measurements because of the surrounding trees and shadows they caused in the MLS data. A representative set of profiles was cut from approx. 5 m to the north of the site. At validation sites 3, 6, 9 and 10 the plate measurements were already so close to the trajectory that only the laser profiles next to the plate measurement were extracted.

As the previous works have shown, the roughness of snow surface depends on the measured length (Church, 1988; Keller et al., 1987; Manninen, 1997b; Manninen et al., 1998). Therefore the 1 metre long laser and plate profiles were analysed as a function of measured length so that for each possible length  $x$  ( $x < 1$  m) an average of rms height is computed according to the equation (Manninen, 2003)

$$\langle \sigma_i \rangle = \frac{1}{(n - in_0)} \sum_{j=1}^{n-in} \sigma_{ij} \quad i = 1, \dots, n_i, \quad (1)$$

where  $\sigma_{ij}$  is the rms height corresponding to a length of  $in_0$  points. The smallest length used for computation is  $n_0$  and it is enlarged with an increment of  $i$  so that the length is  $in_0$ , where  $n_i$  is the total number of different lengths to be used. The computational subsection  $in_0$ , for which rms height is calculated at each time, is moved over the whole profile by an increment of  $j$ . The total number of points in the 1 metre profile is  $n$ .

The logarithm of the rms height  $\sigma$  is usually linearly dependent on the logarithm of  $x$ , so that

$$\sigma(x) = e^a x^b, \quad (2)$$

where  $a$  and  $b$  are constants.

To compare the surface profiles cut from the plate measurements and from the laser data, the rms height variations as a function of length were computed for each of the laser profiles. Profiles with less than 10 points were neglected from the analysis.

## 4. Point data processing

### 4.1. Filtering

The unprocessed (raw) MLS point cloud includes observations with dark response and isolated stray points. Most of the isolated points appear in the sky and between solid objects as stray points due to phase shift ranging. The sky points are mostly dark, but stray points have

typically strong intensity as they represent the reflectivity of solid objects, but ranging fails with multiple hits within the laser beam. Measurement geometry, i.e. laser beam incidence angle, affects the point density on the snow surface, so the points are sparser at longer distances from the scanner trajectory.

The dark points were filtered out of the point cloud simply by setting the intensity limit to 1000. The weakest intensity values from the snow were found to be around 1100, so no loss of essential data was expected. The raw scanner intensity values are expressed in 11 bits, so the complete intensity data range is 0–2048.

The sky and stray points were classified to a sky point class with an isolated point filtering method. The method removes points that are too isolated from the others by searching for points within radius  $r$  from the centre point, and if  $n$  points or more are found, the centre point is preserved. It was found that if less than 5 points lie within the 20 cm radius, they can be removed. Being a geometric method, some of the points actually representing snow surface at far distance (greater than 25 m) from the scanner are treated as noise. This is due to the fact that with fixed angular resolution the point density decreases as a function of distance and incidence angle. Thus we do not delete the points that respond to the filtering right away but mark them as belonging into the sky point class. Doing so we could later restore them with aid of the snow surface information, as described below.

### 4.2. Snow surface classification

After the noise filtering the laser data still includes points from objects other than snow, in this case mostly trees, power line pylons and snow mobile trail markings. The purpose of the snow surface classification was to remove all non-snow points prior to the surface roughness computation. The snow surface classification followed the classification method introduced in Axelsson (1999). The routine builds an initial surface model from the user selected laser points. Triangles in this initial model are mostly below the surface to be modelled with only the vertices touching it. The routine then starts moulding the triangular irregular network model upwards by iteratively adding new laser points to it. Each added point makes the model following the snow surface more closely.

A set of iteration parameters determines how close a point must be to a triangle plane for being accepted as snow surface point and added to the model. Iteration angle  $\alpha_i$  is the maximum angle spanned by a point, the closest triangle vertex, and points projection in the plane normal direction on the local triangle plane. The smaller the iteration angle the less eager the routine is to follow changes in the point cloud (small undulations in snow or hits on low vegetation). Iteration distance  $d$  makes sure that the iteration does not make big jumps upwards when triangles are large. This helps to keep low non-snow objects out of the model. Terrain angle  $\alpha_t$  limits the steepest allowed slope in the snow

surface. With the selected set of parameter values ( $\alpha_t = 45^\circ$ ,  $\alpha_r = 45^\circ$ ,  $d = 50$  cm), and manually pointed initial points, the classification method detects the snow surface points seemingly well, as shown in Fig. 5.

In the second iteration round, the snow surface points initially filtered to the sky point class were restored to the snow surface class in a similar process of classification as described above, but now the known snow surface model was used as the initial model. This process could restore the snow points at long distance from the scanner that were falsely removed by the isolated point filtering.

Despite the good overall performance of the snow point classification, a small number of points in the close vicinity of the scanner (typically within 3 m) tend to be left out of the snow class. They seem to be the peak points of small ripples 3–10 mm in size, and shown as yellow dots among the snow points in Fig. 6. These points become misclassified because of the high point density and angular thresholds used for the snow classification. If the thresholds were changed, the more false positives would have been introduced into the snow class. Therefore the thresholds were left as they were, and the problem was solved by searching for points close to the snow surface class points. We used a 2 cm maximum elevation threshold between the point and the snow surface with 10 cm maximum triangle edge length.

#### 4.3. Computing of snow surface roughness – MLS grid method

The surface roughness algorithm first builds an indexing for the point cloud for selected grid size over the whole point set in the selected point class, i.e. snow class in our case. Within the grid cell, the centroid of the points is computed and points that are within the radius threshold are selected for roughness computation. By adjusting the grid size and radius parameters the surface characteristics can be studied in different sampling densities and levels of detail.

Next, a plane equation is fitted to the selected points around the grid centroid and the minimum distance of each point to the plane in the least squares sense is computed. Analogous to the plate photography method with line fitting procedure, the roughness value of the grid cell is the average of the point distances from the fitted plane.

The surface roughness is computed over the classified snow surface points. Dense surface point cloud allows computation of different grid sampling densities and sample sizes. In Fig. 7 the surface roughness as rms height is illustrated for computation using 5 cm sample size and grid spacing. The white right-angled vectors show validation site 9 location on top of a small round bump, as can be observed from a slight increase in the rms heights. On an open area seen in Fig. 7, the surface characteristics are not very strong, but in the forested section just next

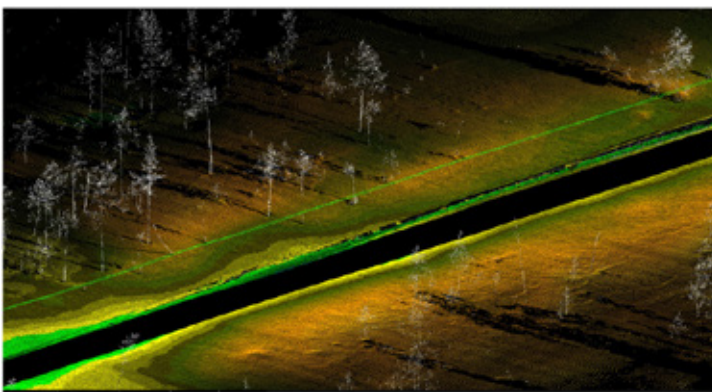


Fig. 5. Classification result for MLS data. Snow surface elevation is illustrated in colours and objects above the snow surface by intensity grey tone of the data. The scanner trajectory is shown as a light green line.

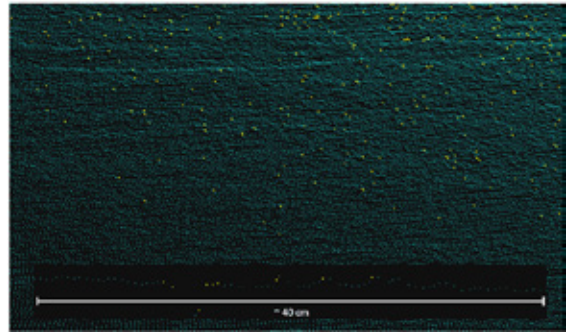


Fig. 6. Misclassified fine scale snow surface points (yellow) among the snow class points (turquoise). The inset shows a close-up of one profile showing the scale and nature of the matter. Scanning took place from the right of the figure.

to the open marshland shown in Fig. 8 shows slightly more coarse surface featuring.

Comparison of the sample size effect on the roughness values is displayed in Fig. 9, where the surface roughness is computed using 10 cm and 100 cm sample sizes over a 1 metre grid. For the illustration, the roughness surfaces were interpolated to a 10 cm grid by triangulating the original roughness points for better visual pleasure. From the image pair we can see that the surface topography, i.e. centimetre-scale features, starts to dominate with the increasing sample size, precisely as expected.

## 5. Evaluation of the MLS derived surface roughness

### 5.1. Results from the plate photography

The linearly rectified laser and plate profiles can be seen in Fig. 10. The corresponding rms height variations as a function of window length for each of the profiles are collected in Fig. 11. The extracted surface profiles can be divided into two groups according to the profile and roughness characteristics. In the first group both the plate and MLS profiles are more or less of equal shape and magnitude, while the second group shows some diversity in the surface shape represented by the profile samples. The effect of the surface topography is also seen from the diverging rms functions.

The laser profiles parallel to the laser swath often have considerably higher point density than the profiles cut across the swaths, which also

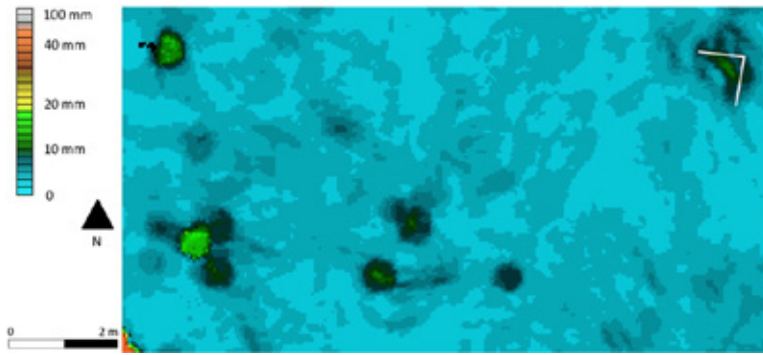


Fig. 7. Snow surface rms height computed for 5 cm grid sampling. White right-angle feature shows roughly validation site 9 location on top of a small bump.

was the principal orientation for the plate profiles. Also the role of the uneven point density, function of range and incidence angle, within laser profiles should be studied in more detail. For example the 3 cm and 5 cm wide box profiles of validation sites 2, 3, 4, 7, 9 and 11 (see Fig. 1) include several sequential points from each laser swath that they intersect. There is a few centimetre spacing between the swaths. It should be investigated in more detail, which profile cutting method best describes the actual surface. One option is to cut the profiles in a way that they consist of only one point from each laser swath.

The other factors that in general have an effect on the roughness estimation with MLS are the laser spot size and wavelength. In this study the laser spot size on the snow surface at range of 25 m is 4 mm, but incidence angle effect elongates the spot to be around 30 mm at the edge of the captured snow surface data. The 785 nm wavelength of the laser in use is only slightly beyond the visible range, thus the penetration and absorption (Warren et al., 2006) are expected to have only little effect on the ranging, and thus on the roughness estimation and comparisons with the plate photography measurements.

At validation sites 6, 9 and 11 the features captured in the profiles are diverged, and the scale of the difference is considerably high. For example at validation site 9 the height variation in the rectified laser profile is about 6 cm. For all the three sites it is obvious that locating the validation profiles with respect to the plate profile has not been completely successful. The variation is thus predicted to be caused by the different placements of the profiles on the snow surface, and as the MLS data show centimetre scale surface topography variation, that affects the result. It is also noticeable that at validation site 9 the surface shows a low

bump, as seen in Fig. 7, while at validation sites 3 and 6 the surface seems to have more of a dune type of topography. The profiles from validation site 3 also show a slight shift in phase on a repeating ripple structure.

The resolution of the plate photography profile is much higher compared to the laser data, especially in the driving direction. Similar laser profile densities can be achieved close to the scanner trajectory in cross-track laser swaths. Therefore the proximity of the plates to the laser profiles is important. However, as Fig. 11 shows, for typical smooth snow surface the local surface variation is of the same magnitude for both of the methods. At validation sites 1, 2, 4, 7, 8, 10 and 11 the physical difference between the rectified plate and laser profiles is within a few millimetres, thus indicating flat surface characteristics. The rms functions derived from the both datasets intersect typically for around 50 cm processing window length, even if there was topography variation of 2–10 mm. For validation site 11 the laser point density was probably too low for proper roughness analysis, as even if the profiles show similar trends, the rms values for cross-track profiles are not fully consistent to the plate profile analysis. However, the profile cut along the swath shows only slightly coarser values.

## 5.2. Roughness analysis

In most of the cases the difference between the rms functions from the plate profiles and the corresponding laser profiles is within 2 mm. This holds especially for the window lengths of 50–60 cm. In the cases where the difference is larger, e.g., for sites 3, 5, 6 and 9, the difference

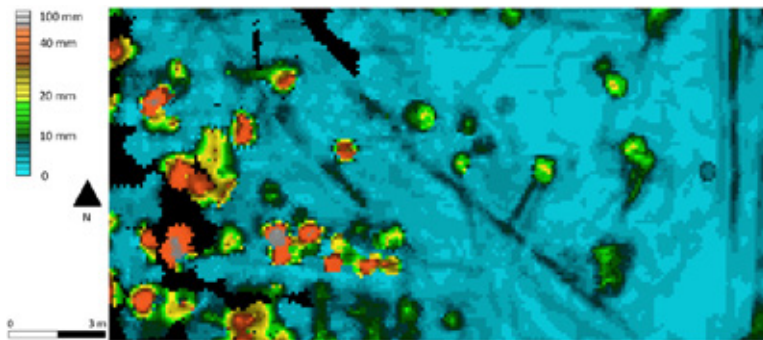
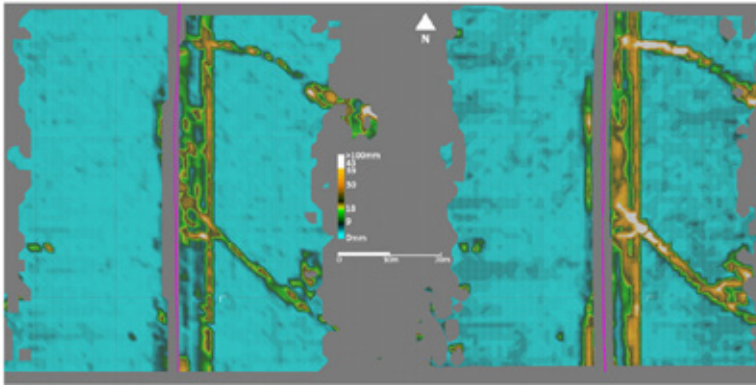


Fig. 8. Snow surface rms height produced by the MLS grid method using 10 cm grid sample size from a forested section of the mapped route. Snow surface shows slightly higher rms height values compared to Fig. 7, and snow surface features around trees are prominent.



**Fig. 9.** Snow surface roughness computed using 10 cm (left) and 100 cm (right) sample diameters at 1 m grid. The increase in sample size reduces the detection of small features, but incorporates larger topographical surface features.

in roughness is still less than 10 mm (see Fig. 10). These differences can mostly be explained by the differences in the location of the laser and plate profiles.

The difference between the rms function of the corresponding laser profiles cut with 3 cm and 5 cm wide boxes seems to be negligible. This indicates that the box width is not significant for relatively smooth surfaces. For surfaces with complex repetitive topographic structures, such as small ripples, the box width may have more effect on the roughness result. The role of the box width on different types of surfaces has to be further investigated to find the most appropriate sampling procedure.

### 5.3. Results from the MLS grid method

The classified snow surface point cloud was processed for surface roughness characterization. The sampling over the surface data was obtained by the 1 metre grid. Ten sample diameters from 10 cm to 100 cm in 10 cm interval were used for each location to compute the surface variation from the local plane. The sample points closest to the laser profiles were selected as representative values. The rms height data are plotted in Fig. 12 and show that the increase in sample size increases the rms height, as expected. Fig. 11 also shows the largest increase in roughness for the sites that have noticeable surface topography based on Fig. 10. 10 cm sample size seems to be problematic for the MLS grid method as it results in relatively large rms height for the smallest sample size in some of the cases, as can be seen from Fig. 12. The cause is yet to be determined, but the most probable explanation is the point distribution and the scan line spacing in particular. Further it could be due to the low amount of points resulting to erroneous plane fitting, or some local surface properties.

Table 2 combines the rms values from the plate profiles and the corresponding surface rms height from the MLS grid method at the validation sites. The closest grid point to the plate validation profiles from the 1 m grid sampling was selected for evaluation of the MLS grid method at each validation site. The roughness values derived from the methods show similar behaviour and magnitude. The rms curves seem to correspond to the detected surface profile topography characteristics (see e.g., profiles 3, 4 and 5 in Fig. 10). Based on the similarity of the surface profiles, the MLS grid method could reproduce the surface roughness similar to the plate photography method.

## 6. Discussion

The results show that mobile laser data can be used for snow surface roughness measurements to obtain similar results to those based on

plate photography. However, the effect of the data characteristics on the derivation of surface roughness needs to be studied in more detail to better comprehend the limitations of the data and to develop procedures with well proven foundation. These characteristics are, e.g., measurement repeatability, effect of snow type on the penetration depth of the used laser wavelength, and data density and its variation during the scanning. The density of the data can be greatly improved by scanning with a faster scanning mode, driving the snow mobile slower, and passing the area at multiple times.

There are some practical aspects that affect the performance of the MLS in characterization of snow surface. The scanning geometry with fixed angular resolution and scanner elevation affects the point distribution within the lidar swaths; on a horizontal flat surface the spatial separation between sequential points increases with the range from the scanner. In forested areas the shadowing of objects becomes more prominent, and thus decreases the spatial coverage by fragmenting the surface data. Varying surface topography at large incidence angles also causes shadows in the data. Furthermore, the scanning frequency affects the along-track point density, which is typically less than the point density within the swath close to scanner, but turns to be denser further away. More studies of the effect of uneven point density on the surface roughness parameters need to be done as well as the effect of point density.

The positioning accuracy of the GPS-IMU system is the most critical part in the error budget of an MLS. Geometric data quality could be controlled by providing control points from the surfaces for elevation control and localization of suitable geometric objects for horizontal control (Kaartinen et al., 2012; Kukko et al., 2012).

The handheld GPS used for locating the plate photography measurements seems inadequate or inappropriate for extracting the laser point data from the point clouds. The localization uncertainty affected the results so that the validation and MLS data do not correspond to each other precisely. This could be improved by using more accurate surveying techniques to locate the plate profiling sites and provide the plate orientation. However, the data show sufficient consistency and MLS could reproduce the surface characteristics.

## 7. Conclusion

We propose a processing chain for the snow surface roughness estimation with mobile laser scanning data and validate the results against the plate photography method. The ROAMER system of the Finnish Geodetic Institute was employed for the MLS data acquisition in a multi-temporal data collection in year 2010 around the premises of the Arctic Research Centre of the Finnish Meteorological Institute, Sodankylä,



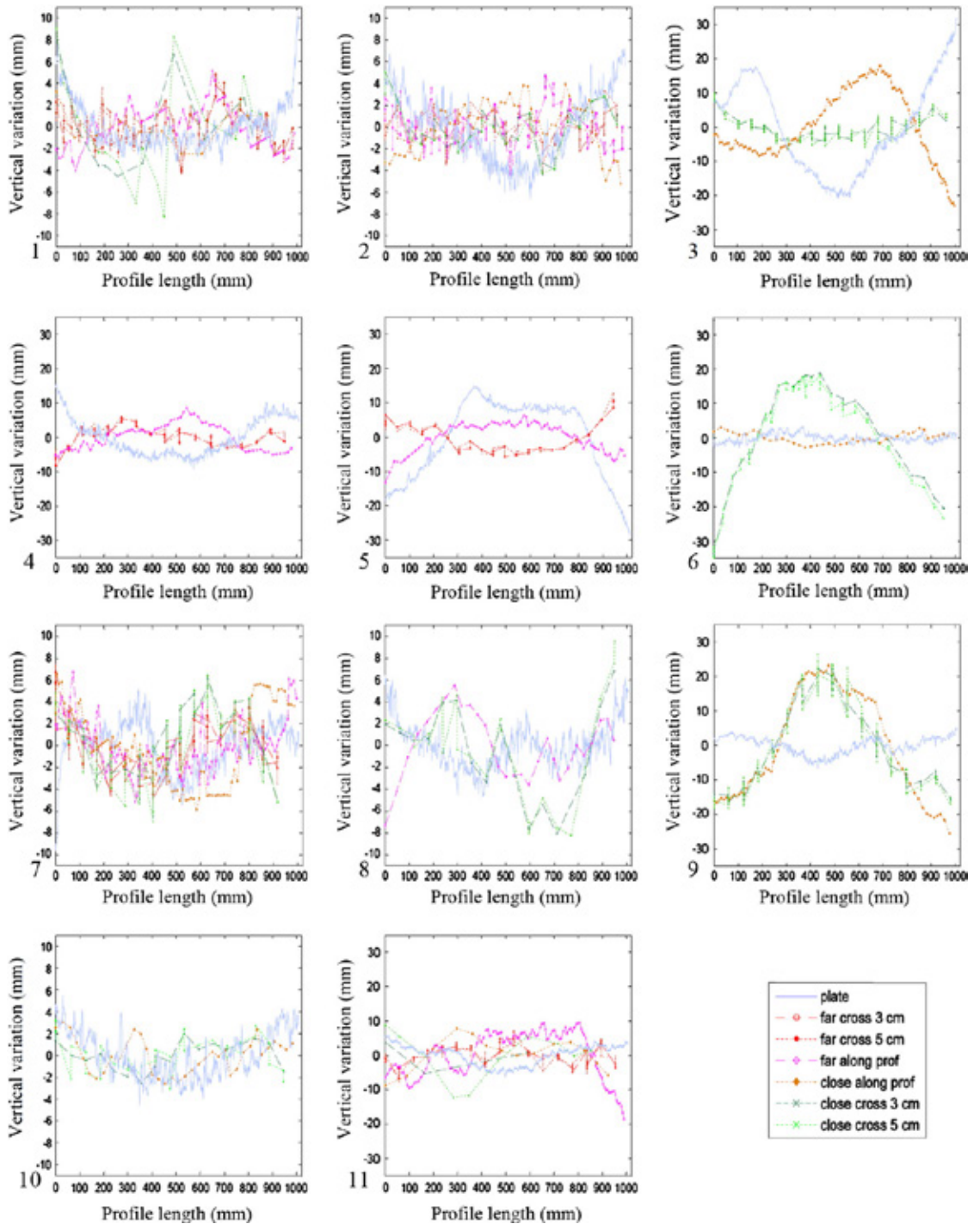


Fig. 10. Snow surface profiles extracted from the MLS data and the corresponding validation plate profiles for the validation sites. MLS profiles taken close to the plate are indicated as “close” and “far” indicates profiles extracted further away from the validation plate profile.

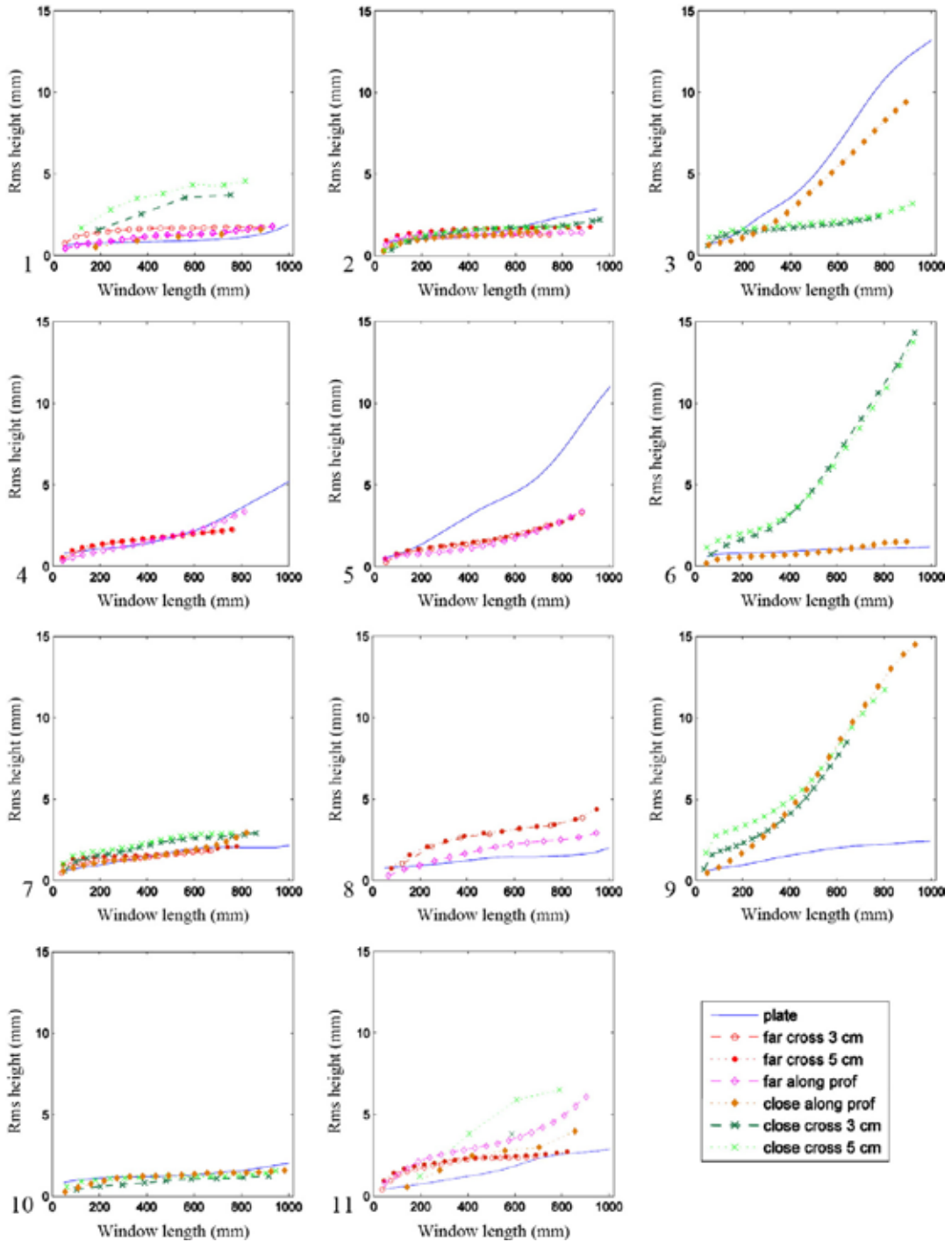


Fig. 11. The rms functions for the snow surface profiles extracted from the MLS data and the corresponding validation plate using plate photography rms computation. MLS profiles taken close to the plate are indicated as "close" and "far" indicates profiles extracted further away from the validation plate profile.

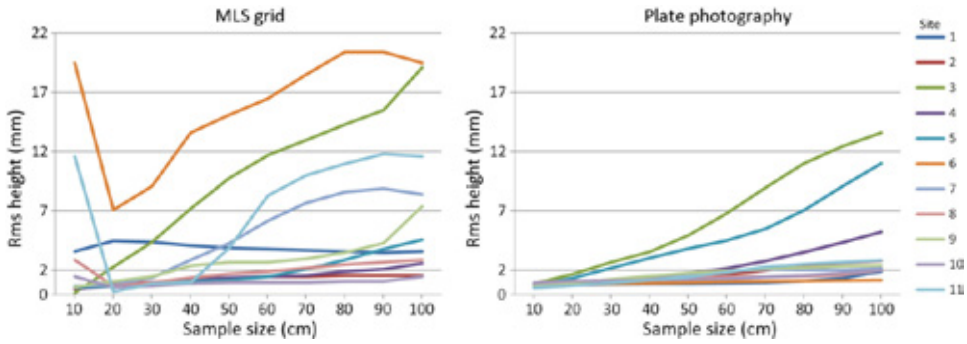


Fig. 12. Surface roughness at the validation sites for the two methods. Left: MLS grid rms height as a function of sample size. Right: Plate rms height as a function of window size.

Finland. MLS derived surface roughness values were compared to field samples by snow plate photography.

We find that MLS enables a detailed surface model production of snow surface topography and snow cover modelling over large areas with unprecedentedly dense sampling. Detailed surface data are essential for precise roughness estimation in different scales. The evaluation shows that the surface shape and roughness modelling in millimetre scale is possible with MLS data. The most limiting factor affecting the roughness computations is the profile spacing, which is a function of scanning frequency and platform speed.

As traditional field work schemes, such as the plate photography, can provide only sparse data distribution over limited area, the proposed MLS grid method provides a fast and efficient method for large area surface roughness characterization, mostly at the same level of precision as with the photographic methods. With active laser technique we could overcome the illumination problems hampering the use of the plate photography method. Overall, three dimensional laser scanning data over the snow surface provides a data source for various studies e.g. monitoring of snow cover change and interpretation of surface morphology in a level of detail not possible earlier. In particular the

MLS method allows high data density over wide spatial coverage for surface roughness studies.

**Acknowledgements**

The research conducted in this study has been funded by the Academy of Finland, the Finnish Meteorological Institute and the FMI ARC: Snow Transition Experiment 2008–2010, the EUMETSAT projects “Satellite Application Facility in Climate Monitoring” and “Satellite Applications on Support to Operational Hydrology and Water Management”, and by the Academy of Finland research project “New techniques in active remote sensing: hyperspectral laser in environmental change detection” (255534). The authors want to thank all parties involved in the field work and those giving constructive comments.

**References**

Alho, P., Vaaja, M., Kukko, A., Kasvi, E., Kurkela, M., Hyypää, J., Hyypää, H., Kaartinen, H., 2011. Mobile laser scanning in fluvial geomorphology: mapping and change detection of point bars. *Z. Geomorphol.* 55, 31–50.

**Table 2**

Surface rms height obtained for the validation sites with different computing radii from the MLS surface data and from the corresponding plate photography with the same window sizes. rms height values in mm.

Validation site	Method	Computing diameter (cm)									
		10	20	30	40	50	60	70	80	90	100
1	Grid	3.6	4.5	4.4	4.1	3.9	3.8	3.7	3.6	3.5	3.6
	Plate	0.7	0.8	0.8	0.9	0.9	0.9	1.0	1.1	1.4	1.9
2	Grid	0.4	0.9	1.0	1.2	1.3	1.5	1.5	1.6	1.6	1.6
	Plate	0.9	1.0	1.1	1.2	1.4	1.7	2.0	2.4	2.7	2.8
3	Grid	0.1	2.3	4.4	7.2	9.8	11.7	13.0	14.3	15.5	19.1
	Plate	0.9	1.8	2.7	3.6	5.0	6.8	9.0	11.0	12.5	13.6
4	Grid	0.5	0.7	1.0	1.3	1.4	1.5	1.6	1.9	2.1	2.6
	Plate	0.9	1.1	1.2	1.4	1.7	2.2	2.8	3.5	4.4	5.2
5	Grid	0.6	0.7	1.0	1.1	1.2	1.5	2.1	2.9	3.8	4.6
	Plate	0.8	1.4	2.2	3.1	3.8	4.5	5.5	7.1	9.1	11.0
6	Grid	19.5	7.1	9.1	13.6	15.1	16.5	18.5	20.4	20.4	19.5
	Plate	0.7	0.8	0.9	0.9	1.0	1.1	1.1	1.1	1.2	1.2
7	Grid	0.7	0.8	1.4	2.9	4.3	6.2	7.7	8.6	8.9	8.4
	Plate	0.7	1.0	1.2	1.5	1.7	2.0	2.1	2.1	2.1	2.2
8	Grid	2.9	0.7	1.0	1.4	1.7	1.9	2.2	2.5	2.7	2.9
	Plate	0.8	0.9	1.0	1.2	1.4	1.5	1.5	1.5	1.6	2.0
9	Grid	0.6	1.1	1.5	2.4	2.7	2.7	3.0	3.5	4.3	7.4
	Plate	0.8	1.0	1.2	1.5	1.8	2.0	2.1	2.2	2.4	2.4
10	Grid	1.5	0.6	0.7	0.9	1.0	1.0	1.0	1.1	1.1	1.5
	Plate	1.0	1.1	1.2	1.2	1.2	1.3	1.4	1.6	1.8	2.0
11	Grid	11.6	0.2	0.9	1.0	3.9	8.3	10.0	11.0	11.8	11.6
	Plate	0.5	0.7	1.0	1.2	1.5	1.8	2.3	2.5	2.7	2.9

- Anttila, K., Kaasalainen, S., Krooks, A., Kaartinen, H., Kukko, A., Manninen, T., Lahtinen, P., Siljamo, N., 2011. Radiometric calibration of TLS intensity: application to snow cover change detection. *Int. Arch. Photogramm. Remote. Sens. Spat. Inf. Sci.* 38 (5/W12).
- Arnold, N.S., Rees, W.G., Devereux, B.J., Amable, G.S., 2006. Evaluating the potential of high-resolution airborne LIDAR data in glaciology. *Int. J. Remote. Sens.* vol. 27 (6), 1233–1251.
- Axelsson, P., 1999. Processing of laser scanner data – algorithms and applications. *ISPRS J. Photogramm. Remote Sens.* 54 (2–3), 138–147.
- Buften, J.L., 1989. Laser altimetry measurements from aircraft and spacecraft. *Proc. IEEE* 77 (3), 463–477.
- Church, E.L., 1988. Fractal surface finish. *Appl. Opt.* 27 (8), 1518–1526.
- Connor, L., Laxon, S., Ridout, A., Krabill, W., McAdoo, D., 2009. Comparison of Envisat radar and airborne laser altimeter measurements over Arctic sea ice. *Remote. Sens. Environ.* 113, 563–570.
- Davidson, M., Le Toan, T., Mattia, F., Manninen, T., Borgeaud, M., 2000. On the characterisation of agricultural random roughness for radar remote sensing studies. *IEEE Trans. Geosci. Remote Sens.* 38 (2), 630–640.
- Dong, W.P., Sullivan, P.J., Stout, K.J., 1992. Comprehensive study of parameters for characterizing three-dimensional surface topography I: some inherent properties of parameter variation. *Wear* 159, 161–171.
- Dong, W.P., Sullivan, P.J., Stout, K.J., 1993. Comprehensive study of parameters for characterizing three-dimensional surface topography II: statistical properties of parameter variation. *Wear* 167, 9–21.
- Dong, W.P., Sullivan, P.J., Stout, K.J., 1994a. Comprehensive study of parameters for characterizing three-dimensional surface topography III: parameters for characterising amplitude and some functional properties. *Wear* 178, 29–43.
- Dong, W.P., Sullivan, P.J., Stout, K.J., 1994b. Comprehensive study of parameters for characterizing three-dimensional surface topography IV: parameters for characterising spatial and hybrid properties. *Wear* 178, 45–60.
- Eitel, J.U.H., Williams, C.J., Vierling, L.A., Al-Hamdan, O.Z., Pierson, F.B., 2011. Suitability of terrestrial laser scanning for studying surface roughness effects on concentrated flow erosion processes in rangelands. *CATENA* 87 (3), 398–407.
- Elder, K., Cline, D., Liston, G., Armstrong, R., 2009. NASA Cold Land Processes Experiment (CLPX 2002/03): field measurements of snowpack properties and soil moisture. *J. Hydrometeorol.* 10, 320–329.
- Fassnacht, S.R., 2004. Estimating alter-shielded gauge snowfall undercatch, snowpack sublimation, and blowing snow transport at six sites in the coterminous United States. *Hydrol. Process.* 18 (18), 3481–3492.
- Fassnacht, S.R., 2010. Temporal changes in small scale snowpack surface roughness length for sublimation estimates in hydrological modelling. *Cuad. Invest. Geog.* 36 (1), 43–57.
- Fassnacht, S.R., Williams, M.W., Corrao, M.V., 2009a. Changes in the surface roughness of snow from millimetre to metre scales. *Ecol. Complex.* 6, 221–229.
- Fassnacht, S.R., Stednick, J.D., Deems, J.S., Corrao, M.V., 2009b. Metrics for assessing snow surface roughness from digital imagery. *Water Resour. Res.* 45.
- Fassnacht, S.R., Toro Velasco, M., Meiman, P.J., Whitt, Z.C., 2010. The effect of Aeolian deposition on the surface roughness of melting snow, Byers Peninsula, Antarctica. *Hydrol. Process.* 24 (14), 2007–2013.
- Flood, M., Gutelius, B., 1997. Commercial implications of topographic terrain mapping using scanning airborne laser radar. *Photogramm. Eng. Remote. Sens.* 63 (4), 327–329 (363–366).
- Garvin, J., Blair, J., Buften, J., Harding, D., 1996. The Shuttle Laser Altimeter (SLA-01) experiment: topographic remote sensing of planet Earth. *EOS Trans. Am. Geophys. Union* 77 (7) (239 pp.).
- Haala, N., Brenner, C., Anders, K.-H., 1998. 3D urban GIS from laser altimeter and 2D map data. *Int. Arch. Photogramm. Remote. Sens. Spat. Inf. Sci.* 32 (3/1), 339–346.
- Heritage, G., Milan, D., 2009. Terrestrial laser scanning of grain roughness in a gravel-bed river. *Geomorphology* 113, 4–11.
- Herzfeld, U.C., 2002. Vario functions of higher order – definition and application to characterization of snow surface roughness. *Comput. Geosci.* 28, 641–660.
- Höfle, B., Geist, T., Rutzinger, M., Pfeifer, N., 2007. Glacier surface segmentation using airborne laser scanning point cloud and intensity data. *Int. Arch. Photogramm. Remote. Sens. Spat. Inf. Sci.* 36 (3/W52), 195–200.
- Hollaus, M., Aubrecht, C., Höfle, B., Steinnocher, K., Wagner, W., 2011. Roughness mapping on various vertical scales based on full-waveform airborne laser scanning data. *Remote Sens.* 3, 503–523.
- Hood, J.L., Hayashi, M., 2010. Assessing the application of a laser range finder for determining snow depth in inaccessible alpine terrain. *Hydrol. Earth Syst. Sci. Discuss.* 7, 417–440.
- Hudson, S.R., 2011. Estimating the global radiative impact of the sea ice-albedo feedback in the Arctic. *J. Geophys. Res.* 116 (D16102) (7 pp.).
- Hyyppä, J., Kelle, O., Lehikoinen, M., Inkinen, M., 2001. A segmentation-based method to retrieve stem volume estimates from 3-D tree height models produced by laser scanners. *IEEE Trans. Geosci. Remote Sens.* 39 (5), 969–975.
- Hyyppä, J., Yu, X., Hyyppä, H., Vastaranta, M., Holopainen, M., Kukko, A., Kaartinen, H., Jaakkola, A., Vaaja, M., Koskinen, J., Alho, P., 2012. Advances in forest inventory using airborne laser scanning. *Remote Sens.* 4, 1190–1207.
- Jaakkola, A., Hyyppä, J., Hyyppä, H., Kukko, A., 2008. Retrieval algorithms for road surface modelling using laser-based mobile mapping. *Sensors* 8, 5238–5249.
- Kaartinen, H., Hyyppä, J., 2006. EuroSDR – project Commission III evaluation of building extraction. Final Report, EuroSDR – European Spatial Data Research, Official Publication, 50, pp. 9–77.
- Kaartinen, H., Hyyppä, J., Kukko, A., Jaakkola, A., Hyyppä, H., 2012. Benchmarking the performance of mobile laser scanning system using a permanent test field. *Sensors* 12, 12814–12835.
- Kaartinen, H., Hyyppä, J., Kukko, A., Lehtomäki, M., Jaakkola, A., Vosselman, G., Oude Elberink, S., Rutzinger, M., Pu, S., Vaaja, M., 2013. Mobile mapping – Road Environment Mapping using Mobile Laser Scanning. EuroSDR Official Publication, 62, pp. 49–95.
- Kaasalainen, S., Kaartinen, H., Kukko, A., 2008. Snow cover change detection with laser scanning range and brightness measurements. *EARSeL eProceedings*, 7, pp. 133–141.
- Kaasalainen, S., Kaartinen, H., Kukko, A., Anttila, K., Krooks, A., 2010. Brief communication: application of mobile laser scanning in snow cover profiling. *The Cryosphere* 5, 135–138.
- Karjalainen, T., 2010. Lumen pinnankarkeuden mittaaminen (Measuring the surface roughness of snow). *Metropolia*. (48 pp., in Finnish).
- Keller, J.M., Crownover, R.M., Chen, R.Y., 1987. Characteristics of natural scenes related to the fractal dimension. *IEEE Trans. Pattern Anal. Mach. Intell. PAMI-9* (1987), 621–627.
- Kraus, K., Pfeifer, N., 1998. Determination of terrain models in wooded areas with airborne laser scanning data. *ISPRS J. Photogramm. Remote Sens.* 53 (4), 193–203.
- Kukko, A., Andrei, C.-O., Salminen, V.-M., Kaartinen, H., Chen, Y., Rönnholm, P., Hyyppä, H., Hyyppä, J., Chen, R., Haggren, H., Kosonen, I., Čapek, K., 2007. Road environment mapping system of the Finnish Geodetic Institute – FGI ROAMER. *Int. Arch. Photogramm. Remote. Sens. Spat. Inf. Sci.* 36 (3/W52), 241–247.
- Kukko, A., Kaartinen, H., Hyyppä, J., Chen, Y., 2012. Multiplatform mobile laser scanning: usability and performance. *Sensors* 12 (9), 11712–11733.
- Lacroix, P., Legrésy, B., Langley, K., Hamran, S.E., Kohler, J., Roques, S., Rémy, F., Dechambre, M., 2008. Instruments and methods: in situ measurements of snow surface roughness using a laser profiler. *J. Glaciol.* 54 (187), 753–762.
- Lehning, M., Grünewald, T., Schirmer, M., 2011. Mountain snow distribution governed by an altitudinal gradient and terrain roughness. *Geophys. Res. Lett.* 38 (L19504):L19504(5).
- Lehtomäki, M., Jaakkola, A., Hyyppä, J., Kukko, A., Kaartinen, H., 2011. Performance analysis of a pole and tree trunk detection method for mobile laser scanning data. *Int. Arch. Photogramm. Remote. Sens. Spat. Inf. Sci.* 38 (5/W12).
- Lohr, U., Eibert, M., 1995. The TopoSys laser scanner-system. In: Fritsch, D., Hobbie, D. (Eds.), *Photogrammetrische Woche 1995*, pp. 263–267.
- Maas, H.-G., Vosselman, G., 1999. Two algorithms for extracting building models from raw laser altimetry data. *ISPRS J. Photogramm. Remote Sens.* 54 (2–3), 153–163.
- Manes, C., Guala, M., Löwe, H., Bartlett, S., Egli, L., Lehning, M., 2008. Statistical properties of fresh snow roughness. *Water Resour. Res.* 44, W11407.
- Manninen, A.T., 1997a. Surface roughness of Baltic sea ice. *J. Geophys. Res. Oceans* 102 (C1), 1119–1139.
- Manninen, A.T., 1997b. Multiscale surface roughness and backscattering. *Prog. Electromagn. Res.* 16, 175–203.
- Manninen, A.T., 2003. Multiscale surface roughness description for scattering modeling of bare soil. *Physica A* 319, 535–551.
- Manninen, T., Rantasuo, M., Le Toan, T., Davidson, M., Mattia, F., Borgeaud, M., 1998. Multiscale surface roughness of bare soil. *Proceedings of the IGARSS'98, Seattle, 6–10 July 1998*, pp. 1203–1206.
- Manninen, T., Anttila, K., Karjalainen, T., Lahtinen, P., 2012. Automatic snow surface roughness estimation using digital photos. *J. Glaciol.* 58 (211), 993–1007.
- Mialon, A., Fily, M., Royer, A., 2005. Seasonal snow cover extent from microwave remote sensing data: comparison with existing ground and satellite based measurements. *EARSeL eProceeding*, 4, pp. 215–225 ([http://www.eurocedings.org/static/vol04\\_2/04\\_2\\_mialon1.pdf](http://www.eurocedings.org/static/vol04_2/04_2_mialon1.pdf)).
- Naesset, E., 1997. Determination of mean tree height of forest stands using airborne laser scanner data. *ISPRS J. Photogramm. Remote Sens.* 52 (2), 49–56.
- Prokop, A., 2008. Assessing the applicability of terrestrial laser scanning for spatial snow depth measurements. *Cold Reg. Sci. Technol.* 54, 155–163.
- Prokop, A., Schirmer, M., Rub, M., Lehning, M., Stocker, M., 2008. A comparison of measurement methods: terrestrial laser scanning, tachymetry and snow probing for the determination of the spatial snow-depth distribution on slopes. *Ann. Glaciol.* 49, 210–216.
- Rees, W.G., 1998. A rapid method for measuring snow surface profiles. *J. Glaciol.* 44 (148), 674–675 (Correspondence).
- Rees, W.G., Arnold, N.S., 2006. Scale-dependent roughness of a glacier surface: implications for radar backscatter and aerodynamic roughness modelling. *J. Glaciol.* 52, 214–222.
- Roujean, J.-L., Manninen, T., Sukuvaara, T., Peltoniemi, J., Kaasalainen, S., Hauteceour, O., Lahtinen, P., Riihelä, A., Siljamo, N., Lötjönen, M., Karjalainen, T., Kontu, A., Suokanerva, H., Aulamo, O., Lemmetyinen, J., Suomalainen, J., Hakala, T., Kaartinen, H., Thölix, L., Meinander, O., Karhu, J., 2010. SNORTEX: remote sensing measurement of snowmelt in European boreal forest. *iLEAPS Newsletter*, 9, pp. 56–58.
- Rutzinger, M., Pratihast, A.K., Oude Elberink, S.J., Vosselman, G., 2011. Tree modelling from mobile laser scanning data-sets. *Photogramm. Rec.* 26, 361–372.
- Schaffhauser, A., Adams, M., Fromm, R., Jörg, P., Luzi, G., Noferini, L., Sailer, R., 2008. Remote sensing based retrieval of snow cover properties. *Cold Reg. Sci. Technol.* 54, 164–175.
- Schirmer, M., Lehning, M., 2011. Persistence in intra-annual snow depth distribution: 2. Fractal analysis of snow depth development. *Water Resour. Res.* 47 (W09517:1–W09517:14).
- Schirmer, M., Wirz, V., Clifton, A., Lehning, M., 2011. Persistence in intra-annual snow depth distribution: 1. Measurements and topographic control. *Water Resour. Res.* 47 (W09516:1–W09516:16).
- Trujillo, E., Ramirez, J.A., Elder, K., 2007. Topographic, meteorological, and canopy controls on the scaling characteristics of the spatial distribution of snow depth fields. *Water Resour. Res.* 43, W07409.

- Van der Veen, C.J., Ahn, Y., Csatho, M., Mosley-Thompson, E., Krabill, W.B., 2009. Surface roughness over the northern half of the Greenland ice sheet from airborne laser altimetry. *J. Geophys. Res.* 114, 1–8.
- Várnai, T., Cahalan, R.F., 2007. Potential for airborne offbeam lidar measurements of snow and ice thickness. *J. Geophys. Res.* 12 (C12S90) (11 pp.).
- Warren, S.G., 1982. Optical properties of snow. *Rev. Geophys.* 20 (1), 67–89.
- Warren, S.G., Wiscombe, W.J., 1980. A model for the spectral albedo of snow. II: snow containing atmospheric aerosols. *J. Atmos. Sci.* 37 (12), 2734–2745.
- Warren, S.G., Brandt, R.E., O’Rawe Hinton, P., 1998. Effect of surface roughness on bidirectional reflectance of Antarctic snow. *J. Geophys. Res.* 103 (E11), 25789–25807.
- Warren, S.G., Brandt, R.E., Grenfell, T.C., 2006. Visible and near-ultraviolet absorption spectrum of ice from transmission of solar radiation into snow. *Appl. Opt.* 45 (21), 5320–5334.
- Weligepolage, K., Gieske, A.S.M., Su, Z., 2012. Surface roughness analysis of a conifer forest canopy with airborne and terrestrial laser scanning techniques. *International journal of applied earth observation and geoinformation: JAG*, 14, pp. 192–203 (1).
- Williams, L.D., Gallagher, J.G., 1987. The relation of millimeter-wavelength backscatter to surface snow properties. *IEEE Trans. Geosci. Remote Sens.* GE-25 (2), 188–193.
- Zhu, L., Hyypää, J., Kukko, A., Kaartinen, H., Chen, R., 2011. Photorealistic building reconstruction from mobile laser scanning data. *Remote Sens.* 3, 1406–1426.
- Zhuravleva, T.B., Kokhanovsky, A.A., 2011. Influence of surface roughness on the reflective properties of snow. *J. Quant. Spectrosc. Radiat. Transf.* 112, 1353–1368.



## PAPER IV

Reprinted from the Cold Regions Science and Technology  
with permission of Elsevier  
© Elsevier







## Calibrating laser scanner data from snow surfaces: Correction of intensity effects



K. Anttila <sup>a,b,\*</sup>, T. Hakala <sup>a,1</sup>, S. Kaasalainen <sup>a,1</sup>, H. Kaartinen <sup>a,1</sup>, O. Nevalainen <sup>a,1</sup>, A. Krooks <sup>a,1</sup>, A. Kukko <sup>a,1</sup>, A. Jaakkola <sup>a,1</sup>

<sup>a</sup> Finnish Geospatial Research Institute FGI, Masala, Finland

<sup>b</sup> Finnish Meteorological Institute, Helsinki, Finland

### ARTICLE INFO

#### Article history:

Received 4 June 2015

Received in revised form 10 September 2015

Accepted 12 October 2015

Available online 27 October 2015

#### Keywords:

Terrestrial laser scanning

Intensity

Incidence angle

Snow

### ABSTRACT

Terrestrial laser scanning data have become more and more commonly used in cryospheric studies as the commercial instruments are getting cheaper and more user-friendly. We have studied the usability of laser scanning intensity data in remote sensing of snow-covered surfaces by focusing on two topics: the effect of incidence angle on the intensity data and the depth which the backscattered laser beam represents. The measurements were made with a phase-based laser scanner using 650–690 nm wavelength. For some of the snow backscatter vs. depth studies measurements were also made with a pulse-based scanner at 905 nm. The incidence angle effect was studied by rotating a snow surface sample relative to the scanner and measuring the difference in the intensity values. The experiment was repeated for different snow types. The snow pack layer that the backscattered laser signal represents was studied by inserting black metal plates horizontally into the snow pack and measuring the changes in the intensity values with plates at different depths. The results suggest that the snow type has no effect on the incidence angle effect and that for dry snow the backscattering of the laser beam takes place from the very surface, but for wet snow, the majority of the signal is backscattered from 0.5 to 1 cm depth. An empirical correction function for the incidence angle effect is also presented.

© 2015 Elsevier B.V. All rights reserved.

### 1. Introduction

As the climate is changing rapidly, it is crucial to understand the processes that affect the climate systems. The behavior of snow and ice cover in the changing climate is still fairly poorly known and that introduces considerable uncertainty to the climate models. Better understanding is required on the links between snow geophysical and scattering properties, changing snow and ice-covered area, timing of snow melt, and the surface albedo, which is an essential climate variable (ECV) defined in the Implementation Plan for the Global Observing System for Climate in Support of the United Nations Framework Convention on Climate Change (UNFCCC) (<http://unfccc.int/2860.php>). Tilt effects are also crucial because they affect the measurement of snow and glacier albedo. Therefore, knowing the effect of incidence angle of the incoming radiation to the snow/ice surface is important in these applications. The measurement geometry effects and their correction have been recently studied by Sicart et al. (2001) and Weiser et al. (2015). The improvement of the global climate models requires data

sets that cover large areas. In practice, this means satellite products. The validation of these products would benefit from in situ data that covers large areas. However, these data are typically not available. Terrestrial laser scanning (TLS) and mobile laser scanning show great potential for gathering the data for validation as well as for analysis (e.g., Egli et al., 2012; Kenner et al., 2011; Kukko et al., 2013).

Terrestrial laser scanning applications on snow surfaces have concentrated on the use of range data (Arnold et al., 2006; Helfricht et al., 2014; Hood and Hayashi, 2010; Prokop, 2008; Prokop et al., 2008; Várnai and Cahalan, 2007). It has proven to be a useful method for mapping inaccessible and dangerous areas, such as potential avalanche sites (for example, Schaffhauser et al., 2008). Some first attempts have been made to use the airborne laser scanning intensity for glacier surfaces (Höfle et al., 2007; Lutz et al., 2003), but the TLS intensity data have, to the best of our knowledge, not yet been widely applied for snow-covered surfaces. The laser reflection and multiple scattering in the snow layer also plays an important role in the usability of TLS range data from snow surfaces. Prokop (2008) found limitations in the application of TLS range measurements for operational avalanche forecasting: if the snow surface was wet and the snow grain size was large (N1 mm), only 50% of the emitted laser signal was received, depending on the angle of incidence. To improve the applicability of TLS data, more accurate knowledge on the incidence angle effect is important. It is also important to know how much the diffuse reflection of laser entering

\* Corresponding author at: Finnish Geospatial Research Institute FGI, Masala, Finland.  
E-mail address: [kati.anttila@fgi.fi](mailto:kati.anttila@fgi.fi) (K. Anttila).

<sup>1</sup> Former Finnish Geodetic Institute.

the snowpack contributes to the backscattered signal being detected (cf. Kaasalainen et al., 2006). This is particularly important in mobile laser scanner applications, which typically span a larger area than stationary TLS, resulting in a great variety of incidence angles and point densities, which, in turn, affect the accuracy of results.

Calibrated laser scanner intensity data can be used in segmentation and classification of the range data (Höfle et al., 2007; Yan et al., 2012). Radiometric calibration systems have been developed to enhance the comparability of different scans (Ahokas et al., 2006; Coren and Sterzai, 2006; Höfle et al., 2007; Kaasalainen et al., 2009; Wagner et al., 2006). In our previous studies on the applicability of laser scanning on snow surface mapping (Anttila et al., 2011; Kukko et al., 2013), we have found some challenges related to the measurement and calibration of TLS data: one of these is the considerable effect the incidence angle has on the intensity data (e.g., Anttila et al., 2011). We have found that the object backscattering properties affect the incidence angle effect (Kaasalainen et al., 2011; Krooks et al., 2013). The backscattering properties of snow depend on the grain size and shape (Kaasalainen et al., 2006) and the surface structure (Zhuravleva and Kokhanovsky, 2011). However, our previous studies have suggested that the snow type may have no effect on the incidence angle effect (Anttila et al., 2011). In this paper, we address this issue by studying the mean intensity value of several different snow surfaces in different incidence angles.

To relate the snow intensity parameters to grain properties, it is important to know how much the laser signal penetrates into the snowpack, and, most importantly, which part of the snow layer the backscattered signal represents. Prokop (2008) has studied this using the range data by placing reflective foils and blankets on the snow and comparing the range data of the different surfaces. He found that there was a less than 1 cm difference in the surface height values. We have studied the same topic using the intensity values. We placed matt black painted metal plates horizontally in the snow pack at different depths and measured the changes in the intensity value. We repeated the measurements with different snow types.

The studies presented in this paper are made on taiga snow in the boreal forest zone. After the introduction, in Section 2, we present the methodologies used for both the experiments. In Section 3, we present the results, and in Section 4, we discuss the results in more detail.

## 2. Methods

The measurements used in this study were made in Kirkkonummi, Southern Finland (60.1°N, 24.5°E). The snow in Southern Finland is typical taiga snow with ice lenses and various layers of different density and crystal type (Sturm et al., 1995). The relevant geophysical properties of each measured snowpack, including crystal types and sizes, layer structure of the snow pack and surface roughness, were documented during the measurements. In addition to these, overall weather conditions, such as air temperature, were monitored for the periods of measuring. The relevant weather and snow properties are introduced along the measurements.

The laser scanning measurements of this study were made with Leica HDS6100, which uses 650–690 nm wavelengths. The beam diameter at exit is 3 mm, and the beam divergence is 0.22 mrad. The range measurements are based on phase detection. The wavelength dependency of the incidence angle effect was studied using measurements made with Hyperspectral Lidar (HSL) developed at the FGI (see Hakala et al., 2012, for more details on the HSL). For snow backscatter vs. depth measurements, data obtained with a Sick LMS151 laser scanner have also been included to compare the results from a phase-based scanner to those with a pulsed one. The Sick scanner is a pulsed 905 nm scanner with an 8 mm beam exit diameter and 15 mrad beam divergence. Therefore, the laser spot diameter on the sample surface can be considered much larger than that of Leica HDS6100.

The intensity detector of the LeicaHDS6100 scanner used here has been found to be linear and follow the  $R^2$  dependence ( $R$  being the range) of the radar range equation (Wagner et al., 2006) at distances greater than 10 m (Kaasalainen et al., 2011):

$$P_r = \frac{P_t D_r^2}{4\pi R^4 \beta_t^2} \sigma \quad (1)$$

where  $P_r$  is the received power,  $P_t$  is the transmitted power,  $D_r$  is the receiver aperture,  $R$  is the range, and  $\beta_t$  is the transmitter beam width.  $\sigma$  is the backscatter cross section, which is related to target reflectivity and the measurement geometry. In this study, all parameters, including the range  $R$ , remained constant, except for  $\sigma$  which depends on the incidence angle (cf. Kaasalainen et al., 2011; Shaker et al., 2011).

According to Höfle and Pfeifer (2007), the  $\sigma$  depends on the incidence angle as follows:

$$\sigma = \pi \rho R^2 \beta_t^2 \cos \alpha \quad (2)$$

where  $\rho$  is the target reflectance,  $R$  is the range,  $\beta_t$  is the laser beam width and  $\alpha$  is the incidence angle. Placing plates in the snowpack affected the surface reflectivity, which is also contained in the cross section parameter  $\sigma$  (Wagner et al., 2006).

### 2.1. Incidence angle

To measure the incidence angle effect a sample of the snow pack was carefully cut from the snow pack without destroying the surface structure (see Fig. 1). The sample was cut by using a thin plastic box, where it was kept during the measurements. The surfaces of the snow samples were approximately 20 cm × 20 cm, and the snow sample was approximately 6–8 cm thick. The surface of the snow sample was scanned several times with each scan having the box (and the snow sample) in a different angle relative to the scanner. Similar measurements were made in different days having different snow types. Images of the surface crystals together with weather information for each day can be seen in Table 1. The crystals have been classified according to Fierz et al. (2009). The different snow types cover fresh dendritic snow, needles, metamorphosed snow, fresh wet snow, and old wet snow.

The incidence angle relative to the snow surface was controlled by rotating the snow sample with an URB100CC rotation stage (Newport, Irvine, CA) (see Fig. 1). The rotation stage was mounted to an aluminum frame along with a mirror. The laser beam was reflected to the sample surface by the mirror. The distance between the laser source, and the sample (via mirror) was about 5 m. The use of a mirror allowed the rotator to turn the sample to greater angles of incidence, and still hold the sample upright enough for the surface to remain intact. During the data analysis, a plane was fitted to the data sets to calculate the incidence angle more accurately.

To investigate the wavelength dependence of the incidence angle effect, multi-wavelength measurements with HSL were carried out in February 21, 2012, using a setup similar to the monochromatic TLS measurements. The backscattered intensity of the continuous light source was recorded at eight wavelength channels (554.8 nm, 623.5 nm, 691.1 nm, 725.5 nm, 760.3 nm, 795.0 nm, 899.0 nm, and 1000.4 nm) for a wet, melting snow sample (see Table 1 for more details on the measurement conditions).

To ensure the stability of the measurement setting a four-step Spectralon® (Labsphere Inc.) reflectance target of 12%, 25%, 50%, and 99%, reflectance was placed in each scan near the snow sample. The 99% backscattering panel values for each scan were compared to ensure the comparability of the different scans. The stability of the snow sample during the measurements was controlled in several ways. Air temperature was measured during the whole set of measurements near the sample to make sure that the changing temperature did not cause too

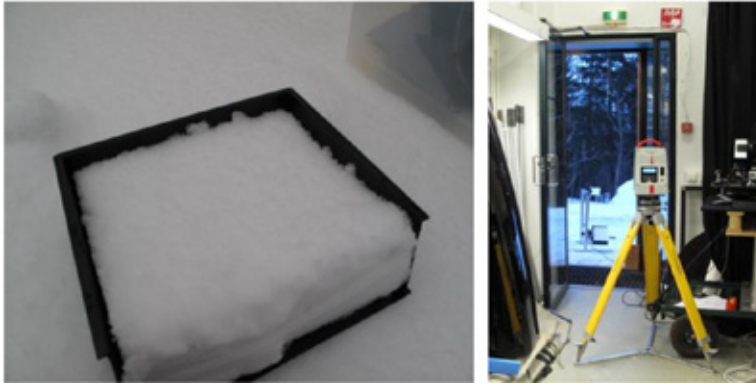


**Fig. 1.** The set up for the incidence angle measurements. Left: The snow sample of natural snow was cut into a plastic container without destroying the surface. Right: During the measurements, the laser scanner was inside the laboratory and the snow sample was outside the laboratory in a rotating tray. The snow sample was scanned through the doorway. A closer look of the rotation stage can be seen in Fig. 2.

much metamorphosis during the measurements. Also, the surface of the snow sample was monitored between the scans and while the sample was turned to make sure that the turning did not cause damage on the sample. Using the mirror enabled the measurement at small incidence angles (i.e., around normal incidence) without tilting the scanner.

**Table 1**

Weather and snow conditions of each incidence angle effect measurement day. The scale in the images of the snow surface crystals is in centimeters.

4.2.2013 Snow depth (cm): 18 Air temperature: 0 °C Surface crystals: DFdc, broken dendrites and needles, fresh fallen snow	
14.2.2013 Snow depth (cm): 41 Air temperature: 0 °C Surface crystals: DFdc, needles and decomposed dendrites, that have partly melted and then refrozen	
21.2.2013 Snow depth (cm): 37 Air temperature: 0 °C Surface crystals: DFdc, old broken crystals that have been clustered but are not yet very rounded	
4.3.2013 Snow depth (cm): 30.5 Air temperature: -5.5 °C Surface crystals: DFdc, needles and broken dendrites	
19.3.2013 Snow depth (cm): 33.5 Air temperature: -6 °C Surface crystals: DFbk/PPsd, fresh fluffy layer of dendrites	

Because the snow sample was visible in each scan both directly and via mirror (Fig. 2), the stability of the snow sample could be verified during the series of scans by comparing measurements at the same incidence angle in the end and beginning of the measurements. The analysis is made on snow samples measured via mirror.

The data were analyzed by extracting the snow sample surface from the point cloud data and calculating the mean and median values of the intensities for each scan. The exact incidence angle of the surface was determined by fitting a plane to the extracted sample. The number of points covering the sample depended on the tilt angle of the sample. To find out how the decreased number of points affected the accuracy of the results, the distributions of the sample intensities were calculated for each scan of each snow type.

## 2.2. Depth of the observed backscatter signal

The depth from which the backscattering is observed by the detector was studied by placing black plates horizontally into the snow pack to different depths and measuring the change in mean intensity of the laser backscatter of the snow surface above the plate (see Fig. 3). The plates were made of aluminum and steel and spray painted black. The sizes of the plates varied from 50 cm × 25 cm to 15 cm × 10 cm. The bigger plates cover a larger area and were used deeper in the snowpack. The smaller plates were easier to place horizontally in the snow and thus more accurate with the depth. These were used closer to the surface.

The first scan of the measured area was made without any plates. After this, the same area was scanned having the plate at the lowest position (down to 20 cm depth) in the snow pack, working the way up so that each plate depth was scanned separately and the plates lower in the snow were left in the snowpack to avoid unnecessary breaking of the snow pack (see Fig. 3 for the placing of the plates). For the first set of measurements, the lowest level of the metal plate (relative to the snow surface) was at 20 cm. Since there was no change in the backscattering intensity, the next measurements were started at higher level, typically 8 or 9 cm. For the highest 5 cm, the measurements were repeated every 1 cm, and near the surface, also 0.5 cm depth was measured if possible. For some measurements, this was too shallow for the snow to keep its structure.

This set of measurements was repeated several times to cover different snow types present at different days. Table 2 shows the different sets of measurements with weather and snow geophysical information. The different measurements covered snow types from fresh loose powder snow to old wet slushy snow. Images of the different snow surface



Fig. 2. Intensity image showing the snow sample directly (B) and indirectly through the mirror (A).

crystals are also shown in Table 2. The different snow types of the measurement sets have been classified to dry and wet snow.

Every set of measurements destroyed the snow surface. Therefore, the measurement site changed from day to day. When the scanner was placed less than 4 m from the snow surface, there was a risk that the amplitude of the incoming pulses was too high and the intensity values were saturated. Therefore, some of the measurements were made from higher altitudes of the scanner, e.g., from a roof of a building. The locations of the scanners are shown in Table 2. The typical sample sizes were approximately 10x10 cm.

3. Results

3.1. Incidence angle

The mean normalized intensities as a function of incidence angle for different samples are shown in Fig. 4. The incidence angle dependency of intensity seems to be similar for all the measured snow types. The error bars in Fig. 4 present the standard deviation of the intensity values.

Table 2

Snow samples of the backscatter depth measurements: weather and snow conditions of each day. The scales in the crystal images are in cm.

26.1.2012 Scanner position: next to the snow, see Figure 3 Snow depth (cm): 34 Air temperature: -5 °C Surface crystals:DFbk/PPsd, dendrites and broken dendrites	
16.2.2012 Scanner position: from a window on a higher floor Snow depth (cm): 32 Air temperature: -2.5 °C Surface crystals: DFBk, dendrites and broken dendrites	
13.3.2012 Scanner position: from a roof Snow depth (cm): 30 Air temperature: +5 °C, half cloudy Surface crystals: RGl, MFcl, large rounded clustered crystals, very wet	
7.2.2013 Scanner position: from a roof Snow depth (cm): 25 Air temperature: 0 °C Surface crystals: DFbk, wet but fresh, sticky dendrites and broken dendrites	
14.2.2013 Scanner position: from a window on a higher floor Snow depth (cm): 75 Air temperature: 0 °C, cloudy Surface crystals:MFcl, wet rounded clusters, some evidence of earlier freezing with sharp edges	

The errors grow together with the incidence angle. This is likely to be caused by the smaller sample sizes of the larger incidence angles. However, the intensity values were approximately normally distributed with typically positive skewness for all the angles. Two examples of distributions can be seen in Fig. 5. The highest intensity values of the



Fig. 3. Left: The snow surface was scanned from above. Right: Metal plates were placed in the snow pack and a Spectralon reflectance panel was placed in the area of the scan.



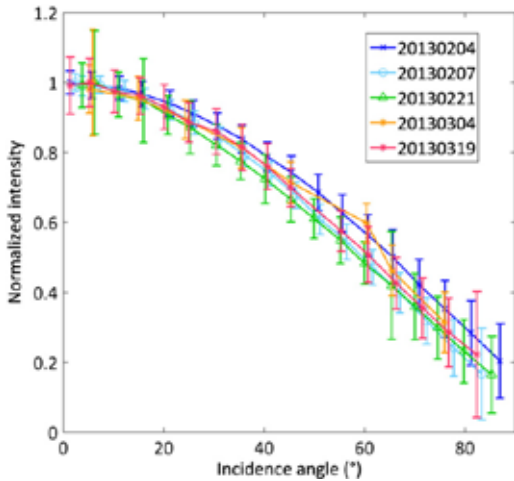


Fig. 4. The mean backscattering intensity of the snow samples measured via mirror and normalized using the maximum value. The error bars show the standard deviation of the snow samples. The results of each set of measurements have been normalized to the maximum intensity value of that set.

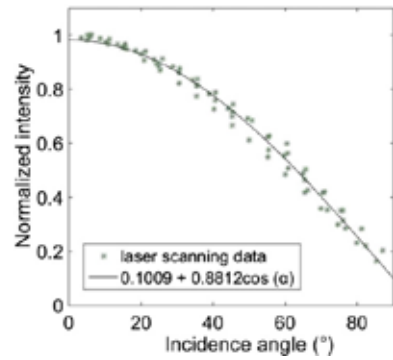


Fig. 6. The mean normalized intensities of the snow samples of all snow types and incidence angles and the fitted cosine function.

sample could be considered outliers. They come from specular reflections of individual crystals. If the crystals are smaller than the spot size of the laser beam, then their effect can be seen also in the value of the surrounding points. Since the intensity values are approximately normally distributed, the mean value represents the sample well even though the deviation is high. The median values were also used in the study, but they did not differ considerably from the mean values, as could be expected if the distributions are approximately normal.

A first-order cosine function for the incidence angle  $\alpha$  (see Eq. (2)) was fitted to the incidence angle data. Due to the measurement setting, the other variables in Eq. (2) ( $\rho, R, \beta$ ) are fixed. Fig. 6 shows the intensity data together with the fitted function.

The fitting of the first-order cosine function gives an empirical correction

$$0.1009 + 0.8812(\cos\alpha)$$

The  $R^2$  for this fitting was 0.9884. This is such a high value that no fitting for higher-order functions was found necessary. A more precise fitting needs to be done when a larger data set including samples of wet snow is available.

The incidence angle dependency at different wavelengths measured with the HSL can be seen in Fig. 7. The dependency appears similar at all the wavelengths measured. We found some discrepancy between Leica and HSL measurements, which is most likely caused by uncertainty in the measurement of the incidence angle in the HSL measurements because of the small number of points in the sample. The difference between the Leica and HSL measurements varied between different HSL experiments, but the incidence angle behavior was similar for all HSL

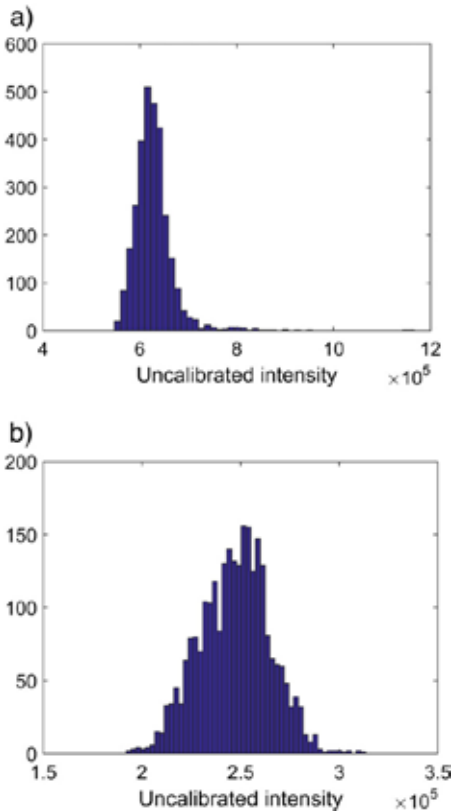


Fig. 5. The distribution of intensity values of the snow sample measured (a) 21 February 2013 in 10.9° angle and (b) 4 March 2013 in 65.5° angle.

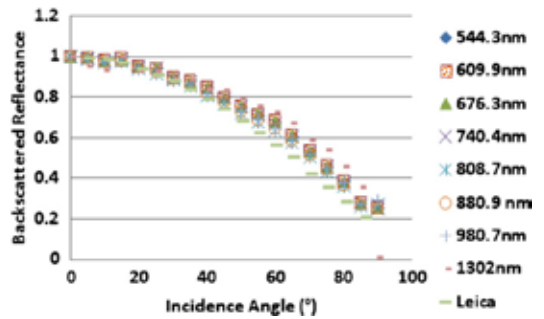


Fig. 7. The mean backscattering intensity of the snow sample measured with the hyperspectral lidar on 21 February 2012 and Leica HDS6100 (wavelength 676.3 nm) on 4 February 2013. The data have been normalized to 1 at 0° incidence angle.

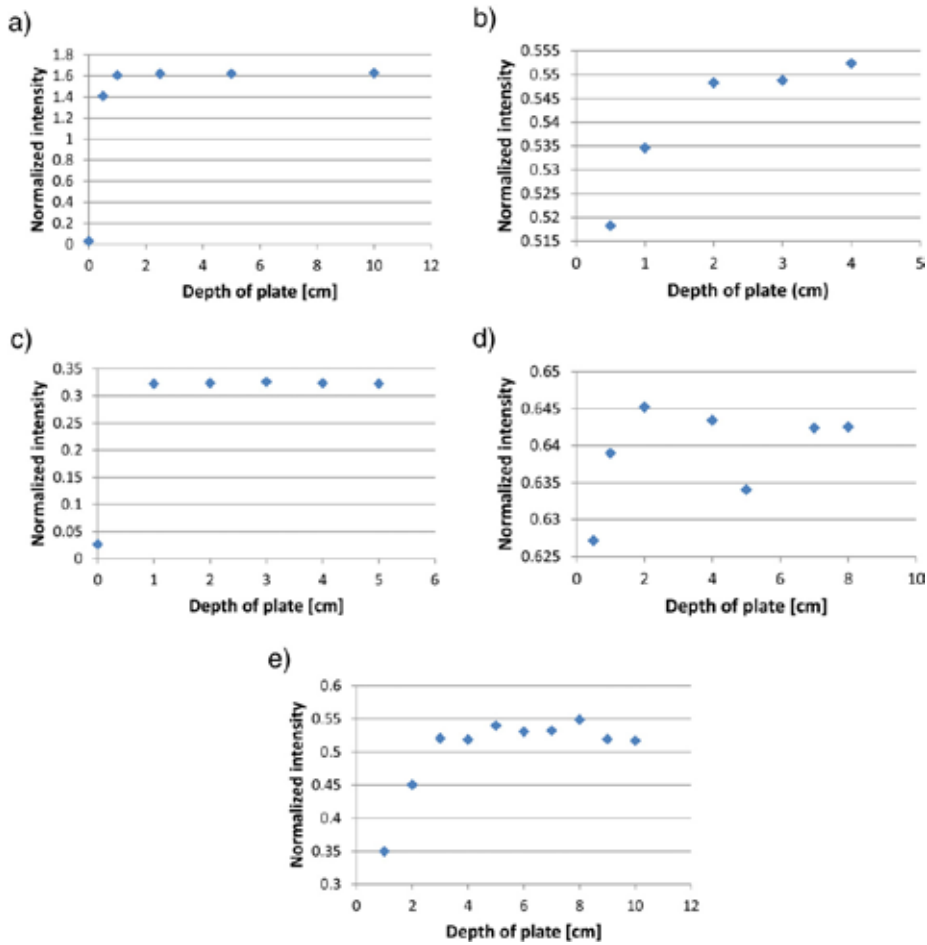


Fig. 8. The normalized intensities of the snow surfaces measured with Leica HDS6100. The depths of the plates are shown in the horizontal axes. The measured dates are (a) 26.1.2012: dry dendrites, (b) 16.2.2012: dry dendrites, (c) 13.3.2012: wet rounded and clustered, (d) 7.2.2013: wet fresh dendrites, and (e) 14.2.2013: wet rounded clusters.

wavelengths in each experiment. Therefore, these results are preliminary and the spectral dependence of the incidence angle data should be studied in more detail in the future. Particularly, more snow types should be included in the HSL study.

### 3.2. Depth of the observed backscatter signal

The mean normalized intensity values for measurements of different snow types with plates at different depths are shown in Fig. 8 for Leica and Fig. 9 for the SICK scanner. The values are normalized using the mean intensity value of a Spectralon plate with 99% backscattering. The Spectralon was kept at the same location relative to the scanner and snow samples for each scan of the same snow. However, since the different snow data sets were scanned at different locations, the range and incidence angle of the Spectralon plate relative to the scanner and snow samples is different between different data sets. Therefore, the normalized intensity values are comparable within a snow data set, but not between the measurements of different days. This, however, does not affect the results, i.e., the depth from which the laser signal is being observed.

It seems that for dry snow the backscattering takes place at the very surface of the snow, i.e., there was no change in the intensity

values at depths > 1 cm. This result is similar to that obtained with the Sick scanner (Fig. 9), for which the laser spot size is much larger than that for the Leica scanner (approximately 5 mm at 5 m distance for Leica). For wet snow, the black metal plate starts to affect the backscattering intensity already at 0.5 to 1 cm. This indicates that the majority of the backscattered signal observed by the scanner detector comes from approximately this depth. The intensity values of

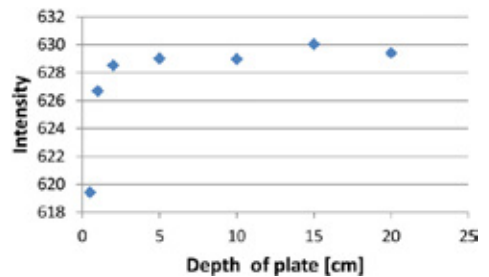


Fig. 9. Intensity data at different plate depths for SICK LMS151 measurements. The measured snow surface was dry and the crystals were dendrites.

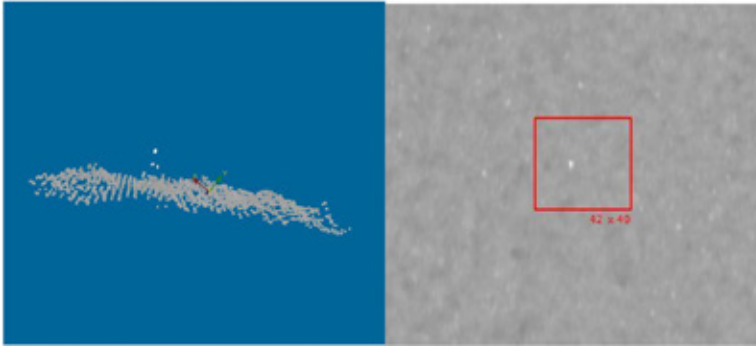


Fig. 10. An intensity image of a point cloud where the specular reflection has caused error in the range measurement (measurements from 8 February 2013).

the measurements of the same snow surface with no plates in the snow were similar to the intensities measured with the plate at the deepest position. This confirms that the lowest position of the plate was deep enough not to affect the intensity value. Since the natural snow surface is not a featureless plane, the depths of the plates should be considered approximate.

#### 4. Discussion

##### 4.1. Incidence angle effect

The results suggest that the incidence angle effect is similar for most snow types and wavelengths measured here and therefore the same correction function could be used. The incidence angle effect measurements with LeicaHDS6100 also included a sample of wet snow. There were some problems with errors in the intensity values between scans with this sample. We could not find an obvious reason for this, so the data were excluded from the analysis. However, it is noteworthy that despite this, when the results were plotted, they followed the same behavior for incidence angle effect than the rest of the snow types. This is in agreement with our previous experiments on the incidence angle effect from different types of snow, including wet and melting snow (Anttila et al., 2011). Further studies are needed to confirm the results, especially for wet snow, but the preliminary results suggest that the incidence angle effect might be possible to correct with a similar correction function for most snow types. This would simplify the calibration of TLS snow intensity data. What is also further needed is data for snow with impurities.

##### 4.2. Depth of the observed backscatter signal

The results indicate that the backscattering takes place mostly at the surface (i.e., at < 1 cm) for dry snow, but for wet snow the laser beam scatters back from up to 1–2 cm depth. This is in accordance with an observation that wet snow appears more transparent in the first place because of the liquid water contained in the snowpack. The rounded wet snow lacks facets that would scatter the laser beam. Large rounded snow grains have been observed earlier to have weaker laser backscatter than smaller ones (Kaasalainen et al., 2006), and the laser scanner intensity from melting snow has been found to decrease (Anttila et al., 2011).

Knowing the depth the backscattered signal represents is also important for snow depth measurements: our results for dry snow are similar to those by Prokop (2008), who found no significant penetration of the laser signal into the snowpack in range measurements, or at least the observed reflection represented the depth of < 1 cm.

##### 4.3. Other issues

The deviation of the backscattering intensity values is considerably large for snow surfaces. This is due to the fine scale surface roughness, that is, crystals that are positioned in very different angles with respect to the laser beam. The effect of the large deviation on the mean value of the measured sample is best reduced by increasing the sample size. It has been shown in other studies that if the sample size is large enough, then the mean value is still representative of the value being measured (Kaasalainen and Viikinkoski, 2012). Since the deviation, that is, the existence of considerably bright or dark points, is directly linked to the crystal type on the surface and the surface roughness, it could potentially offer a means to classify the different snow type.

Specular reflections from individual ice crystals are typical for snow surfaces. These extremely bright points cause error in the range measurements. Fig. 10 shows a sample of point cloud looked from the side (on the left). It shows a clear peak in the data, when in fact there was no such peak in the measured surface. On the right, there is an intensity image of the same surface, with the sample on the left image marked with red. There is a very bright point in the middle of the sample causing the peak in the left side image. Since the foot print of the laser beam is larger than the crystal size, the specular reflection also affect all the points that are less than half of the diameter of the footprint away from the specularly reflecting crystal. This is an issue that needs to be addressed while using laser scanning data on snow-covered surfaces. It does not make the data unusable but it will need to be taken into account in the analysis.

More snow types should be studied in the future, since, e.g., the alpine snow and snow on glaciers and ice sheets is considerably different in geophysical properties. Measuring wet snow proved to have challenges in both experiments. We plan to study further the experimentation and the scattering properties of wet snow in the future.

#### 5. Conclusions

The results presented here indicate that

- The incidence angle dependence of laser scanner intensity is similar for different snow types. This indicates a prospect of correcting the incidence angle effect with a single function for many types of snow. We also experimented an empirical form  $\cos \alpha$  of a correction function and found it to be practical in this case.
- The incidence angle dependence of laser scanning intensity appears similar for all wavelengths between 500 and 1000 nm. More measurements are needed to confirm these results, especially at near-infrared wavelengths.

- The backscattering of the laser beam comes from the maximum of 1 cm depth in the snowpack. This confirms that the laser scanner signal essentially observes the snow surface, even though the incident laser light would penetrate deeper in the snowpack.
- The melting of snow affects the measurements and needs to be taken into account while analyzing the data.

Terrestrial laser scanning has been found to be a promising tool for efficient monitoring of snow and ice surfaces, especially in hazardous and inaccessible areas, e.g., steep terrain (Kenner et al., 2011; Prokop et al., 2008). TLS will provide a quantitative spatial and temporal characterization of important features and effects, such as glacier melt, permafrost, snow depth distribution, or avalanche prediction, but more research on optimized accuracy and calibration are still needed to make the TLS instruments fully operational in these conditions. Including TLS intensity data into the analysis will improve the optimal use of range data and provide further information on the surface properties. Therefore, the findings in this study will contribute for improving the applicability and accuracy of TLS data in snow cover detection.

### Acknowledgments

This research was funded by the Academy of Finland research projects “New Techniques in Active Remote Sensing: Hyperspectral Laser in Environmental Change Detection” and “Mobile Hyperspectral Laser Remote Sensing” (grant numbers 218144 and 137925). The authors would like to thank Matti Lehtomäki from FGI and Terhikki Manninen from the Finnish Meteorological Institute for all their help and support during the measurements and writing the paper.

### References

- Ahokas, E., Kaasalainen, S., Hyypää, J., Suomalainen, J., 2006. Calibration of the Optech ALTM 3100 laser scanner intensity data using brightness targets. *Int. Arch. Photogramm. Remote. Sens. Spat. Inf. Sci.* 34, 3–6.
- Anttila, K., Kaasalainen, S., Krooks, A., Kaartinen, H., Kukko, A., Manninen, T., Lahtinen, P., Siljamo, N., 2011. Radiometric calibration of TLS intensity: application to snow cover change detection. *Int. Arch. Photogramm. Remote. Sens. Spat. Inf. Sci.* 38 (5 / W12).
- Arnold, N.S., Rees, W.G., Devereux, B.J., Amable, G.S., 2006. Evaluating the potential of high-resolution airborne LiDAR data in glaciology. *Int. J. Remote Sens.* 27 (6), 1233–1251.
- Coren, F., Sterzal, P., 2006. Radiometric correction in laser scanning. *Int. J. Remote Sens.* 27, 3097–3104.
- Egli, L., Jonas, T., Grünwald, T., Schirmer, M., Burlando, P., 2012. Dynamics of snow ablation in a small Alpine catchment observed by repeated terrestrial laser scans. *Hydrol. Process.* 26 (10), 1574–1585.
- Fierz, C., Armstrong, R.L., Durand, Y., Etchevers, P., Greene, E., McClung, D.M., Nishimura, K., Satyawali, P.K., Sokratov, S.A., 2009. The International Classification for Seasonal Snow on the Ground. IHP-VII Technical Documents in Hydrology N°83, IACS Contribution N°1. UNESCO-IHP, Paris.
- Hakala, T., Suomalainen, J., Kaasalainen, S., Chen, Y., 2012. Full waveform hyperspectral LiDAR for terrestrial laser scanning. *Opt. Express* 20 (7), 7119–7127. <http://dx.doi.org/10.1364/OE.20.007119>.
- Helfrich, K., Kuhn, M., Keuschng, M., Heilig, A., 2014. Lidar snow cover studies on glaciers in the Ötztal Alps (Austria): comparison with snow depths calculated from GPR measurements. *Cryosphere* 8, 41–57.
- Höfle, B., Pfeifer, N., 2007. Correction of laser scanning intensity data: data and model-driven approaches. *ISPRS J. Photogramm. Remote Sens.* 62, 415–433.
- Höfle, B., Geist, T., Rutzinger, M., Pfeifer, N., 2007. Glacier surface segmentation using airborne laser scanning point cloud and intensity data. *Int. Arch. Photogramm. Remote. Sens. Spat. Inf. Sci.* 36 (3/W52), 195–200.
- Hood, J.L., Hayashi, M., 2010. Assessing the application of a laser range finder for determining snow depth in inaccessible alpine terrain. *Hydrol. Earth Syst. Sci. Discuss.* 7, 417–440.
- Kaasalainen, M., Viikinkoski, M., 2012. Shape reconstruction of irregular bodies with multiple complementary data sources. *Astron. Astrophys.* 543, A97.
- Kaasalainen, S., Kaasalainen, M., Mielonen, T., Suomalainen, J., Peltoniemi, J.I., Näränen, J., 2006. Optical properties of snow in backscatter. *J. Glaciol.* 52, 574–584.
- Kaasalainen, S., Hyypää, H., Kukko, A., Litkey, P., Ahokas, E., Hyypää, J., Lehner, H., Jaakkola, A., Suomalainen, J., Akujärvi, A., 2009. Radiometric calibration of LiDAR intensity with commercially available reference targets. *IEEE Trans. Geosci. Remote Sens.* 47, 578–598.
- Kaasalainen, S., Jaakkola, A., Kaasalainen, M., Krooks, A., Kukko, A., 2011. Analysis of incidence angle and distance effects on terrestrial laser scanner intensity: search for correction methods. *Remote Sens.* 3 (10), 2207–2221.
- Kenner, R., Phillips, M., Daniho, C., Denier, C., Thee, P., Zraggen, A., 2011. Investigation of rock and ice loss in a recently deglaciated mountain rock wall using terrestrial laser scanning: Gemsstock Swiss Alps. *Cold Reg. Sci. Technol.* 67 (3), 157–164.
- Krooks, A., Kaasalainen, S., Hakala, T., Nevalainen, O., 2013. Correction of intensity incidence angle effect in terrestrial laser scanning. *ISPRS Ann. Photogramm. Remote Sens. Spat. Inf. Sci.* (II-5/W2), 145–150 [www.isprs-ann-photogramm-remote-sens-spatial-inf-sci.net/II-5-W2/145/2013/](http://www.isprs-ann-photogramm-remote-sens-spatial-inf-sci.net/II-5-W2/145/2013/).
- Kukko, A., Anttila, K., Manninen, T., Kaartinen, H., Kaasalainen, S., 2013. Snow surface roughness from mobile laser scanning data. *Cold Reg. Sci. Technol.* 96, 23–35.
- Lutz, E.K., Geist, T., Stötter, J., 2003. Investigations of Airborne Laser Scanning Signal Intensity on glacial surfaces: utilizing comprehensive Laser Geometry Modeling and Surface Type Modeling; (a case study: Svartiseibreen, Norway). *Int. Arch. Photogramm. Remote. Sens. Spat. Inf. Sci.* 34 (3/W13).
- Prokop, A., 2008. Assessing the applicability of terrestrial laser scanning for spatial snow depth measurements. *Cold Reg. Sci. Technol.* 54, 155–163.
- Prokop, A., Schirmer, M., Rub, M., Lehning, M., Stocker, M., 2008. A comparison of measurement methods: terrestrial laser scanning, tachymetry and snow probing for the determination of the spatial snow-depth distribution on slopes. *Ann. Glaciol.* 49, 210–216.
- Schaffhauser, A., Adams, M., Fromm, R., Jörg, P., Luzzi, G., Noferini, L., Sailer, R., 2008. Remote sensing based retrieval of snow cover properties. *Cold Reg. Sci. Technol.* 54, 164–175.
- Shaker, A., Yan, W.Y., El-Ashmawy, N., 2011. The effects of laser reflection angle on radiometric correction of the airborne lidar intensity data. *Int. Arch. Photogramm. Remote. Sens. Spat. Inf. Sci.* 38 (5/W12), 213–217.
- Sicart, J.E., Ribstein, P., Wagnon, P., Brunstein, D., 2001. Clear-sky albedo measurements on a sloping glacier surface: a case study in the Bolivian Andes. *J. Geophys. Res.* 106 (D23), 31729–31737. <http://dx.doi.org/10.1029/2000JD000153>.
- Sturm, M., Holmgren, J., Liston, G., 1995. A seasonal snow cover classification system for local to global applications. *J. Clim.* 8, 1261–1283.
- Várnai, T., Cahalan, R.F., 2007. Potential for airborne off-beam lidar measurements of snow and ice thickness. *J. Geophys. Res.* 112, C12S90 (11 pp.).
- Wagner, W., Ullrich, A., Ducic, V., Melzer, T., Studnicka, N., 2006. Gaussian decomposition and calibration of a novel small footprint full-waveform digitizing airborne laser scanner. *ISPRS J. Photogramm. Remote Sens.* 60, 100–112.
- Weiser, U., Olefs, M., Schöner, W., Weyss, G., Hynke, B., 2015. Correction of albedo measurements due to unknown geometry. *Cryosphere Discuss.* 9, 2709–2744.
- Yan, W.Y., Shaker, A., Habib, A., Kersting, A.P., 2012. Improving classification accuracy of airborne LiDAR intensity data by geometric calibration and radiometric correction. *ISPRS J. Photogramm. Remote Sens.* 67, 35–44.
- Zhuravleva, T.B., Kokhanovsky, A.A., 2011. Influence of surface roughness on the reflective properties of snow. *J. Quant. Spectrosc. Radiat. Transf.* 112, 1353–1368.



# PAPER V

Reprinted from the Remote Sensing  
with permission of MDBI



V



Article

# The Role of Climate and Land Use in the Changes in Surface Albedo Prior to Snow Melt and the Timing of Melt Season of Seasonal Snow in Northern Land Areas of 40°N–80°N during 1982–2015

Kati Anttila \* , Terhikki Manninen , Emmihenna Jääskeläinen, Aku Riihela   
and Panu Lahtinen

Finnish Meteorological Institute, Meteorological Research Unit, FI-00101 Helsinki, Finland; terhikki.manninen@fmi.fi (T.M.); emmihenna.jaaskelainen@fmi.fi (E.J.); aku.riihela@fmi.fi (A.R.); panu.lahtinen@fmi.fi (P.L.)

\* Correspondence: kati.anttila@fmi.fi; Tel.: +358-50-4412298

Received: 14 August 2018; Accepted: 9 October 2018; Published: 11 October 2018



**Abstract:** The rapid warming of the Northern Hemisphere high latitudes and the observed changes in boreal forest areas affect the global surface albedo and climate. This study looks at the trends in the timing of the snow melt season as well as the albedo levels before and after the melt season in Northern Hemisphere land areas between 40°N and 80°N over the years 1982 to 2015. The analysis is based on optical satellite data from the Advanced Very High Resolution Radiometer (AVHRR). The results show that the changes in surface albedo already begin before the start of the melt season. These albedo changes are significant (the mean of absolute change is 4.4 albedo percentage units per 34 years). The largest absolute changes in pre-melt-season albedo are concentrated in areas of the boreal forest, while the pre-melt albedo of tundra remains unchanged. Trends in melt season timing are consistent over large areas. The mean of absolute change of start date of melt season is 11.2 days per 34 years, 10.6 days for end date of melt season and 14.8 days for length of melt season. The changes result in longer and shorter melt seasons, as well as changed timing of the melt, depending on the area. The albedo levels preceding the onset of melt and start of the melt season correlate with climatic parameters (air temperature, precipitation, wind speed). The changes in albedo are more closely linked to changes in vegetation, whereas the changes in melt season timing are linked to changes in climate.

**Keywords:** snow; albedo; climate

---

## 1. Introduction

Climate change over the Northern Hemisphere high latitudes and boreal forest zone has affected the snow and vegetation cover and, thus, the surface albedo [1–12]. Previous studies have shown that the duration and timing of the snow melt season has changed differently in different areas [13–17]. The snow cover extent has decreased especially significantly in the spring [3,5,7], and the surface albedo during the melt season months has also decreased, largely due to a decline in the area covered by snow [10]. These changes affect the local and global energy budgets [6]. The changing climate also changes the vegetation. The increased size of vegetation decreases wintertime albedo by covering the land surface and casting larger shadows on snow-covered surfaces. This is particularly relevant in the late winter. Changes in vegetation affect the local climate and the scattering properties of the forest (with larger shadows and increased multiple scattering due to increased forest height or density) [11]. The changes in the vegetation are also linked to changes in the spatial coverage of permafrost.

Changes in the timing and duration of the melt season, as well as in the surface albedo, are important parameters for climate models [18,19]. They can be used as comparison data for model parameters during the run. More accurate information on these parameters is needed to improve the models. In particular, the albedo of vegetated surfaces overlain by snow, such as boreal forests, introduce uncertainty to the model outputs [20–22].

Changes in the albedo of snow-covered surfaces can be caused by changes in a number of variables, such as climate, impurities in snow, vegetation, permafrost and changes in the properties of the snow surface [23–27]. Some of these factors also interact with each other. For example, changes in air temperature, precipitation, and wind speed affect both the snow cover extent and snow surface properties, which in turn change the snow surface albedo [10,24,27]. The optical scattering properties of a snow surface are most heavily determined by grain size and shape [28], with grain size being the main physical factor responsible for snow-albedo variations [24]. These, together with climatic factors such as wind, air temperature, and the existence of vegetation affect snow surface roughness, which also affects the brightness of the surface [29,30].

The vast area covered by seasonal snow provides a reason to study it at global scale. This can be characterized using satellite remote sensing. Snow cover and surface albedo have been analyzed from satellite data for decades [31–33]. The first studies covered small areas and short periods of time, and the available data was limited in coverage and resolution. These studies form the basis for the new satellite-derived data records, which offer better spatial and temporal coverage and, thus, enable climatic studies of various key parameters. The timing of the melt season has typically been estimated using passive microwave satellite data [14,15], which are sensitive to the presence and amount of liquid water. Therefore, microwave data are good at detecting changes in the snow moisture content, but do not react to thin snow covers, which affect the surface albedo significantly, but have very low liquid water content. Moreover, microwave data cannot easily differentiate between wet snow and wet ground. Surface albedo data have also been used to determine the timing of melt season [34], but the spatial and temporal coverage of these studies has been limited. There are many different definitions for the start and end of melt [35]. One way to define these dates is to use the time when the open areas are less than half covered with snow [35]. The choice of definition depends on the intended application of the data.

Previous studies on snow cover have shown a decrease in the area covered by snow, as in the melt season albedo [2,3,5,10], but whether or not climate change has caused the albedo of the snow surface to change prior to the onset of melt has so far been unclear. Studies of changes in snow season surface albedo have typically been based on either specific calendar months assumed to represent the melt season [10], or on the maximum albedo of the snow season [36]. This paper presents a study of the changes in the surface albedo of the land areas of the Northern Hemisphere between latitudes 40°N and 80°N prior to the melt season. This has an effect on the global energy budget, as well as the length of the melt season and the surface albedo during the melt season. The study also investigates the changes in the timing of the melt season. The analysis utilizes 5-day mean surface albedo data, derived from optical satellite data for the years 1982 to 2015, to determine the start and end dates of the melt season and the corresponding surface albedo levels. The trends of these parameters over the 34-year period and their relationships to land use and trends in climatic parameters are also investigated.

## 2. Data

This study is based on the 5-day mean surface albedo data of the Satellite Application Facility for Climate Monitoring (CM SAF, funded by EUMETSAT) CLOUDS, ALbedo and RADIATION second release Surface ALbedo (CLARA-A2 SAL) data record [37,38], which is constructed using Advanced Very High Resolution Radiometer (AVHRR) data. The albedo is defined as the broadband shortwave directional-hemispherical reflectance, i.e., the black-sky albedo. The retrieved albedo corresponds to the wavelength range 0.25–2.5  $\mu\text{m}$  and the observations are averaged to a  $0.25^\circ \times 0.25^\circ$  grid, which is

also the resolution of the final product. The albedo values are given in the range 0–100%. At the time of the analysis this was the longest available homogeneous data record of surface albedo.

The basis of the derivation of the 5-day mean albedo product used here is similar to CLARA-A1 SAL [39]. The albedo values for a five day period are first determined by observation and then averaged. After cloud masking the satellite data, the effect of topography and inclined slope and related shading on location and reflectance of the satellite data is corrected. The land pixels are then corrected for atmospheric effects on the radiation. The atmospheric correction utilizes a dynamic aerosol optical depth (AOD) time series [40] as input. The AOD time series was constructed using the total ozone mapping spectrometer (TOMS) and ozone monitoring instrument (OMI) aerosol index data [40]. The scattering properties of the surface are described by bidirectional reflectance distribution functions (BRDF) for different land-use types. The land-use classes are derived from four different land-use classifications, using always the classification which has been constructed from data that is temporally closest to the observation in question. Finally, the 0.6 and 0.8 micrometer (AVHRR channels 1 and 2) albedos are converted into broadband albedo. The reflectance characteristics of snow surfaces vary between different snow types [41]. Therefore the albedo of snow- and ice-covered areas is derived by averaging the broadband bidirectional reflectance values of the AVHRR overpasses into pentad and monthly means. The albedo of open water, such as oceans, is constructed using solar zenith angle and wind speed. The existence of sea ice is verified using the Ocean and Sea Ice Satellite Application Facility (OSI SAF) sea ice extent data [42].

The data record has been validated against in situ data and compared with the Moderate Resolution Imaging Spectroradiometer (MODIS) MCD43C3 edition 5 data set [43,44]. The mean relative retrieval error of CLARA-A2 SAL is  $-0.6\%$ , the mean root mean square error (RMSE) is 0.075 and the decadal relative stability (over Greenland Summit) is 8.5%. Larger differences between the in situ measurements and the satellite-based albedo value are mostly related to the heterogeneity of the land surface within CLARA-A2 SAL pixels [45]. A comparison between CLARA-A2 SAL and MODIS MCD43C3 showed that the two products are in good agreement. The relative difference between the two products is typically between  $-10\%$  and  $10\%$ , with the global mean CLARA-A2 SAL surface albedo being 2–3% higher than the MCD43C3 global mean surface albedo for some periods. One has to take into account that the SAL product includes a topographic correction in mountainous areas, whereas the MODIS product does not [43], and that mountains typically cause underestimation of albedo due to shadowing [37]. The water areas are excluded from the comparison as the MODIS product is not defined over water areas or sea ice.

Our study utilizes the global version of the CLARA-A2 SAL products and covers the land areas between latitudes  $40^{\circ}\text{N}$  and  $80^{\circ}\text{N}$ , and the years from 1982 to 2015. Using a 5-day mean albedo limits the role of possible individual low-quality albedo values with large retrieval errors (due to observation geometry, cloud contamination or geolocation error). Furthermore, using sigmoid fitting (described in Section 3) for the analysis limits the effect of possible erroneous individual mean albedo values.

The influence of climatic parameters on melt season and albedo was studied using ERA-Interim reanalysis data [46] for 14 day period before the previously defined date for the onset of melt. The parameters extracted from the data were air temperature (2 m), wind speed (10 m above ground), accumulated precipitation, amount of snow fall (giving also the accumulated rain) and the number of days on which the maximum temperature during that period was above  $0^{\circ}\text{C}$ ,  $-4^{\circ}\text{C}$  and  $-10^{\circ}\text{C}$ . These parameters were chosen due to their possible effect on snow reflectance, metamorphism and albedo. The air temperature affects the amount of liquid water and heat flux within the snow pack. Wind can affect the surface albedo by affecting the mechanical breaking of the surface crystals, by producing wind related surface structures such as ripples and ablation and accumulation areas. It can also affect the amount of vegetation visible above the snow surface and fraction of bare ground by removing snow partly or altogether from some areas. It also typically affects the amount of snow on trees. In the case of evergreen trees, this can have a significant effect on surface albedo. Precipitation can affect the surface albedo through adding fresh snow crystals on the surface and on vegetation and

by affecting the snow depth. In the case of rain-on-snow, this can bring heat into the snow pack thus affecting the melt processes. The three temperature thresholds were chosen based on the relationship between air temperature, snow metamorphism and albedo. The 0 °C was chosen since it is the melting point for snow in normal conditions. The −4 °C was used to take into account the fact that snow metamorphism starts already at sub-zero temperatures. In the wide variety of snow albedo models, the simplest parameterizations presume a steady albedo for colder temperatures, and then a linear decline in snow surface albedo for air temperatures from −5 °C to 0 °C. At −4 °C the heating of the sun can already affect the snow surface crystals; −10 °C was chosen to represent a temperature at which the air temperature does not considerably affect the snow surface crystals, so if the maximum temperature of the day stays colder than this it can be presumed there is no change in the snow surface due to the temperature. The data was originally in 6-hourly temporal resolution (for snow fall 12 hourly) from which it was further processed to daily values. The resolution of the ERA-Interim data was 0.25°.

The role of land use in the trends in melt season albedo and timing is assessed using data from GlobCover2009 [47]. The data was coarsened to the same resolution as the melt season data (0.25°) by choosing the most common land-use class within the melt season grid cell. Figure 1 shows the GlobCover data at CLARA-A2 SAL resolution. The GlobCover land-use classes present in the study area are listed in Table 1.

**Table 1.** GlobCover2009 classes found to be most common within one surface albedo (SAL) resolution unit in the study area and the number of occurrences of each class as the most common land-use class in one resolution unit of melt season data.

LUC Class	Label	Number of Occurrence
11	Post-flooding or irrigated croplands (or aquatic)	420
14	Rainfed croplands	5137
20	Mosaic cropland (50–70%)/vegetation (grassland/shrubland/forest) (20–50%)	5771
30	Mosaic vegetation (grassland/shrubland/forest) (50–70%)/cropland (20–50%)	2996
50	Closed (>40%) broadleaved deciduous forest (>5 m)	7775
70	Closed (>40%) needleleaved evergreen forest (>5 m)	2472
90	Open (15–40%) needleleaved deciduous or evergreen forest (>5 m)	31415
100	Closed to open (>15%) mixed broadleaved and needleleaved forest (>5 m)	3605
110	Mosaic forest or shrubland (50–70%)/grassland (20–50%)	2299
120	Mosaic grassland (50–70%)/forest or shrubland (20–50%)	1883
130	Closed to open (>15%) (broadleaved or needleleaved, evergreen or deciduous) shrubland (<5 m)	1371
140	Closed to open (>15%) herbaceous vegetation (grassland, savannas or lichens/mosses)	3869
150	Sparse (<15%) vegetation	28741
180	Closed to open (>15%) grassland or woody vegetation on regularly flooded or waterlogged soil–Fresh, brackish or saline water	1639
190	Artificial surfaces and associated areas (urban areas >50%)	103
200	Bare areas	7523
210	Water bodies	115239
220	Permanent snow and ice	11022

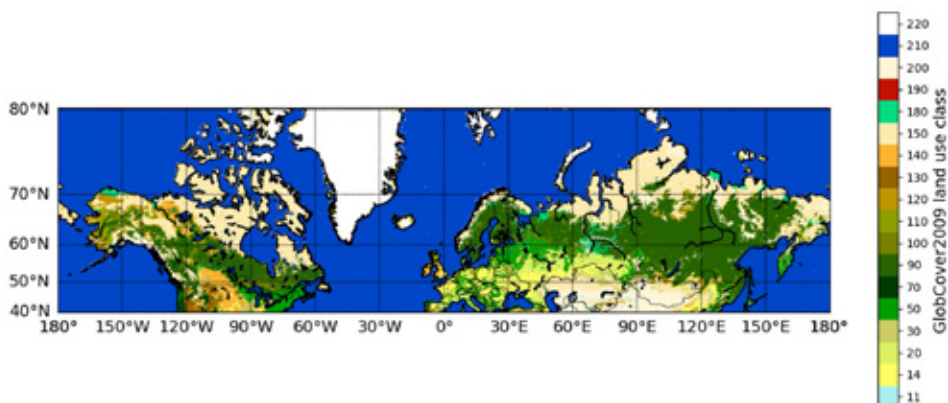


Figure 1. GlobCover2009 land-use classes coarsened to melt season data resolution.

### 3. Methods

The melt season parameters were determined by fitting sigmoids to CLARA-A2 SAL pentad (5 day) mean albedo values using non-linear regression [48]. For each grid cell and year the 5-day mean albedo values from the end of January until the end of August were used for the sigmoid fitting. Figure 2 shows two examples of sigmoid fitting. To include all changes in albedo during the melt season, the dates of snow melt at the onset was taken to be the date at which the sigmoid reached 99% of its variation range (i.e., a change of 1% (relative) from the pre-melt albedo level). Likewise the end of the snow melt season was defined to be the date at which the sigmoid reached 1% of its variation range. These thresholds were chosen in order to include the whole dynamic change in surface albedo during melt season. The length of the melt season was then the difference between the start and end date of melt. The albedo values corresponding to the dates of the onset and end of melt were used as the representative albedo values preceding and following the melt season.

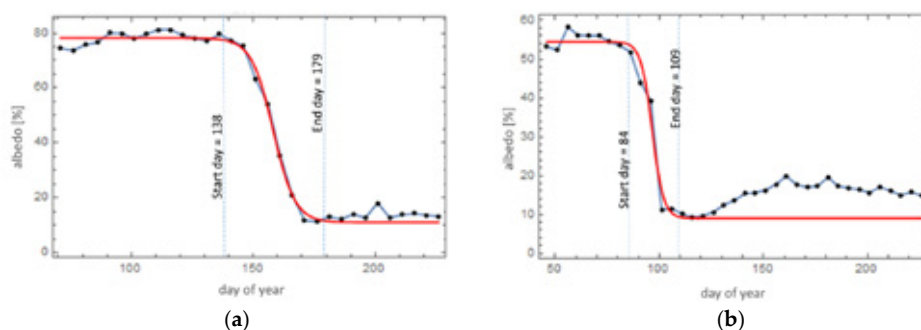
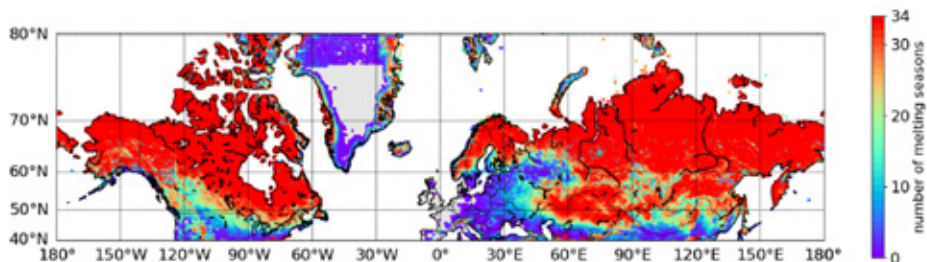


Figure 2. Sigmoid fitting for 5-day mean albedo data for (a) location 55.375°N, 47.625°E for year 2006 and (b) location 68.125°N, 120.125°E for the year 2007. The growth of vegetation after snow melt is manifested in (b) where the albedo values after melt season increase slightly as the vegetation starts to produce leaves.

In some cases the snow melt onset could not be determined, because the melt had already started before the first cloud-free albedo pentad of the year was available for the grid cell in question. The final analyses included only the grid cells for which (1) both the snow melt onset and end days were retrieved successfully; (2) the albedo difference between the start and end date of melt was larger than 5% absolute albedo units; and (3) data meeting these two criteria were available for at least 10 years. The mean values of  $R^2$  and RMSE of the final sigmoid regressions were 0.989 and 5.55 (albedo

percentage), respectively. The corresponding median values were 0.993 and 4.75. In the analyses only the grid cells for which  $R^2 > 0.95$  and  $RMSE < 20$  (for the sigmoid fitting) were included. This led to discarding about 2% of the data. The final dataset consisted of 2.46 million grid cell level melt seasons. Figure 3 shows the number of years with successful melt season retrievals per resolution unit.



**Figure 3.** Number of successful retrievals of melt season per resolution unit during the 34 years.

The effect of random error in the albedo data on the derivation of the melt season timing was estimated by using 6 different sigmoids with different levels of albedo prior to melt. After constructing artificial data around these sigmoids, the data was modified by introducing relative random error of +12.5% to −12.5% to it. This error is larger than the level of typical variation of albedo values. These data with random error were then used to produce sigmoids and to extract the melt season parameters. The analysis was repeated for 100 different cases for each of the six chosen pre-melt levels with random error. The effect of relative random error in the albedo data on the start date of melt was 1.3 days (standard deviation) and 1.1 days for the end dates of melt.

The trends for the melt season parameters (start and end times of melt, the length of the melt season and albedo levels before and after the melt season) for each grid cell over the 34 years were detected using linear regression. The trends were determined using rolling 5-year means. Only 5-year means with data from at least 3 years were included in the trend fitting, and the fitting was carried out only for grid cells that had at least 20 mean values during the 34 years. This gave 72092 grid cell level estimates of trends in pre melt season albedo. From these 30% had  $R^2$  larger than 0.5.

The climatic dependencies of the melt season parameters were studied using ERA-Interim re-analysis data [46] for air temperature at 2 m, precipitation and wind speed prior to melt. The time interval used in the analysis was 14 days prior to melt. Correlation analysis between ERA-Interim climate data and surface albedo or day of onset of melt were carried out only for the grid cells for which data were available for at least 20 years. The analysis was performed by looking at the linear correlation coefficient between the melt season parameter in question and the climatic parameters.

The GlobCover2009 land-use data set (Figure 1) was coarsened to the same resolution as the melt season data (CLARA-A2 resolution of  $0.25^\circ$ ). The area of the boreal forest was determined by looking at GlobCover classes 70, 90 and 100. The tundra areas were determined as the grid cells with land-use class 140, 150 and 200 that are north of  $55^\circ\text{N}$  in North America and  $65^\circ\text{N}$  in Europe.

## 4. Results

### 4.1. Albedo Before and After the Melt Season

The change in albedo of Northern Hemisphere land areas between  $40^\circ\text{N}$  and  $80^\circ\text{N}$  before the melt season shows large spatial variations (Figure 4). The changes are concentrated in large areas with homogeneous change characteristics. These areas are listed in Table 2. The areas are shown on a map together with place names in Figure 5. For the observations with clear trends ( $R^2 > 0.5$ , 30% of all observations) the pre-melt albedo decreased by 2.4 absolute albedo percentage units on average over the whole study area over the 34 years of record. The statistically reliable trends in pre-melt season albedo are concentrated in the region of the boreal forest zone. This can be seen in Figure 4b, which



shows the land-use classes for the resolution units with albedo trends with  $R^2 > 0.5$ . The trends in the boreal forest zone show decreasing pre-melt albedo in the southern half of the Central Siberian Plain and Scandinavia, and increasing pre-melt albedo in the north of Mongolia and China. In North America the direction of changes varies over short distances, whereas in Eurasia there are larger areas with similar direction of change in albedo.

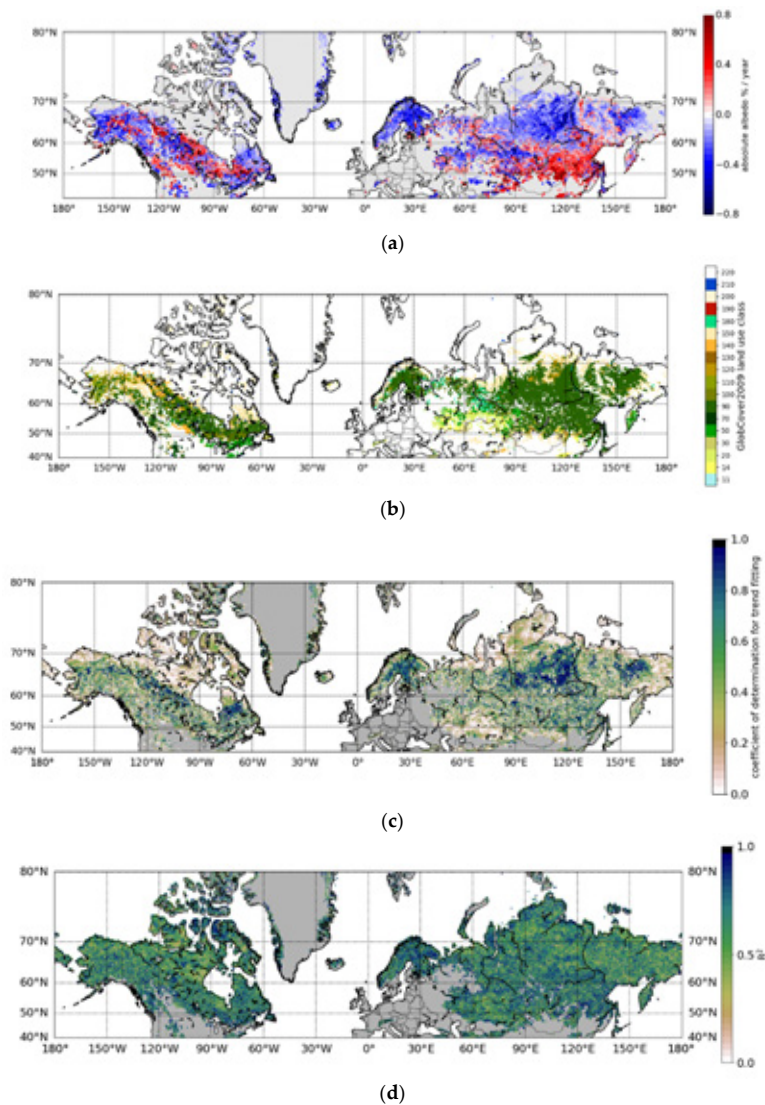


**Figure 4.** (a) The rate of change in albedo before melt season (absolute albedo % per year) between 1982 and 2015 using 5 year rolling mean albedo (showing cases for which  $R^2$  of the fitting was larger than 0.5). The positive rates of change mean higher albedo and negative lower albedo values. (b) The GlobCover land-use class for the areas with clear trends in pre-melt albedo. (c) The coefficient of determination ( $R^2$ ) value for trends in albedo before the onset of melt. (d)  $R^2$  value for multiple variable linear correlation between albedo before melt season and 6 climatic parameters for 14 days prior onset of melt. The climatic parameters used are the mean air temperature, number of days with maximum temperature above  $0\text{ }^{\circ}\text{C}$ ,  $-4\text{ }^{\circ}\text{C}$  and  $-10\text{ }^{\circ}\text{C}$ , accumulated precipitation and mean wind speed.

**Table 2.** The mean trends ( $R^2 > 0.5$ ) for all the melt season and climatic parameters in areas with observed consistently homogenous change. The trends for snowfall and rain were not included in the table due to the fact that the trends for the pre-defined regions presented in the table were so weak that they were less than the yearly variation of the parameter. All climate parameters are derived for 14 days preceding the onset of snow melt. The number of observations in the area are described in the parenthesis. The area “RCM” refers to the area around the border of Russia, China and Mongolia. The negative trends for the melt season timing mean earlier onset or end of melt and shorter melt season and the positive trend directions mean later onset and end of melt and longer melt seasons.

	Pre-Melt Albedo	Post-Melt Albedo	Start Day of Melt (Days Per Year)	End Day of Melt (Days Per Year)	Melt Season Length (Days Per Year)	Mean Air Temp. (K/Year)	No. Days Above 0 °C (Days Per Year)	No. Days Above > -4 °C (Days Per Year)	No. Days Above > -10 °C (Days Per Year)	Accum. Precip (mm/Year)	Wind Speed (m/s Per Year)
Cent. Sib. Plain 7809	-0.25 (4100)	-0.08 (1765)	-0.61 (2486)	-0.50 (2243)	0.46 (317)	-0.12 (370)	-0.06 (359)	-0.11 (373)	-0.11 (399)	-0.28 (169)	0.01 (112)
RCM 7191	0.15 (2505)	-0.09 (1872)	-0.95 (1030)	0.71 (577)	1.51 (925)	-0.25 (720)	-0.09 (573)	-0.14 (667)	-0.18 (604)	-0.58 (477)	0.01 (378)
Labrador 2640	-0.09 (1111)	-0.06 (603)	0.28 (95)	-0.59 (289)	-0.94 (228)	0.21 (380)	0.03 (113)	0.16 (193)	0.19 (499)	0.33 (84)	0.00 (142)
Rocky Mts 2840	-0.05 (449)	-0.07 (626)	-1.18 (170)	1.17 (303)	2.13 (280)	-0.21 (254)	-0.12 (197)	-0.19 (243)	-0.18 (197)	-0.12 (127)	0.01 (104)
Alaska 4866	-0.15 (1121)	-0.08 (1024)	-0.43 (156)	-0.22 (204)	0.37 (267)	-0.08 (176)	-0.05 (214)	-0.16 (268)	-0.07 (161)	-0.09 (130)	0.01 (101)
Europ. Arctic 3526	-0.29 (1233)	-0.01 (227)	-0.79 (510)	-0.39 (102)	0.88 (303)	-0.12 (276)	-0.06 (217)	-0.06 (376)	-0.09 (252)	-0.09 (102)	0.02 (121)
Canad. archip. 1796	-0.11 (222)	-0.26 (432)	-0.61 (79)	0.03 (79)	0.81 (95)	0.01 (32)	-0.06 (20)	-0.1 (30)	-0.04 (29)	0.33 (27)	-0.03 (83)
The Alps 299	-0.17 (22)	-0.12 (34)	-1.48 (28)	1.53 (19)	2.69 (30)	-0.18 (5)	-0.27 (5)	-0.18 (4)	-0.04 (3)	-0.00 (8)	-0.02 (7)

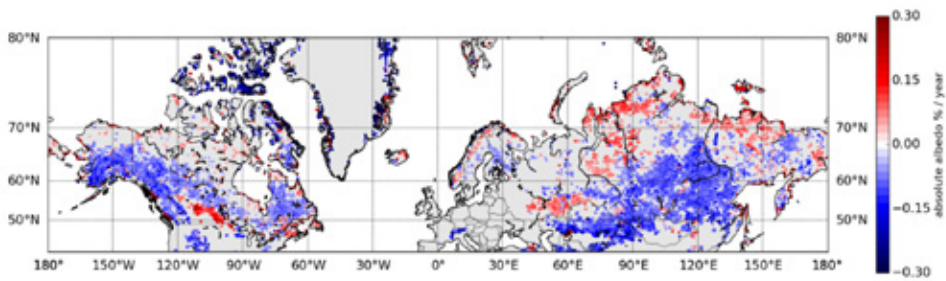


Figure 5. The areas listed in Table 2.

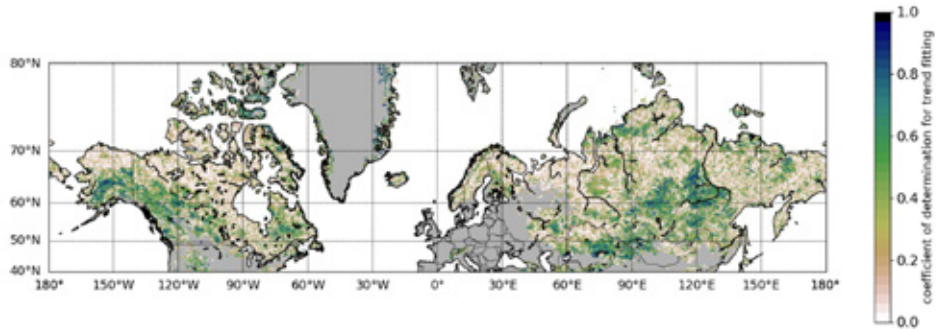
Most of the tundra areas show no significant change in albedo prior to melt. This can be seen in Figure 4c, which shows the  $R^2$  values for all albedo trend retrievals. For all the areas with an  $R^2$  value, the retrieval of melt season parameters was successful, but the data show no reliable trends (having  $R^2$  values lower than 0.5). The slope values of these excluded trends are typically close to 0. In many areas the annual variability of the pre-melt albedo values is so large that even 34 years is not long enough to determine a small trend in the albedo value. In southern Eurasian tundra the pre-melt albedo shows weak negative trends, but no trends in the higher latitudes. The Kola Peninsula and northern Finnish Lapland show strong negative trends ( $-0.29$  albedo percentage units per year).

The role of vegetation in the observed pre-melt albedo changes can be estimated by looking at the albedo levels right after the snow has melted, before the vegetation has started greening. Figure 6 shows the trends for albedo after melt as well as the corresponding  $R^2$  values for the trend fitting. The trends in the level of albedo after melt are much weaker than those in the pre-melt season albedo before melt season, which can be expected since the differences in the albedo between different biomes are much smaller than the changes in the snow cover. The post-melt albedo of the northern Eurasian tundra decreased over the study period. In more southerly areas of tundra, however, there are no clear trends. In the boreal forest zone the trends are towards lower albedo values in most of the area, except for the area west of the River Ob in Russia. One potential reason for the darkening of the boreal forest zone after the melt season could be the increased size of trees and denser forests, causing more shadowing of the surface and increased multiple scattering. The darkening of the southern tundra prior to melt could be explained by the reported shrubification of tundra [49].

The role of climate change in altering the pre-melt season albedo was studied using the linear fitting between the melt season data and the ERA-Interim reanalysis data [45] on air temperature, precipitation, wind speed and the number of days with maximum temperature above  $0\text{ }^{\circ}\text{C}$ ,  $-4\text{ }^{\circ}\text{C}$  and  $-10\text{ }^{\circ}\text{C}$  for 14 days prior to onset of melt. Figure 7 shows the 34-year trends in air temperature, accumulated precipitation and wind speed. Changes in all these climatic parameters contributed to the changes in the pre-melt albedo (mean  $R^2$  for the whole area being 0.64 and the 80th percentile being 0.79) (Figure 4d). In the area around the borders of China, Mongolia and Russia (Figure 5) the climatic parameters explained almost all of the albedo change. The mean air temperature was the dominant influence (mean  $R^2 = 0.51$  for the whole area). It was the largest explanatory factor in particular in Yablonovyy and Verhojansk Mountain Ranges, Northern West Siberian Plain, Kola Peninsula, Baffin Island and Central Siberian Plain.

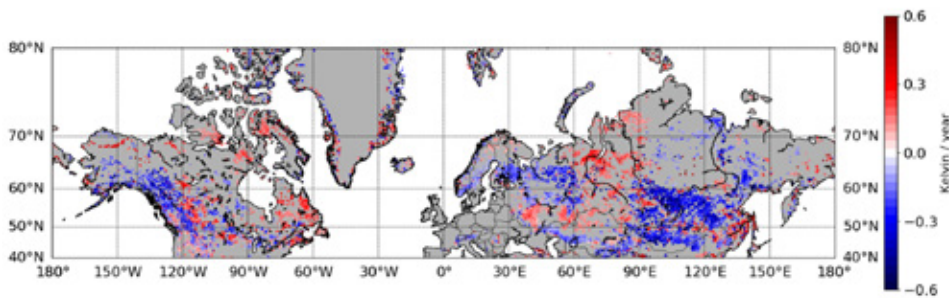


(a)



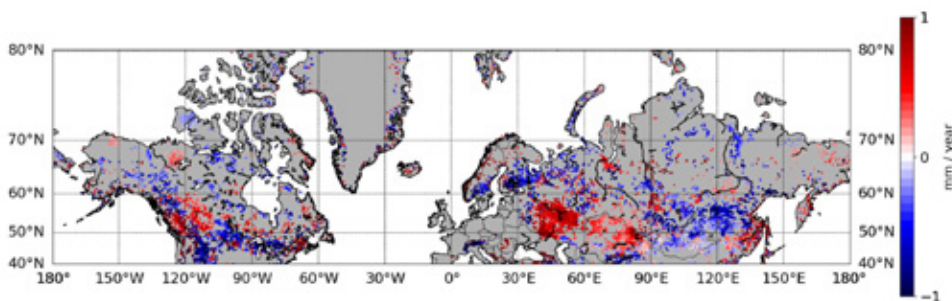
(b)

**Figure 6.** (a) The rates of change for the albedo after melt season (absolute albedo % per year) between 1982 and 2015 using 5-year rolling mean albedo (showing cases for which  $R^2$  of the fit was larger than 0.5). (b) The coefficient of determination ( $R^2$ ) value for trends in albedo after the end of melt.

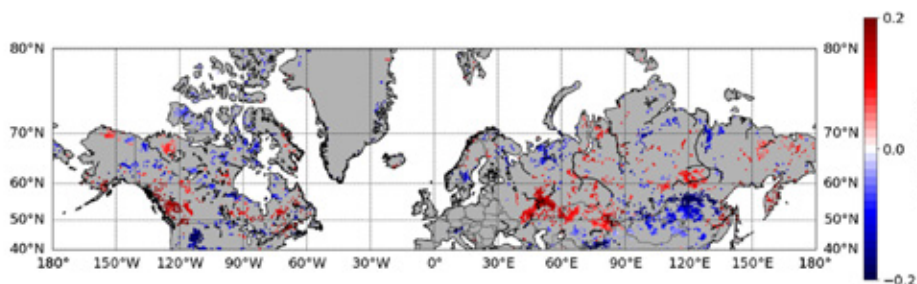


(a)

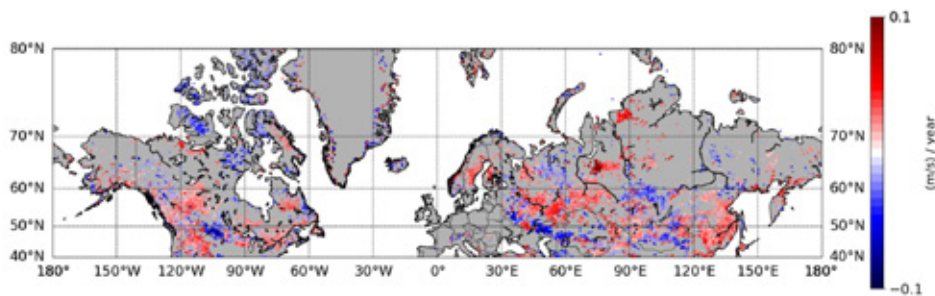
**Figure 7.** Cont.



(b)



(c)



(d)

**Figure 7.** ERA-Interim trends for 1982–2015 for (a) mean air temperature (b) accumulated precipitation (c) snowfall (units are given as amount of snow converted into liquid water) (d) wind speed for 14 days prior to melt onset. The maps show trends for which the coefficient of determination was larger than 0.5.

#### 4.2. Melt Season Timing

In addition to the changes in albedo, the timing of the melt season has also changed (Figures 8–10 and Table 2). The changes are, as with albedo, significant and spatially consistent but they also vary within the study area. The observations with high values for coefficient of determination ( $R^2 > 0.5$ ) are concentrated in large distinct areas. The changes were in general towards longer melt seasons and earlier onset of melt. The mean start date of melt season in the pixels for which melt season data are available for the whole 34 years, became 6.1 days earlier over the 34 years. Similarly, the melt ended on average 5.2 days earlier and the melt season, therefore, became 1 day longer on average. The majority of the observations showed no clear reliable trends (Figure 11), but in many areas the changes were significant (Figures 8–10). In many areas the inter-annual variation in the start and/or end dates of the melt season were so large that it was not possible to detect a statistically significant trend. In Eurasia



all the parameters showed changes over large homogenous areas, but in North America the trends are typically more localized and variable.

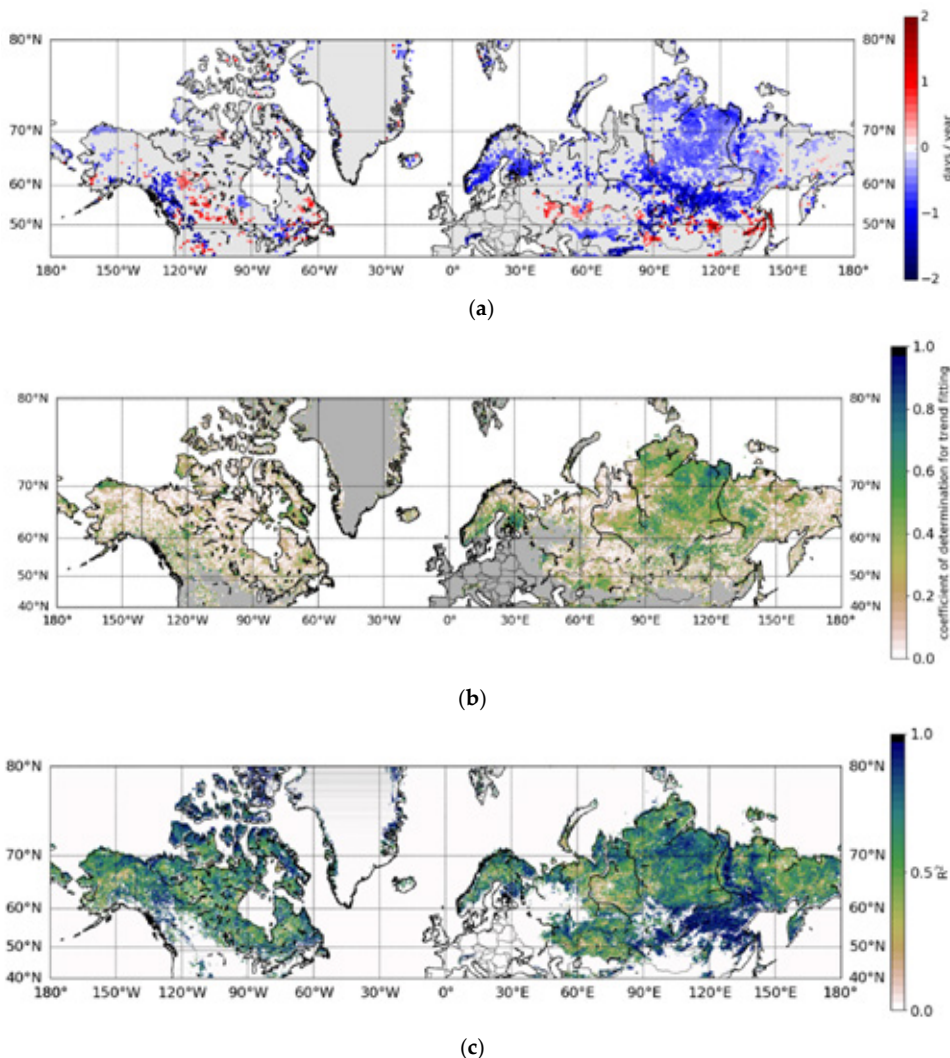


**Figure 8.** (a) The rates of change for the start day of melt between 1982 and 2015 using 5-year rolling mean albedo (showing cases for which  $R^2$  of the fit was larger than 0.5). The negative rates of change mean earlier onset of melt and the positive rates of change mean later dates of onset of melt. (b) The coefficient of determination ( $R^2$ ) values for the trend fitting for start day of melt. (c) The multiple variable correlation ( $R^2$ ) between ERA-Interim climate data and start day of melt.  $R^2$  value for linear correlation between the time that melt season started (day of year) and 3 climatic parameters for 14 days prior to the onset of melt. The climatic parameters used are the mean air temperature, accumulated precipitation and mean wind speed.

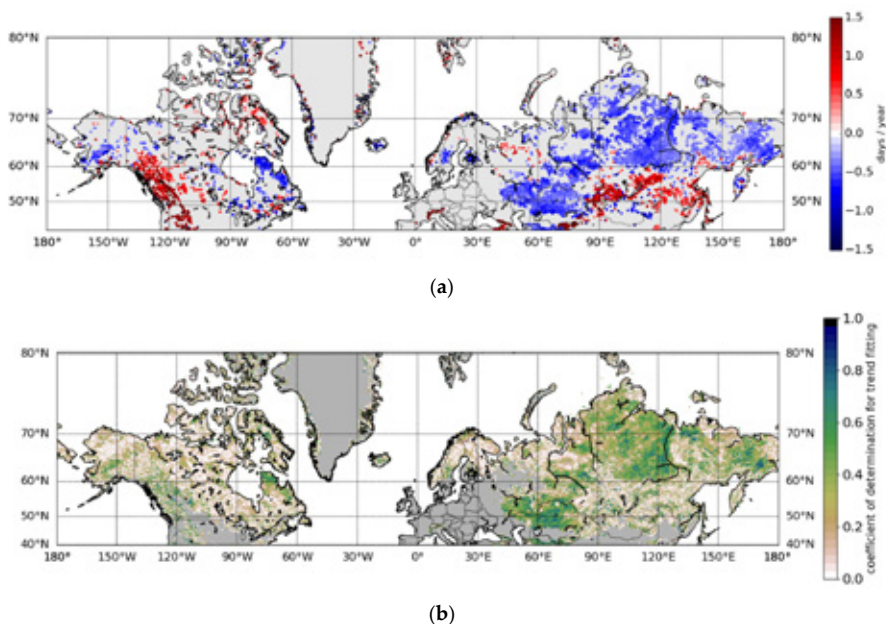


**Figure 9.** (a) The rates of change for the end date of melt between 1982 and 2015 using 5-year rolling mean (showing cases for which  $R^2$  of the fit was larger than 0.5). The negative rates of change mean earlier end of melt and the positive rates of change mean later dates of end of melt. (b) The coefficient of determination ( $R^2$ ) values for the trend fitting for end day of melt.

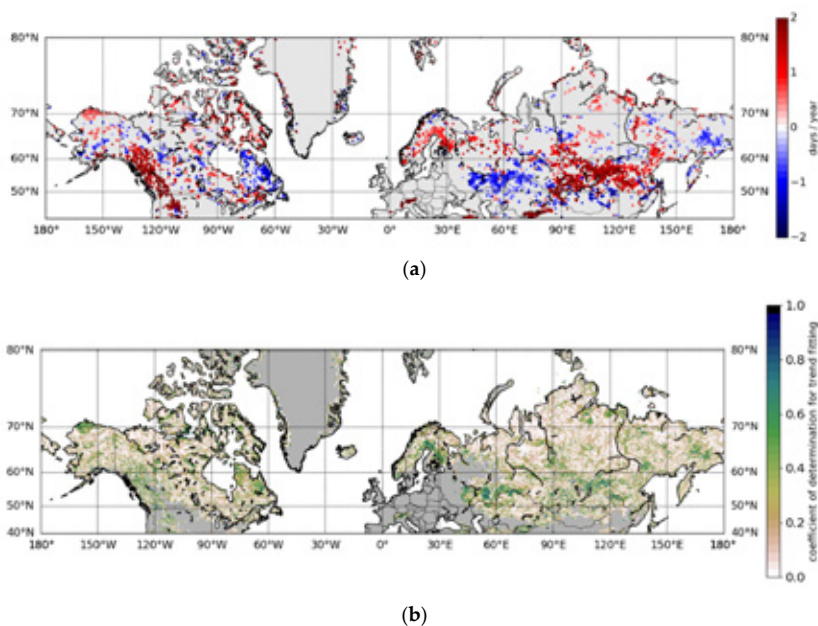


**Figure 10.** (a) The rates of change for the length of melt season between 1982 and 2015 using 5-year rolling mean (showing cases for which  $R^2$  of the fit was larger than 0.5). The negative rates of change mean shorter melt seasons and the positive rates of change mean longer melt season. (b) The coefficient of determination ( $R^2$ ) values for the trend fitting for length of melt season.

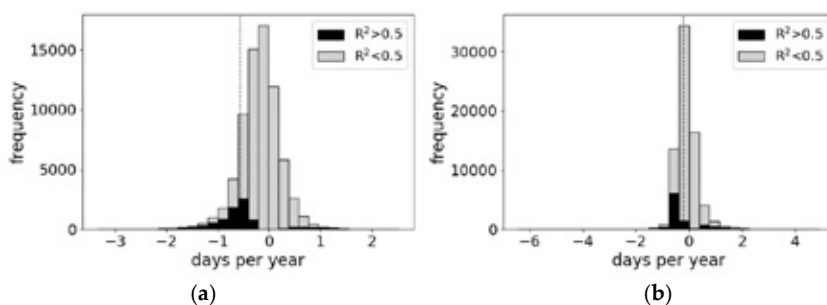


**Figure 11.** The rate of change observations for (a) start and (b) end day of melt. The dashed line shows the mean value of the observations for which  $R^2$  is larger than 0.5.

The distribution of all the computed trends for start and end day of melt can be seen in Figure 11. The majority of the trends had  $R^2$  values lower than 0.5, and the rate of change of these were typically close to zero but slightly towards earlier onset and end of melt.

The trends in melt season timing showed no significant dependency on the land use. In the Central Siberian Plain the melt started and ended earlier (Table 2), resulting in earlier melt seasons across the whole region regardless of the vegetation type (both boreal and tundra). The decreasing trends for mean air temperature before the melt onset in the Central Siberian Plain (Figure 7a, Table 2) show similar spatial patterns as the melt season timing parameters. This can be explained by the fact that the air temperatures prior to melt are not derived from the same time of year, but change together with the start date of melt. With earlier onset of melt, the air temperatures are also derived from an earlier period. In the mid-winter the air temperature is more heavily influenced by the lack of heating from the Sun, whereas later in the spring other climatic factors start to affect the air temperature more significantly. Earlier onset of melt can be associated with colder air temperatures prior to melt onset and more rapid change in the air temperature from cold mid-winter values to melting conditions.

In the area around the borders of Russia, Mongolia and China the melt starts earlier and ends later (Table 2), resulting in longer melt seasons. This is also the case for the Canadian Rocky Mountains. In North America, the northern parts of Labrador Peninsula, which are tundra, also show trends towards a shorter melt season and earlier end of melt.

Using the climatic data from ERA-Interim, three parameters (mean air temperature, mean wind speed and accumulated precipitation) are required to explain the changes in the start date of melt, giving a mean  $R^2$  value of 0.65 for the whole study area (Figure 8). In some regions, the mean wind speed and accumulated precipitation (for 14 days prior to melt) are strongly correlated with the starting time of the melt, while the mean air temperature is not (Figure 12), thus supporting the multivariate explanation. For example, wind speed affects the start of melt more than air temperature in the Southern West Siberian Plain and the Southern Byrranga Mountains. Changes in wind conditions affect snow surface scattering by affecting sublimation, mechanical metamorphism of the surface crystals, and distribution of the snow, thus affecting the albedo and depth of snow, and the length of the melt season. The distribution of impurities, such as litter from vegetation on the snow cover, can change due to wind conditions. Impurities increase both the absorption of solar energy into the snow pack and the melt rate. Precipitation (together with air temperature) correlates with the start of melt particularly in the Yablonovyy Range and south of Taymur Peninsula. The trends in the 5-year rolling mean of climatic parameters in individual grid cells show similar spatial patterns as the melt season parameters. The trends in these areas are summarized in Table 2.



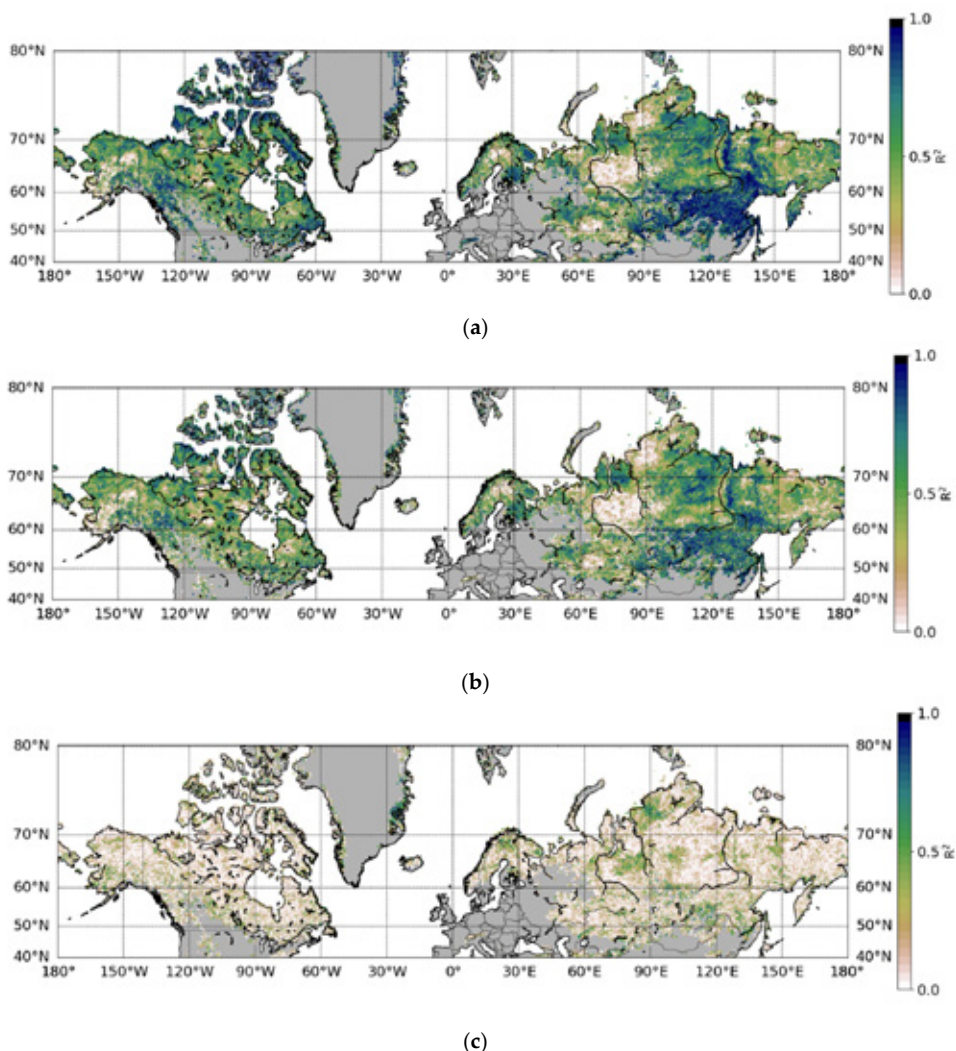


**Figure 12.** The correlation ( $R^2$ ) between start day of melt and (a) mean air temperature (b) total precipitation and (c) wind speed for 14 days prior to the onset of melt.

## 5. Discussion

The magnitude of changes in albedo prior to melt season seem to be linked strongly to vegetation characteristics, whereas the changes in melt season timing seem to be more strongly linked to climatic factors. The influence of vegetation on surface albedo prior to melt can be understood by considering the difference between the albedo of vegetation and the albedo of snow. Even a small increase in the vegetation cover can alter the surface albedo by several absolute albedo percentage units [49,50], whereas changes in climatic factors prior to melt affect the snow depth and/or the surface crystal structure, and have smaller (but still significant) impact on the surface albedo. Changes in the number of days with snow on the trees are an obvious exception to this, putting emphasis on the influence of climatic parameters on surface albedo. Increased precipitation in vegetated areas would mean increased albedo while, in open areas, such as tundra, more precipitation would more strongly affect the depth and surface crystal structure of the snow pack, with a weaker effect on the surface albedo.

The start date of melt is linked to the air temperature. Increasing temperatures would result in earlier melt onset. However, in this study the focus was on the temperature prior to melt. That means that the time period in question changes from year to year. An increase in air temperatures prior to melt onset would mean that at the start of melt the snow pack is already warmer and the surface crystals may have been affected by melt and sublimation. Conversely, lower air temperatures, such as in the area around the borders of Russia, Mongolia and China, would result in a colder snowpack, and, in the case of a thin snow cover, resulting from low rates of precipitation, colder ground. This would mean slower melt. Both the end date of melt and the length of the melt season are affected by the air temperature, snow depth, snowpack characteristics, and the ground temperature. These are all regulated by climatic factors. For changes in vegetation to cause significant changes in the melt season timing, such as observed in this study, the vegetation would need to change considerably, for example from bare ground to tree cover. At larger spatial scales, such changes take more than 34 years.

The relationship between vegetation and climate is not straightforward. Existing studies of changes in vegetation, permafrost and impurities in snow [26,51–55] reveal similar spatial patterns of consistent change as do the melt season parameters, but the effect is not the same in all areas. None of the aforementioned factors alone are able to explain the changes over the whole study area. In fact, they can have opposite effects on the albedo in different regions.

The inconsistency in the effects of vegetation on winter time albedo can be partly explained by the different response of vegetation to the changing climate. According to Xu et al. [26], in Eurasia the normalized difference vegetation index (NDVI) is positively correlated with warming temperature, whereas in North America the effect varies in different regions and patterns of greening and browning in North America are fragmented [26]. It is noteworthy that while the NDVI data describe growing season conditions and are thus not directly translatable to winter conditions, they should be considered an indicator of changes that may also be visible in winter, such as growth in shrub size and coverage. The observed changes in vegetation cannot be directly translated to changes in surface albedo. According to Myers-Smith et al. [56] shrub growth is responsive to different drivers in different regions. Sturm et al. [50] found that if shrubs protrude above the snow and cover 10% of the surface, the albedo will decrease by 30%. The spatial coverage of continuous permafrost shows similar spatial patterns with many of the trends for the melt season parameters. For example, at the southern edge of Central Siberian Plain and in Labrador Peninsula continuous permafrost ends in the same area as the trends for melt season change. The difference in trends for melt season parameters can be due to changes in permafrost coverage causing changes in land use, such as vegetation or formation of melt ponds, or by different response of vegetation and snow cover to climatic changes in areas with and without permafrost.

## 6. Conclusions

The surface albedo before the onset of melt shows clear but spatially varying trends. The clearest trends are observed in the boreal forest zone, and can be as large as 9 absolute albedo percentage units over the 34-year-long study period. This is about 10–15% of the albedo of clean snow cover with no vegetation protruding above the snow surface. At grid cell level, both the albedo prior to melt onset and the start date of the melt season are responsive to changes in air temperature, wind speed and precipitation amount, with air temperature being the most significant driving factor. At most latitudes the mean albedo before the onset of melt has decreased over the 34 years.

The timing of the melt season shows strong rates of change in localized areas. These changes are better explained by climatic factors than land-use changes. Areas with consistent homogenous changes are larger in Eurasia than in North America. In the Central Siberian Plain the melt season takes place earlier than before. In the Canadian Rocky Mountains and the area around the borders of Russia, China and Mongolia, the melt season starts earlier, ends later, and lasts longer than before.

All in all, both the timing of the melt season and the albedo prior to the melt season changed in large areas between 1982 and 2015. In most areas, both the start and end dates of the melt season

have advanced, and the albedo prior to melt onset has decreased, indicating a darkening of winter snow surfaces.

**Author Contributions:** Data curation, K.A., T.M., E.J., A.R. and P.L.; Formal analysis, K.A.; Funding acquisition, T.M.; Investigation, K.A.; Methodology, T.M.; Project administration, K.A.; Supervision, T.M.; Writing—original draft, K.A.

**Funding:** This research was financially supported by the CM SAF project funded by The European Organisation for the Exploitation of Meteorological Satellites (EUMETSAT).

**Acknowledgments:** The authors would like to thank the CM SAF team, Vesa Laine and Kaj Andersson for their co-operation in producing the CLARA-A2 SAL data record, and Outi Meinander for supporting discussions. EUMETSAT supported financially the generation of the CLARA-A2 SAL, which is available at [www.cmsaf.eu](http://www.cmsaf.eu).

**Conflicts of Interest:** The authors declare no conflict of interest.

## References

- Hall, A. The role of surface albedo feedback in climate. *J. Clim.* **2004**, *17*, 1550–1568. [[CrossRef](#)]
- Smith, N.; Saatchi, S.; Randerson, J. Trends in high northern latitude soil freeze and thaw cycles from 1988 to 2002. *J. Geophys. Res.* **2004**, *109*, D12101. [[CrossRef](#)]
- Déry, S.; Brown, R. Recent Northern Hemisphere snow cover extent trends and implications for the snow-albedo feedback. *Geophys. Res. Lett.* **2007**, *34*, L22504. [[CrossRef](#)]
- Solomon, S.; Qin, D.; Manning, M.; Averyt, K.; Marquis, M.; Averyt, K.B.; Tignor, M.; Miller, H.L. *Climate Change 2007: The Physical Science Basis; Working Group I Contribution to the Fourth Assessment Report of the IPCC*; Cambridge University Press: Cambridge, UK; New York, NY, USA, 2007; Volume 4.
- Brown, R.D.; Robinson, D.A. Northern Hemisphere spring snow cover variability and change over 1922–2010 including an assessment of uncertainty. *Cryosphere* **2011**, *5*, 219–229. [[CrossRef](#)]
- Flanner, M.; Shell, K.; Barlage, M.; Perovich, D.; Tschudi, M. Radiative forcing and albedo feedback from the Northern Hemisphere cryosphere between 1979 and 2008. *Nat. Geosci.* **2011**, *4*, 151–155. [[CrossRef](#)]
- Derksen, C.; Brown, R. Spring snow cover extent reductions in the 2008–2012 period exceeding climate model projections. *Geophys. Res. Lett.* **2012**, *39*. [[CrossRef](#)]
- Foster, J.L.; Cohen, J.; Robinson, D.A.; Estilow, T.W. A look at the date of snowmelt and correlation with the Arctic Oscillation. *Ann. Glaciol.* **2013**, *54*, 196–204. [[CrossRef](#)]
- IPCC. *Climate Change 2013: The Physical Science Basis; Contribution of Working Group I to the Fifth Assessment Report of the Intergovernmental Panel on Climate Change*; Stocker, T.F., Qin, D., Plattner, G.-K., Tignor, M., Allen, S.K., Boschung, J., Nauels, A., Xia, Y., Bex, V., Midgley, P.M., Eds.; Cambridge University Press: Cambridge, UK; New York, NY, USA, 2013; p. 1535.
- Atlaskina, K.; Berninger, F.; Leeuw, G. Satellite observations of changes in snow-covered land surface albedo during spring in the Northern Hemisphere. *Cryosphere* **2015**, *9*, 1879–1893. [[CrossRef](#)]
- Manninen, T.; Stenberg, P. Simulation of the effect of snow covered forest floor on the total forest albedo. *Agric. For. Meteorol.* **2009**, *149*, 303–319. [[CrossRef](#)]
- Fassnacht, S.; Cherry, M.; Venable, N.; Saavedra, F. Snow and albedo climate change impacts across the United States Northern Great Plains. *Cryosphere* **2016**, *10*, 329–339. [[CrossRef](#)]
- Li, Q.; Ma, M.; Wu, X.; Yang, H. Snow Cover and Vegetation-Induced Decrease in Global Albedo from 2002 to 2016. *J. Geophys. Res. Atmos.* **2018**, *123*, 124–138. [[CrossRef](#)]
- Markus, T.; Stroeve, J.C.; Miller, J. Recent changes in Arctic sea ice melt onset, freezeup, and melt season length. *J. Geophys. Res.* **2009**, *114*, C12024. [[CrossRef](#)]
- Wang, L.; Derksen, C.; Brown, R.; Markus, T. Recent changes in pan-Arctic melt onset from satellite passive microwave measurements. *Geophys. Res. Lett.* **2013**, *40*, 1–7. [[CrossRef](#)]
- Chen, X.; Liang, S.; Cao, Y.; Cao, T.; Wang, D. Observed contrast changes in snow cover phenology in northern middle and high latitudes from 2001–2014. *Sci. Rep.* **2015**, *5*. [[CrossRef](#)] [[PubMed](#)]
- Malnes, E.; Karlsen, R.S.; Johansen, B.; Bjerke, J.W.; Tømmervik, H. Snow season variability in a boreal-Arctic transition area monitored by MODIS data. *Environ. Res. Lett.* **2016**, *11*, 125005. [[CrossRef](#)]
- Rautiainen, K.; Parkkinen, T.; Lemmetyinen, J.; Schwank, M.; Wiesmann, A.; Ikonen, J.; Derksend, C.; Davydove, S.; Davydovae, A.; Boike, J.; et al. SMOS prototype algorithm for detecting autumn soil freezing. *Remote Sens. Environ.* **2016**, *180*, 346–360. [[CrossRef](#)]

19. Bhatt, U.; Walker, D.A.; Rauynolds, M.K.; Bienek, P.A.; Epstein, H.E.; Comiso, J.C.; Pinzon, J.E.; Tucker, C.J.; Steele, M.; Ermold, W.; et al. Changing seasonality of panarctic tundra vegetation in relationship to climatic variable. *Environ. Res. Lett.* **2017**, *12*, 055003. [[CrossRef](#)]
20. Essery, R. Large-scale simulations of snow albedo masking by forests. *Geophys. Res. Lett.* **2013**, *40*. [[CrossRef](#)]
21. Thackeray, C.W.; Fletcher, C.G.; Derksen, C. Quantifying the skill of CMIP5 models in simulating seasonal albedo and snow cover evolution. *J. Geophys. Res. Atmos.* **2015**, *120*, 5831–5849. [[CrossRef](#)]
22. Abe, M.; Takata, K.; Kawamiya, M.; Watanabe, S. Vegetation masking effect on future warming and snow albedo feedback in a boreal forest region of northern Eurasia according to MIROC-ESM. *J. Geophys. Res. Atmos.* **2017**, *122*. [[CrossRef](#)]
23. Warren, S. Impurities in snow: Effects on albedo and snowmelt (review). *Ann. Glaciol.* **1984**, *5*, 177–179. [[CrossRef](#)]
24. Domine, F.; Salvatori, R.; Legagneux, L.; Salzano, R.; Fily, M.; Casacchia, R. Correlation between the specific surface area and the short wave infrared (SWIR) reflectance of snow. *Cold Reg. Sci. Technol.* **2006**, *46*, 60–68. [[CrossRef](#)]
25. Ménégoz, M.; Krinner, G.; Balkanski, Y.; Cozic, A.; Boucher, O.; Ciaia, P. Boreal and temperate snow cover variations induced by black carbon emissions in the middle of the 21st century. *Cryosphere* **2013**, *7*, 537–554. [[CrossRef](#)]
26. Xu, L.; Myneni, R.; Chapin, F., III; Callaghan, T.; Pinzon, J.; Tucker, C.; Zhu, Z.; Bi, J.; Ciaia, P.; Tømmervik, H.; et al. Temperature and vegetation seasonality diminishment over northern lands. *Nat. Clim. Chang.* **2013**, *3*, 581–586. [[CrossRef](#)]
27. Wiscombe, W.J.; Warren, S.G. A model for the spectral albedo of snow. I: Pure snow. *J. Atmos. Sci.* **1980**, *37*, 2712–2733. [[CrossRef](#)]
28. Shi, J.; Dozier, J. Estimation of Snow Water Equivalence Using SIR-C/X-SAR, Part II: Inferring Snow Depth and Particle Size. *IEEE Trans. Geosci. Remote Sens.* **2000**, *38*, 2475–2488.
29. Warren, S.; Brandt, R.; Hinton, P. Effect of surface roughness on bidirectional reflectance of Antarctic snow. *J. Geophys. Res.* **1998**, *103*, 25789–25807. [[CrossRef](#)]
30. Nagler, T.; Rott, H. Retrieval of wet snow by means of multitemporal SAR data. *Trans. Geosci. Remote Sens.* **2000**, *38*, 754–765. [[CrossRef](#)]
31. Robinson, D.A.; Kukla, G. Albedo of a Dissipating Snow Cover. *J. Clim. Appl. Meteorol.* **1984**, *23*, 1626–1634. [[CrossRef](#)]
32. Robinson, D.A.; Kukla, G. Maximum Surface Albedo of Seasonally Snow-Covered Lands in the Northern Hemisphere. *J. Clim. Appl. Meteorol.* **1985**, *24*, 402–411. [[CrossRef](#)]
33. Kuittinen, R. Determination of areal snow-water equivalent values using satellite imagery and aircraft gamma-ray spectrometry. In *Hydrologic Applications of Space Technology: Proceedings of an International Workshop on Hydrologic Applications of Space Technology, Held in Cocoa Beach, FL, USA, 19–23 August 1985*; IAHS Press: Oxfordshire, UK; Institute of Hydrology: Wallingford, UK, 1986; Volume 160, pp. 181–189.
34. Rinne, J.; Aurela, M.; Manninen, T. A Simple Method to determine the timing of snow melt by remote sensing with application to the CO<sub>2</sub> balances of northern mire and heath ecosystems. *Remote Sens.* **1986**, *1*, 1097–1107. [[CrossRef](#)]
35. Solantie, R.; Drebs, A.; Hellsten, E.; Saurio, P. *Lumipeitteen tuo-, lähtö- ja Kestoaioista Suomessatalvina 1960/1961–1992/1993*; Finnish Meteorological Institute, English Summary; Meteorological publications: Helsinki, Finland, 1996; Volume 34, 159p.
36. Barlage, M.; Zeng, X.; Wei, H.; Mitchell, K.E. A global 0.05° maximum albedo dataset of snow-covered land based on MODIS observations. *Geophys. Res. Lett.* **2005**, *32*, L17405. [[CrossRef](#)]
37. Anttila, K.; Jääskeläinen, E.; Riihelä, A.; Manninen, T.; Andersson, K.; Hollman, R. Algorithm Theoretical Basis Document: CM SAF Cloud, Albedo, Radiation Data Record Ed. 2—Surface Albedo. 2016. Available online: [https://icdc.cen.uni-hamburg.de/fileadmin/user\\_upload/icdc\\_Dokumente/EUMETSAT-CMSAF/SAF\\_CM\\_FMI\\_ATBD\\_GAC\\_SAL\\_2\\_3.pdf](https://icdc.cen.uni-hamburg.de/fileadmin/user_upload/icdc_Dokumente/EUMETSAT-CMSAF/SAF_CM_FMI_ATBD_GAC_SAL_2_3.pdf) (accessed on 14 August 2018).
38. Karlsson, K.-G.; Anttila, K.; Trentmann, J.; Stengel, M.; Meirink, J.F.; Devastale, A.; Hanschmann, T.; Kothe, S.; Jääskeläinen, E.; Sedlar, J.; et al. CLARA-A2: The second edition of the CM SAF cloud and radiation data record from 34 years of global AVHRR data. *Atmos. Chem. Phys.* **2017**, *17*, 5809–5828. [[CrossRef](#)]
39. Riihelä, A.; Manninen, T.; Laine, V.; Andersson, K.; Kaspar, F. CLARA-SAL: A global 28 yr timeseries of Earth's black-sky surface albedo. *Atmos. Chem. Phys.* **2013**, *13*, 3743–3762. [[CrossRef](#)]

40. Jääskeläinen, E.; Manninen, T.; Tamminen, J.; Laine, M. The Aerosol Index and Land Cover Class Based Atmospheric Correction Aerosol Optical Depth Time Series 1982–2014 for the SMAC Algorithm. *Remote Sens.* **2017**, *9*, 1095. [[CrossRef](#)]
41. Peltoniemi, J.I.; Suomalainen, J.; Hakala, T.; Puttonen, E.; Näränen, J.; Kaasalainen, S.; Torppa, J.; Hirschmugl, M. Reflectance of various snow types: Measurements, modelling and potential for snow melt monitoring. In *Light Scattering Reviews 5: Single Light Scattering and Radiative Transfer*; Springer Praxis Books: Berlin/Heidelberg, Germany, 2010; Chapter 9; pp. 393–450. [[CrossRef](#)]
42. Eastwood, S. Sea Ice Product User's Manual OSI-401-a, OSI-402-a, OSI-403-a, Version 3.11. 2014. Available online: [http://osisaf.met.no/docs/osisaf\\_ss2\\_pum\\_ice-conc-edge-type\\_v3p11.pdf](http://osisaf.met.no/docs/osisaf_ss2_pum_ice-conc-edge-type_v3p11.pdf) (accessed on 14 August 2018).
43. Schaaf, C.B.; Gao, F.; Strahler, A.H.; Lucht, W.; Li, X.; Tsang, T.; Strugnell, N.C.; Zhang, X.; Jin, Y.; Muller, J.-P.; et al. First operational BRDF, albedo nadir reflectance products from MODIS. *Remote Sens. Environ.* **2002**, *83*, 135–148. [[CrossRef](#)]
44. Anttila, K.; Jääskeläinen, E.; Riihelä, A.; Manninen, T.; Andersson, K.; Hollman, R. Validation Report: CM SAF Cloud, Albedo, Radiation Data Record Ed. 2—Surface Albedo. 2016. Available online: [https://icdc.cen.uni-hamburg.de/fileadmin/user\\_upload/icdc\\_Dokumente/EUMETSAT-CMSAF/SAF\\_CM\\_FMI\\_ATBD\\_GAC\\_SAL\\_2\\_3.pdf](https://icdc.cen.uni-hamburg.de/fileadmin/user_upload/icdc_Dokumente/EUMETSAT-CMSAF/SAF_CM_FMI_ATBD_GAC_SAL_2_3.pdf) (accessed on 14 August 2018).
45. Riihelä, A.; Laine, V.; Manninen, T.; Palo, T.; Vihma, T. Validation of the Climate-SAF surface broadband albedo product: Comparisons with in situ observations over Greenland and the ice-covered Arctic Ocean. *Remote Sens. Environ.* **2010**, *114*, 2779–2790. [[CrossRef](#)]
46. Dee, D.P.; Uppala, S.; Simmons, A.; Berrisford, P.; Poli, P.; Kobayashi, S.; Andrae, U.; Alonso-Balmaseda, M.; Balsamo, G.; Bauer, P.; et al. The ERA–Interim reanalysis: Configuration and performance of the data assimilation system. *Q. J. R. Meteorol. Soc.* **2011**, *137*, 553–597. [[CrossRef](#)]
47. Arino, O.; Ramos, J.; Kalogirou, V.; Defourny, P.; Achard, F. GlobCover 2009. In Proceedings of the Living Planet Symposium, Bergen, Norway, 28 June–2 July 2010.
48. Böttcher, K.; Aurela, M.; Kervinen, M.; Markkanen, T.; Mattila, O.P.; Kolari, P.; Metsämäki, S.; Aalto, T.; Arslan, A.N.; Pulliainen, J. MODIS tile-series-derived indicators for the beginning of the growing season in boreal coniferous forest—A comparison with the CO<sub>2</sub> flux measurements and phenological observations in Finland. *Remote Sens. Environ.* **2014**, *140*, 625–638. [[CrossRef](#)]
49. Sturm, M.; Douglas, T.; Racine, C.; Liston, G. Changing snow and shrub conditions affect albedo with global implications. *J. Geophys. Res.-Biogeosci.* **2005**, *110*, G01004. [[CrossRef](#)]
50. Bonan, G.B.; Pollard, D.; Thompson, S.L. Effects of boreal forest vegetation on global climate. *Nature* **1992**, *359*, 716. [[CrossRef](#)]
51. Rigina, O. Environmental impact assessment of the mining and concentration activities in the Kola Peninsula, Russia by multivariate remote sensing. *Environ. Monit. Assess.* **2002**, *75*, 11–31. [[CrossRef](#)] [[PubMed](#)]
52. Piao, S.; Wang, X.; Ciais, P.; Zhu, B.; Wang, T. Changes in satellite-derived vegetation growth trend in temperate and boreal Eurasia from 1982 to 2006. *Glob. Chang. Biol.* **2011**, *17*, 3228–3239. [[CrossRef](#)]
53. Buitenwerf, R.; Rose, L.; Higgins, S. Three decades of multi-dimensional change in global leaf phenology. *Nat. Clim. Chang.* **2015**, *5*, 364–368. [[CrossRef](#)]
54. Bullard, J.; Baddock, M.; Bradwell, T.; Crusius, J.; Darlington, E.; Gaiero, D.; Gassó, S.; Gisladottir, G.; Hodgkins, R.; McCulloch, R.; et al. High-latitude dust in Earth system. *Rev. Geophys.* **2016**, *54*, 447–485. [[CrossRef](#)]
55. Helbig, M.; Wischnewski, K.; Kljun, N.; Chasmer, L.E.; Quinton, W.L.; Detto, M.; Sonntag, O. Regional atmospheric cooling and wetting effect of permafrost thaw-induced boreal forest loss. *Glob. Chang. Biol.* **2016**, *22*, 4048–4066. [[CrossRef](#)] [[PubMed](#)]
56. Myers-Smith, I.H.; Elmerdorf, S.; Becl, P.; Wilmking, M.; Hallinger, M.; Blok, D.; Tape, K.D.; Rayback, S.A.; Macias-Fauria, M.; Forbes, B.C.; et al. Climate sensitivity of shrub growth across the tundra biome. *Nat. Clim. Chang.* **2015**, *5*, 887–891. [[CrossRef](#)]







**FINNISH METEOROLOGICAL INSTITUTE**

Erik Palménin aukio 1  
P.O. Box 503  
FI-00101 HELSINKI  
tel. +358 29 539 1000  
**WWW.FMI.FI**

FINNISH METEOROLOGICAL INSTITUTE

CONTRIBUTIONS No. 149

ISBN 978-952-336-063-1 (paperback)

ISSN 0782-6117

Erweko

Helsinki 2019

ISBN 978-952-336-064-8 (pdf)

Helsinki 2019

